A quantum-mechanical study of the dynamical properties of spin-ice materials

A thesis submitted for the degree of
Doctor of Philosophy

by

Bruno Tomasello

School of Physical Sciences

University of Kent

Canterbury
UK

November 2014

Dedicato a Maya, Beatrice e Luca

Declaration

This thesis has not been submitted as an exercise for a degree at any other university.

Except where stated, the work described therein was carried out by me alone.

I give permission for the Library to lend or copy this thesis upon request.

SIGNED:

Acknowledgements

I wish to open my acknowledgements with the following expression:

$$\frac{|\mathcal{JQ}\rangle \otimes |\mathcal{CC}\rangle + |\mathcal{CC}\rangle \otimes |\mathcal{JQ}\rangle}{\sqrt{2}} ,$$

where $|\mathcal{JQ}\rangle$ stays for Jorge Quintanilla, my main adviser, and $|\mathcal{CC}\rangle$ stays for Claudio Castelnovo, my "unofficial" co-adviser. By this I mean to express symbolically the gratitude I feel for the work I have accomplished during these years thanks to their patience and perseverance. I feel they are best represented in a "maximally entangled state" as for me it is very hard to separate the advices I received from one without thinking to the contribution of the other. Sincerely, thanks a lot.
On this note I acknowledge SEPnet, not only for funding my PhD, but also for setting up the network that has given to me the chance to meet both of them.

I also wish to thank Prof. Roderich Moessner for his continuous interest on the project of my PhD, for his original inputs on the study itself and for his generous availability in hosting me in Dresden at the Max Planck Institut für Physik komplexer Systeme during these last two months. The time I have spent here has been incredibly productive.

I am very grateful to my co-adviser Sean Giblin for being always present for me during my years at the ISIS neutron source. I have very nice memories of our discussions about physics and of the good times together.

I want to acknowledge Lucian Pascut for helping me so much in studying the crystal-field theories that I used in this work. Even more for being a very good friend throughout these years and for helping me to find a basketball team and friends in Oxford.

I'm glad I have had some PhD fellows around during these years. It may be "essential" but I simply want to give their names (in alphabetical order) in memory of the time I have enjoyed with them: Alex, Agata, Atahl, Bayan, Benjamin, Francesco, Gabriele, Giovanni, Hannah, Jimmel, Joe, Jordi, Morena, Paul, Vickaran, and many others.

I am very thankful to the members of my family. To the "new" members even more! The memories of the time spent together are a great source of good company abroad.

I am grateful to the people I lived with during these years. From the very first months in Didcot through the two years in Oxford and the last one in Canterbury, I feel very lucky in having found some close friends among them.

I'd like to conclude these acknowledgements by thanking my Italian friends in London. They represent for me the link joining my old life in Catania with the more recent one abroad. They also deserve acknowledgements for hosting me in their homes during the conferences held in the City.

Summary

The spin-ice materials $Ho_2Ti_2O_7$ (HTO) and $Dy_2Ti_2O_7$ (DTO) are part of a large family of compounds called magnetic pyrochlore oxides. Typically, the magnetism of these systems arises from the rare-earth ions (RE^{3+}) which sit at the vertices of a lattice of corner-sharing tetrahedra and couple with the degrees of freedom of the crystal leading to a wide spectrum of exotic phenomena.

In spin-ices the magnetic moments of the individual RE^{3+} ions are large enough to let their mutual dipolar interactions be the leading factors for the thermodynamics. Moreover, the strength and the symmetries of their local crystalline environment are such that each ion behaves like a magnetic dipole with only two allowed configurations: it points either parallel or opposite to the axis joining the vertex where it sits to the centre of the tetrahedron. As a result, the ground state of the system is macroscopically degenerate because the ferromagnetic interactions between the 4 Ising-like spins in each tetrahedron cannot be satisfied simultaneously, and, in turn, the manifold of possible configurations minimising the energy (2 spins inward - 2 spins outward) increases with the size of the system. This exotic ground state is such that the Ising configurations of the dipoles map to the disordered vector-displacements of the protons in the water molecules of conventional ice; hence the name spin-ice. Violations of the (2in-2out) ice rules take the systems out of the ground state into more energetic configurations. More precisely, the flipping of a spin between two adjacent ground-state tetrahedra creates a local excitation (1in-3out in a tetrahedron, 3in-1out in the neighbouring one) that is made of two fractionalised opposite magnetic fluxes. Once the two fluxes are created they can separate and freely hop across the lattice as their motion does not involve any higher order violation of the ice-rules. The low temperature properties of spin-ice depend heavily, if not exclusively, on the density and mobility of such flux-defects which effectively behave as magnetic monopoles mutually interacting via a Coulomb potential.

Beside the success of many experiments which exploit the physics of the monopoles in their exclusively classical formulation, there has been an increasing curiosity about the microscopic mechanisms which dictate their propagation across the lattice. At present,

the dynamics of the monopoles are still puzzling showing different responses under different probes and non-identical behaviours between the two compounds HTO and DTO. As the monopoles themselves consist of packed magnetic fluxes originating from the magnetic moments of the RE^{3+} ions, investigating the microscopical mechanisms underlying their motion requires revisiting the foundations of the classicality which emerges from the quantum substrate of the interactions of the magnetic ions. This is the subject of the work presented in this thesis.

With particular focus on the interplay between the local crystal-symmetries and the mutual interactions between the RE^{3+} ions, the present study gives an accurate description of the microscopic mechanisms which occur in the pyrochlore substrate in the presence of a monopole. The results suggest that the motion of the monopoles is achieved thanks to the spin-tunnelling of the RE^{3+} ions which accounts for the flipping of the Ising spins, necessary for the propagation of a monopole. A major improvement, compared to the standard theory of spin ice, is the role of the exchange interactions that are overcome by the dipolar ones in the ice-state but possess a dynamical resilience which manifests in the presence of a monopole. Furthermore, the present study brings to light the articulated statistical structure of the kinematic spin-constraints which are expected to dictate the diffusion of the free monopoles and their response under different probes also in conditions out of equilibrium. From a more general perspective, the mathematical and physical models developed during this work promise to be of interest also in other magnetic systems. Primarily, in the other pyrochlore oxides whose microscopical structure is akin to the spin-ice one; secondarily, in other RE^{3+} compounds where the interplay between quantum and classical physics leads to the manifestation of unusual dynamical effects.

Contents

List of Tables

List of Figures

"We expect to encounter fascinating and, I believe, very fundamental questions in fitting together less complicated pieces into a more complicated system and understanding the basically new types of behavior that can result."

P.W. Anderson [1]

1 Introduction

"Condensed matter physics is a branch of physics which studies systems of many particles in the 'condensed' (i.e. solid or liquid) states" [2]. As such, this discipline characterises different compounds by analysing the collective behaviour they display in the different states of matter. The various states which the system can possess are called *phases*, and their characterisation is ultimately defined by the observable thermodynamics. In this perspective, it is often the case that systems which may look very diverse are characterised by the same phases because of the similarities they exhibit in their collective response to the respective external parameters [3]. This implies that the character of a given phase does not necessarily reflect directly the actual state of *agglomeration* of the entities constituting the system, but it merely refers to the state of the degrees of freedom which couples to the external tuning parameters.

In magnetic systems, for example, it is typical to distinguish between liquid, gas phases, etc., without referring to the actual state of the individual molecular, atomic or subatomic bodies in the system. Terms such as spin-liquid, spin-glass, etc. instead refer to the type of behaviour observed in the magnetism of a given material under certain conditions. The conditions themselves are typically characterised by varying different external parameters which pertain also to the local constituents of the material and in effect dictate its state as an agglomerate. Usually, however, these are tuned to probe specific degrees of freedom of the system within very specific ranges of parameters in order not to create conflicts with the self organisation of the constituents. This is one of the reasons why the experimental settings for investigating the exotic properties of novel magnetic compounds typically require low temperatures, namely to guarantee the actual stable phase of a given magnetic compound and "immerse" the system into a particular state which allows the neat observation of the phenomena of interest.

A more general characterisation often used to characterise the different phases of a system is the change of symmetries which occur in phase transitions. In this context the system is described as entering in a phase where a symmetry is partially or totally lost

with the consequent occurrence of a reorganisation of the available degrees of freedom.

A very original class of magnetic systems are the so called spin-ice materials. In these systems, at very low temperatures, the magnetic degrees of freedom impose reciprocally a very unusual kind of "constrained freedom" and, as such, they are said to be *frustrated*.

Geometrical frustration occurs in any physical system whose constituents are arranged in such a way that it is impossible to minimise all the pairwise interactions simultaneously [4]. An archetypical case is shown in Fig. 1.1 where the frustration arises from the antiferromagnetic interaction of Ising spins sitting at the vertices of an equilateral triangle: the two spins at the bottom minimise their mutual interaction by pointing in opposite directions; however, a third spin at the top vertex leads to frustration in the system since a spin configuration which minimises the interaction energy with one maximises it for the other. Moreover, extending the size of the system, for example by making a two dimensional lattice of triangles with antiferromagnetic Ising spins would lead to a larger frustration that can be estimated in the existence of non-zero entropy of the ground state found from the amount of equivalent (frustrated) configurations which minimise the energy of the system.

Spin-ice materials represent a three-dimensional realisation of a frustrated spin system with ferromagnetic interactions [5]. As shown in Fig. 1.2C the three-dimensional lattice consists in a network of corner sharing tetrahedra hosting the magnetic degrees of freedom (spins) at the vertices joining them. The tetrahedral arrangement of the network (pyrochlore lattice) is not exclusive of spin-ices; it characterises a large family of compounds that are called magnetic pyrochlore oxides [6, 7]. The various pyrochlores differ from each other in their chemical elements and in the anisotropies which characterises the ions carrying the magnetic degrees of freedom. Different compounds have, in general, different magnetic properties which span from superconductors, spin-glasses, spin-liquids, etc. This thesis is only focused on the spin-ice materials $Ho_2Ti_2O_7$ (HTO) and $Dy_2Ti_2O_7$ (DTO). In both systems the magnetic ions are only the rare earths (RE), Ho^{3+} for the former and Dy^{3+} for the latter. In the periodic table these are the elements with the largest magnetic moments ($|\mathbf{m}| \approx 10\mu_B$) in the lanthanide series (RE). As such, once the spin-ice crystal is formed they sit at the vertices of the pyrochlore lattice and, because of the local crystalline fields, they assume a very peculiar

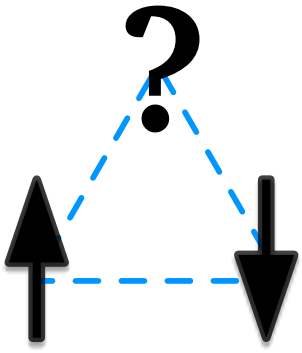

Figure 1.1: Frustration in the antiferromagnetic interaction between spins in an equilateral triangle. Either of the two allowed (up or down) states for a third spin on the upper vertex leads to a frustrated configuration in the triangle, hence the symbolic question mark.

type of anisotropy: each spin can either point inward or outward a tetrahedron only in the direction of the axis (the local $\langle 111 \rangle$) joining the vertex to the centre of the tetrahedron. From these anisotropies and the dipolar interactions which give a net ferromagnetic nearest neighbour (n.n.) coupling to the spins, the spin-ice ground state is characterised by a manifold of degenerate states where each tetrahedron has to satisfy the so called ice-rules: two of the spins point in, the other two point out (2in-2out) [5].

The name spin-ice was coined because of the type of frustration that was measured from the zero-point entropy (in Ref. [8] it was found $S_0 = \frac{R}{2}\ln(\frac{3}{2})$, the same as the Pauling estimation for water-ice) and allowed a direct mapping between the 2in-2out configurations and the disorder arrangement of the protons in the water molecules of ordinary ice [9, 10] (see Fig. 1.2A,B). A particular signature of what is now considered the spin-ice physics, was the lifting of the ground state degeneracy under applied magnetic field and the discovery of a liquid-gas type transition which, as a first order phase transition, justified the absence of a long ranged ordered ground state as the consequence of the absence of a broke symmetry change of phase [11]. Soon after the pattern found in diffuse neutron scattering experiments confirmed the absence of long range order and the leading role of the long ranged dipolar interactions in the spin-ice ground state physics [12].

The frustration of the ground state was later understood in a simplified view which has characterised ever since the history and understanding of the spin-ice physics. Starting from the ground state manifold where all tetrahedra obey the ice-rules, in Ref. [13] it was shown that energy excitations above the ground state behave as localised singularities of magnetic flux which can be deconfined across the lattice. The frustration of the ground state, is due to the absence of the monopoles which are the only dynamical objects allowed by the topological constraints of the system. In other words the spin-ice ground

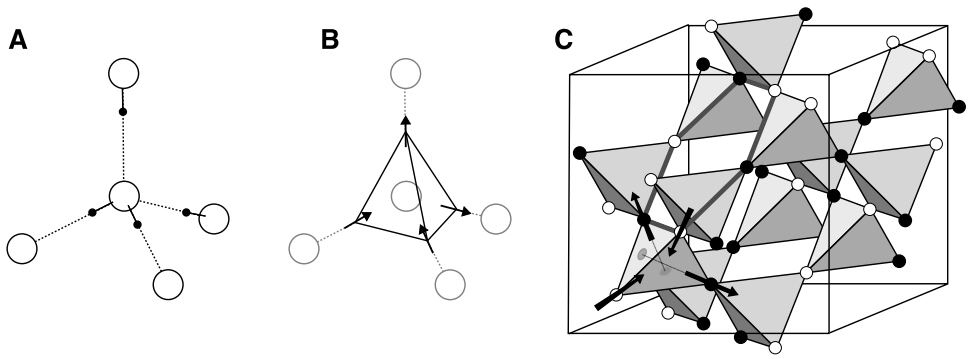

Figure 1.2: This figure is from Ref. [5]. The diagram **A** illustrates a water molecule in the tetrahedral coordination of the ice structure with proton positions located by displacement vectors that occupy a lattice of linked tetrahedra (two protons near-two protons far). **B** shows the case of spin ice where the displacement vectors are replaced by rare earth (RE) magnetic moments ("spins") sitting at the vertices of the coordination tetrahedron (two spins in-two spins out). **C** illustrates the pyrochlore lattice of corner-sharing tetrahedra, as occupied by the magnetic RE^{3+} ions in the spin ice materials (magnetic dipoles on the vertices pointing along the local $\langle 111 \rangle$ axis). The filling colour for the vertices of the tetrahedra accounts for the direction of the local spin and reproduces the ice-rules in this lattice: 2 white (in) 2 black (out).

state can be defined as the vacuum for the monopoles. The mapping between dipoles and dumbbells of magnetic charges shown in Fig. 1.3, demonstrated that the magnetic defects can hop across the lattice by flipping adjacent spins as a direct consequence of the topological properties and the anisotropy of the spins on the pyrochlore lattice. Moreover it was also realised that they mutually interact via a Coulomb potential, that is also the reason why these magnetic defects are commonly called *magnetic monopoles*. The magnetic monopoles then, consist of local violations of the ice rules, and remarkably they are quasiparticles localised in real space. The charge of the monopoles is defined exploiting the dumbbell model as $Q_\alpha = \pm 2|\mathbf{m}|/a_d$ with $|\mathbf{m}|$ magnitude of the magnetic moment of the dipole and a_d the distance between the centres of two neighbouring tetrahedra. One of the first insights brought by the picture of the monopole was the explanation for the occurrence of a liquid-gas phase transition observed previously in Ref. [14].

After the discovery of the monopoles a large variety of experiments verified the consistency of their description. The first experiments involved neutron scattering techniques to detect the Coulomb phase [15] and the traces of flipped spins the monopoles were leaving under applied fields [16]. Soon after it was also proposed and measured via muon-spin-rotation that the motion of the monopoles occurs as in a weak electrolyte using the theory of Onsager for the Wien effect [17]; this was later contrasted by other measurements done with analogous probes [18]. A considerable experimental effort has been carried in trying to determine the dynamics of the monopoles under different kinds of experimental setup. Some of these are based on ac-susceptibility techniques [19, 20], other on squid-interferometry by studying the relaxations timescales after an applied magnetic field is removed [21]. Other setups include the use of non-equilibrium techniques such as thermal quenches [22], magnetic field quenches [23] and more recently magnetothermal avalanche quenches [24].

The common response found in all experiments is that the relaxation timescales are

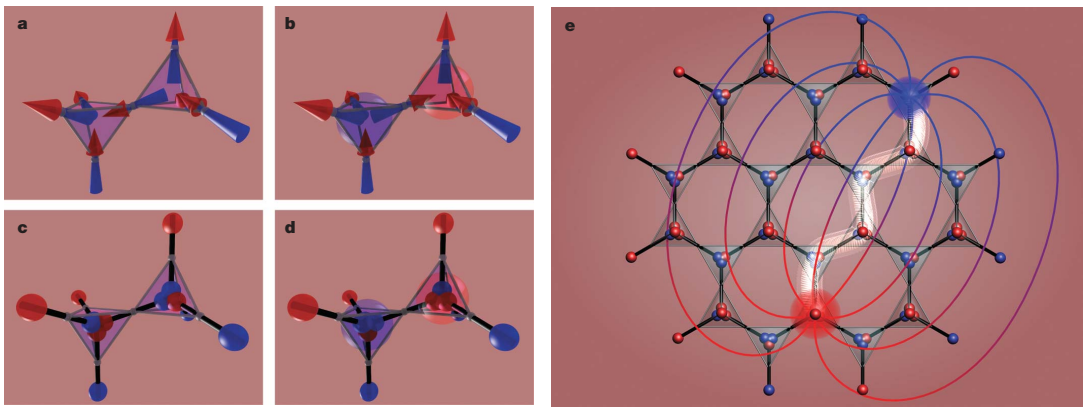

Figure 1.3: This figure is from Ref. [13]. The left hand side shows the dumbbell picture (c,d) obtained by replacing each spin in a and b by a pair of opposite magnetic charges placed on the adjacent sites of the diamond lattice. Note the different configurations between the ground state (2in-2out in a, no charges in c) and the excited state (central shared spin flipped in b, bound pair of magnetic monopoles in d). On the right panel (e) a pair of separated monopoles generates a magnetic field. Highlighted in white is the chain of inverted dipoles connecting them.

very slow, showing that the mobility of the monopole is heavily constrained by the underlying spin structure of the pyrochlore lattice. Furthermore several experiments measured more than one slope in the relaxation times, suggesting the occurrence of more than a single mechanism regulating the propagation of the monopoles. However, from a general perspective the picture of the monopole motion remains still an open question. A theoretical model to account for the microscopic physics regulating the propagation of the monopoles is needed to be able to answer the current puzzles. This thesis gives a microscopic description of the physics which governs the magnetic ions regulating the monopole dynamics. The main question to address is: which are the mechanisms leading to a spontaneous flipping of a spin in the presence of a monopole?

The minimal model to investigate this and related questions has to include nearest-neighbour exchange and long-range dipole-dipole interactions as in Refs. [12, 5]

$$H = \frac{J}{3}\sum_{\langle ij\rangle} S_i S_j + D r_{nn}^3 \sum_{(ij)} \left[\frac{\mathbf{z}_i\cdot\mathbf{z}_j}{|\mathbf{r}_{ij}|^3} - \frac{3(\mathbf{z}_i\cdot\mathbf{r}_{ij})(\mathbf{z}_j\cdot\mathbf{r}_{ij})}{|\mathbf{r}_{ij}|^5}\right] S_i S_j, \tag{1.1}$$

where, each of the variables $S_i = \pm 1$ describes a classical Ising spin sitting at site i defined along the local $\langle 111\rangle$ axis, and the sum over $\langle ij\rangle$ runs only over nearest neighbour pairs as opposed to (ij) which is over all pairs across the lattice (no double counting in both cases). Typically the convention requires that $S_i = +1$ ($S_i = -1$) if the spin is parallel (antiparallel) to the unit vector $\mathbf{z}_i$ which points from a vertex of the reference tetrahedron towards the centre (a set of $\mathbf{z}_i$ for the sites of a tetrahedron will be given in Eq. (4.22)). r_{ij} is the distance between any two spins on sites i and j and r_{nn} separates two neighbouring spins and set the scale of the pyrochlore lattice.

In the real compounds, $Ho_2Ti_2O_7$ (HTO) and $Dy_2Ti_2O_7$ (DTO), the Ising degrees of freedom arise from the magnetic moments $\boldsymbol{m}_i = mS_i\mathbf{z}_i$ of the RE^{3+} ions, respectively Ho^{3+} and Dy^{3+} ions, which are forced by the local crystal-field symmetry to point either in or out of a tetrahedron as pictorially represented in Fig. 1.2. The magnitude $|\mathbf{m}| \approx 10\mu_B$, with μ_B the Bohr magneton, and the nearest neighbour distance $r_{nn} \approx 3.54$Å sets the energy scale for the dipolar interaction to $D = \mu_0 m^2/4\pi r_{nn}^3 = 1.41$K. In contrast, the (antiferromagnetic) exchange coupling is measured experimentally as $J \approx -1.56\text{K}, -3.72\text{K}$, respectively, for HTO and DTO.

This model accurately predicts the 2-in/2-out spin ice ground state manifold [5] and a finite density of magnetic monopole excitations at finite temperatures [13]. A good understanding of the observed dynamics can be obtained by inserting phenomenologically an adjustable monopole hopping time τ and studying the simulated time-evolution of the model described by Eq. (1.1) through discrete steps of that duration [25, 26].

On the other hand, the above model per se does not lead to spin flip dynamics. At the classical level, a purely transverse field on a spin makes the two states $S_i = \pm 1$ degenerate. Quantum-mechanically, the transverse field induces a finite splitting ΔE_{01} between approximate bonding and anti-bonding combinations of these states which in turn leads to a finite spin-flip timescale

$$\tau \sim h/\Delta E_{01} \tag{1.2}$$

for spontaneous quantum mechanical tunnelling between the $S_i = +1$ and $S_i = -1$

states. This calls for a study of the quantum dynamics of an individual RE spin in the presence of a purely-transverse magnetic field in these materials as a way to estimate the parameter τ. That is the main subject of the present work.

To build a realistic model for the quantum mechanics in spin-ice materials it is necessary to go beyond the Ising dipolar approximation and take into account the quantum mechanical properties of the magnetic ions that are expected to exhibit quantum dynamics. In simple words, it is necessary to revisit the fundamental structure of the RE^{3+} ions immersed in the crystalline environment of spin-ice materials, with the aim to understand how the local properties of the system are modified by the presence of a monopole. To achieve this task it is necessary to understand more about the magnetism of a RE^{3+} ion.

The magnetism of the rare earths has its origin in the angular momenta of the 4-f electrons in the atoms [27]. To investigate the real dynamical degrees of freedom of the Ising dipoles which account for the propagation of the monopoles it is necessary to study the microscopic structure characterising the environment of the RE^{3+} ions. This, as shown in the following, consists in revisiting the Schrödinger equation which governs the electrons in the 4-f shell of the magnetic ions. More exactly, it requires to assess which kind of representation is the most suitable to adopt for describing the magnetic states resulting from the interaction of the RE^{3+} ion with its crystal-field environment.

The notion of the *crystal-field* (CF) potential is based on the crucial assumption that any bound ion feels the global interaction of its surroundings in the form of a one-electron potential [28]. Then, the effective Hamiltonian of the open-shell electrons of a metal ion (in SI units) reads

$$\hat{H} = \sum_{i=1}^{n} \left[-\frac{\hbar^2}{2m_e}\hat{\nabla}_i^2 - \frac{k_e\, Ze^2}{|\hat{\boldsymbol{r}}_i|} \right] + \sum_{i>j}^{n} \frac{k_e\, e^2}{|\hat{\boldsymbol{r}}_i - \hat{\boldsymbol{r}}_j|} + \sum_{i=1}^{n} \zeta(|\boldsymbol{r}_i|)\, \hat{\mathbf{l}}_i \cdot \hat{\mathbf{s}}_i - e\sum_{i=1}^{n} V_{ext}(\hat{\boldsymbol{r}}_i) \quad (1.3)$$

where the summation is limited to the open-shell electrons only, the n electrons in the 4-f shell for a RE^{3+} ion ($\boldsymbol{r}_i$ is the coordinate of the i-th electron with charge e and mass m_e in the reference frame centred in the nucleus of the ion; $k_e = 1/4\pi\epsilon_0$ is the Coulomb constant). The Hamiltonian in Eq. (1.3) consists of the *free-ion* part and the *ion-crystal interaction* part. The former includes, in sequence of appearance, the kinetic energy of the electrons, their spherically symmetric potential energy, the inter-electron mutual Coulomb interaction and the spin-orbit coupling energy; the latter accounts solely for the interaction of electrons from the central ion with the surrounding environment in the crystal. The so called crystal-field potential, which accounts for the electrostatic interaction of the electrons in the ion with the neighbouring ligands, plays the leading role in such ion-crystal interaction V_{ext} [27, 28, 29].

Exact solutions of the Schrödinger equation for the Hamiltonian in Eq. (1.3) are not possible. Nonetheless, an ensemble of symmetry-based assumptions together with phenomenological parametrisation for the effective degrees of freedom of the magnetic ions allow a meaningful description for the physics observed in a large variety of rare-earth and transition-metal complexes [28].

Firstly, in the framework of the *central field* approximation, one assumes that it is possible to construct a potential energy function $V_c(\boldsymbol{r}_i)$ which is a spherically symmetric one-electron operator and is a good approximation to the actual potential energy of

the i-th electron in the field of the nucleus and the other $n-i$ electrons [29]. Moreover, the spherically symmetric part of the potential from the surrounding ligands can also be absorbed in the central potential $V_c(\boldsymbol{r}_i)$, since, even if dominating because of its magnitude, it causes no energy splittings of the electronic levels. This assumption is not a priori obvious particularly considering various complications arising from non-orthogonality of interacting states and possibility of different electronic excitations which could should mix the free-ion states. Fortunately, it has turned out, that a phenomenological parameterisation of crystal-field effect by means of the one-electron potential expanded in the series of spherical tensor operators works exceptionally well [28].

Secondly, to construct the wave functions for a multi-electron atom on the basis of the central field approximation, one needs to choose a coupling scheme of momentum summation to determine the wave functions of the n independent electrons. For the 4-f electrons of RE^{3+} ions it is convenient to adopt the *Russell-Saunders* coupling scheme where the spins $\hat{\mathbf{s}}_i$ of the individual electrons are coupled by their exchange interactions in the total spin $\hat{\mathbf{S}}$, while the direct Coulomb interaction similarly combines the $\hat{\mathbf{l}}_i$ into the total orbital momentum $\hat{\mathbf{L}}$. Then, the *Hund's rules* dictate how to combine these in the total angular momentum $\hat{\mathbf{J}} = \hat{\mathbf{L}} + \hat{\mathbf{S}}$ depending on the number n of electrons in the f subshell [29, 27].

In the context of trivalent rare earth ions, the Russell-Saunders coupling describes completely a given electronic state as a linear combination of the basis

$$|f^n SLJM_J\rangle \equiv |M_J\rangle\,, \tag{1.4}$$

where L, S and J are the (conserved) quantum numbers for, respectively, the orbital ($\hat{\mathbf{L}}$), the spin ($\hat{\mathbf{S}}$) and the total ($\hat{\mathbf{J}}$) angular momenta of the system of n electrons in the f shell. $M_J = -J, -J+1, \ldots, J$ are the allowed quantum numbers for the projection of the total angular momentum along the quantisation axis. A table with the (ground state) values of J, L, S for the trivalent RE^{3+} ions can be found in Ref. [27]; for Ho^{3+} and Dy^{3+} ions these are respectively $8, 6, 2$ and $15/2, 5, 5/2$.

As we shall see in the rest of thesis, the Hamiltonians and all the other quantum mechanical observables are described in terms of the angular momentum operators acting on such representation of kets. These are defined in the following set of equations:

$$\hat{J}^2\,|M_J\rangle = J(J+1)\,|M_J\rangle \tag{1.5a}$$

$$\hat{J}_z\,|M_J\rangle = M_J\,|M_J\rangle \tag{1.5b}$$

$$\hat{J}_\pm\,|M_J\rangle = \sqrt{J(J+1) - M_J(M_J \pm 1)}\,|M_J \pm 1\rangle\,, \tag{1.5c}$$

with,

$$\hat{J}^2 \equiv \hat{J}_x^2 + \hat{J}_y^2 + \hat{J}_z^2 \tag{1.5d}$$

$$\hat{J}_+ \equiv \hat{J}_x + i\,\hat{J}_y \tag{1.5e}$$

$$\hat{J}_- \equiv \hat{J}_x - i\,\hat{J}_y\,, \tag{1.5f}$$

where the angular momentum operators are expressed as dimensionless operators[1].

The theoretical study presented in this thesis starts with the effective crystal-field Hamiltonian $\hat{\mathcal{H}}_{CF}$ for Ho^{3+} and Dy^{3+} in spin-ice materials. As thoroughly discussed in Chapter 2, such Hamiltonian includes all the electrostatic effects in Eq. (1.3) and characterises each system with a set of phenomenological parameters which can be measured by different experimental means, ideally by inelastic neutron scattering.

The two (classical) Ising states $S_i = \pm 1$ of the individual spins in Eq. (1.1), correspond to the two (quantum) states of the ground state doublet of $\hat{\mathcal{H}}_{CF}$ in $Ho_2Ti_2O_7$ and $Dy_2Ti_2O_7$ which are strongly polarised in both systems ($|\psi_0\rangle \approx |+J\rangle\,, |\psi_1\rangle \approx |-J\rangle$). In general, only one of two is selected by the presence of a dipolar field longitudinal to the local Ising axis, that is typical in the spin-ice state and act as a "projective" perturbation on the crystal-field Hamiltonian by splitting the energy for the two opposite configurations. Nonetheless, as we shall see in the rest of this thesis, since the RE^{3+} ions are intrinsically quantum mechanical objects, transitions between the two opposite states can occur spontaneously because of the perturbation carried by a monopole which quenches the longitudinal field and leaves a purely transverse one. The results of this theory suggest that, although the monopoles emerge from the (classical) substrate of frozen RE^{3+} ions, their propagation across the lattice has a local quantum-dynamical impact on the degrees of freedom of a RE^{3+} ion which in turn characterises the mechanisms dictating the hopping of the monopoles themselves.

Structure of the thesis

The original work presented in this thesis is distributed throughout the following four chapters (2,3,4,5). Conclusions and an outlook for research in this field are immediately afterwards, in Chapter 6. Appendix A and Appendix B complement, respectively, Chapter 2 and Chapter 4. In the following paragraphs the content of each chapter is summarised separately with references guiding the reader through the thesis.

Chapter 2 focuses on the emergence of quantum-dynamics in spin-ice pyrochlore oxides. The first part of the chapter (sections 2.1-2.3) discusses how the Ising character of the individual RE^{3+} ions, i.e. the classical spins in Eq. (1.1), results from the coupling of their spin-orbit degrees of freedom with the *crystalline* environment hosting them. The remaining part of the chapter presents a study of the quantum-mechanical effects due to the interplay between perturbative magnetic fields and local symmetries of the crystal. This culminates in section 2.5 which analyses the (quantum) *spin-tunnelling* between the two (classical) Ising configurations of a spin-ice RE^{3+} ion under magnetic fields *transverse* to the local Ising axis.

Chapter 3 investigates the internal magnetic fields resulting on the RE-sites of spin-ice materials from the *dipolar* interactions between the magnetic moments of the RE^{3+} ions. The general form of such interaction is derived in section 3.1, while section 3.2 gives a detailed study of the dipolar fields resulting on the RE-sites in the presence of a *monopole*. Such study, conducted over pyrochlore-clusters of two distinct sizes, reveals different *statistical weights* of the spin configurations on the resulting fields on the RE-

[1] This, as we shall see, is a convenient choice for the rest of the thesis as it allows a straightforward description of the crystal-field interactions by tabulated matrix elements and experimentally fitted parameters.

sites next to a monopole. The two-tetrahedra cluster (section 3.2.2.1) shows that, in a RE-coordination tetrahedron hosting a monopole, of the three spins which are energetically and topologically allowed to flip two experience a magnetic field purely transverse to the local Ising axes, while the other has an identically null resulting field. The eight-tetrahedra cluster (section 3.2.2.2) confirms these results, modulo minor perturbations, suggesting that the monopoles stimulates only *locally* the quantum dynamics of (a fraction of) the surrounding RE^{3+} ions.

Chapter 4 is a study of the most "intimate" quantum-mechanical interaction between neighbouring RE^{3+} ions: the effective magnetic coupling arising from the *virtual exchange* of electrons. Firstly, in section 4.1, following the common (classical) approximation which treats the RE^{3+} ions as antiferromagnetically coupled magnetic moments, a toy-model is used for studying the effective-exchange between nearest neighbours spins distributed on a pyrochlore lattice with local Ising anisotropies. The resulting fields found on a RE-site next to a monopole have exactly the same statistics obtained from the dipolar fields in Chapter 3. The implications on the quantum dynamics due to the strength of the resulting fields, however, undermine the classical approximation and call for a fully quantum-mechanical model which is thoroughly derived in sections 4.2-4.5. These sections exploit and generalise the approach conducted by S. Onoda and Y. Tanaka in Ref. [30] for similar pyrochlore oxides exhibiting collective quantum fluctuations. Section 4.2 provides the mathematical framework necessary to formulate the hybridisation Hamiltonian between the magnetic RE^{3+} ions on the pyrochlore lattice and the interconnected oxygen ions (O1) on the diamond lattice (the latter mediate the virtual exchange of electrons between the former). Section 4.3 gives such a *hybridisation* Hamiltonian in the formalism of many-body fermionic operators. Section 4.4 describes a strong-coupling perturbation theory which generalises the work of Onoda et al. in Ref. [30] to obtain a fully quantum-mechanical Hamiltonian for the exchange coupling between RE^{3+} ions in a pyrochlore oxide. Finally, in section 4.5, this (many-body) exchange Hamiltonian is converted to a (one-body) *quasi-quantum* model which leads to a straightforward implementation with the models in Chapter 2 and Chapter 3.

Chapter 5 gathers up the theoretical models presented in the preceding chapters to give a realistic description of the quantum spin-flip which underpins the hopping of a monopole in spin-ice. Section 5.1 presents an original model of *quantum-quench* which implements both dipolar and effective-exchange fields in the time-evolution of a quantum-mechanical RE^{3+} ion next to a monopole. Section 5.2 discusses the implications of this model in the more general context of a monopole propagating through the lattice by means of consecutive spin-flips. The results, at least in a short-ranged view, seem to suggest the following two deductions: i) the (random) walk of a monopole acquires a correlated character from the statistics in the arrangements of the spins that the monopole finds on its way; ii) the consecutive spin-flips consist of quantum mechanical RE^{3+} ions which, because of environment-induced decoherence [31], cannot maintain long-timed quantum dynamics and therefore collapse in more stable (classical) states.

Chapter 6 concludes the whole thesis by highlighting the original results presented in the main chapters and suggesting possible directions for future work on spin-ice and related physical systems.

Funding institutions and technical support

The study and related work presented in this thesis has been funded, primarily, by *SEPnet* (UK, sepnet.ac.uk) and, secondarily, by the *Max Planck Institut für Physik komplexer Systeme* (MPI-pks, Germany, mpipks-dresden.mpg.de).

The computer-based calculations for this work have been performed by means of *GNU-Octave* (open source – gnu.org/software/octave) and *Mathematica* (under licence of MPI-pks).

The original figures presented in this thesis have been produced using the following computer-graphic utilities:

- *GNUplot* — official page at gnuplot.info (open source) — command-line driven graphing utility;
- *VESTA* — official page at jp-minerals.org/vesta (open source) — 3D visualisation program for structural models;
- *Mathematica* — official page at wolfram.com/mathematica (MPI-pks licence) — front-end computer algebra fitted with a 3D visualisation interface;
- *OmniGraffle* — official page at omnigroup.com/omnigraffle (home edition) — diagramming software and digital illustration application.

The thesis itself is written by means of *MacTeX* (tug.org/mactex), a free software distribution for front-end typing in LaTeX.

"As it results from the very nature of things, the spherical symmetry of the surroundings of a site in a crystal lattice or an atom in a molecule can never occur. Therefore, the eigenfunctions and eigenvalues of any bound ion or atom have to differ from those of spherically symmetric respective free ions. In this way, the most simplified concept of the crystal field effect or ligand field effect in the case of individual molecules can be introduced."

J. Mulak, Z. Gajek [28]

2

The crystalline environment of a RE^{3+} ion in spin ice: a playground for emerging magnetodynamics

The study of the crystal-field interactions is often the starting point for the characterisation of new phases of matter in condensed matter systems. In spin ice, summarising, the interaction between RE^{3+} ions with large dipolar moments and their electric crystalline environment sets the physical constraints driving the emergence of frustration in a system which otherwise would typically freeze in a broken-symmetry ordered phase [5]. This means that in general by studying the single-ion CF interactions of the magnetic atoms in spin ices, it is possible to revisit the physical mechanisms behind the classical Hamiltonian in Eq. (1.1), thereby, in principle, opening up the investigation of open questions from original points of view.

Since the population and the motion of the monopoles proposed in Ref. [13] is controlled by flipping (real) individual RE^{3+} spins with large total angular momentum J, it is necessary to investigate how, and whether, a transition from a polarised "Ising-like" state to the other can be achieved even against the very strong crystal field barrier separating the two states. To tackle these questions we describe the single-ion interaction with the surrounding effective fields in a theoretical framework typically used for mesoscopic systems, such as molecular magnets [32, 33, 34], where it is known that (tuneable) magnetic fields can induce quantum tunnelling between states separated by high crystal-field barriers.

Hence, to investigate the dynamical properties of the magnetic ions in spin ices it is required to

i) study the most realistic model reproducing the ground state properties behind the Ising physics of the single magnetic sites,

ii) investigate which mechanisms may induce transitions between the two opposite

configurations,

iii) verify the likelihood that the internal degrees of freedom, i.e. the interactions between the components, allow, or even favour under specific circumstances, the occurrence of a spontaneous single "spin"-flip.

Such three steps summarise in loose words the whole work presented in this thesis. The present chapter, however, is already "self exhaustive" as it contains, at least in general perspective, all of them. More precisely, the following sections present, firstly, the crystal-field environment characteristic of spin ice materials, and, secondly, the simplest instance of competing fields, e.g. magnetic transverse fields, which can induce relevant dynamical effects compatible with the local symmetries. The remaining chapters are dedicated to the derivation and analysis of the internal interactions and local configurations, which act as "dynamical stimulator" for the mechanism that here is presented as the keystone for the flipping of a large magnetic ion to occur: the quantum mechanical *spin-tunnelling*.

2.1 The microscopic structure of spin ice pyrochlores

The general formulae for magnetic pyrochlore oxides are $A_2B_2O_6$ and $A_2B_2O_7$ where the A and B species are typically RE and transition metal (TM) cations [7, 6]. The so called spin ices, $Ho_2Ti_2O_7$ and $Dy_2Ti_2O_7$, belong to the latter one, which has $A_2^{+3}B_2^{+4}O_7$ as formulation for the oxidation states. The ideal pyrochlore structure is governed by the space group $F_{d\bar{3}m}$ which regulates the symmetries for both A and B sub-lattices shown in Fig. 2.1. The two sub-lattices interpenetrate with each other, and consist of networks of corner-sharing tetrahedra. Both A and B cations are at inversion centres and either of these can be used as the origin for the unit cell; the preferred description has usually A, Fig. 2.1a, as an inversion centre and B, Fig. 2.1b, as the origin (origin choice 2 in table No. 227 of the International Tables of Crystallography [35]).

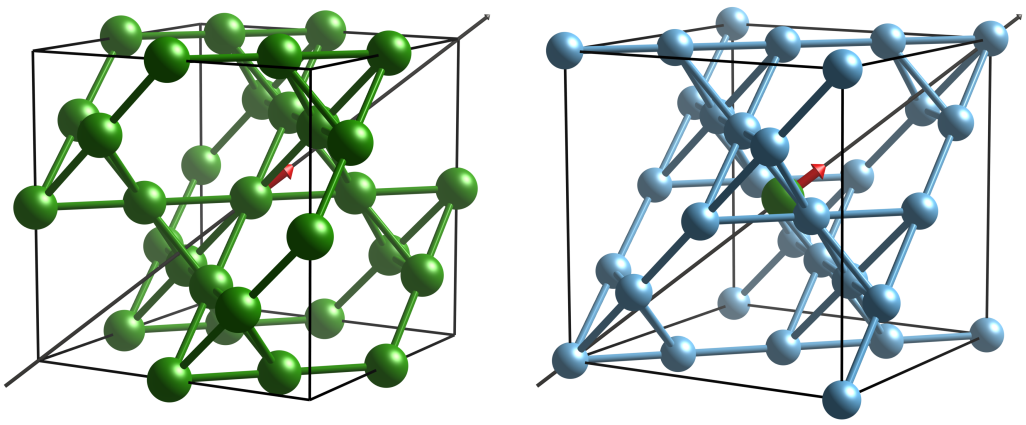

(a) **(b)**

Figure 2.1: The A and B sub-lattices, respectively left and right, in the cubic pyrochlore unit cell. The two networks of corner-sharing tetrahedra interpenetrate each other. On the right hand figure, showing the B lattice, the central site from the other network (A) is left in the centre to emphasise the reciprocal positioning of the two sub-lattices.

In the spin ice materials, Holmium titanate (HTO) and Dysprosium titanate (DTO), the A magnetic sites host, respectively, the Ho^{3+} and Dy^{3+} ions, while the non-magnetic B sites are occupied by the Ti^{4+} ions. All the mechanisms concerned with the magnetism of these materials, pertain then to the properties of the RE^{3+} ions; the non magnetic ions Ti^{4+} act as structural ligands stabilising the stoichiometry of these systems.

The magnetic properties of the RE^{3+} ions, however, depend strongly on the environment surrounding them. The so called crystal-field interactions, i.e. the Stark effect due to the negative charges of the oxygen ions, affect intrinsically their allowed quantum states for the single magnetic ion, leading to collective features which differentiate or assimilate each pyrochlore oxide with another. The physics dictated by the crystalline fields of the oxygens is so fundamental that often it is preferred to use the expression $A_2B_2O_6O'$ (instead of $A_2B_2O_7$) simply to emphasise the role played by the oxygens according to their crystallographic and ligand character (this distinction will be more clear in section 2.3 in the context of the spin ice crystal-field model). For now, making use of Figs. 2.2-2.3, it is important to highlight that such distinction emerges already in their simple positions in the crystal lattice. Referring to a given RE^{3+} (A) site, e.g. a Ho^{3+} ion in the figures, the oxygens are arranged around it in an anti-prismatic fashion which is often referred to as a distorted cube. The level of "distortion" is, however, huge compared to the ideal cube, as two of the oxygens, often named O1, form a linear O-A-O stick oriented normal to the average plane of the six-membered O2 arranged in triangles above and below the central A ion. The A-O1 and A-O2 bond distances are different: the former, of around 2.2 Å, is among the shortest bonds ever found in nature; the latter can vary depending on the compound although in general is between 2.4−2.5 Å. This implies that each RE^{3+} ion is characterised locally by a very pronounced axial symmetry along the local $\langle 111 \rangle$ axis which joins the two centres (O1 sites) of the tetrahedra at whose shared vertex the magnetic ion sits (see Figs. 2.2a,2.3a). The axial symmetry if affected by the anti-prismatic arrangement of the O2 ions with respect to the central RE^{3+} ion. These, as shown more clearly in Fig. 2.3a and in particular in Figs. 2.5,2.8 in the context of the D_{3d} crystal-field symmetry, are grouped in triangles lying on planes, above and below the RE^{3+} ion, which are parallel to each other. Another important role assigned to the O1 is the mediation of the superexchange interaction between n.n. magnetic ions (Fig. 4.3) as extensively discussed in Chapter 4.

For clarity, the central magnetic ion used as reference in Figs. 2.2-2.3 and later in Figs. 2.5,2.8 is the same at the inversion centre in Fig. 2.1. This is an arbitrary choice which is convenient as it features the local easy axis for the RE^{3+} ion parallel to the global crystallographic $\langle 111 \rangle$ direction passing through the unit cell in Fig. 2.1 from the origin to the opposite vertex. As we shall see in the following sections, another convenient choice for the local coordinate system of the magnetic ion, consists in using a local reference with the *quantisation* axis parallel to the $\langle 111 \rangle$ direction of the local easy axis. To avoid confusion it is important to specify that the "local" reference frame having the $\langle 111 \rangle$ axis joining the two centres of the tetrahedra is not only more conventional but also a mere translation of the global coordinate system $\mathbf{X}, \mathbf{Y}, \mathbf{Z}$. In contrast, the coordinate system $\mathbf{x}_0, \mathbf{y}_0, \mathbf{z}_0$, together with the others, $\mathbf{x}_i, \mathbf{y}_i, \mathbf{z}_i$ with $i = 1, 2, 3$, often used in this thesis, correspond to actual rotations of the global one (these

are more convenient to tackle the quantum mechanical features at a localised single ion level).

Before getting into the details of the local description of the quantum mechanics of a RE^{3+} ion in spin ice pyrochlores it is first necessary to introduce the terminology and framework of the crystal-field interaction. The simplest realistic approximation for it is the so called point-charge model.

2.2 Point-charge model for magnetic ions in crystalline electric fields

This section is dedicated to the *point-charge model* approximation for describing the interaction between a magnetic ion and the crystalline electric fields due to the ligands surrounding it [36, 37]. If the crystalline electric field effects are taken as a perturbation on the appropriate free-ion wave functions and energy levels, the problem becomes that of finding the perturbing Hamiltonian and its matrix elements. Even if, as an approximation, this possess some weaknesses (it neglects the finite extent of charges in the ions, the overlap of the magnetic ions' wave functions with those of neighbouring atoms, and the "screening" of the magnetic electrons by the outer electron shells of the magnetic ion), it serves to illustrate the principles involved in the calculations, in particular to see how crystalline symmetries play a leading role [36]. The basic assumption of the point-charge model is that the electric field felt by the central metal ion is generated by negative point-charges, which are situated around the central metal ion according to the symmetry of the site. The negative charges are placed on the atomic positions of the ligands. The perturbation of the central metal ion is considered as purely electrostatic, neglecting every covalent contribution [37].

The present section is organised according to its aims:

i) provide a general expression for the crystal field Hamiltonian $\hat{\mathcal{H}}_{CF}$ in the point-charge approximation (section 2.2.1),

ii) discuss the most common representations used in the literature for the calculation of its matrix elements $\langle JM'|\,\hat{\mathcal{H}}_{CF}\,|JM\rangle$ between the states $|JM\rangle$ of the total angular momentum of the electrons in the magnetic ion (sections 2.2.2 and 2.2.3).

Following this, section 2.3 will give their explicit formulae in the case of the D_{3d} point-group symmetry which characterises the crystal-field environment of a RE^{3+} ion in spin ice materials.

Determination of the Perturbing Hamiltonian

On the basis of a simple point-charge model the determination of the perturbing Hamiltonian consists in the evaluation of the electrostatic potential $V_{CF}(r,\theta,\phi)$ that the electrons of the magnetic ion experience because of the surrounding point-like charges [1].

[1] The main approximation is to neglect the distribution of electrons of the negative ions around the central magnetic one considering them as single point-like charges.

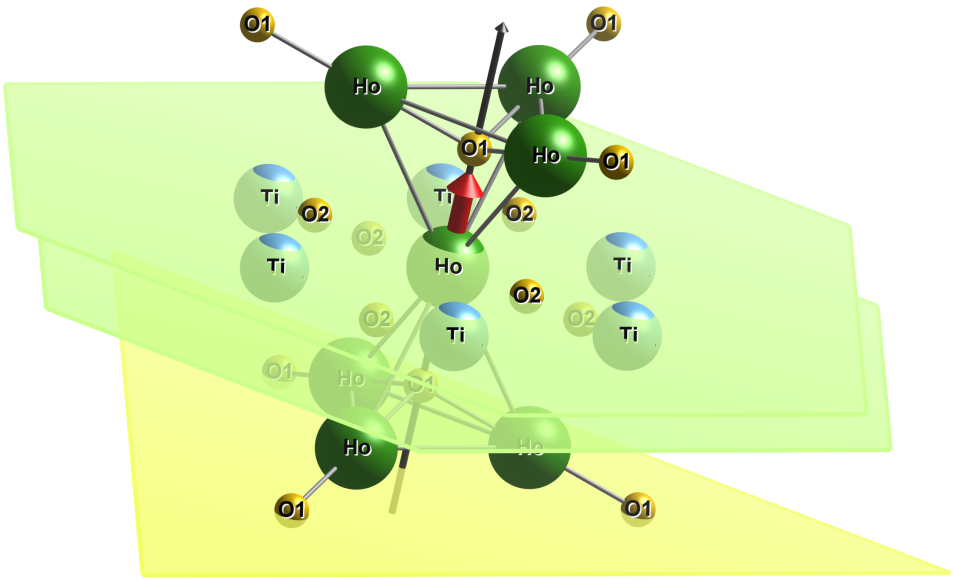

(a) Perspective view

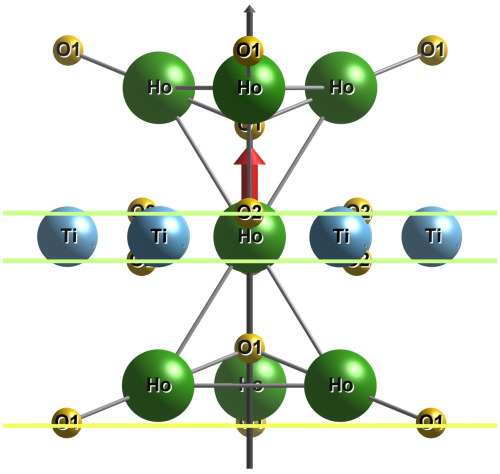

(b) Side view

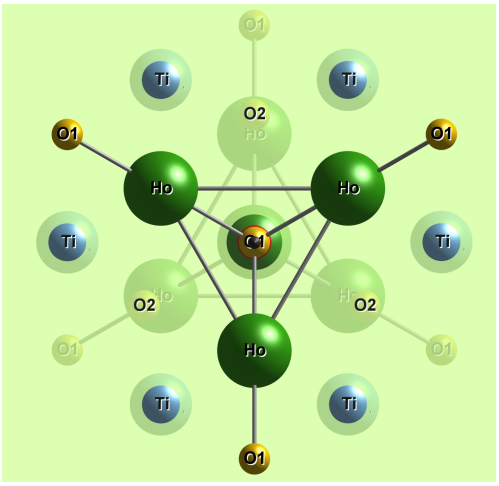

(c) Top view

Figure 2.2: Microscopic picture of the environment surrounding a central magnetic ion of a pyrochlore oxide. The compound used here is $Ho_2Ti_2O_7$; replacing Ho^{3+} and Ti^{4+} respectively with the appropriate RE^{3+} and TM^{4+} ions any magnetic pyrochlore oxide is represented. The central Ho^{3+} ion is labelled by means of a red arrow to represent the orientation of the magnetic dipole pointing towards the upper tetrahedron. The axis passing through the central Ho^{3+} and the two O1 ions, centred in the two respective tetrahedra, gives the local quantisation axis (z_0) for the central site. The transverse plane $\mathbf{x}_0, \mathbf{y}_0$, shown explicitly in Fig. 2.8, here is parallel to the green ones, containing the two triangles of the O2 sites, and the yellow one for the O1 sites further below.

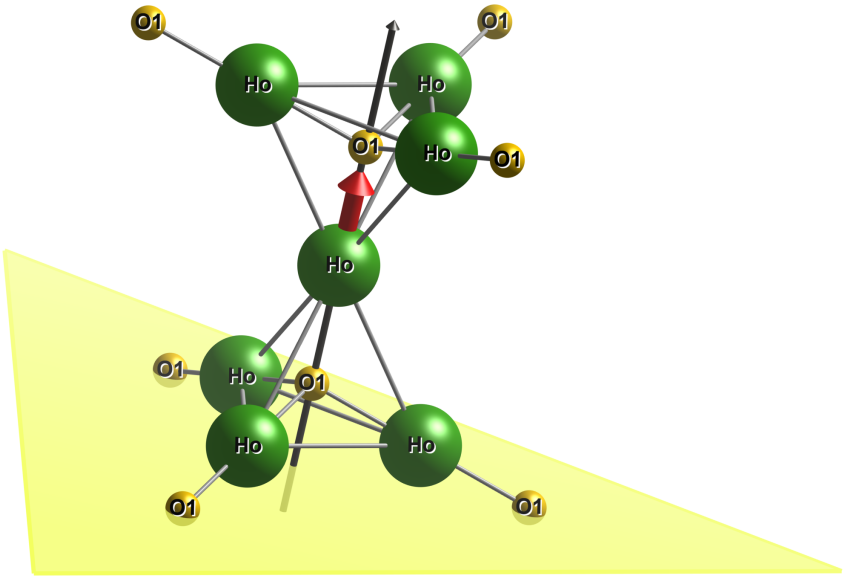

(a)

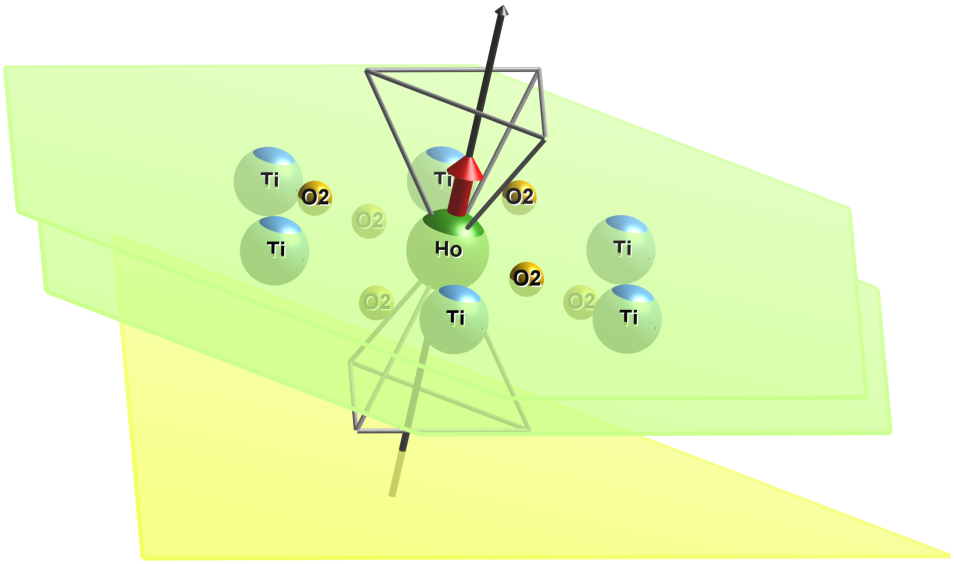

(b)

Figure 2.3: Sectioning of the chemical structure represented in Fig. 2.2 in the same perspective view as Fig. 2.2a. This is done to help distinguishing between the different chemical species of this complex structure (the green and yellow planes are left to show consistently the positioning of the objects left or removed from Fig. 2.2a). In (a) only the holmium and the O1 oxygen ions are left. These sit respectively at the vertices and centres of the corner sharing tetrahedra for the magnetic pyrochlore lattice. The outer O1 oxygens are left to locate the centres of the neighbouring tetrahedra with respect to the two shown. In (b) only the Titanium and the O2 oxygen ions neighbouring the central holmium are represented. These, together with the two O1 ions along the local $\langle 111 \rangle$ axis passing through the central holmium, constitute the crystal-field environment shown in Fig. 2.5.

The explicit expression

$$V_{CF}(r,\theta,\phi) = \sum_j \frac{Q_j}{|\boldsymbol{R}_j - \boldsymbol{r}|} \tag{2.1}$$

gives the potential in position $\boldsymbol{r} = (r,\theta,\phi)$ due to a finite number of surrounding point-charges fixed at different positions $\boldsymbol{R}_j$ (see Fig. 2.4).

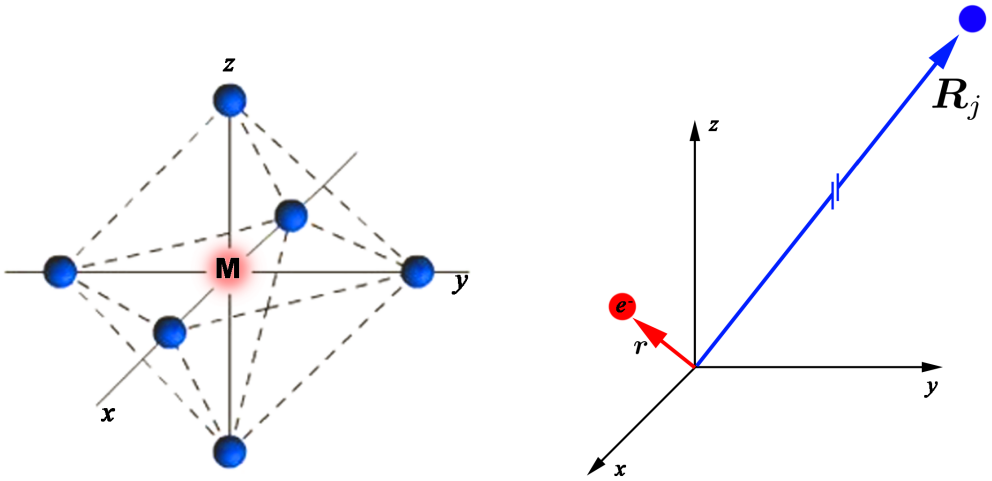

(a) (b)

Figure 2.4: a) Schematic example of a magnetic ion **M** (red-shaded region) in its crystalline environment; the ions (blue spheres) surrounding it create an electrostatic field on **M** that is called crystal-field. The geometry of the ions gives the point group symmetry for the crystal-field representation of the Hamiltonian. This example shows an octahedral arrangement of the crystalline ions around **M**. b) Pictorial representation for the coordinate $\boldsymbol{R}_j$ for an external ion (blue) compared to $\boldsymbol{r}$ for an electron (red) of the central ion **M**. The reference frame is centred on the magnetic ion, the coordinate $\boldsymbol{r}$ is closer than $\boldsymbol{R}_j$ to the origin because the electron belongs to the orbitals of **M** while the outer ion is further away.

The perturbing potential energy of the magnetic ion, due to the interactions of its electrons e_i with the surrounding crystalline point-charges, is given by the crystal-field Hamiltonian

$$\hat{\mathcal{H}}_{CF} = -\sum_i |e_i| V_{CF}(\hat{\mathbf{r}}_i)\,. \tag{2.2}$$

Each i-th electron feels a potential $V_{CF}(\mathbf{r}_i) \equiv V_{CF}(r_i,\theta_i,\phi_i)$ at position $\boldsymbol{r}_i$; only the electrons in the unfilled shells of the magnetic ion have to be considered for the crystalline perturbation. Hence the $\sum_i$ runs only over the external electrons, closed shells are affected by the crystal-field only in high order of perturbation.

To study the effect of the crystalline electric fields on the outer electrons of a magnetic ion, it is convenient to make use of spherical coordinates[36]. This comes from the spherical symmetries of the electrons of any atomic system; the eigenfunctions of the Schrödinger equation are conveniently factorised in terms of a radial function and an angular one, the latter expressed as linear combination of *spherical harmonics* [38].

2.2.1 The crystal-field potential from the spherical harmonic addition theorem

In the following, summarising from Ref. [36] and Ref. [37], the evaluation of the angular dependence of the crystalline electric potential near a magnetic ion is given, firstly in terms of spherical harmonics, secondly in terms of tesseral harmonics [2]. The method of calculation is based on the spherical harmonic addition theorem, which expresses the angle ω_{ij} between two vectors $\boldsymbol{r}_i$ and $\boldsymbol{R}_j$ in terms of the polar angles of each vector, (θ_i, ϕ_i) and (θ_j, ϕ_j) respectively:

$$P_k^0(\cos\omega_{ij}) = \frac{4\pi}{2k+1} \sum_{q=-k}^{k} (-1)^q \, Y_k^{-q}(\theta_j, \phi_j) \, Y_k^q(\theta_i, \phi_i) \,, \tag{2.3}$$

where P_k^0 are the Lengedre polynomials. These P_k^q are the *Legendre functions* [3]:

$$\begin{aligned} P_k^0(\mu) &= \frac{1}{2^k \, k!} \frac{d^k}{d\mu^k} (\mu^2 - 1)^k \,, \\ P_k^{|q|}(\mu) &= (1-\mu^2)^{\frac{|q|}{2}} \frac{d^{|q|}}{d\mu^{|q|}} P_k^0(\mu) \qquad \text{with} \quad \mu = \cos\theta; \end{aligned} \tag{2.4}$$

and the spherical harmonics, Y_k^q, are defined as

$$Y_k^q(\theta, \phi) = \mathcal{N}_k^{|q|} \; P_k^{|q|}(\cos\theta) \; e^{iq\phi} \tag{2.5}$$

with $\mathcal{N}_k^{|q|}$ normalisation constant

$$\mathcal{N}_k^{|q|} = (-1)^{\frac{q+|q|}{2}} \sqrt{\frac{2k+1}{4\pi} \frac{(k-|q|)!}{(k+|q|)!}} \,. \tag{2.6}$$

For discrete distribution of point-charges not penetrating the electronic shells of the magnetic ion ($R_j > r_i$), the distance $|\boldsymbol{R}_j - \boldsymbol{r}_i|$ can be expressed using the following expansion

$$\frac{1}{|\boldsymbol{R}_j - \boldsymbol{r}_i|} = \sum_{k=0}^{\infty} \frac{r_i^{\,k}}{R_j^{(k+1)}} \, P_k^0(\cos\omega_{ij}) \,, \tag{2.7}$$

so that the crystalline potential in Eq. (2.1) is given by

$$V_{CF}(r_i, \theta_i, \phi_i) = \sum_j Q_j \sum_{k=0}^{\infty} \frac{r_i^{\,k}}{R_j^{(k+1)}} \, P_k^0(\cos\omega_{ij}) \,, \tag{2.8}$$

where $\sum_j$ runs over the point-charges surrounding the magnetic ion [39, 37]. Here the radial and angular dependence of the potential are factorised. The angular part is known because of the harmonic addition theorem, Eq. (2.3), which relates the solid

[2] A complete list of spherical harmonics and tesseral harmonics is given in Ref. [37]

[3] The term Legendre functions here covers both the Legendre *polynomials* P_k^0 and the *associated* Legendre polynomials P_k^q with $q \neq 0$.

angle ω_{ij} and the planar angles (θ_i, ϕ_i) and (θ_j, ϕ_j) by means of spherical harmonics and Legendre functions. In the context of the crystal-field interaction, (θ_i, ϕ_i) represents the angular position of the i-th electron and (θ_j, ϕ_j) gives the angular distribution of the surrounding point-like ions.

To avoid using functions with imaginary quantities, it is often convenient to switch from spherical harmonics to *tesseral harmonics*. These are real by definition:

$$Z_{k0} = Y_k^0 \qquad \text{and} \qquad \left.\begin{aligned} Z_{kq}^c &= \frac{1}{\sqrt{2}}[Y_k^{-q} + (-1)^q Y_k^q] \\ Z_{kq}^s &= \frac{i}{\sqrt{2}}[Y_k^{-q} - (-1)^q Y_k^q] \end{aligned}\right\} \quad q > 0 \tag{2.9}$$

that is

$$\begin{aligned} Z_{k0} &= Y_k^0\,, \\ Z_{kq}^c(\theta,\phi) &= \sqrt{\frac{2k+1}{2}\frac{(k-q)!}{(k+q)!}}\, P_k^q(cos\theta)\, \frac{\cos(q\phi)}{\sqrt{\pi}}\,, \\ Z_{kq}^s(\theta,\phi) &= \sqrt{\frac{2k+1}{2}\frac{(k-q)!}{(k+q)!}}\, P_k^q(cos\theta)\, \frac{\sin(q\phi)}{\sqrt{\pi}}\,. \end{aligned} \tag{2.10}$$

Z_{kq}^c and Z_{kq}^s are called respectively *sine* and *cosine* tesseral harmonic functions [36, 40]. Then, in terms of tesseral harmonics, the addition theorem in Eq. (2.3) reads

$$P_k^0(\cos\omega_{ij}) = \frac{4\pi}{2k+1}\sum_\alpha\, Z_{k\alpha}(\boldsymbol{r}_i)\, Z_{k\alpha}(\boldsymbol{R}_j)\,, \tag{2.11}$$

where the Z functions are evaluated for the points $\boldsymbol{R}_j$ and $\boldsymbol{r}_i$. Note, the summation over α means that for each k there are terms Z_{k0} and Z_{kq}^c, Z_{kq}^s for all q.
Now, by sustituting this expression into Eq. (2.8), the crystal-field potential is an explicit function of the tesseral harmonics

$$V_{CF}(r_i,\theta_i,\phi_i) = \sum_j Q_j \sum_{k=0}^{\infty} \frac{r_i^k}{R_j^{(k+1)}} \left[\frac{4\pi}{2k+1}\sum_\alpha\, Z_{k\alpha}(\theta_i,\phi_i)\, Z_{k\alpha}(\theta_j,\phi_j)\right], \tag{2.12}$$

with i indexing the electrons in the unfilled shells of the magnetic ion and j for the point-like ions around it. For a finite number N of surrounding charges it is convenient to define the following quantity

$$\xi_{k\alpha} = \sum_{j=1}^{N} \frac{4\pi}{2k+1} Q_j \frac{Z_{k\alpha}(\theta_j,\phi_j)}{R_j^{(k+1)}} \tag{2.13}$$

so that the crystalline potential for the i-th electron reads [36]

$$V_{CF}(r_i,\theta_i,\phi_i) = \sum_{k=0}^{\infty} r_i^k\, \xi_{k\alpha} \sum_\alpha Z_{k\alpha}(\theta_i,\phi_i). \tag{2.14}$$

From this and Eq. (2.2), after applying the canonical transformation from variables to operators ($\mathbf{r}_i \to \hat{\mathbf{r}}_i$), it is straightforward to obtain the crystal-field Hamiltonian in Eq. (2.2) for the n magnetic electrons of a given atomic system.

2.2.2 Tensor operators for the crystal-field Hamiltonian

In analogy with the compact expressions in Eqs. (2.13-2.14), it is convenient to introduce the following CF parameters

$$\begin{aligned} B_0^k &= -e\,\langle r^k\rangle \sqrt{\frac{4\pi}{2k+1}} \sum_j \frac{Q_j}{R_j^{k+1}} Z_{k0}(\theta_j,\phi_j) \\ B_q^k &= -e\,\langle r^k\rangle \sqrt{\frac{2\pi}{2k+1}} \sum_j \frac{Q_j}{R_j^{k+1}} Z_{kq}^c(\theta_j,\phi_j) \\ B'^k_{\ q} &= -e\,\langle r^k\rangle \sqrt{\frac{2\pi}{2k+1}} \sum_j \frac{Q_j}{R_j^{k+1}} Z_{kq}^s(\theta_j,\phi_j), \end{aligned} \tag{2.15}$$

which depend on the angular distribution of the ligands, $\mathbf{R}_j = (R_j, \theta_j, \phi_j)$, but also incorporate the charge of the electrons and the average $\langle r^k\rangle$ of the central magnetic ion. This is the radial integral $\langle r^k\rangle = \int_{r=0}^{\infty} R_{nl}^2(r)\, r^k dr$, where R_{nl} here is the radial part of the wave function characterised by the principal (n) and orbital (l) quantum numbers. Such quantity often shows discrepancies with the values measured in experiments, thereby it is often preferred to fit directly the B parameters in Eq. (2.15) if the point group, and so the most symmetric representation of the Hamiltonian, are already known [41, 42, 37].

This implies that the crystal-field Hamiltonian acts directly on the angular part of the wave functions for the electrons of the magnetic ion. Whence the quantisation is applied only to the angular dependence of the electrons in the unfilled shells of the magnetic ion [4], and the CF Hamiltonian in Eq. (2.2) can be written explicitly as

$$\begin{aligned} \hat{\mathcal{H}}_{CF} = \sum_{i=1}^{n}\sum_{k=0}^{\infty} \Bigg\{ B_0^k\, \hat{C}'^k_0(i) + \sum_{q=1}^{k} \Big[B_q^k \left(\hat{C}'^k_{-q}(i) + (-1)^q \hat{C}'^k_q(i)\right) \\ + \mathrm{i}\, B'^k_{\ q} \left(\hat{C}'^k_{-q}(i) - (-1)^q \hat{C}'^k_q(i)\right) \Big] \Bigg\}, \end{aligned} \tag{2.16}$$

where $(i) \equiv (\theta_i, \phi_i)$ indicates the angular dependence of the tensor operator (for the i-th electron)

$$\hat{C}'^k_q(i) = \sqrt{\frac{4\pi}{(2k+1)}}\, \hat{Y}_k^q(\theta_i,\phi_i), \tag{2.17}$$

which preserve the same transformation rules as the spherical harmonics [43, 44, 28, 37,

[4] The other variables, including r^k that is averaged in $\langle r^k\rangle$, are left as classical quantities and gathered together inside the CF parameters in Eq. (2.15).

40]. In real physical systems the index k for the crystal-field expansion in Eq. (2.16) runs over a limited number of terms. In RE^{3+} ions, being systems with f unfilled shell, $k = 0, 1, \ldots, 7$. The even and odd k-terms have different physical roles: the even terms govern the crystal-field splitting, the odd ones determine the intensity of induced electric-dipole transitions. The values of q are limited by the point group of the RE-site with respect to the surrounding ions [37].

The representation for the kets defining the basis for the Hilbert space of $\hat{\mathcal{H}}_{CF}$ can vary. In the context of trivalent RE ions, it is usually convenient to work in the Russell-Saunders coupling scheme, that is

$$|f^n SLJM_J\rangle \equiv |JM_J\rangle \,, \tag{2.18}$$

where L, S and J are the quantum numbers for, respectively, the orbital ($\hat{\mathbf{L}}$), the spin ($\hat{\mathbf{S}}$) and the total ($\hat{\mathbf{J}} = \hat{\mathbf{L}} + \hat{\mathbf{S}}$) angular momenta for the whole system of the n electrons in the f shell. These states are often referred to by $|M_J\rangle$, with $M_J = -J, -J+1, \ldots, J$ quantum numbers for the projection of the total angular momentum along the quantisation axis, because they represent quantum states with strong spin-orbit coupling, where J is a conserved quantum number for the 4-f electrons driving the magnetism of these systems. The Clebsch-Gordan coefficients and Wigner-Eckart theorem regulate the transformation from the single-electron angular representation to these ones with the total angular momenta M_J [36, 43].

In the following subsection the crystal-field (CF) Hamiltonian for the magnetic pyrochlore oxides is given in two different notations. After the tensor operators $\hat{C}_q^k$, used for example in Ref. [45] to fit the B parameters of $Ho_2Ti_2O_7$ to inelastic neutron-scattering data, the Hamiltonian is given in terms of *Stevens' equivalent operators* to allow a more immediate action of $\hat{\mathcal{H}}_{CF}$ on the $|JM_J\rangle$ states of the RE^{3+} ion.

2.2.3 Stevens' equivalent operators for crystal-field Hamiltonians

The magnetic ions of the rare earth pyrochlore oxides feature a point group symmetry (D_{3d}, see subsection 2.3) which allows only even k-terms in the expansion (2.16). For such rare earth systems, the crystal electric field interaction for the f electrons is often described in terms of the *Stevens'* operators equivalent method. Being a function of the total angular momentum operators,

$$\hat{O}_q^k \equiv \hat{O}_q^k \left(\hat{J}_z, \hat{J}_\pm\right) \,, \tag{2.19}$$

the Stevens' operators simplify the calculation of the matrix elements $\langle JM'_J| \hat{\mathcal{H}}_{CF} |JM_J\rangle$ of the crystal-field Hamiltonian in Eq. (2.2) over the states in Eq. (2.18). The explicit formulae of all the operators for RE^{3+} ions in pyrochlore oxides will be listed below in Eq. (2.28).

The definition of the Stevens' operators is often given in terms of the following equivalence with the tesseral harmonics, Eq. (2.9), expressed in Cartesian coordinates

[36, 44, 28, 40]:

$$\begin{aligned}\sum_i Z_{k0}(\hat{x}_i,\hat{y}_i,\hat{z}_i) &= D_0^k\,\theta_k\,\langle r^k\rangle\,\hat{O}_0^k \\ \sum_i Z_{kq}^{c,s}(\hat{x}_i,\hat{y}_i,\hat{z}_i) &= D_q^k\,\theta_k\,\langle r^k\rangle\,\hat{O}_q^k(c,s)\,.\end{aligned} \tag{2.20}$$

The D_q^k are the factors outside the square brackets $[\ldots]$ for the list of tesseral harmonics in Cartesian coordinates in Table IV of Ref. [36]. The θ_k (with $k=2,4,6$; $\theta_2=\alpha_J, \theta_4=\beta_J, \theta_6=\gamma_J$) calculated by Stevens for different RE ions [46] are given in Table VI of the same Ref. [36]. In Table 2.2 the values for $\alpha_J, \beta_J, \gamma_J$ are given for the two magnetic ions Ho^{3+} and Dy^{3+} of interest for spin ice materials.

The $\hat{O}_q^k(c)$ are the most commonly used operator equivalents $\hat{O}_q^k$, but the $\hat{O}_q^k(s)$ are the sine-term operator equivalents. Thus, the even k-terms of the crystal-field Hamiltonian in Eq. (2.16) for a RE ion give

$$\hat{\mathcal{H}}_{CF} = \sum_{k=2(k:even)}^{6} \langle r^k\rangle\;\theta_k \left[A_0^k\,\hat{O}_0^k + \sum_{q>0}^{k}\Big(A_q^k(c)\,\hat{O}_q^k(c) + A_q^k(s)\,\hat{O}_q^k(s)\Big)\right]. \tag{2.21}$$

Exact diagonalisation of the matrix $\langle JM_J'|\,\hat{\mathcal{H}}_{CF}\,|JM_J\rangle$ gives the crystal-field energy levels as a function of the parameters $A_q^k, \theta_k, \langle r^k\rangle$. The following relationships relate these CF parameters to the B_q^k parameters for the tensor operators [40] [5]:

$$\begin{aligned}\frac{A_0^k(c)\langle r^k\rangle}{B_0^k} &= \sqrt{\frac{4\pi}{2k+1}}D_0^k; \\ \frac{A_q^k(c)\langle r^k\rangle}{B_q^k} &= \frac{A_q^k(s)\langle r^k\rangle}{B'^k_q} = (-1)^q\sqrt{\frac{8\pi}{2k+1}}D_q^k\,.\end{aligned} \tag{2.22}$$

See also Ref. [47, 44] for more detailed tables. The B_q^k, B'^k_q and $\langle r^k\rangle$ are defined here in subsection 2.2.2 (from Ref. [37]).

In Table 2.1 the relationships in Eq. (2.22), between the CF parameters B_q^k and A_q^k, are given explicitly for the case of a RE^{3+} ion in a crystalline environment with a D_{3d} point-group symmetry. This is of interest in the context of the following subsection, where the crystal-field Hamiltonian for spin ices is introduced in both formalisms.

Below, the CF parameters listed in Table 2.3 show directly the values estimated by experimental results for both for $Ho_2Ti_2O_7$ and $Dy_2Ti_2O_7$ [45, 48].

Introducing a shorter notation for the cosine Stevens' parameters

The choice of the parameters depends on the formalism used to describe the crystal-field Hamiltonian. In the next subsection after introducing the Hamiltonian in the tensor operator formalism, it is preferred to switch to Stevens' operators mainly because of the simplicity to evaluate the matrix elements $\langle JM_J'|\,\hat{\mathcal{H}}_{CF}\,|JM_J\rangle$ using the

[5] The relationships in Eq. (2.22) are from Ref. [40], although in this thesis they have been re-adapted to use the definitions for the B_0^k, B_q^k, B'^k_q operators from Ref. [37].

$B_0^2 = 2A_0^2 \langle r^2 \rangle$	$B_0^4 = 8A_0^4 \langle r^4 \rangle$	$B_0^6 = 16A_0^6 \langle r^6 \rangle$
	$B_3^4 = -\frac{2}{35}\sqrt{35}A_3^4 \langle r^4 \rangle$	$B_3^6 = -\frac{8}{105}\sqrt{105}A_3^6 \langle r^6 \rangle$
		$B_6^6 = \frac{16}{231}\sqrt{231}A_6^6 \langle r^6 \rangle$

Table 2.1: Relationship between the crystal-field parameters for the two different notations. Here are listed only the ones of interest for the CF Hamiltonian discussed in this thesis. For a complete list see Refs. [47, 44, 37].

	Ho^{3+}	Dy^{3+}
α_J	$\frac{-1}{450}$	$\frac{-2}{315}$
β_J	$\frac{-1}{30030}$	$\frac{-8}{135135}$
γ_J	$\frac{-5}{3864861}$	$\frac{4}{3864861}$

Table 2.2: The θ_k values (respectively $\alpha_J, \beta_J, \gamma_J$ for $k = 2, 4, 6$) for holmium and dysprosium trivalent ions [36].

tables in Hutchings' work [36]. The symmetry of the system discussed in this thesis is such that only the cosine Stevens' operators are necessary for the crystal-field Hamiltonian. Hence, to simplify the notation of the work presented below, the generic CF Hamiltonian in the Stevens' formalism will be

$$\hat{\mathcal{H}}_{CF} = \sum_{k=2(k:even)}^{6} \sum_{q\geq 0}^{k} \widetilde{\mathrm{B}}_q^k \hat{O}_q^k \tag{2.23}$$

where $\hat{O}_q^k = \hat{O}_q^k(c)$ and $\widetilde{\mathrm{B}}_q^k = \langle r^k \rangle \theta_k A_q^k(c)$. The $\widetilde{\mathrm{B}}_q^k$ parameters can be expressed also in terms of the B_q^k parameters, using the following expressions equivalent[6] to Eq. (2.22):

$$\begin{aligned} \widetilde{\mathrm{B}}_0^k &= \sqrt{\frac{4\pi}{2k+1}}\theta_k D_0^k B_0^k; \\ \widetilde{\mathrm{B}}_q^k &= (-1)^q \sqrt{\frac{8\pi}{2k+1}}\theta_k D_q^k B_q^k \quad , \quad \text{for } q > 0\,. \end{aligned} \tag{2.24}$$

[6] After making this choice of notation we noticed that also Hutchings in his work on the point-charge model introduces these same $\widetilde{\mathrm{B}}_q^k$ parameters (see eq.(5.6) of page 265 Ref. [36]). Unfortunately they are labelled as B_q^k, which in our case would lead to confusion with the parameters introduced in Eq. (2.15) and used in Refs. [37, 45, 40].

2.3 Crystal-field Hamiltonians for RE^{3+} ions in spin ices

The local crystalline symmetry for the RE^{3+} ions in the $RE_2TM_2O_7$ pyrochlores is a trigonal D_{3d} (-3m) point group symmetry. As schematically shown in Fig. 2.5, the RE^{3+} ion sitting in the corner of the two neighbouring tetrahedra has a total of eight oxygen ions and six Titanium ions surrounding it. The strong axial alignment of the O1 ions (above and below the central RE^{3+} ion) gives the Ising anisotropy for the spin ices. The antiprismatic character of the D_{3d} symmetry is due to the arrangement of the O2 ions displaced above and below the central ion (note the triangles emphasising the O2 oxygens sitting on the same planes).

2.3.1 The crystal-field Hamiltonian for the D_{3d} point-group symmetry

All D_{nd} with odd n have null odd k-terms in the crystal-field expansions of Eqs. (2.16,2.21) [37]. In the tensor operators formalism, the CF Hamiltonian for a magnetic ion in a crystalline D_{3d} point-group symmetry reads [7]

$$\begin{aligned}\hat{\mathcal{H}}_{CF} = & B_0^2\hat{C}_0^2 + B_0^4\hat{C}_0^4 + B_3^4(\hat{C}_3^4 - \hat{C}_{-3}^4) \\ & + B_0^6\hat{C}_0^6 + B_3^6(\hat{C}_3^6 - \hat{C}_{-3}^6) + B_6^6(\hat{C}_6^6 + \hat{C}_{-6}^6)\,.\end{aligned} \tag{2.25}$$

This is for the central RE^{3+} ion with local quantisation axis along $\mathbf{z}_0$ parallel to the $\langle 111\rangle$ direction of the crystallographic cell [45]. Exact diagonalisation of the crystal-field Hamiltonian gives the energy levels regulating the electronic configurations allowed for the RE^{3+} ion by the crystalline environment. Since J is a good quantum number, the the CF Hamiltonian matrix is given with respect to the ket representation $|JM_J\rangle$ in Eq. (2.18); the dimensions of the CF matrix are $(2J+1)\times(2J+1)$. The spectrum is in general made of multiplets and singlets, as the Stark splitting, induced by the crystalline electric fields, removes only partially the $2J+1$ degeneracy of the ground state multiplet. For example the HTO spectrum in Fig. 2.6a features singlets and doublets, whilst the spectrum of DTO is only made of doublets Fig. 2.6b. This discrepancy is due to Kramers' theorem which states that singlets are not allowed for spectra of atoms with an odd number n of unpaired electrons (Dy^{3+} has $n = 9$ electrons while Ho^{3+} has $n = 10$).

[7] As often used in the crystal-field literature, here the sum over the 4-f electrons ($\sum_{i=1}^{n}$) is omitted together with the index i. This CF Hamiltonian, together with many others for different symmetries, can be found also in Ref. [37]; in this reference, where also the general Hamiltonian in Eq. (2.16) is given, the convention for the operators with odd q are opposite in sign to the Hamiltonian in Eq. (2.25). In this thesis the latter one is preferred in order to use the original set of CF parameters (Table 2.1) fitted to the energies measured in Ref. [45].

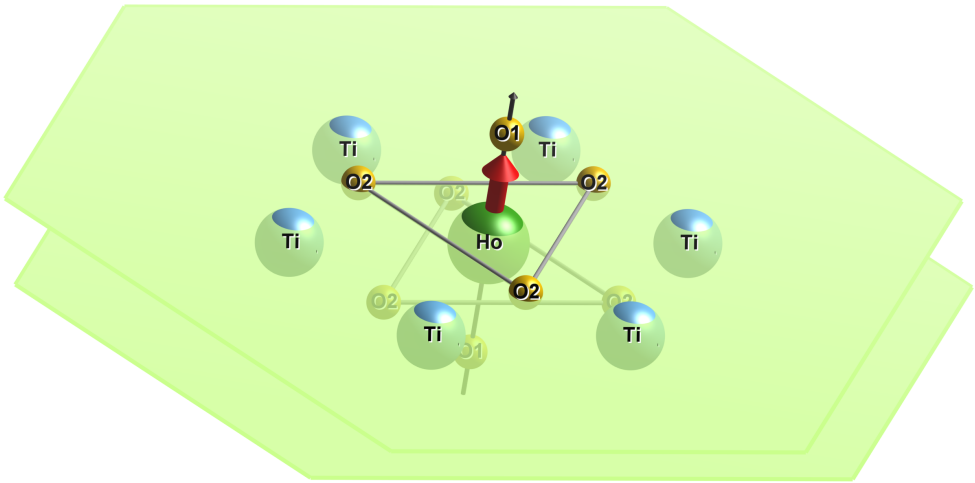

(a) Perspective view

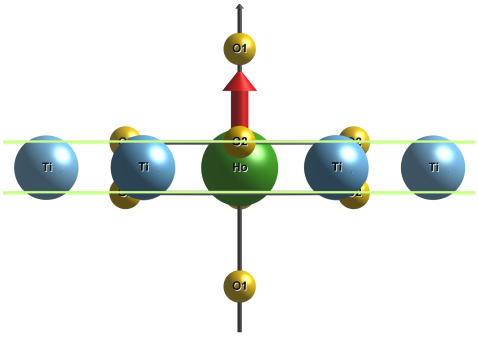

(b) Side view

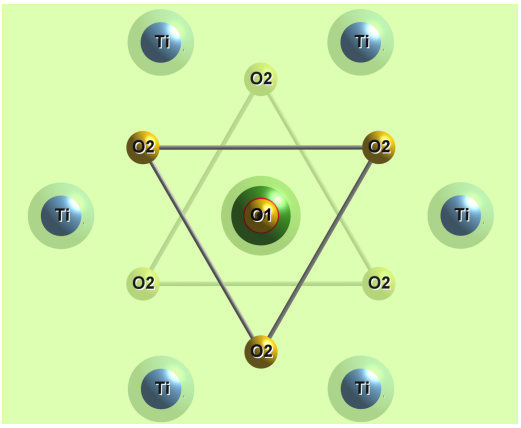

(c) Top view

Figure 2.5: The crystal-field environment of a RE^{3+} ion in a magnetic pyrochlore oxide. Here as example is shown $Ho_2Ti_2O_7$: the eight O^{2-} ions characterise the D_{3d} trigonal symmetry, the Ti^{4+} ions are arranged in an hexagon coplanar with the Ho^{3+} ion in the centre. (a), (b) and (c) show respectively a top-side, side and top view of the same structure. The edges of the triangles connect the coplanar O2 oxygens: there are three above and three below (equidistant to) the plane of the RE^{3+} ion and the hexagon of the Ti^{4+} ions. The two green planes shown are parallel with each other (they contain the respective upward and downward triangles of the O2 ions). The antiprismatic arrangement of the six O2 gives the D_{3d} point-group symmetry for the Ho^{3+} ion sitting in the centre. The O1 ions, aligned along the $\langle 111 \rangle$ axis with the central RE^{3+}, drive the local Ising anisotropy of the magnetic ion.

The CF Hamiltonian for the D_{3d} point-group symmetry can be expressed also as [8]

$$\hat{\mathcal{H}}_{CF} = \widetilde{\mathrm{B}}_0^2\,\hat{O}_0^2 + \widetilde{\mathrm{B}}_0^4\,\hat{O}_0^4 + \widetilde{\mathrm{B}}_3^4\,\hat{O}_3^4 + \widetilde{\mathrm{B}}_0^6\,\hat{O}_0^6 + \widetilde{\mathrm{B}}_3^6\,\hat{O}_3^6 + \widetilde{\mathrm{B}}_6^6\,\hat{O}_6^6, \tag{2.27}$$

where $\hat{O}_q^k = \hat{O}_q^k(c)$ are the (cosine) Stevens' operators and $\widetilde{\mathrm{B}}_q^k$ are the respective parameters, introduced in Eq. (2.24). A list of the Stevens operators and their matrix elements in the $|M_J\rangle$ basis is given in Hutchings' work [36]. The following is a complete list of the Stevens' operators for the crystal-field of a RE^{3+} ion in magnetic pyrochlore oxides[9]:

$$\begin{aligned}
\hat{O}_0^2 &= \Big[3\hat{J}_z^2 - J(J+1)\Big];\\
\hat{O}_0^4 &= 35\hat{J}_z^4 - 30J(J+1)\hat{J}_z^2 + 25\hat{J}_z^2 + 3J^2(J+1)^2 - 6J(J+1);\\
\hat{O}_3^4 &= \frac{1}{4}\Big[(\hat{J}_+^3 + \hat{J}_-^3)\hat{J}_z + \hat{J}_z(\hat{J}_+^3 + \hat{J}_-^3)\Big];\\
\hat{O}_0^6 &= 231\hat{J}_z^6 - \Big[315J(J+1) - 735\Big]\hat{J}_z^4\\
&\quad + \Big\{105J^2(J+1)^2 - 525J(J+1) + 294\Big\}\hat{J}_z^2\\
&\quad - 5\hat{J}^3(J+1)^3 + 40J^2(J+1)^2 - 60J(J+1);\\
\hat{O}_3^6 &= \frac{1}{4}\Big\{\Big(\hat{J}_+^3 + \hat{J}_-^3\Big)\Big[11\hat{J}_z^3 - \Big(3J(J+1) + 59\Big)\hat{J}_z\Big]\\
&\quad + \Big[11\hat{J}_z^3 - \Big(3J(J+1) + 59\Big)\hat{J}_z\Big]\Big(\hat{J}_+^3 + \hat{J}_-^3\Big)\Big\};\\
\hat{O}_6^6 &= \frac{1}{2}\Big(\hat{J}_+^6 + \hat{J}_-^6\Big).
\end{aligned} \tag{2.28}$$

The value $J(J+1)$ comes from the eigenvalue of $\hat{J}^2$ as defined, together with $\hat{J}_z, \hat{J}_+, \hat{J}_-$, in Eq. (1.5).

2.3.2 Crystal-field energies and parameters for spin ice compounds

The experimental techniques based on inelastic neutron scattering are the most suitable to measure accurately the crystal-field energies in real compounds. From these measurements a reliable estimation of the CF parameters can be inferred beyond the level of accuracy allowed by the point-charge approximation. For RE^{3+} ions it is typi-

[8] This is the shorter notation for the Stevens' formalism that is introduced in this thesis in Eqs. (2.23-2.24). The Hamiltonian equivalent to Eq. (2.25) and Eq. (2.27) reads

$$\begin{aligned}
\hat{\mathcal{H}}_{CF} = {}& \alpha_J\,\langle r^2\rangle\, A_0^2(c)\hat{O}_0^2(c) + \beta_J\,\langle r^4\rangle\,\Big(A_0^4(c)\hat{O}_0^4(c) + A_3^4(c)\hat{O}_3^4(c)\Big)\\
&+ \gamma_J\,\langle r^6\rangle\,\Big(A_0^6(c)\hat{O}_0^6(c) + A_3^6(c)\hat{O}_3^6(c) + A_6^6(c)\hat{O}_6^6(c)\Big)
\end{aligned} \tag{2.26}$$

which is the more extended and more common notation in the literature [46, 36, 44, 40].

[9] Since in the Hamiltonian (2.26) only the (c) Stevens' operators appear from now on $A_q^k(c)\hat{O}_q^k(c) = A_q^k\hat{O}_q^k$.

cal to consider the Russell-Saunders representation in Eq. (2.18) (with J fixed by the number of n electrons in the f shell), set the full point charge Hamiltonian based on the local symmetry of the surrounding negative ions (usually known from non-magnetic diffraction techniques), and readjust the parameters by fitting the diagonalisation of such Hamiltonian to the spectrum measured.

The crystal-field energies and parameters common in the literature of spin ice materials are based mainly on the experiment presented by Rosenkranz et al. in Ref. [45]. In this the neutron scattering measurement of all the CF energy levels allowed a complete parametrisation of the Hamiltonian in Eq. (2.25). The full list of the B_k^q parameters for HTO is reported, directly from Ref. [45], in Table 2.3a. To allow the implementation of the Stevens' equivalent Hamiltonian in Eq. (2.27), these have also been converted, by means of Eq. (2.24), to the corresponding $\widetilde{\mathrm{B}}_k^q$ in Table 2.3b. For DTO, to the best of our knowledge, no neutron scattering experiment has been carried out successfully to determines the CF parameters. The parameters in Table 2.3 are converted directly from the ones suggested in Ref. [48] as an interpolation of the values known for $Ho_2Ti_2O_7$ and $Tb_2Ti_2O_7$.

	HTO	DTO
B_0^2	68.2	51.1
B_0^4	274.8	306.2
B_3^4	83.7	90.5
B_0^6	86.8	100.4
B_3^6	−62.5	−74.4
B_6^6	101.6	102.9

(a)

	HTO	DTO
$\widetilde{\mathrm{B}}_0^2$	-7.6×10^{-2}	-1.6×10^{-1}
$\widetilde{\mathrm{B}}_0^4$	-1.1×10^{-3}	-2.3×10^{-3}
$\widetilde{\mathrm{B}}_3^4$	8.2×10^{-3}	1.6×10^{-2}
$\widetilde{\mathrm{B}}_0^6$	-7.0×10^{-6}	6.5×10^{-6}
$\widetilde{\mathrm{B}}_3^6$	-1.0×10^{-4}	9.9×10^{-5}
$\widetilde{\mathrm{B}}_6^6$	-1.3×10^{-4}	1.0×10^{-4}

(b)

Table 2.3: The crystal-field parameters (in meV) for both $Ho_2Ti_2O_7$ (HTO) and $Dy_2Ti_2O_7$ (DTO). The table on the left (a) lists the B_k^q for the tensor operators, while the one on the right (b) lists the $\widetilde{\mathrm{B}}_k^q$ for the Stevens' equivalent correspondent. The parameters for HTO have been measured by means of inelastic neutron scattering in Ref. [45]. The ones for DTO were derived as an interpolation of the parameters know for $Ho_2Ti_2O_7$ and $Tb_2Ti_2O_7$ in Ref. [48]. The definitions of such parameters are given respectively in Eq. (2.15) and Eqs. (2.23-2.24).

Since the total angular momentum quantum number is $J = 8$ for Ho^{3+} and $J = 15/2$ for Dy^{3+}, the CF Hamiltonian, being a perturbation within the ground-state J multiplet in the LS coupling in Eq. (2.18), is a matrix of small dimensions: 17 and 16 respectively for HTO and DTO. Using the set of parameters in Table 2.3b

and the Stevens' operators in Eq. (2.28) it is straightforward to perform numerical diagonalisation and obtain the spectra illustrated in Fig. 2.6. As expected from Kramers theorem, the two systems show different structure of the spectra; the order of magnitude for the energies, however, is roughly the same. For Ho^{3+} the spectrum is made of five singlets and six doublets (Fig. 2.6a), while for Dy^{3+}, due to Kramers degeneracy, all the eight energy levels are doublets (Fig. 2.6b). In both systems the energy gap between the ground state energy and the first excited level exceeds 200 K, implying that even at room temperatures only the lowest CF excited states are populated. This means also that at low temperatures the CF ground state of the RE^{3+} ions characterise heavily not only the static and dynamical properties at a microscopical (local) level, but also from a macroscopic (collective) point of view, i.e. in the thermodynamics.

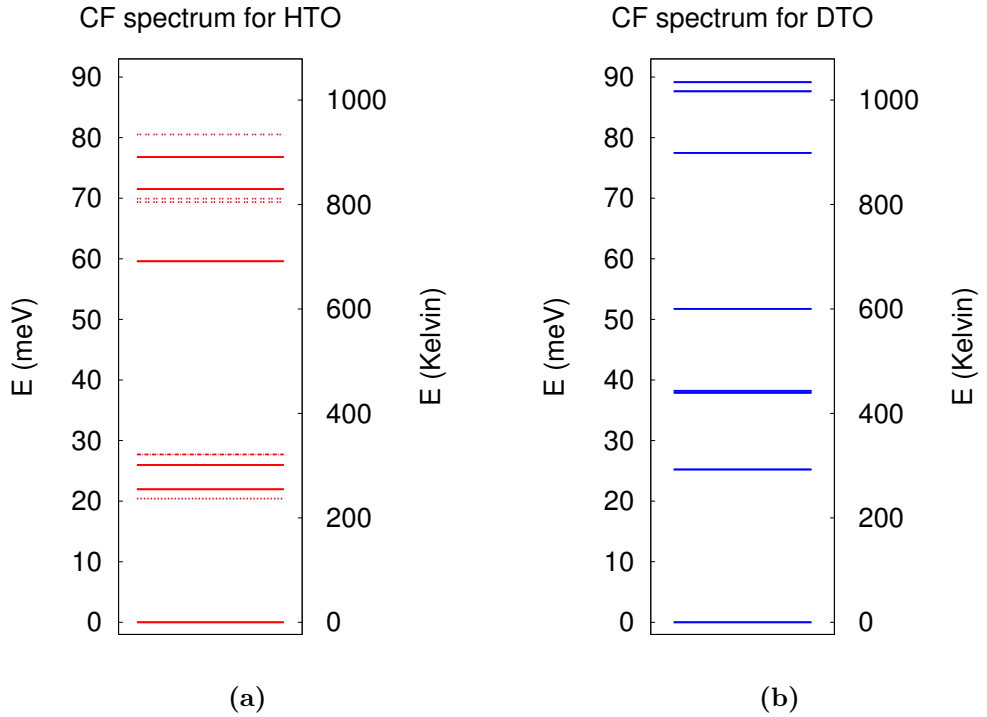

Figure 2.6: The crystal-field spectra for HTO and DTO, left panel (a) and right panel (b) respectively. The spectra can be found by exact diagonalisation of either of the Hamiltonians in Eqs. (2.25,2.27) using the respective coefficients in Table 2.3. The spectrum of HTO features both doublets (solid lines) and singlets (dashed or dotted lines). In meV, bottom to top, the series of doublets is 0, 21.96, 25.99, 59.59, 71.51, 76.80 while the one of singlets is 20.42, 27.71, 69.36, 69.94, 80.52. In contrast DTO features only doublets since Dy^{3+} is a Kramers ion. These are eight in total: 0, 25.23, 38.0, 38.21, 51.75, 77.49, 87.65, 89.16 (bottom to top in meV). Note the thicker line just below 40 meV is not a quadruplet indeed, it corresponds to the two doublets 38.0, 38.21.

For both HTO and DTO the ground state is a doublet which can be described as corresponding to states where the magnetic moment is pointing largely in opposite directions along the local quantisation axis $\mathbf{z}_0$ in Fig. 2.8. The two eigenfunctions for the ground state doublets are displayed in Fig. 2.7. These can be well approximated to the fully polarised states $|M_J\rangle = |\pm J\rangle$ which give the Ising-like behaviour to the

magnetic ions of a spin ice material.

Once the magnetic ion sits in one of the two states with opposite polarisation in Fig. 2.7, there is a very high crystal field barrier (the height of the spectra in Fig. 2.6) which prevent the spontaneous "flip" to the other state. Hence, if on one side the CF environment guarantees the local anisotropy which makes the ions alike classical Ising spins, on the other hand it also imposes very strong energetic constraints in the possible dynamics of the real magnetic ions. A microscopical description of the mechanisms driving a single RE^{3+} ion from one ground state configuration to the opposite one is necessary to account for the local flip of an Ising spin, i.e. to investigate how the magnetic monopoles hop across the lattice. In the following section it is shown how this transitions between the two states, and more in general dynamical effects, can be stimulated by the presence of a transverse field pointing transversely to the local easy axis of the RE^{3+} ion.

2.4 Perturbative effects of a magnetic field

The degeneracy of the crystal-field spectra is completely removed in the presence of a magnetic field $\mathbf{B}$:

$$\hat{\mathcal{H}} = \hat{\mathcal{H}}_{CF} - g_J \mu_B \, \hat{\mathbf{J}} \cdot \mathbf{B}. \tag{2.29}$$

In this equation, $\mu_B = e\hbar/2m_e$ is the Bohr magneton (e is the charge and m_e the mass of an electron) and g_J is the Landé factor for the RE^{3+} ion with total angular momentum $\hat{\mathbf{J}}$ ($g_J = 5/4$ and $g_J = 4/3$, respectively, for Ho^{3+} and Dy^{3+}). Now the strength and direction of the field, together with the CF parameters, characterise the resulting energies and states of the RE^{3+} ion.

To tackle the Hamiltonian in Eq. (2.29) it is convenient to use a coordinate system locally defined at the RE-site. The local coordinate system $\mathbf{x}_0, \mathbf{y}_0, \mathbf{z}_0$ used for a RE-site throughout this thesis is defined by

$$\mathbf{x}_0 = \frac{1}{\sqrt{6}}(1,1,-2), \qquad \mathbf{y}_0 = \frac{1}{\sqrt{2}}(-1,1,0), \qquad \mathbf{z}_0 = \frac{1}{\sqrt{3}}(1,1,1), \tag{2.30}$$

with respect to the canonical axes $\mathbf{X}, \mathbf{Y}, \mathbf{Z}$ of the global coordinate system of the crystal lattice. This choice is preferred as the crystal-field Hamiltonian in Ref. [45] is expressed in a coordinate system with the local quantisation axis along the global $\langle 111 \rangle$ direction. Hence in all the previous figures the $\langle 111 \rangle$ axis passing through the central RE^{3+} ion is parallel to $\mathbf{z}_0$, the local quantisation axis for Eq. (2.29). Other sets of local coordinate systems will be given in Eq. (4.22) in the context of the quantum mechanical interaction between neighbouring RE^{3+} ions in a pyrochlore lattice. The coordinate systems $\mathbf{x}_0, \mathbf{y}_0, \mathbf{z}_0$ and $\mathbf{X}, \mathbf{Y}, \mathbf{Z}$ are represented in Fig. 2.8 and later in Fig. 4.2.

As shown in the previous section, the crystal-field in spin ices is so strong that the spectra are characterised by large energy gaps of the order of 100 Kelvin. This means that the magnetic field is expected to represent a small perturbation for a wide set of values, which in fact overlaps with most of the range allowed in common scientific laboratories.

Here, however, particular interest is given to the magnetic fields that are present *inside* spin ice compounds (the whole Chapter 3 is focused on dipolar fields on the RE-sites).

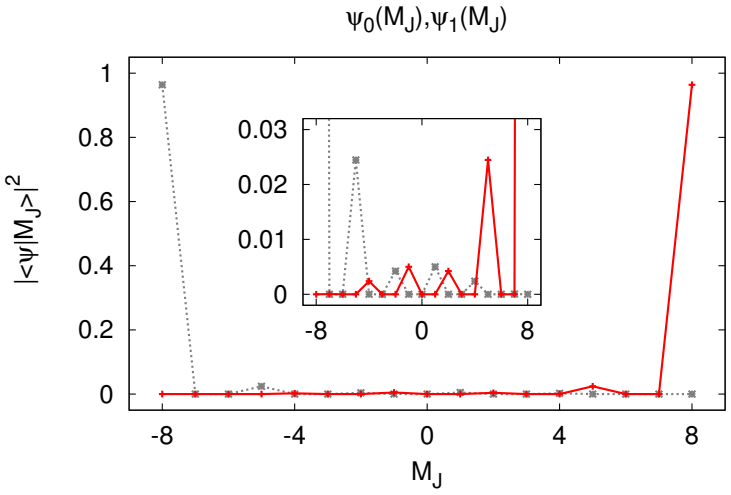

(a) HTO

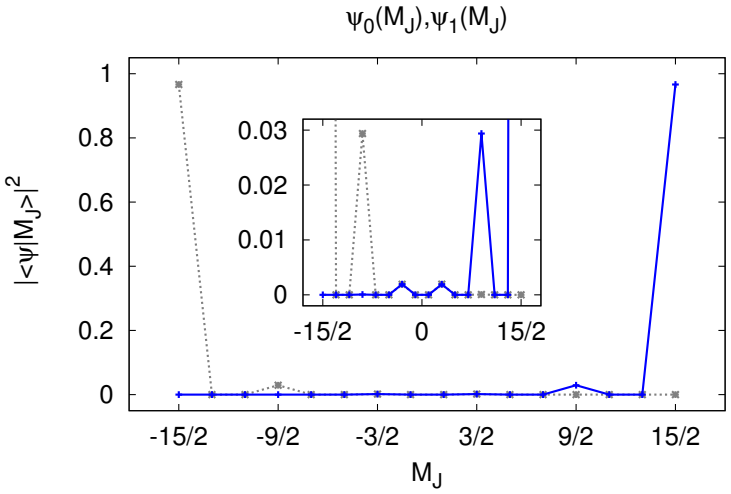

(b) DTO

Figure 2.7: Stationary wave functions, $|\psi_0\rangle$, $|\psi_1\rangle$, of a Ho^{3+} ion (top panel) and a Dy^{3+} ion (bottom panel) for the crystal field GS doublet of the Hamiltonian in Eqs. (2.25-2.27). In colour solid lines are shown the states $|\psi_0\rangle$ with positive polarisation along the local quantisation axis $\mathbf{z}_0$; in grey dotted lines are the states $|\psi_1\rangle$ with negative polarisation. The explicit expression for both $|\psi_0\rangle$ and $|\psi_1\rangle$ in HTO is given in Eq. (A.35) in Appendix A. The insets have rescaled vertical axes to visualise the non-zero values for intermediate $|M_J| < J$ (the states are actually almost polarised because the values for $|M_J| = J$ are much higher than the others). These quantities were obtained using the CF parameters given in Table 2.3 from Ref. [45] for $Ho_2Ti_2O_7$ and Ref. [48] for $Dy_2Ti_2O_7$.

holmium and dysprosium ions, indeed, possess large dipolar moments ($\approx 10\mu_B$) which are known to produce strong dipolar fields internal to the samples [12, 49]. Hence, although the effect of an externally tuneable magnetic field on the single ion physics is of relevant interest for spin ices, this would require a dilution of the magnetic ions in order to neglect the presence of mutual dipolar interactions between them. Moreover, investigating the interplay occurring between crystalline and internal dipolar fields on the RE-sites in conventional spin ices is of higher interest because it gives the possibility to comprehend how the presence of the monopoles locally affects the single ion physics and eventually opens up the dynamics above the fully frustrated spin-ice ground state. This question will be addressed in Chapter 5 by studying the dynamics of a RE^{3+} ion in spin ice under in the presence of the local dipolar and (effective) exchange fields.

2.4.1 Zeeman splitting of the crystal-field ground state doublet

The removal of the degeneracy for the ground state doublet consists, typically, in the selection of one of the two polarised states in Fig. 2.7. Which one of the two, depends on the longitudinal component of the magnetic field in Eq. (2.29) along the polarisation (easy) axis, and determine the Ising configuration in which the magnetic ion points (in theory for a time indefinitely long). This mechanism is the reason for the spin ice frustrated ground state that is peculiar of spin ices: the dipolar fields, which the magnetic ions mutually induce into each other, possess a net longitudinal component acting as a projector on the polarised states of the crystal-field of the RE-sites.

This implies that if the longitudinal component is suddenly removed, meaning that only a (perturbative) field purely transverse to the local easy axis is left, then the RE^{3+} has the ground state and the first excited one consisting respectively of bonding and anti-bonding combinations of the two opposite polarised states in Fig. 2.7. The energy splitting ΔE_{01} between such states is still very small compared to the gaps due to the presence of the crystal-field, and this, as we shall see in section 2.5, is the key element giving to the magnetic ion a finite probability to tunnel through the CF barrier and point into a configuration opposite to the initial one.

As show in Chapter 3, the presence of a monopole typically induces a dipolar field purely transverse to a neighbouring RE^{3+} ion easy axis. Hence, understanding the dynamics opened up by the monopoles requires studying the evolution of the RE^{3+} states under such fields.

The quantum mechanical expression for the coupling of the total angular momentum to the transverse magnetic field is

$$\hat{\mathbf{J}} \cdot \mathbf{B}_{\perp} = \frac{1}{2} |\mathbf{B}| \left(e^{-i\phi} \hat{J}_{+} + e^{i\phi} \hat{J}_{-} \right) . \tag{2.31}$$

In the local coordinate system $\mathbf{x}_0, \mathbf{y}_0, \mathbf{z}_0$ for the RE^{3+} ion shown in Fig. 2.8 ϕ is the angle of the field, with respect to $\mathbf{x}_0$, on the plane transverse to $\mathbf{z}_0$. It is spins subject to such purely transverse field that may flip spontaneously via quantum-mechanical tunnelling.

Diagonalisation of the Hamiltonian in Eq. (2.29) in the presence of the field in Eq. (2.31) gives, as expected, a finite splitting between the two members of the CF ground state doublet, ΔE_{01}. We find that this splitting is the smallest gap in the energy spectrum,

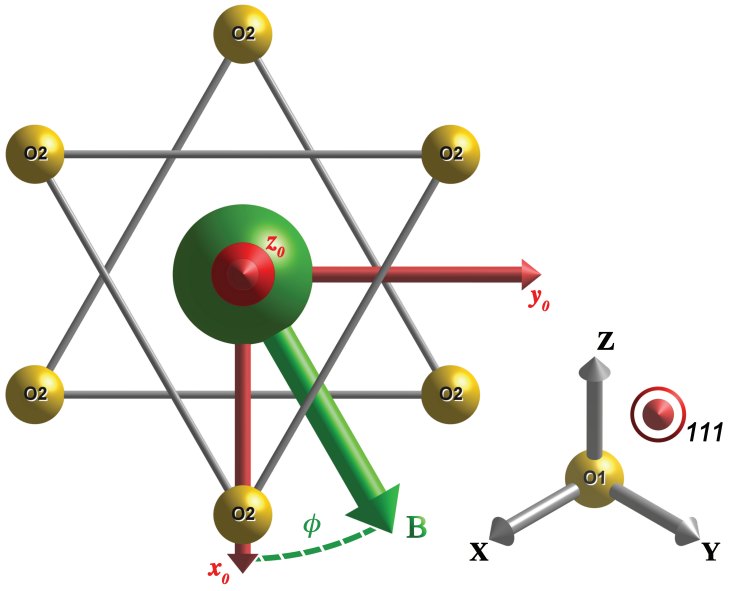

Figure 2.8: The same top-view used for the crystal-field environment in Fig. 2.5c. Here it is emphasised the position of the coplanar O2 ions (yellow spheres), three above and three below the central RE^{3+} ion (green sphere), with respect to the angle ϕ of a transverse magnetic field $\mathbf{B}$ applied to the central ion. The three (red) axes $\mathbf{x}_0, \mathbf{y}_0, \mathbf{z}_0$ indicate the local coordinate frame used for the Hamiltonian Eq. (2.31). Note this choice of coordinates has the local quantisation axis $\mathbf{z}_0$, pointing perpendicularly outward the plane of the figure itself, parallel to the $\langle 111 \rangle$ direction of the global coordinates $\mathbf{X}, \mathbf{Y}, \mathbf{Z}$. More about the local and global coordinate systems in magnetic pyrochlore oxides is discussed in section 4.2 in the context of the superexchange of electrons, mediated by the O1 sites, between RE^{3+} ions with different local easy axes.

thereby setting the rate, $\tau \sim \hbar/\Delta E_{01}$ in Eq. (1.2), for the spontaneous spin flips. The dependence of ΔE_{01} on $|\mathbf{B}|$ is shown in Fig. 2.9 for both HTO and DTO at different angles ϕ; vice versa, the splitting vs the angle ϕ is shown in Fig. 2.10 at different magnitudes of the transverse field.

For very large fields the anisotropic effect of the CF environment becomes negligible; all the curves merge into the single flat line of the Larmor frequency ω_{L}corresponding to a splitting

$$\Delta E_{01} = \hbar\omega_{\mathrm{L}} = g_J \mu_B \, |\mathbf{B}| \; . \tag{2.32}$$

As is clear from the plot, due to the strong crystal-fields in HTO and DTO, such regime is experimentally unattainable; here it is displayed for clarity and completeness [10]. It also serves the purpose of showing the strength of the energy scales set by the crystal-field which allow the magnetic ones to be considered as small perturbations.

At lower fields, when the two competing terms in Eq. (2.29) have comparable energies, the response of the system becomes anisotropic. This anisotropy is much stronger for

[10] This, however, is the result of assuming that the spin-orbit coupling, making $J = L + S$ a good quantum number, is still quite strong with respect to the magnetic field applied. In reality for strong enough fields the orbital and spin angular momenta, L and S, would decouple with each other and precess around the field independently (Paschen-Back effect).

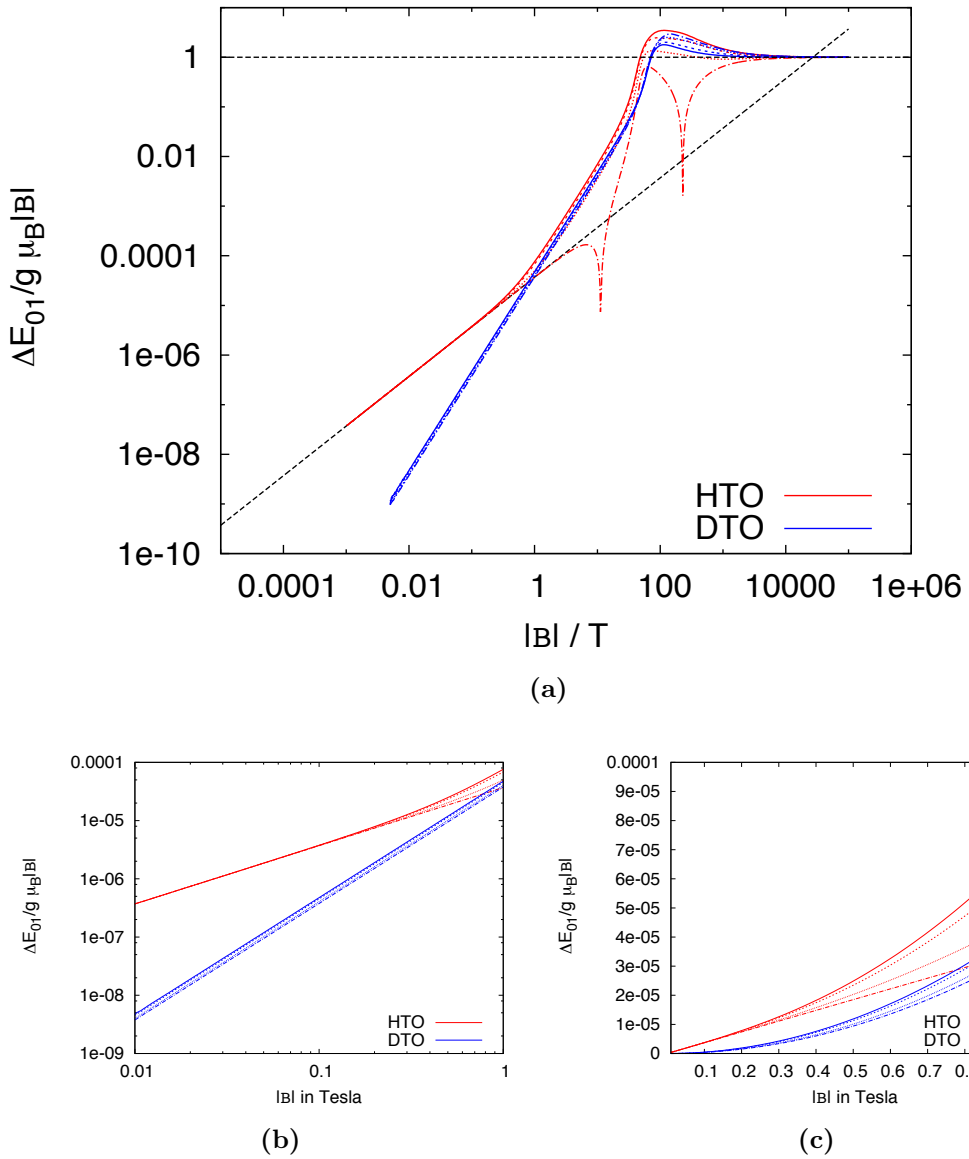

Figure 2.9: Splitting of the ground state doublet of a rare earth ion in spin ice under the influence of a magnetic field that is purely transverse to the local $\langle 111 \rangle$ direction. The red curves correspond to the non-Kramers ion Ho^{3+}, while the blue curves correspond to the Kramers ion Dy^{3+}. Note the y axis is dimensionless to allow a consistent comparison of the two systems and detect clearly the power-law behaviours. For each case the different curves correspond to fixed angles of the transverse field: $\phi = 0\,^\circ$ (solid curve), $\phi = 10\,^\circ$, (short-dashed), $\phi = 20\,^\circ$ (dotted) and $\phi = 30\,^\circ$ (dotted-dashed). In (a) the two black dashed lines show the limiting behaviours: at very hight fields corresponding to the Larmor precession in Eq. (2.32); for the low fields regime only the black dashed line for HTO is shown, derived analytically from degenerate perturbation theory, [see Eq. (2.36) and more details in Appendix A]. Figures (b) and (c) show the same splittings for limited regime of transverse fields, respectively in a log-log and a normal scale.

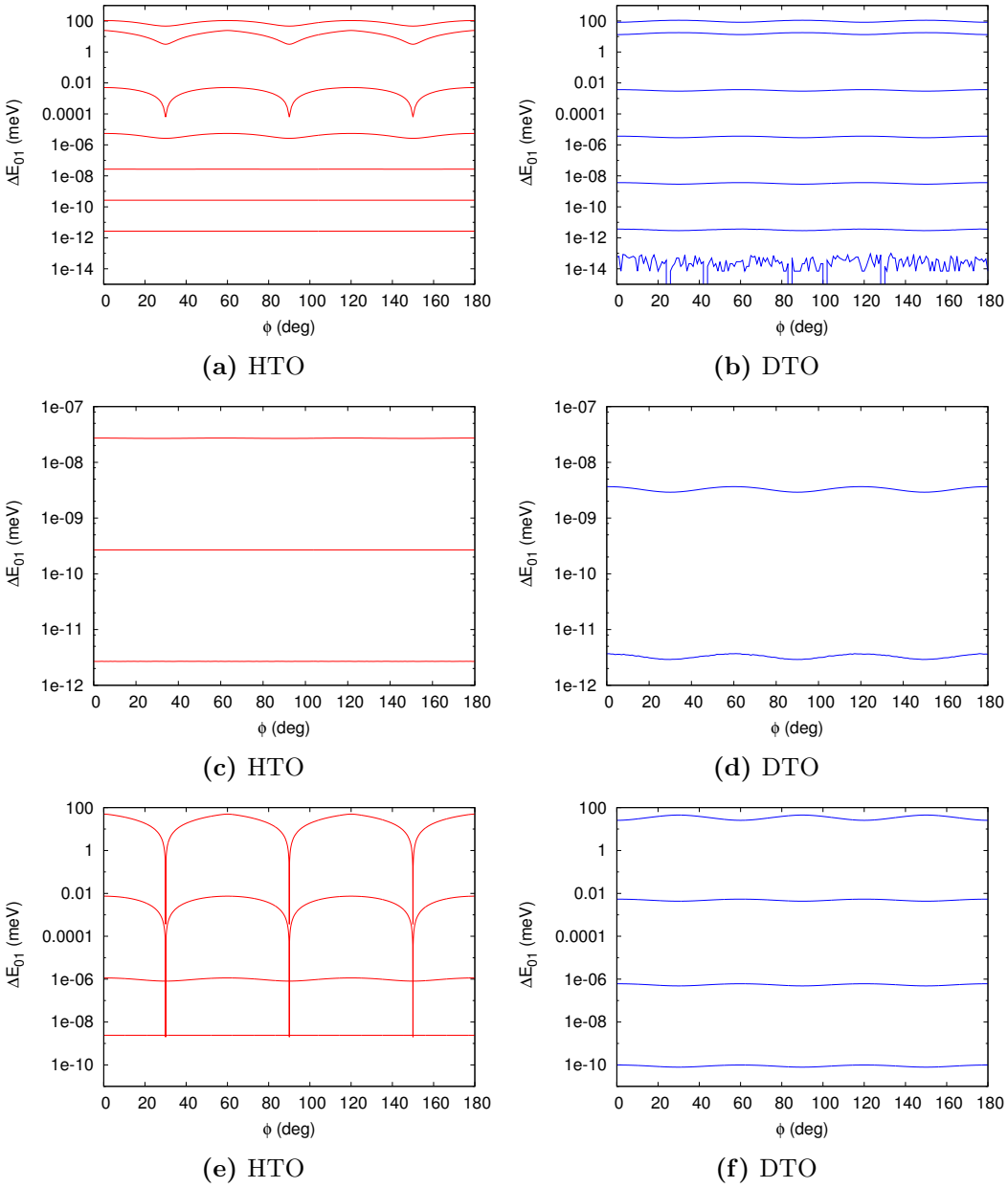

(a) HTO **(b)** DTO

(c) HTO **(d)** DTO

(e) HTO **(f)** DTO

Figure 2.10: The ground state splitting, in meV for both HTO (left) and DTO (right), as a function of the angle ϕ of the magnetic field transverse to the $\langle 111 \rangle$ axis. Each curve corresponds to a fixed strength of the field. In (a) and (b) the seven curves span, bottom to top, the order of magnitudes from 10^{-3} to 10^{3} Tesla. For HTO the magnitude of the oscillations depends heavily on the strength of the field: the oscillations are suppressed at low fields and more pronounced at intermediate ones. In contrast DTO have oscillations always smooth and proportionate to the strength of the field applied. Note DTO shows a change in the sign of the oscillations when the field is increased above around 10 Tesla. The blue fragmented curve is an artefact due to the breakdown of the numerical reliability for the splitting of DTO at fields 10^{-3} T. The panels (c) and (d) show the same curves only for the smallest fields to emphasise the vanishing of the oscillations for HTO in contrast to DTO ($10^{-3}, 10^{-2}, 10^{-1}$ T for HTO and $10^{-2}, 10^{-1}$ for DTO). The panels (e) and (f) are at four particular values of the transverse field: B=0.03 T and B=0.55 T, the two lower curves, are the typical dipolar fields on a RE-site next to a monopole found with Monte Carlo simulations (see end of section 3.2.2.2); B=11.31 T and B=228.33 T, the two upper ones, are the fields, for HTO, which make the splitting close at $\phi = 30\,^{\circ}$.

Ho^{3+} than for Dy^{3+} and, in particular, for $\phi = 30\,^\circ$ it leads to some resonances (due to level crossing between E_0 and E_1) shown in Fig. 2.9a (red dotted-dashed line) and in Fig. 2.10e.

Finally, for lower still fields, of the order of 1 T or below, the ion enters the quantum tunnelling regime where the behaviour of ΔE_{01} is given by the following power-laws:

$$\Delta E_{01} = \alpha^{(2)}_{HTO} |\mathbf{B}|^2 \qquad \text{for HTO,} \tag{2.33a}$$

$$\Delta E_{01} = \alpha^{(3)}_{DTO} |\mathbf{B}|^3 \qquad \text{for DTO.} \tag{2.33b}$$

Ground state splitting from degenerate perturbation theory

The above low-field behaviours can be understood, using degenerate perturbation theory, by considering the Zeeman interaction in Eq. (2.31) as a small perturbation with respect to CF Hamiltonian:

$$\hat{\mathcal{H}} = \hat{\mathcal{H}}_{\text{CF}} - \lambda \hat{V}\,. \tag{2.34}$$

Here $\hat{\mathcal{H}}_{\text{CF}}$ is exactly solved and $|\psi^{(0)}_n\rangle$ is the (unperturbed) CF-eigenstate with energy $E^{(0)}_n$ ($n = 0, ..., 2J$). The perturbation $\hat{V} \equiv \mathcal{E}_{\mathbf{CF}}\, \hat{\mathbf{J}} \cdot \mathbf{B}/|\mathbf{B}|$ is tuned by $\lambda = g_J \mu_B |\mathbf{B}| / \mathcal{E}_{\mathbf{CF}}$, where $\mathcal{E}_{\mathbf{CF}}$ is an arbitrary reference energy scale, e.g. related to the CF bandwidth. A thorough perturbation theory is presented in Appendix A; here only the result found for the splitting of a RE^{3+} ion in a spin ice crystalline environment is given:

$$\begin{aligned}\Delta E_{01} = {} & \lambda \sqrt{(V_{00} - V_{11})^2 + 4 |V_{01}|^2} \\ & + \lambda^2 \sqrt{\left(\sum_{k>1} \frac{|V_{0k}|^2 - |V_{1k}|^2}{\Delta E^{(0)}_{0k}} \right)^2 + 4 \left| \sum_{k>1} \frac{V_{0k} V_{k1}}{\Delta E^{(0)}_{0k}} \right|^2} + \mathcal{O}\left(\lambda^3\right)\end{aligned} \tag{2.35}$$

In this expression $V_{nm} \equiv \langle \psi^{(0)}_n | \hat{V} | \psi^{(0)}_m \rangle$ and $\Delta E^{(0)}_{0k} = E^{(0)}_k - E^{(0)}_0$. As discussed in the appendix, the purely transverse field together with the D_{3d} CF symmetry give a very particular structure to the matrix elements V_{nm} of spin ice systems. In fact, for both HTO and DTO we find no contribution at the first order ($V_{00} = V_{11} = V_{01} = 0$, see appendix for details), meaning that the splitting occurs, in the lowest case, at the second order. In Appendix A it is also shown that for doubly-degenerate unperturbed energy levels, $|\psi^{(0)}_D\rangle, |\psi^{(0)}_{D+1}\rangle$, the matrix elements of the perturbation obey $V_{D,1} = V_{0,D+1}$, $V_{D+1,1} = -V_{0,D}$, which translates into a vanishing contribution of the doublets in the expressions for the quadratic term in Eq. (2.35).

Section A.3 describes more in details the occurrence of a different splitting in the two systems. The main property that can be summarised by such analysis is that the difference in the power-law dependence is already present intrinsically in the crystal-field spectra. The main reason is that if the summation in Eqs. (2.35, A.42) is over the whole excited spectrum (including both doublets and singlets), then this will be equal to the sum of the contributions *only* from the singlets, like Eq.(A.37), since the terms from the doublets cancel out due to the relationships in Eq.(A.40). This is the case for HTO, where in fact we find a parabolic low field dependence, while for DTO this does

not happen since no singlets are present (Kramers system) and all of the contributions from doublets cancel out (parabolic dependence suppressed). These results show how a quantum mechanical perturbation of the low field physics for HTO and DTO account for a behaviour which would be otherwise missed by a classical approach! Moreover it sheds light on the actual reason behind the numerical results showing different field-dependence for the two different systems.

Then, since Dy^{3+} is a Kramers ion, all unperturbed energy levels in this case are doublets and thus the quadratic correction vanishes identically, leading to the cubic dependence on applied field in Eq. (2.35). On the other hand, Ho^{3+} is not a Kramers ion and does feature some singlets in its unperturbed energy spectrum. These are responsible for the quadratic regime, visible in Fig. (2.9), with the following coefficient in Eq. (2.33a):

$$\alpha^{(2)}_{HTO} = 2.68 \times 10^{-6} \frac{\text{meV}}{\text{T}^2} \,. \tag{2.36}$$

For Dy^{3+} where, as remarked above, this quadratic term vanishes it is difficult to obtain the cubic term using perturbation theory (see Appendix A.3). Fitting the numerical results (blue curve in Fig. 2.10) for the coefficient in Eq. (2.33b) gives the angular dependence on ϕ

$$\alpha^{(3)}_{DTO} = 6.8 \times 10^{-7} \left(1 + A\cos(6\phi)\right) \frac{\text{meV}}{\text{T}^3} \tag{2.37}$$

with $A = 0.114$.

Fig. 2.9a shows that the cubic power-law found for DTO has a smooth behaviour from the smaller fields up to around 100 Tesla. In contrast, the quadratic power law characterising HTO breaks around 0.1 Tesla, holding up to just below 10 Tesla only for $\phi = 30\,^\circ$. For the other angles, in the range from 1 to 10 Tesla also the splittings for HTO follow a cubic behaviour together with an angular dependence similar to the one for DTO. The results found with the perturbation theory seem to suggest that the angular dependence is driven by the cubic terms of the field in the power expansion of the energy splitting. The disappearance of such dependence at low fields in the case of HTO can be understood in terms of the non vanishing second-order term. This does not depend explicitly on the angle and suppresses the strength of the angular dependence. The anisotropic effect arising for higher fields coincides with the manifestation of the cubic law together with the angular dependence.

The anisotropic effects found for the ground state splitting have direct implications in the magneto-static behaviour of the RE^{3+} ions. This is illustrated in Fig. 2.11 where the different components of the magnetic moment, of the two Ho^{3+} and Dy^{3+} ions in their ground state under a transverse field, are shown as surfaces depending on the angle ϕ and strength $|\mathbf{B}|$ of the field. The similarities and discrepancies between the two systems reflect, as expected, the behaviour found for the splitting. These figures are interesting also from a pedagogical point of view, allowing the direct comparison between the behaviour of a free ion under a magnetic field (here in the regime of very strong fields) to the very peculiar case of the magnetic ions in the crystalline environment of spin ices. The local CF anisotropy, in fact, is so strong that the two components on the $\mathbf{x}_0, \mathbf{y}_0$ plane are negligible for all magnetic fields that are only a perturbation for the crystal-field. Moreover the anisotropic effects characterise heavily the magnetic moment along the $\mathbf{z}_0$ direction, which behave quite differently in the two

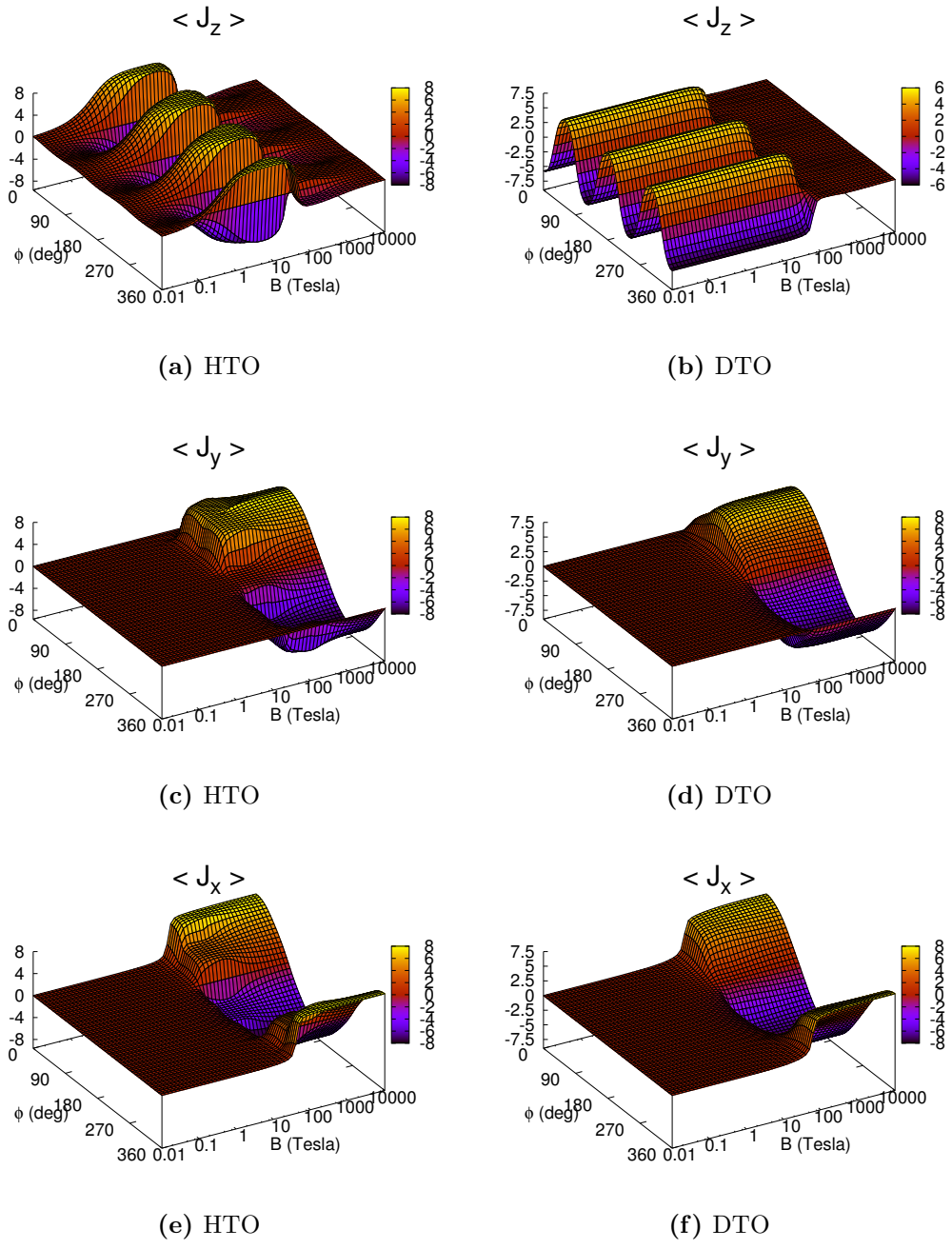

(a) HTO **(b)** DTO

(c) HTO **(d)** DTO

(e) HTO **(f)** DTO

Figure 2.11: The expectation values for the three components of the total angular momentum $\hat{\mathbf{J}}$ over the (static) ground state of the Hamiltonian in Eq. (2.29) for a single RE^{3+} ion under the spin-ice crystal-field and a magnetic field transverse to the local easy axis (this is $\mathbf{z}_0$ in the local system of coordinates $\mathbf{x}_0, \mathbf{y}_0, \mathbf{z}_0$ in Fig. 2.8). Each α component, with $\alpha = z, y, x$, from the top to the bottom panel, shows $\langle \hat{J}_\alpha \rangle = \sum_{M_J} \langle \psi | M_J \rangle \langle M_J | \hat{J}_\alpha | \psi \rangle$ as function of the angle ϕ and the strength $|\mathbf{B}|$ of the field in Fig. 2.8. Consequently, the three α-directions of the magnetic moment of the RE^{3+} ion are given by $m_\alpha = g_J \mu_B \langle \hat{J}_\alpha \rangle$. For both HTO (left) and DTO (right) the x, y components are negligible for fields below 10 T. In contrast the m_z components feature periodic dependence on the the angle ϕ below 10T; this is a manifestation of the strong axial anisotropy characterising the ground state of the spin ice RE^{3+} ions. Note the different type of response in the two systems: smooth in the angular dependence and with a constant periodicity across 3 orders of magnitude (from 10 T down to 10^{-2} T) for DTO, more abrupt in the angular features and strongly dependent on the strength for HTO (highest around 10 T, then smaller for lower fields).

systems.

These results suggest that also in the magneto-dynamics of the RE^{3+} ions under transverse fields, differences may arise between the two systems, HTO and DTO, and for the different angles and strength of the fields. To this analysis is devoted the next section, with particular emphasis on the probability of tunnelling between the two polarised configurations corresponding to the Ising states of the classical picture.

2.5 Quantum spin tunnelling of a RE^{3+} ion in spin ice

In the previous sections it has been shown how the two Ising states of a single RE^{3+} ion in spin ice are in fact related to the two states of the ground doublet obtained from the crystal-field interaction. Moreover, it has been assessed how the local perturbation of a magnetic field acts on the possible states of the CF Hilbert space (see also Appendix A), allowing also the transition from a polarised ground state to the opposite one.

The first meaningful step in studying the dynamics of a complex system such as spin ice, consists in probing the unitary time evolution under the type of fields that are expected to induce the tunnelling of the local magnetic moment of a RE^{3+} ion between the two lowest crystal-field states. To this end we focus on a particular rare-earth ion and take an initial state, $|\psi(0)\rangle$ at time $t = 0$, which is fully polarised along the local 111 axis, as assumed by the classical Ising model of Eq. (1.1) [11]. This is a good approximation to the ground state of the Hamiltonian in Eq. (2.29) for a RE^{3+} ion in the presence of a net longitudinal field (this is the typical field of the spin ice state with no monopoles as shown in Chapter 3). Then, at a time $t > 0$ a field purely transverse to the local polarisation axis is applied and the system evolves under unitary dynamics:

$$|\psi(t)\rangle = e^{-i\,\hat{\mathcal{H}}t/\hbar}\,|\psi(0)\rangle\ . \tag{2.38}$$

The evolution of the RE ions Ho^{3+} and Dy^{3+} is shown in Figs. 2.12-2.14 for different magnitudes $|\mathbf{B}|$ and angles ϕ of a field transverse to the local quantisation axis $\mathbf{z}_0$ [12].

The figures show the density plot of the probability distributions $|\langle M_J\,|\psi(t)\rangle|^2$ to find the state of the RE^{3+} ion at a certain value M_J at a given time $t > 0$. The initial condition at $t = 0$, as a reference for these examples is taken on the state $|M_J\rangle = |-J\rangle$, i.e. with the dipole moment on the RE-site pointing along the local $\bar{1}\bar{1}\bar{1}$ direction. Overlaid to each plot for the probability density is a curve for the averaged polarisation $\langle\hat{J}_z(t)\rangle = \sum_{M_J} M_J\,|\langle M_J\,|\psi(t)\rangle|^2$. The results, as predicted from the analysis on the ground state splitting ΔE_{01} and the static magnetic moments in section 2.4.1, vary depending on the strength $|\mathbf{B}|$ and angle ϕ of the transverse field, and shed light on the implications of these for the dynamics of the two RE^{3+} ions.

As can be seen in all figures, the averaged polarisation $\langle\hat{J}_z(t)\rangle$ oscillates coherently between the initial state and one pointing in the opposite direction. Note that the flipping is not always complete because in the crystal field the ground state and the first excited state are only approximately bonding and anti-bonding combinations of

[11] This axis, as previously underlined, corresponds to the local quantisation axis $\mathbf{z}_0$ for the CF representation in Figs. 2.5,2.8 and Eqs. (2.26,2.29).

[12] The evolution in Eq. (2.38) is under the Hamiltonian in Eq. (2.29), having the respective CF parameters for HTO and DTO from Table 2.3.

pointing along 111 and $\bar{1}\bar{1}\bar{1}$ [13]. In addition, there is a faster "jitter" of this quantity which is due to the approximation to the fully polarised states in the initial conditions. These small oscillations found in the curve of the $\langle \hat{J}_z(t) \rangle$ will be removed once more realistic eigenstates of the Hamiltonian in Eq. (2.29) are used (see discussion in Chapter 5). Here however, the focus is on presenting the occurrence of the tunnelling of a RE^{3+} ion in the most simple and general context compatible with the implementation of a realistic crystal-field Hamiltonian [14]. The results are shown for three main values of the field $|\mathbf{B}|$ which represent three different regimes of the behaviours found for the two different systems. These are $|\mathbf{B}| = 0.1, 1, 10$ Tesla because they mark the boundary of three different regions in the behaviour of the splitting in Fig. 2.9.

For fields $|\mathbf{B}| \leq 0.1\,\mathrm{T}$ the splitting ΔE_{01} is regulated by two different power laws in Eq. (2.33), i.e. the two systems are expected to behave differently. In fact, as shown in Fig. 2.12, the dependence of the tunnelling mechanism on ϕ is negligible for HTO while clearly present for DTO. This is because the coefficient $\alpha^{(2)}_{HTO}$ regulating the quadratic dependence of the splitting, found from perturbation theory in Eq. (2.36), is simply a constant. According to this, the independent value of ΔE_{01} with respect to ϕ ensures the same timescale τ for the full tunnelling at all angles ϕ. In contrast, the behaviour of DTO depends clearly on the angle of the transverse field and features a full tunnelling only for $\phi = 30\,^\circ$. This is because of the cubic power law regulating the splitting ΔE_{01} for DTO, as the coefficient $\alpha^{(3)}_{DTO}$ in Eq. (2.37) has a neat angular dependence on ϕ. These features are manifest in Fig. 2.12 where, for both HTO (left) and DTO (right), the time evolution under a transverse field with $|\mathbf{B}| = 0.1\,\mathrm{T}$esla, is given at different angles ($\phi = 0\,^\circ, 15\,^\circ, 30\,^\circ$ from the top to the bottom). For this value of the field, the two systems have characteristic tunnelling timescales differing by one order of magnitude ($\tau \approx 0.07\,\mathrm{ms}$ for HTO and $\tau \approx 0.7\,\mathrm{ms}$ for DTO). For lower still fields the two timescales evolve according to the different slopes of the splitting in Fig. 2.9, hence increasing and diverging from each other.

For fields $|\mathbf{B}| > 0.1\,\mathrm{T}$ the behaviour of the splittings ΔE_{01} change and may vary drastically depending on the angles ϕ (for example in the resonances for HTO in Figs. 2.9-2.10). In the region between 0.1 and 1 Tesla the splitting for HTO start diverging from the simple quadratic behaviour and becomes ϕ-dependent. The behaviour of the tunnelling, in fact, shows more similarities between HTO and DTO. Note in Fig. 2.13 that the probability of tunnelling decreases in a similar manner for both systems for angles smaller than $30\,^\circ$. However, at $\phi = 30\,^\circ$ the full tunnelling is present for both systems and, in this particular case of $|\mathbf{B}| = 1\,\mathrm{T}$ features the same timescale $\tau \approx 0.7\mu\,\mathrm{s}$

[13] To be more precise, we find that (i) for the ground and first excited states the probability distributions $|\langle M_J\,|\psi(t)\rangle|^2$ are only approximately even; (ii) the phase differences between $\langle J\,|\psi(t)\rangle$ and $\langle -J|\psi(t)\rangle$ are only approximately equal to 0 in one case and π in the other case; and (iii) the probability amplitudes are finite for other values of M_J as well.

[14] Indeed a full tunnelling of a large magnetic ion, such as Ho^{3+} or Dy^{3+}, can be modelled theoretically by using simpler models. For example, in the context of this research, it was investigated the more pedagogical case of a magnetic ion under a fictitious CF environment with $\hat{\mathcal{H}}_{CF} \propto \sum_{M_J} |M_J|^2\,|M_J\rangle\,\langle M_J|$. Also in this case the full tunnelling is found although, for a crystal-field well of the same height as the spin ice one, fields of the order of 30 Tesla would be necessary to achieve it. Interestingly this kind of potential has an algebraic expression similar to the one used for investigating tunnelling and density of states for cold atoms trapped in optical lattices [50]. Although this result is not directly relevant for spin ices, it is of general interest as it represents an instance in which the language of physics applies to systems which may look very diverse but are fundamentally governed by analogous mechanisms.

(this agrees with the occurrence of the intersection between the curves for the splitting of HTO and DTO in Figs. 2.9 at $|\mathbf{B}| \lesssim 1\,\mathrm{T}$).

For a transverse field of $|\mathbf{B}| = 10\,\mathrm{T}$ Fig. 2.14 shows a drastic change in the behaviour of HTO while a simply rescaled behaviour for the timescales of DTO. In both cases the full tunnelling is again found only at $\phi = 30\,^\circ$, the timescales are now very short and the difference in order of magnitudes is reversed (DTO is faster than HTO). Again such behaviour is clarified by the dependence of ΔE_{01} for the two different systems, although the total suppression of the tunnelling for HTO remains to be investigated (in terms of the characterisation based on the dependence of the splitting ΔE_{01} it would be expected to find very similar features with DTO since the curves almost overlap around 10 T for $\phi = 0\,^\circ, 15\,^\circ$).

From the analysis on the curves for the static magnetic moment in Fig. 2.14a it can be argued that the tunnelling for HTO is prevented because of the plateaus characterising m_z for the field values of around 10 Tesla. It is likely that because of interplay between the magnetic field and the anisotropy in HTO, the magnetic ion Ho^{3+} is more susceptible to the transverse field responding with a stronger anisotropy along preferred directions of $\mathbf{z}_0$. On the other hand the smooth periodic behaviour found for $\langle \hat{J}_z(t) \rangle$ in Fig. 2.14a also agrees with the tunnelling features which are basically constant from 10 Tesla to all lower fields.

Nonetheless, in the context of the research presented here it is not necessary to assess these questions for magnetic fields which, not surprisingly, compete more with the strength of the crystal-field. Such fields are few order of magnitudes above the typical dipolar fields characteristic of spin ice, as we shall see in Chapter 3. The study of the dynamics presented in this chapter is only to give an overview on the behaviour expected from the tunnelling rates, with particular emphasis on the dependence on the strengths and directions of the transverse fields.

The remaining part of this thesis is dedicated to the investigation of the kind of interactions induced on the RE^{3+} whenever a monopole is sitting nearby. Together with the internal dipolar fields, thoroughly analysed in Chapter 3, it has been necessary also to consider, in Chapter 4, the role of the exchange interactions. The results found for the tunnelling under such interactions acting on a RE-site near a monopole are compared in Chapter 5, in the context of a quantum-quench model proposed in this thesis to describe the propagation of a monopole in spin-ice materials.

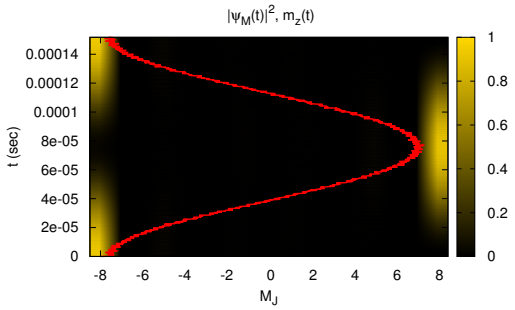

(a) HTO ($|\mathbf{B}| = 0.1$ Tesla, $\phi = 0\,^\circ$)

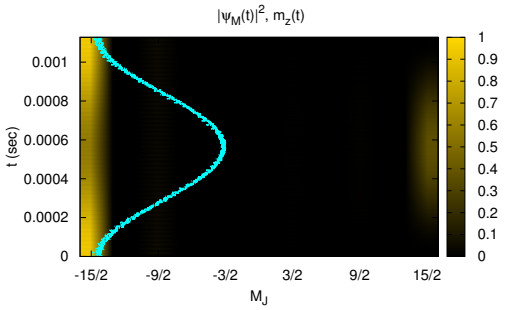

(b) DTO ($|\mathbf{B}| = 0.1$ Tesla, $\phi = 0\,^\circ$)

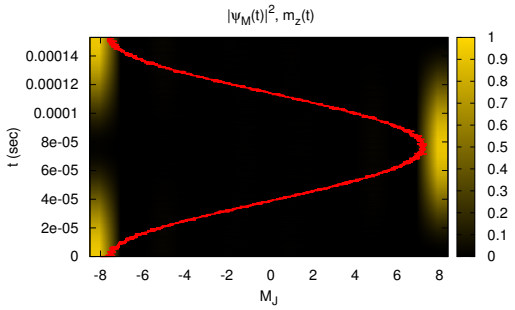

(c) HTO ($|\mathbf{B}| = 0.1$ Tesla, $\phi = 15\,^\circ$)

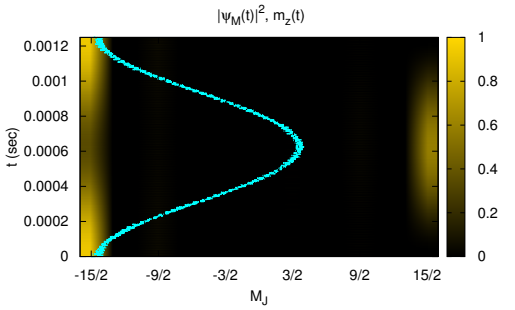

(d) DTO ($|\mathbf{B}| = 0.1$ Tesla, $\phi = 15\,^\circ$)

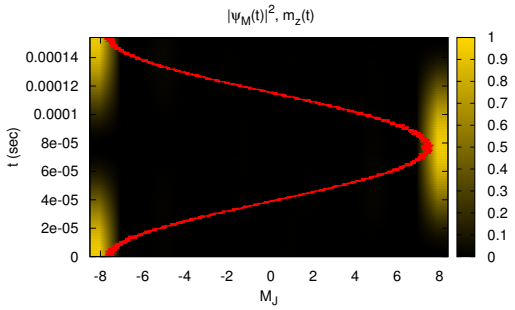

(e) HTO ($|\mathbf{B}| = 0.1$ Tesla, $\phi = 30\,^\circ$)

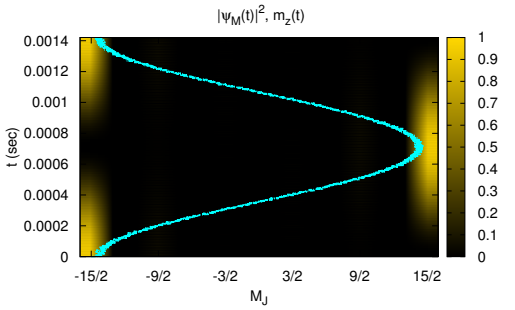

(f) DTO ($|\mathbf{B}| = 0.1$ Tesla, $\phi = 30\,^\circ$)

Figure 2.12: Time-evolution under a transverse field of strength $|\mathbf{B}| = 0.1\,\mathrm{T}$. The density plots show the probability density $|\langle M_J|\psi(t)\rangle|^2$, where $|\psi(t)\rangle$ is the state of a RE^{3+} ion at time t after the application of the field. At $t = 0$ the state of the magnetic ion is polarised in $|\psi(0)\rangle = |-J\rangle$, which corresponds to $|-8\rangle$ and $|-\frac{15}{2}\rangle$ respectively for HTO (left) and DTO (right). The vertical axes show the time, in seconds, while the horizontal ones account for the value of $M_J = -J, \ldots, +J$. The curve overlaid on each density plot gives the expectation value $\langle \hat{J}_z(t)\rangle = \sum_{M_J} M_J\,|\langle M_J\,|\psi(t)\rangle|^2$. The panels, top to bottom, show the time-evolution for the angles $\phi = 0\,^\circ, 15\,^\circ, 30\,^\circ$ of the field on the $\mathbf{x}_0, \mathbf{y}_0$ plane in Fig. 2.8. At $|\mathbf{B}| = 0.1\,\mathrm{T}$ both systems show a finite probability of tunnelling from the initial configuration to the opposite one. HTO accomplishes a full tunnelling for all values of ϕ, while DTO only at $\phi = 30\,^\circ$ (the lowest probability of tunnelling is found for $\phi = 0\,^\circ$). Note the flipping timescales differ by one order of magnitude for the two systems (at $\phi = 30\,^\circ$, $\tau \approx 0.07\,\mathrm{ms}$ for HTO and $\tau \approx 0.7\,\mathrm{ms}$ for DTO).

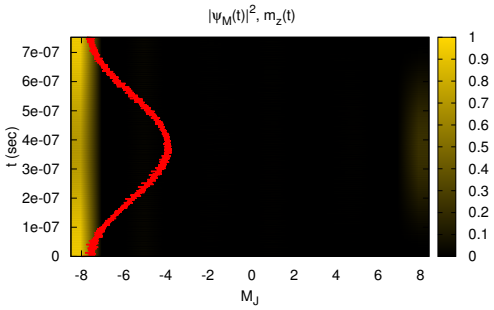

(a) HTO ($|\mathbf{B}| = 1$ Tesla, $\phi = 0\,^\circ$)

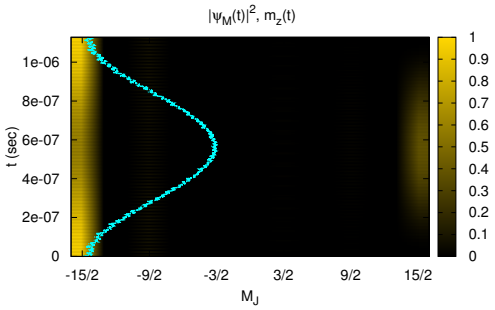

(b) DTO ($|\mathbf{B}| = 1$ Tesla, $\phi = 0\,^\circ$)

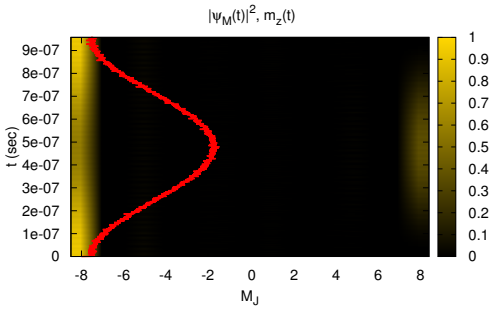

(c) HTO ($|\mathbf{B}| = 1$ Tesla, $\phi = 15\,^\circ$)

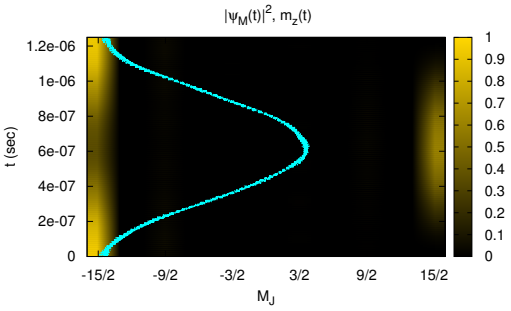

(d) DTO ($|\mathbf{B}| = 1$ Tesla, $\phi = 15\,^\circ$)

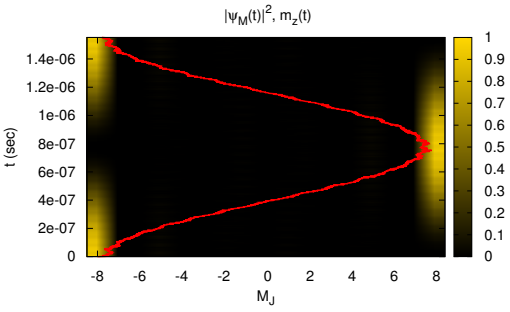

(e) HTO ($|\mathbf{B}| = 1$ Tesla, $\phi = 30\,^\circ$)

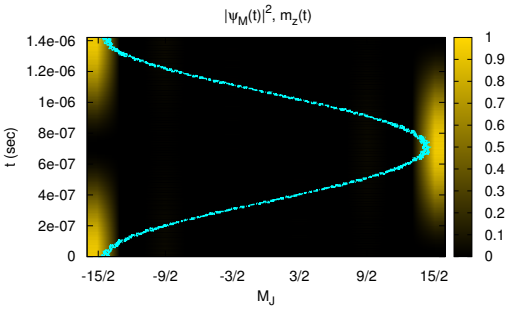

(f) DTO ($|\mathbf{B}| = 1$ Tesla, $\phi = 30\,^\circ$)

Figure 2.13: The same type of time-evolution shown in Fig. 2.12 but for fields of strength $|\mathbf{B}| = 1\,\mathrm{T}$. In this case also for HTO the probability of tunnelling is affected by the angle ϕ of the field on the $\mathbf{x}_0, \mathbf{y}_0$ plane in Fig. 2.8. In both systems the probability of having the wave function on the other end of the polarisation axis reaches its maximum for $\phi = 30\,^\circ$ and its minimum at $\phi = 0\,^\circ$. Here the flipping timescales differ less between the two systems (at $\phi = 30\,^\circ$, $\tau \approx 0.7\mu\,\mathrm{s}$ for both HTO and DTO; see the intersection of the red and blue dotted-dashed curves occurring around 1 Tesla in Figs. 2.9).

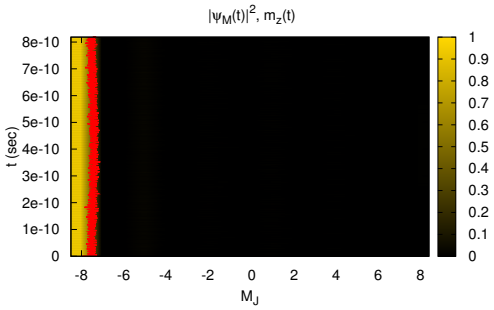

(a) HTO ($|\mathbf{B}| = 10$ Tesla, $\phi = 0\,^\circ$)

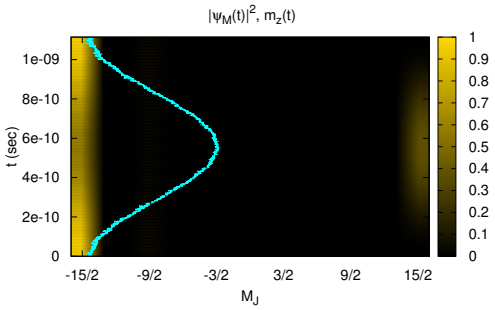

(b) DTO ($|\mathbf{B}| = 10$ Tesla, $\phi = 0\,^\circ$)

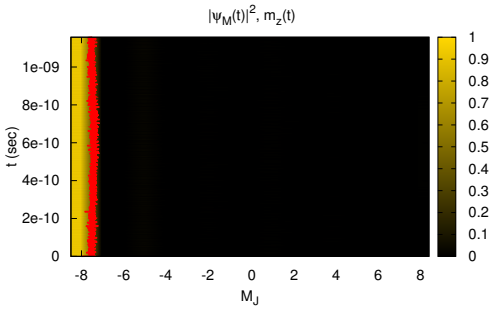

(c) HTO ($|\mathbf{B}| = 10$ Tesla, $\phi = 15\,^\circ$)

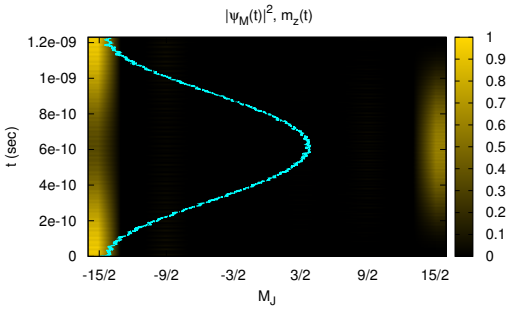

(d) DTO ($|\mathbf{B}| = 10$ Tesla, $\phi = 15\,^\circ$)

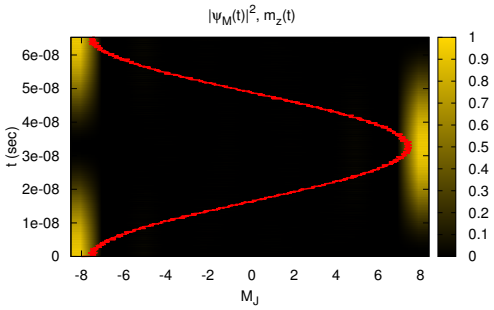

(e) HTO ($|\mathbf{B}| = 10$ Tesla, $\phi = 30\,^\circ$)

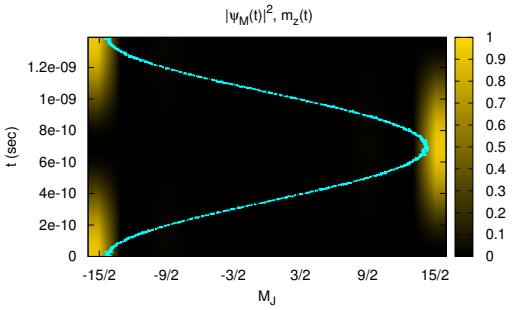

(f) DTO ($|\mathbf{B}| = 10$ Tesla, $\phi = 30\,^\circ$)

Figure 2.14: The same type of time-evolution shown in Figs. 2.12,2.13, here for fields of strength $|\mathbf{B}| = 10\,\mathrm{T}$. In this case also for HTO the probability of tunnelling is totally suppressed for angles $\phi \neq 30\,^\circ$. Both systems show full quantum tunnelling at $\phi = 30\,^\circ$ but with very different timescales (at $\phi = 30\,^\circ$, $\tau \approx 3\mu$s for HTO while $\tau \approx 0.6\,$ns for DTO).

"In contrast to electrostatics, the basic laws of magnetic fields did not follow straightforwardly from man's earliest contact with magnetic materials. The reasons are several, but they all stem from the radical difference between magnetostatics and electrostatics: there are no free magnetic charges. *This means that magnetic phenomena are quite different from electric phenomena and that for a long time no connection was established between them. The basic entity in magnetic studies was what we now know as a magnetic dipole."*

J. D. Jackson [51]

3

Dipolar fields inside spin ice

In the previous chapter it has been shown how the quantum mechanical features of a RE^{3+} ion can manifest in a spin-ice system because of local magnetic fields. Summarising, it has been found that such fields, in the regime where they act as small perturbations with respect to the crystal-field interaction, act as stabiliser or dynamical stimulator for the RE^{3+} depending on their directions with respect to the axes characterising the local the D_{3d} symmetry of the crystal-field.

Since the spin ices are known for being magnetic systems with strong classical correlations [5], resulting from the dipolar interactions between the RE^{3+} ions, the present chapter consists in a starting point for revisiting the local properties of the RE-sites in terms of the interplay between the internal dipolar fields and the single-ion physics discussed in Chapter 2. In the latter the focus was on analysing the local physics of a RE-ion in spin ice from a quantum mechanical point of view; in the present chapter the aim is to evaluate the typical dipolar fields found on RE^{3+} site depending on the configurations of the surrounding dipoles. Particular attention is given to the fields emerging in the presence of a monopole since these, as we shall see below, are purely transverse to the local $\langle 111 \rangle$ axis. Such fields, as shown in section 2.5, induce quantum dynamics of the magnetic moment of the RE^{3+}. Consequently, as will be discussed in Chapter 5, they play a pivotal role in the quantum spin tunnelling which drives the propagation of the monopoles themselves.

The pyrochlore oxides $Ho_2Ti_2O_7$ and $Dy_2Ti_2O_7$ are characterised by RE ions with large magnetic moments $|\mathbf{m}| \approx 10\mu_B$. The strength of the internal magnetic fields they generate inside the sample is a direct manifestation of the classical dipolar correlations characterising these systems [5, 52]. At temperatures allowing the emergence of monopoles the behaviour of the internal fields becomes more rich, since the former act as sources and sinks of the latter. Moreover, the freedom of the monopoles to move across the lattice suggests the presence of spatial and temporal fluctuations in the distribution of magnetic fields resulting from that motion.

Monte Carlo simulations together with NMR measurements have been used to investigate the dependence between field distributions across the lattice and the positions of monopoles [49]. The monopole contribution has been considered by looking at the internal fields in the magnetic voids of a RE-pyrochlore lattice; these are the RE-tetrahedra hosting the monopoles centred at the (non magnetic) O1 sites. The Monte Carlo simulations in Ref. [49] have been carried out by keeping a monopole-antimonopole pair at fixed distance and letting the dipoles span the available 2in-2out configurations. The line shape for the histograms of the magnetic field strength at the O1 sites shows a very good agreement with the zero-field NMR measurements carried out at temperatures in the range of 0.1-0.6 K. The discrepancy between the theoretical distribution being peaked at 4.5 Tesla versus the NMR one at 3.4 Tesla is interpreted as due to the classical Monte Carlo simulations which cannot grasp the physics beyond the dipolar picture (for example the spatial distribution of the $4f$ RE-electrons or the RE-O1 chemical bonding).

The results of the above study suggest that internal fields in spin ice are within the order of magnitude where they can be considered as perturbation of the CF Hamiltonian. As noted above, the study presented in Ref. [49], however, is focused on the estimation of fields only at the centres of the tetrahedra. These are not directly relevant for the quantum spin tunnelling of the RE-spins (sitting at the corners of the tetrahedra) discussed in section 2.5. Thus, having access to the internal fields at the RE-sites is fundamental to investigate the role of quantum spin-tunnelling in the hopping of a monopole. As we shall see, the internal fields can be very different on RE-sites near a monopole [1], encouraging speculations on how the monopoles themselves modify the local fields to propagate along certain directions rather than others (this will be investigated more explicitly in Chapter 5).

This chapter discusses the type of dipolar fields on some of the RE-sites for different types of spin-ice configurations of the magnetic dipoles. This is done by studying the resulting magnetic fields on a central RE-site in spin ice clusters of dipoles. Different sizes are investigated and compared with each other (also very briefly to results of Monte Carlo simulations). We find that the presence of a monopole gives purely tranverse fields on the RE-sites next to it, hence stimulating the quantum spin tunnelling which allows the monopole to hop.

3.1 Preliminaries: magnetic dipolar fields

The magnetic dipoles are the basic entities in the studies of magnetostatics. Classically a magnetic dipole can be represented as a little magnetic needle which tends to align in a certain direction when placed near a magnetic material [51]. This tendency to align consists in a mechanical torque that any magnetic dipole undergoes to minimise its magnetic energy of interaction with the applied field.

The smallest magnetic dipoles known in nature are those originating from the electrons bounded in atomic systems. As mentioned in the previous chapters, the relationship between the electron quantum-numbers and the dipolar moment of a magnetic atom lies at the foundation of quantum physics and relativity: it depends mainly on the

[1] Compared to the typical fields in the spin-ice (2in-2out) state.

coupling between the orbital and the spin degrees of freedom of the electrons. In spite of this, because of the strength of the dipolar moments of the RE-ions in Ho^{3+} and Dy^{3+} , the simplified notion of atomic dipole as a microscopic needle is used in this chapter since it represents a suitable way to discuss the internal magnetic fields found in spin ices.

3.1.1 Magnetic dipoles and their fields

In classical physics the vector potential

$$\mathbf{A}(\mathbf{r}) = \frac{\mu_0}{4\pi}\frac{\mathbf{m}\times\mathbf{r}}{r^3} \tag{3.1}$$

of a magnetic dipole $\mathbf{m}$ produces a magnetic induction [51]

$$\mathbf{B}(\mathbf{r}) = \nabla\times\mathbf{A}(\mathbf{r}) = \frac{\mu_0}{4\pi}\left(\frac{3(\mathbf{m}\cdot\mathbf{r})\mathbf{r}}{r^5} - \frac{\mathbf{m}}{r^3}\right). \tag{3.2}$$

The vector $\mathbf{r}$ represents the position of a given point with respect to the location of the dipole itself. Hence for a system of N dipoles

$$\mathbf{B}(\mathbf{r}) = \frac{\mu_0}{4\pi}\sum_{i=1}^{N}\left(\frac{3(\mathbf{m}_i\cdot(\mathbf{r}-\mathbf{r}_i))(\mathbf{r}-\mathbf{r}_i)}{|\mathbf{r}-\mathbf{r}_i|^5} - \frac{\mathbf{m}_i}{|\mathbf{r}-\mathbf{r}_i|^3}\right). \tag{3.3}$$

To derive the internal dipolar fields in a magnetic system such as spin ice, it is convenient to rewrite Eq. (3.3) in the following form:

$$\mathbf{B}(0) = \frac{\mu_0|\mathbf{m}|}{4\pi}\sum_{i=1}^{N} S_i\frac{3(\hat{e}_i\cdot\hat{\mathbf{r}}_i)\hat{\mathbf{r}}_i - \hat{e}_i}{|\mathbf{r}_i|^3}, \tag{3.4}$$

where $\mathbf{r}_i = -\mathbf{r}_{i0} = \mathbf{r}_i - \mathbf{r}_0$. Here the resulting field is calculated at the origin of the coordinates to emphasise the symmetries of the dipolar configurations. Furthermore all the dipoles have the same magnitude $|\mathbf{m}|$ and the unit vectors $\hat{e}_i$ point in several fixed directions. Only two possible orientations $S_i = \pm 1$ are allowed for each spin ($\mathbf{m}_i = S_i\hat{e}_i|\mathbf{m}|$).

The expression in Eq. (3.4) helps to visualise the resulting field in cases where the dipoles have a symmetrical arrangement. Moreover it facilitates the distinction between constructive and destructive orientations of the spins; for example by looking at pairs of dipoles with same easy axis $\hat{e}_i$. Fig. 3.2 represents an example of similar configurations leading to different dipolar fields on the central site of a small spin-ice cluster (the coordinate flip of two parallel spins gives a totally different resulting field). To describe the way similar configurations could be constructive or destructive for the resulting fields we discuss in what follows a few cases in detail.

3.1.2 Pairwise dipoles

We start by considering the simplest case: a dimer of magnetic moments $\mathbf{m}_1, \mathbf{m}_2$ with the same strength $|\mathbf{m}|$ and the same easy axis $\hat{e}$. The resulting field (3.4) at the midpoint

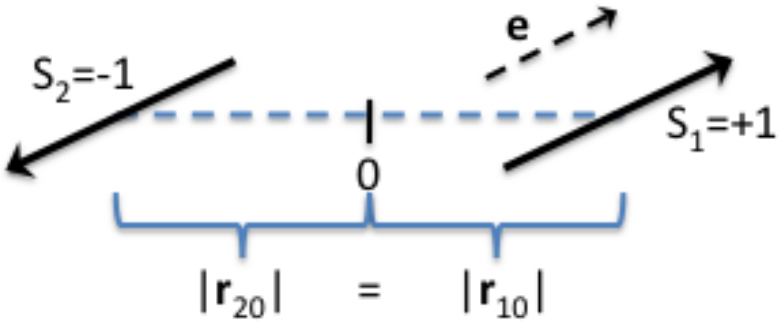

Figure 3.1: A dimer of dipoles with the same anisotropy and opposite orientations ($S_1 = -S_2$). This configuration gives a null field at the midpoint.

between them is

$$\begin{aligned}\mathbf{B}(0) &= \frac{\mu_0|\mathbf{m}|}{4\pi|\mathbf{r}|^3}\Big\{S_1\Big(3(\hat{e}\cdot\hat{\mathbf{r}}_1)\hat{\mathbf{r}}_1 - \hat{e}\Big) + S_2\Big(3(\hat{e}\cdot\hat{\mathbf{r}}_2)\hat{\mathbf{r}}_2 - \hat{e}\Big)\Big\} \\ &= \frac{\mu_0|\mathbf{m}|}{4\pi|\mathbf{r}|^3}\Big(S_1 + S_2\Big)\Big(3(\hat{e}\cdot\hat{\mathbf{r}})\hat{\mathbf{r}} - \hat{e}\Big),\end{aligned} \tag{3.5}$$

where the second line is obtained since $(\hat{e}\cdot\hat{\mathbf{r}}_2)\hat{\mathbf{r}}_2 = (\hat{e}\cdot\hat{\mathbf{r}}_1)\hat{\mathbf{r}}_1$ and $\hat{\mathbf{r}} = \hat{\mathbf{r}}_1 = -\hat{\mathbf{r}}_2$. Hence if the spins have opposite orientations ($S_1 = -S_2$), the total field at the midpoint is null (see Fig. 3.1); if they have the same orientation ($S_1 = S_2$) the resulting field is twice the field of one. Although this example is trivial, it turns out to be a useful tool to calculate the total dipolar field in the centre of a spin ice cluster in terms of pairwise, constructive or destructive, interaction between spins with the same anisotropy.

3.1.3 Nearest neighbour dipolar fields on a RE-site

In spin ice materials the simplest model for the internal fields on the RE-sites consists of a cluster of 6 spins arranged as nearest neighbours to a central site of a two-tetrahedra pyrochlore structure (Fig. 3.2); here for simplicity the origin of the reference frame is on the central site itself to make the implementation of Eq. (3.5) straightforward.

The field of the central dipole is not considered because self-interaction is neglected in Eqs. (3.1-3.5); only the magnetic fields due to the surrounding dipoles matter (this is OK for point-like dipoles). The unit vector $\hat{e}_0 = \frac{1}{\sqrt{3}}(1,1,1)$ in the origin is used as reference for the orientations of the other dipoles: $S_i^0 = \pm 1$ means that $\mathbf{m}_i \cdot \hat{e}_0 \gtrless 0$ respectively [2], where $\mathbf{m}_i = S_i^0\hat{\mathbf{m}}_i$ and $i = 1, 2, \ldots, 6$. The three dipoles in the upper (positive) octant are labelled $\mathbf{m}_1, \mathbf{m}_2, \mathbf{m}_3$, whilst the other three in the lower (negative) one are $\mathbf{m}_4, \mathbf{m}_5, \mathbf{m}_6$.

The central site, in the origin, sits in the midpoint of the segments $\mathbf{r}_j - \mathbf{r}_{j+3}$ connecting the pairs of dipoles with the same easy axis $\hat{e}_j = \hat{e}_{j+3}$ with $j = 1, 2, 3$; this allows the calculation and visualisation of the resulting fields in terms of a convenient choice of

[2] The suffix 0 in S_i^0 is used to emphasise that the orientation of $\mathbf{m}_i$ is expressed with respect to $\hat{e}_0$. This is different from the "2in-2out notation" where the signs S_i account for the inwardness/outwardness of each spin in the frame of a given tetrahedron.

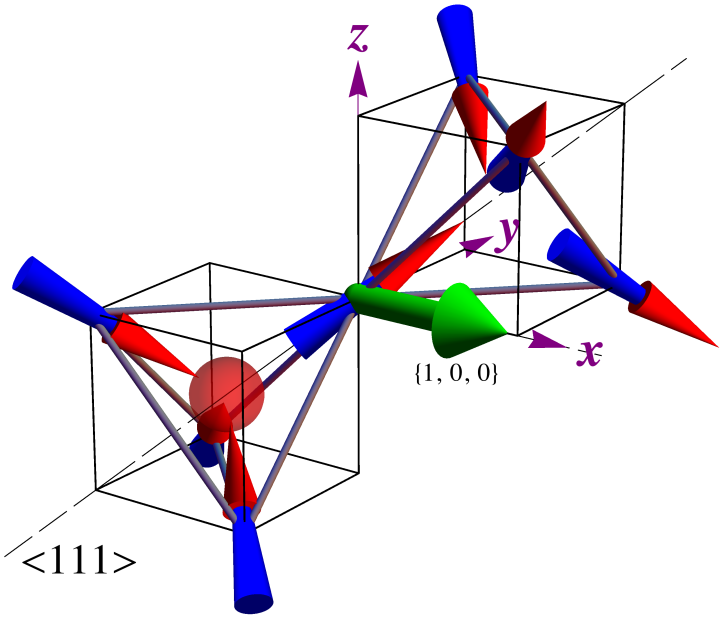

(a)

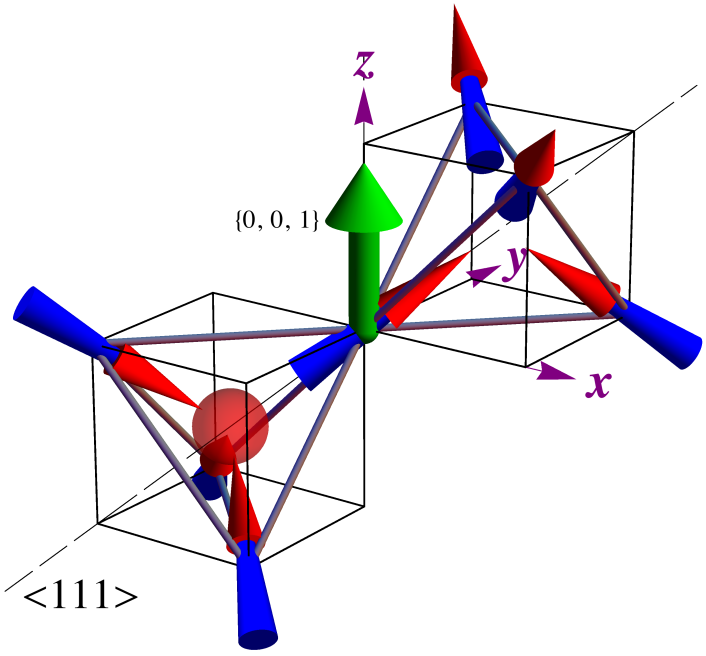

(b)

Figure 3.2: Examples of similar dipolar configurations leading to different resulting fields in a central site (2in-2out in the upper tetrahedron 3in-1out in the lower one). The green arrow represents the direction of the resulting field (vectors in curly brackets); the size and length of this field is only of illustrative purpose. The central spin has small probability to flip because the resulting field has a finite longitudinal component along the $\langle 111 \rangle$ axis.

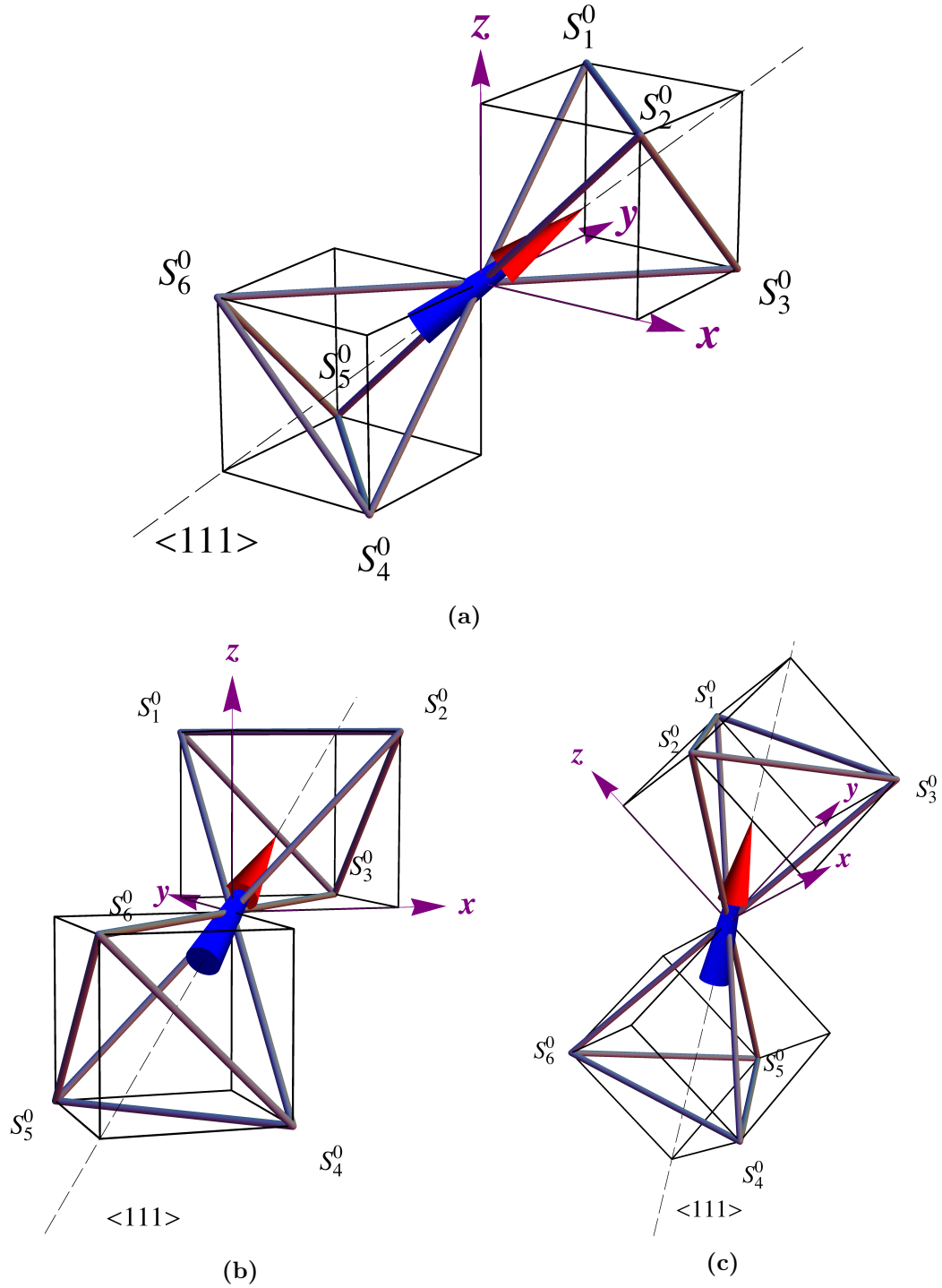

Figure 3.3: Different perspectives of the two-tetrahedra cluster with origin of coordinates (purple) on the central site. The dashed line is the local $\langle 111 \rangle$ axis of the reference frame (also the easy axis of the central dipole). This is used as reference direction for the Ising states of all the dipoles ($S_i^0 = \hat{\mathbf{m}}_i \cdot \hat{e}_0 = \pm 1$).

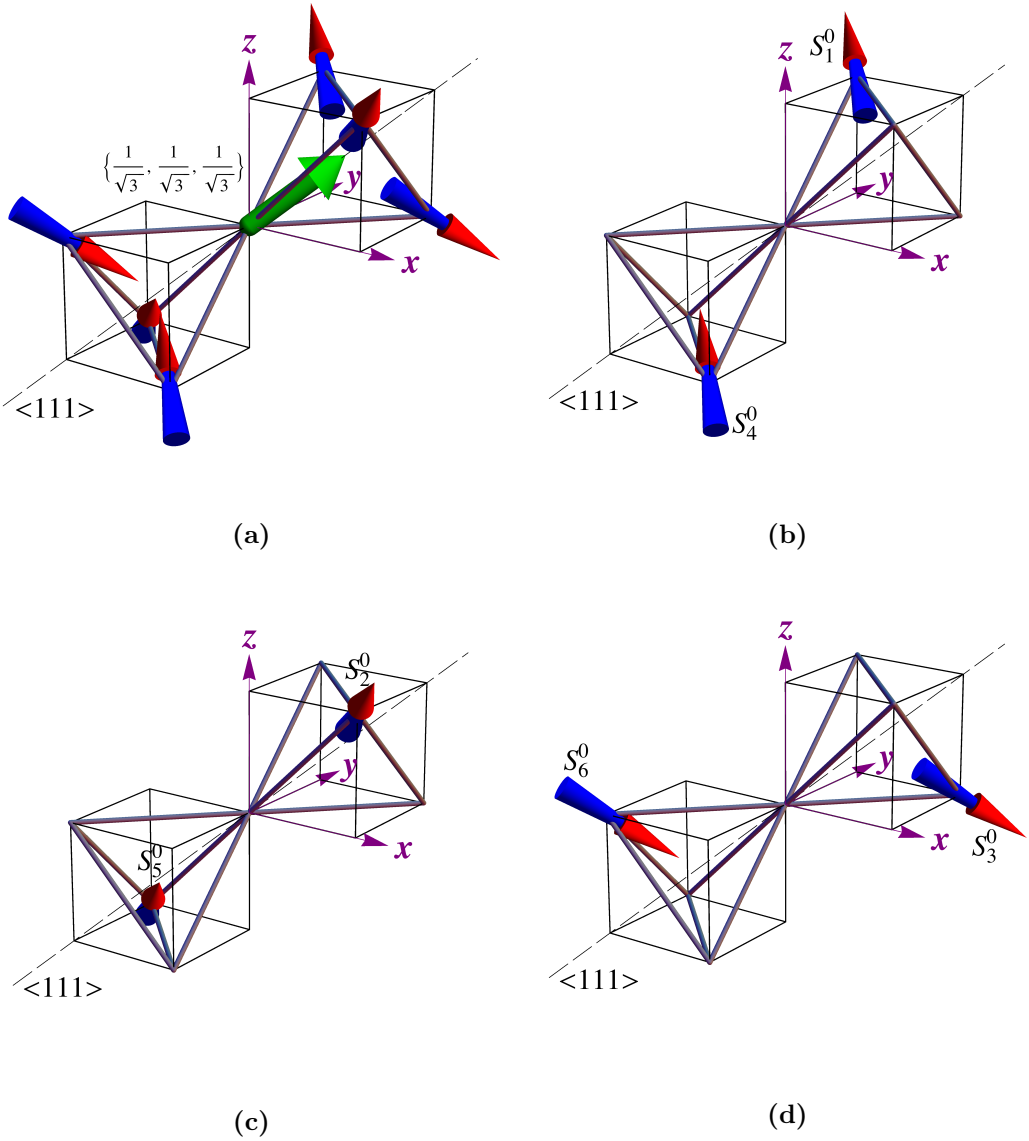

Figure 3.4: An example of the dipolar field (green arrow) on the central site of a two-tetrahedra cluster, resulting from the 6 nearest neighbour dipoles. (a) shows the configuration of the 6 spins: in this example all polarised up. The central dipole is not shown for clarity and because it is irrelevant for the resulting field; if it points upward there is a non-contractible monopole-antimonopole pair in the two-tetrahedra [22]. This is because the flipping of the central site is energetically forbidden by the resulting longitudinal field along its $\langle 111 \rangle$ axis. Figures (b), (c), (d) are guidelines to visualise the decomposition of the 6 spins, giving the resulting field, in terms of the paired dipoles used in Eq. (3.8).

pairwise combinations of dipoles, making use of Eq. (3.5). The spin-ice easy axes of the dipoles are defined by the unit vectors

$$\begin{aligned}\hat{e}_1 = \hat{e}_4 &= \frac{1}{\sqrt{3}}(-1,1,1),\\ \hat{e}_2 = \hat{e}_5 &= \frac{1}{\sqrt{3}}(1,-1,1),\\ \hat{e}_3 = \hat{e}_6 &= \frac{1}{\sqrt{3}}(1,1,-1),\end{aligned} \tag{3.6}$$

while the unit vectors for the spin sites $\mathbf{r}_i$ with respect to the origin are

$$\begin{aligned}\hat{\mathbf{r}}_1 = -\hat{\mathbf{r}}_4 &= \frac{1}{\sqrt{2}}(0,1,1),\\ \hat{\mathbf{r}}_2 = -\hat{\mathbf{r}}_5 &= \frac{1}{\sqrt{2}}(1,0,1),\\ \hat{\mathbf{r}}_3 = -\hat{\mathbf{r}}_6 &= \frac{1}{\sqrt{2}}(1,1,0).\end{aligned} \tag{3.7}$$

Then using Eq. (3.5) the calculation of the dipolar fields resulting in the central site of the 6-spin cluster is given by

$$\begin{aligned}\mathbf{B}(0) = \frac{\lambda\mu_0\mu_B}{4\pi|\mathbf{r}_{nn}|^3}\Bigg\{&\Big(S_1^0+S_4^0\Big)\Big(3(\hat{e}_1\cdot\hat{\mathbf{r}}_1)\hat{\mathbf{r}}_1-\hat{e}_1\Big)\\ &+\Big(S_2^0+S_5^0\Big)\Big(3(\hat{e}_2\cdot\hat{\mathbf{r}}_2)\hat{\mathbf{r}}_2-\hat{e}_2\Big)\\ &+\Big(S_3^0+S_6^0\Big)\Big(3(\hat{e}_3\cdot\hat{\mathbf{r}}_3)\hat{\mathbf{r}}_3-\hat{e}_3\Big)\Bigg\},\end{aligned} \tag{3.8}$$

where the string of values $\{S_1^0, S_2^0, \ldots, S_6^0\}$ together with $\lambda = {}^{|\mathbf{m}|}/_{\mu_B}$ and $|\mathbf{r}_{nn}|$, the nearest neighbour distance for the dipoles, uniquely determine the resulting field [3] (in spin ice $\lambda \approx 10$ and $|\mathbf{r}_{nn}| \approx 3.57$Å).

Eq. (3.8) can be generalised for the resulting field on a central site for a cluster of $N = 2n$ spin-ice dipoles

$$\mathbf{B}(0) = \frac{\lambda\mu_0\mu_B}{4\pi}\sum_{j=1}^{n}\frac{\Big(S_j^0+S_{j+3}^0\Big)\Big(3(\hat{e}_j\cdot\hat{\mathbf{r}}_j)\hat{\mathbf{r}}_j-\hat{e}_j\Big)}{|\mathbf{r}_j|^3}, \tag{3.9}$$

where each spin $S_j^0\hat{e}_j$ is in the region above the plane perpendicular to $\langle 111\rangle$ and passing through the origin; the spin $S_{j+3}^0\hat{e}_j$ is its symmetric with respect to the origin ($\mathbf{r}_j = -\mathbf{r}_{j+3}$).

[3] Note S_0^0 is not considered since there is no self-interaction term in Eqs. (3.1-3.3).

3.2 Dipolar fields on a RE-site next to a monopole

In general different spin configurations $\{S_i^0\}$ lead to different dipolar fields on a given (central) RE-site. Since the subject of interest here is to investigate how the internal magnetic fields characterise the motion of the monopole-like defects across the lattice, the main focus of this section is on the dipolar fields induced in a RE-site next to a monopole.

Whenever the magnetic fields resulting from the dipoles surrounding the RE-site are transverse to its easy axis, as explained in the previous chapter, the tunnelling of the magnetisation for the magnetic RE ion can occur. Hence the monopole can hop across the lattice depending on the internal fields on the RE ions driven by the static configurations of the surrounding dipoles. In spite of its simplicity this model can lead to misinterpretations if tackled only from an intuitive point of view. Indeed it can happen that very similar configurations, even identical in terms of energy of the whole system, can feature quite different resulting fields. For example, the spin configurations of two tetrahedra shown in Fig. 3.2 both have a north monopole (3in/1out) in the lower tetrahedron and no monopole (2in/2out) in the upper one; yet the resulting fields (green arrow) in the central site point along different directions (perpendicular to each other). Furthermore in this case the resulting field is not purely transverse to the $\langle 111 \rangle$ axis of the central RE-site, in either of the two cases, hence it cannot induce the tunnelling (in the sense discussed in the previous chapter) of the central dipole. These are two examples of a class of configurations where a site next to a monopole (here the central one) cannot flip [4]; its flipping in fact, would lead to a 4in energetically costly configuration. This is quite distinct to the hopping of a monopole to the upper tetrahedron. Eventually the monopole sitting on the lower tetrahedron can hop into another of the neighbouring ones (not show in Fig. 3.2) linked to the other dipoles, namely those pointing "in". In the following the different type of resulting fields for these "flippable" spins next to a monopole are discussed.

3.2.1 Analytical calculation (two-tetrahedra cluster)

The 1-monopole/no monopole configurations in a two-tetrahedra cluster are of interest as they represent a "local snapshot" of a free monopole moving across the lattice. In Fig. 3.2 we just observed a monopole whose motion towards the upper tetrahedron is forbidden by the local constraints. To discuss the other configurations, which lead to the hopping of the monopole via flipping of the central spin, a two-tetrahedra cluster is again chosen as a "reference" to study in detail the possible configurations of the dipoles and resulting fields. If the central dipole is opposite to $\hat{e}_0$, any combination of *2in/1out* configurations [5] of the remaining 6 spins gives 1-north monopole in the lower tetrahedron and no monopole in the upper one (see Figs. 3.5-3.6). Analogously if the central dipole has the same orientation as $\hat{e}_0$ then any combination of *2in/1out* configurations features one-north monopole in the upper tetrahedron and no monopole in the lower one. Although these two "snapshots" account for the two "instants" picturing the hopping of a monopole, no conclusions can be deduced at this stage

[4] The only one pointing out of the tetrahedron hosting the monopole.

[5] Both for the 3 spins in the upper triangle $(\mathbf{m}_1, \mathbf{m}_2, \mathbf{m}_3)$ and the 3 in the lower one $(\mathbf{m}_4, \mathbf{m}_5, \mathbf{m}_6)$.

about directionality of their motion. The focus is only on the type of resulting fields induced by static configuration of the 6 dipoles nearest neighbours to a RE-site.

In the following the fields on the central site are calculated for configurations of dipoles with a 1-north monopole in the lower tetrahedron and no monopole in the upper one. Such 1Nm/0m model (for two-tetrahedra with only one *north* monopole) represents an archetype for the study the resulting fields on the RE-site near a monopole; analogous is the 1Sm/0m case (where S stands for *South*). In the figures representing these 1Nm/0m spin-cluster states the location of the monopole is not shown for clarity; the aim is mainly to visualise the relationship between the pairwise configurations of the dipoles and the resulting fields. In these examples the North monopole is kept always in the tetrahedron below (3in-1out) to study the fields allowing the hopping into the one above (here kept in a 2in-2out configuration). The same configurations are summarised in Fig. 3.7, at the end of this section, where the North monopole is shown in the left panels $\boldsymbol{A}, \boldsymbol{B}, \boldsymbol{C}$, to allow an immediate comparison with the right panels $\boldsymbol{A'}, \boldsymbol{B'}, \boldsymbol{C'}$, where a South monopole is shown.

Transverse field (Config. $\boldsymbol{A}$, Fig. 3.5a)	Transverse field (Config. $\boldsymbol{B}$, Fig. 3.5b)	Null Field (Config. $\boldsymbol{C}$, Fig. 3.6)
$S_1^0 = +1$	$S_1^0 = -1$	$S_1^0 = -1$
$S_2^0 = -1$	$S_2^0 = +1$	$S_2^0 = -1$
$S_3^0 = -1$	$S_3^0 = -1$	$S_3^0 = +1$

Table 3.1: In the two-tetrahedra cluster, these are the 3 possible configurations for $\{S_j^0\}$ with $j = 1, 2, 3$ which combined with $\{S_4^0 = 1, S_5^0 = 1, S_6^0 = -1\}$ lead to a 1-north monopole/no monopole state. Here the central spin can flip; the monopole is in the lower or upper tetrahedron depending on whether $S_0^0 = -1$ or $S_0^0 = 1$ respectively. Pictorial representations are given in Figs. 3.5-3.6.

Since the resulting fields do not depend on symmetry transformation of the whole system, in this two-tetrahedra cluster only three configurations $\{S_i^0\}$ really matter; the others, obtained as permutations of the S_i^0, correspond to trivial rotations of the whole two-tetrahedra system around the $\langle 111 \rangle$ axis passing through the origin.

The 3 non-equivalent configurations leading to a 1Nm/0m case are represented in Figs. 3.5-3.6; they all give a null resulting field along the $\langle 111 \rangle$ axis. More precisely $\boldsymbol{A}$ in Fig. 3.5a and $\boldsymbol{B}$ in Fig. 3.5b give a resulting field purely transverse to the easy axis of the central dipole; whilst an identically zero field is found in the case $\boldsymbol{C}$ in Fig. 3.6. The spin configurations are listed in Table 3.1, where only the upper ones are shown since the lower spins are fixed as $\{S_4^0 = 1, S_5^0 = 1, S_6^0 = -1\}$. Although these configurations constitute specific choices for the present case, it is straightforward to verify their general validity [6]. The other 1Nm/0m configurations are obtained by two rotations, clockwise and anticlockwise, of 120 degrees around the $\langle 111 \rangle$ axis of the whole

[6] Notice these were chosen only as a convenient toy-model to summarise the main properties of the dependence between spin-configurations and resulting-fields.

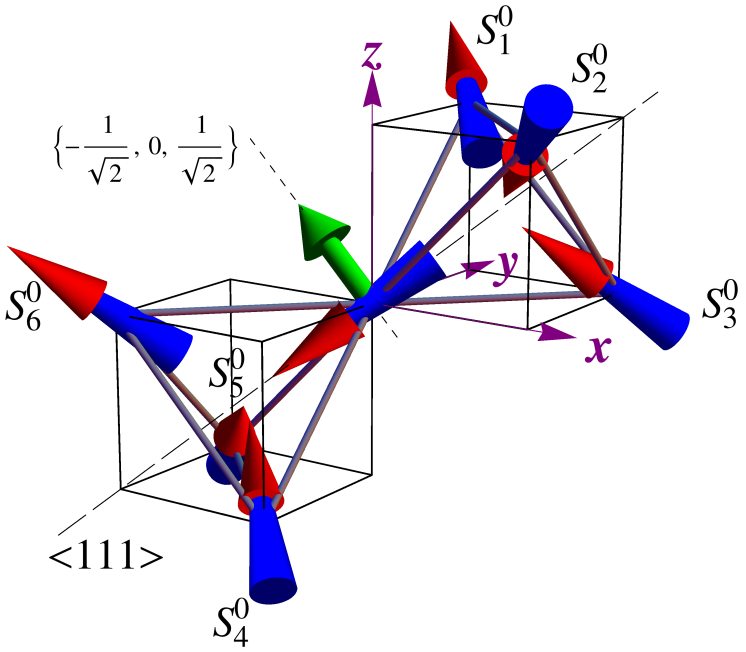

(a) - Configuration ***A***

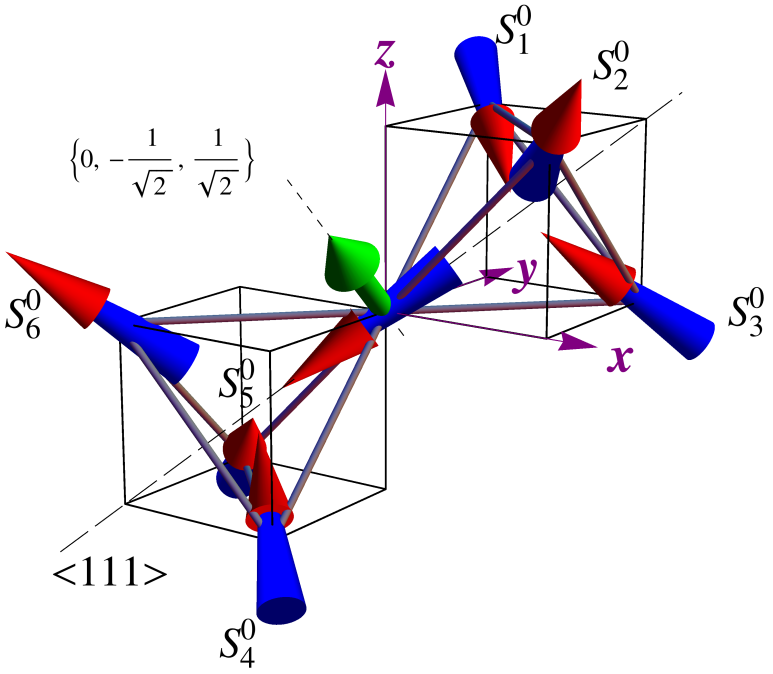

(b) - Configuration ***B***

Figure 3.5: The two configurations with a north monopole (1Nm/0m; 3in-1out below and 2in-2out above) giving a purely transverse field in the central site (see Table 3.1). These are shown again in Figs. 3.7 to allow a direct comparison with the analogous cases featuring a south monopole. In the main text we refer to the top one as ***A*** and the bottom one as ***B***.

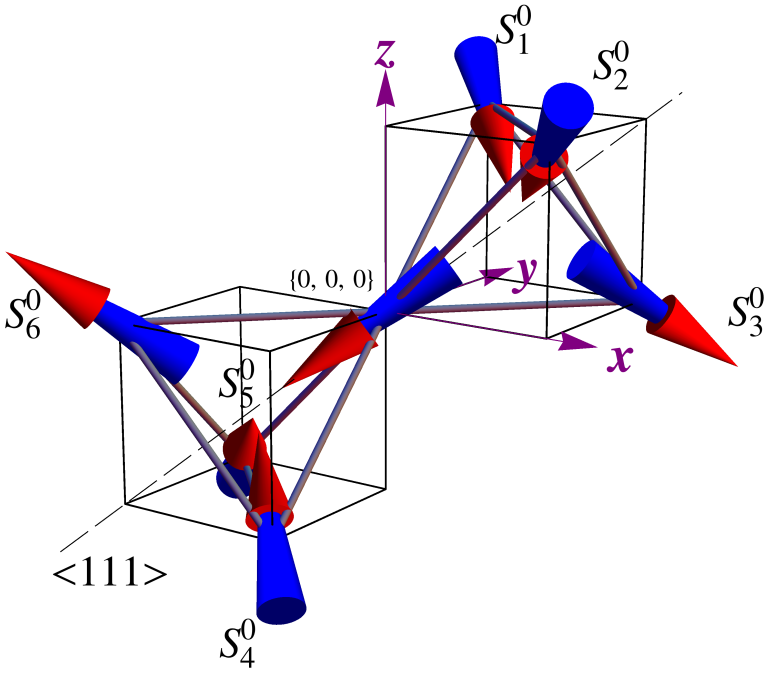

Figure 3.6: Another configuration (***C***), the one on the right in Table 3.1, with a north monopole ($1\mathrm{N}m/0m$; 3in-1out below and 2in-2out above); this gives a null resulting field in the central site (third column in Table 3.1). Note how each dipole in the upper tetrahedron is pointing opposite to its symmetric in the lower one ($S_j^0 = -S_{j+3}^0$, with $j = 1, 2, 3$). This is shown again in Figs. 3.7 to allow a direct comparison with the others in Fig. 3.5 and with analogous cases featuring a south monopole.

two-tetrahedra systems shown in Figs. 3.5-3.6. Hence each two-tetrahedra cluster in a 1monopole/no monopole state has 6 spin configurations with a purely transverse field and 3 with a null resulting field. In the following a brief calculation for the resulting transverse field of Config. ***A*** shown in Fig. 3.5a is derived.

Analytical calculation of the resulting field in a two-tetrahedra cluster

In Table 3.1 the spin configuration on the left column gives

$$\begin{aligned} S_1^0 + S_4^0 &= 2; \\ S_2^0 + S_5^0 &= 0; \\ S_3^0 + S_6^0 &= -2. \end{aligned} \tag{3.10}$$

for Config. ***A*** in Fig. 3.5a. Substituting these in Eq. (3.8) we obtain

$$\begin{aligned} \mathbf{B}(0) &= \frac{\lambda\mu_0\mu_B}{4\pi r_{nn}^3}\left\{2\left(3\sqrt{\frac{2}{3}}\hat{\mathbf{r}}_1 - \hat{e}_1\right) + 0 - 2\left(3\sqrt{\frac{2}{3}}\hat{\mathbf{r}}_3 - \hat{e}_3\right)\right\} \\ &= \frac{\lambda\mu_0\mu_B}{2\pi r_{nn}^3}\left\{3\sqrt{\frac{2}{3}}(\hat{\mathbf{r}}_1 - \hat{\mathbf{r}}_3) - (\hat{e}_1 - \hat{e}_3)\right\} \end{aligned} \tag{3.11}$$

given that $\hat{e}_j \cdot \hat{\mathbf{r}}_j = \sqrt{2/3}$ for all $j = 1, 2, 3$. Then, using the explicit representation for $\hat{e}_j$ and $\hat{\mathbf{r}}_j$ from Eqs. (3.6-3.7), this becomes

$$\begin{aligned}\mathbf{B}(0) &= \frac{\lambda\mu_0\mu_B}{2\pi r_{nn}^3}\left\{\frac{3}{\sqrt{3}}\left[\begin{pmatrix}0\\1\\1\end{pmatrix}-\begin{pmatrix}1\\1\\0\end{pmatrix}\right]-\frac{1}{\sqrt{3}}\left[\begin{pmatrix}-1\\1\\1\end{pmatrix}-\begin{pmatrix}1\\1\\-1\end{pmatrix}\right]\right\} \\ &= \frac{\lambda\mu_0\mu_B}{2\sqrt{3}\pi r_{nn}^3}\begin{pmatrix}-1\\0\\1\end{pmatrix}\end{aligned} \tag{3.12}$$

which is manifestly perpendicular to the $\langle 111\rangle$ axis passing through the central site. In spin ice the strength of the field is ≈ 0.33 Tesla and its unit vector [7] is $(-\frac{1}{\sqrt{2}}, 0, \frac{1}{\sqrt{2}})$ as shown in curly brackets in Fig. 3.5a.

Analogously it can be derived that for Config. ***B*** at the centre of Table 3.1 (Fig. 3.5b) the resulting field points along $(0, -\frac{1}{\sqrt{2}}, \frac{1}{\sqrt{2}})$ and has also modulus ≈ 0.33 Tesla. Another 4 configurations with this same strength of the purely transverse field are obtained by the 120 deg rotations of the whole two-tetrahedra system around the $\langle 111\rangle$ axis.

The *null* resulting field found in Config. ***C*** (Fig. 3.6) can be quickly recognised as one of the three $1\mathrm{N}m/0m$ cases where the paired dipoles in Eq. (3.8) are pointing opposite to each other $S_j^0 = -S_{j+3}^0$ (see right column in Table 3.1).

The preceding discussions and results can be easily transposed on two-tetrahedra systems with a South monopole ($1\mathrm{S}m/0m$), where one of the tetrahedra is in a 1in-3out configuration and the other in a 2in-2out one. This would imply changing the signs of all the spin configurations $\{S_i^0\}$ discussed in this section, hence leading to resulting fields on the RE-site with opposite directions with respect to the ones obtained here for the $1\mathrm{N}m/0m$ cases. In Fig. 3.7 the right panels show the spin-configurations with a South monopole in comparison with the cases with a north monopole on the left ones. For symmetry reasons the magnitude of the resulting fields is the same for analogous spin-configurations.

3.2.2 Dipolar field histograms

The use of histograms is very convenient to analyse the dipolar fields resulting on a given site of the lattice. For example the same results discussed analytically in the previous section are visually summarised in the histogram shown in Fig. 3.8b. This represents the field distributions from all the dipole-configurations compatible with a $1\mathrm{N}m/0m$ state for the two-tetrahedra cluster depicted in Fig. 3.8a. The central spin is fixed pointing down for the same reasons already discussed in the previous sections[8]. The field-distributions in Fig. 3.8b confirm the results for the cases depicted in Figs. 3.7 and also for the other six equivalent configurations not shown (corresponding to 120 deg rotations of the whole system around the central $\langle 111\rangle$ axis).

The three-dimensional histogram in Fig. 3.8, together with the others in the following

[7] Note the resulting field is also perpendicular to $\hat{\mathbf{r}}_2$, whose associated dipoles $\mathbf{m}_2, \mathbf{m}_5$ have destructive interaction in the case considered ($S_2^0 = S_5^0$).

[8] A spin pointing up would correspond to configurations like the ones in Fig. 3.2 where the flipping would be energetically unfavourable.

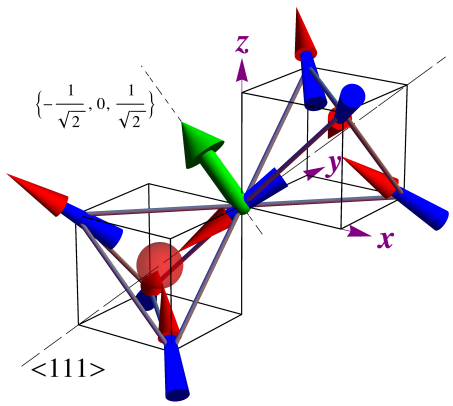

(a) - Configuration $\boldsymbol{A}$

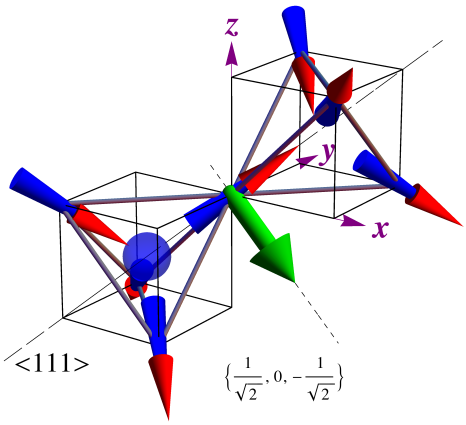

(a′) - Configuration $\boldsymbol{A'}$

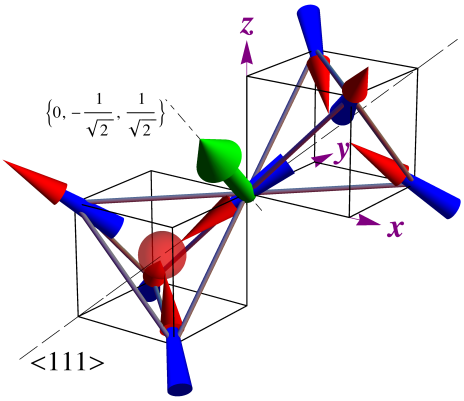

(b) - Configuration $\boldsymbol{B}$

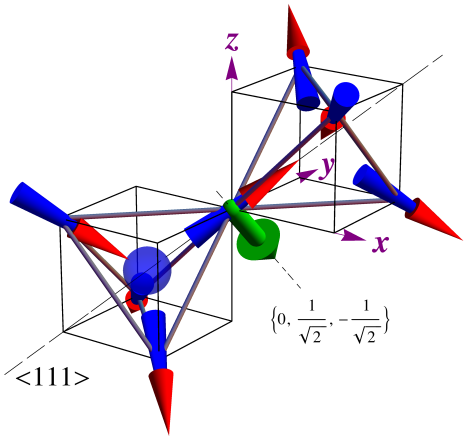

(b′) - Configuration $\boldsymbol{B'}$

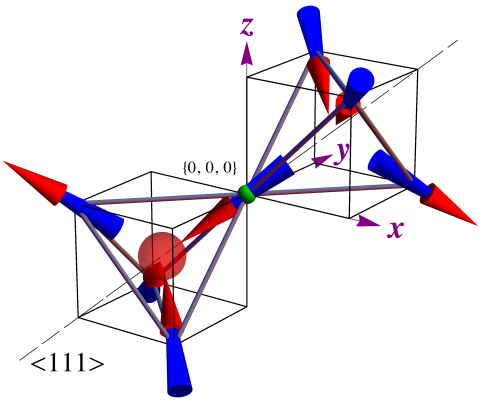

(c) - Configuration $\boldsymbol{C}$

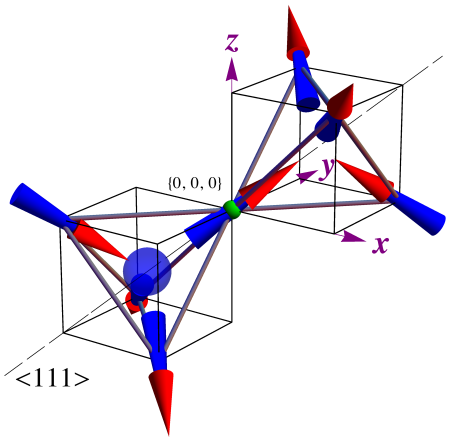

(c′) - Configuration $\boldsymbol{C'}$

Figure 3.7: Examples of dipolar configurations in a two-tetrahedra cluster hosting monopoles of opposite charge in the lower tetrahedron. The figures on the left have a North magnetic monopole while those on the right a South pole. The resulting fields are always purely transverse to the $\langle 111 \rangle$ axis apart from the bottom ones where the field is identically zero.

pages, have the following settings: the horizontal axes represent the magnitudes of the transverse and longitudinal components of the resulting dipolar fields with respect to the central $\langle 111 \rangle$ direction; the vertical axis corresponds to the probability of obtaining a certain value for $(B_{Transverse}, B_{Longitudinal})$ from all the spin-configurations compatible with the constraints imposed on the system.

3.2.2.1 Two-tetrahedra cluster

The histogram for the two-tetrahedra cluster configurations satisfying the 1Nm/0m state is given in Fig. 3.8. The distribution of the field strengths is peaked at the two values $(0.33, 0)$ and $(0, 0)$ Tesla for the respective transverse and longitudinal components of the resulting fields in the central ion. The different size of the two columns accounts for the respective probabilities, 2/3 and 1/3, of finding a purely transverse field or a null one in agreement with the results discussed in subsection 3.2.1.

Analogously Fig. 3.9 shows the histogram for a two-tetrahedra cluster without monopoles (2in-2out in both). The central spin is kept fixed pointing down to allow a direct comparison with the previous case where the lower tetrahedron hosts a monopole. Here the histograms are peaked at different values with respect to the case with a monopole 1Nm/0m. More precisely these show the same net longitudinal component of the field for both peaks: $(0.19, 0.68)$ and $(0.38, 0.68)$ Tesla. Note that for symmetry reasons also in this case the two probabilities are 2/3 and 1/3 for the two respective values of the total magnitude.

These results show how the histograms of the field distributions can be used as a quick assessment in establishing the role of the magnetic monopoles in altering the dipolar fields in the RE-sites surrounding them. For example the comparison between the simple two-tetrahedra cases in Fig. 3.8 and Fig. 3.9 suggests that the presence of the monopole (being the only one different constraint between the two) affects the dipolar fields on the central site by removing the longitudinal component characterising the ground-state. In the context of the dynamics discussed in this thesis, where the spin-flip process consists in a spin-tunnelling driven by a purely transverse magnetic field, this confirms that the monopole itself modifies the dipolar fields and can induce the tunnelling for some of the dipoles which lead to the hopping of the monopole itself. Since considering only a small cluster to investigate these mechanisms could represent a restriction in the reliability of this model, it is convenient to consider a larger cluster. In the following an analogous approach is used for a cluster of eight tetrahedra.

3.2.2.2 Eight-tetrahedra cluster

The eight-tetrahedra cluster considered in this section is a "natural extension" of the two-tetrahedra one used so far; the former is obtained by considering the further neighbouring tetrahedra [9] of the latter one. Again the lattice is chosen so that the central dipole is the most symmetric of the sites [10]. Fig. 3.10 gives a representation of the

[9] The arrangement of the tetrahedra follows the pyrochlore lattice structure.

[10] This, as discussed in subsection 3.1.2, facilitates the visualisation of dipoles contributing to the resulting fields on the central site and makes the analytical calculation by means of Eq. (3.9) straightforward.

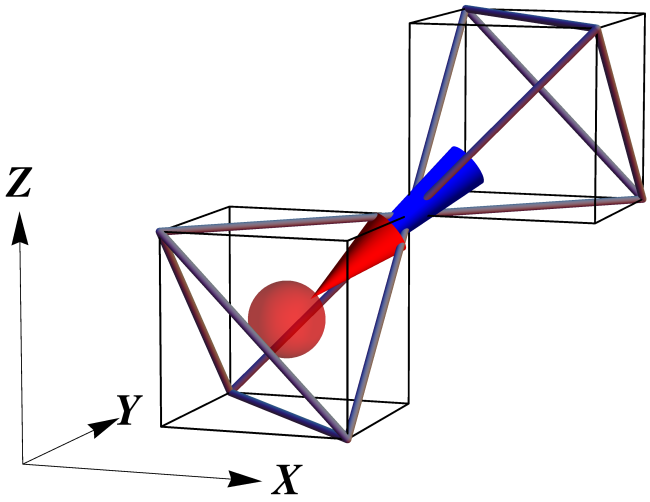

(a)

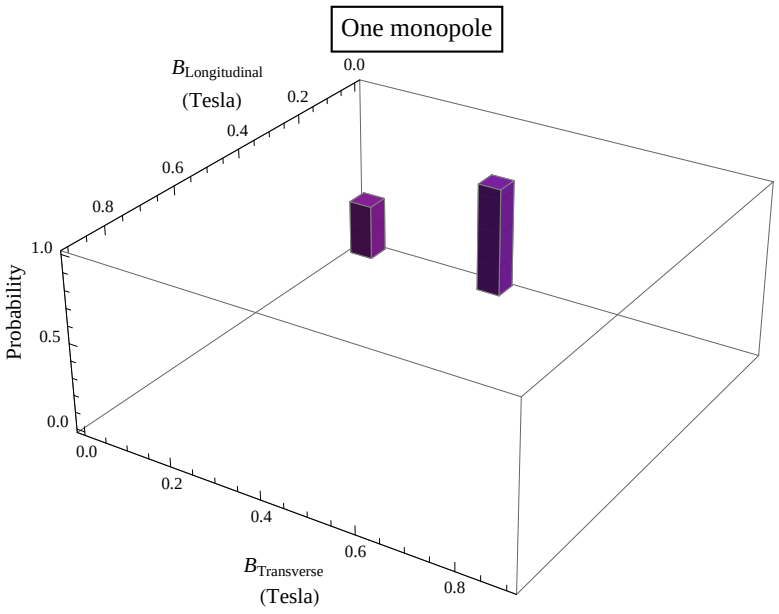

(b)

Figure 3.8: Two-tetrahedra cluster featuring a 1Nm/0m monopole state (3in-1out below; 2in-2out above). The top panel (a) reproduces the geometry of the cluster showing only the central spin that is fixed throughout the calculation. The bottom panel (b) shows the histogram of the dipolar-field distributions resulting on the central site from all the possible states of the neighbouring dipoles. The resulting fields on the central RE-site are characterised by null longitudinal component along the local ⟨111⟩ direction (i.e. the dipolar fields are either null or purely transverse).

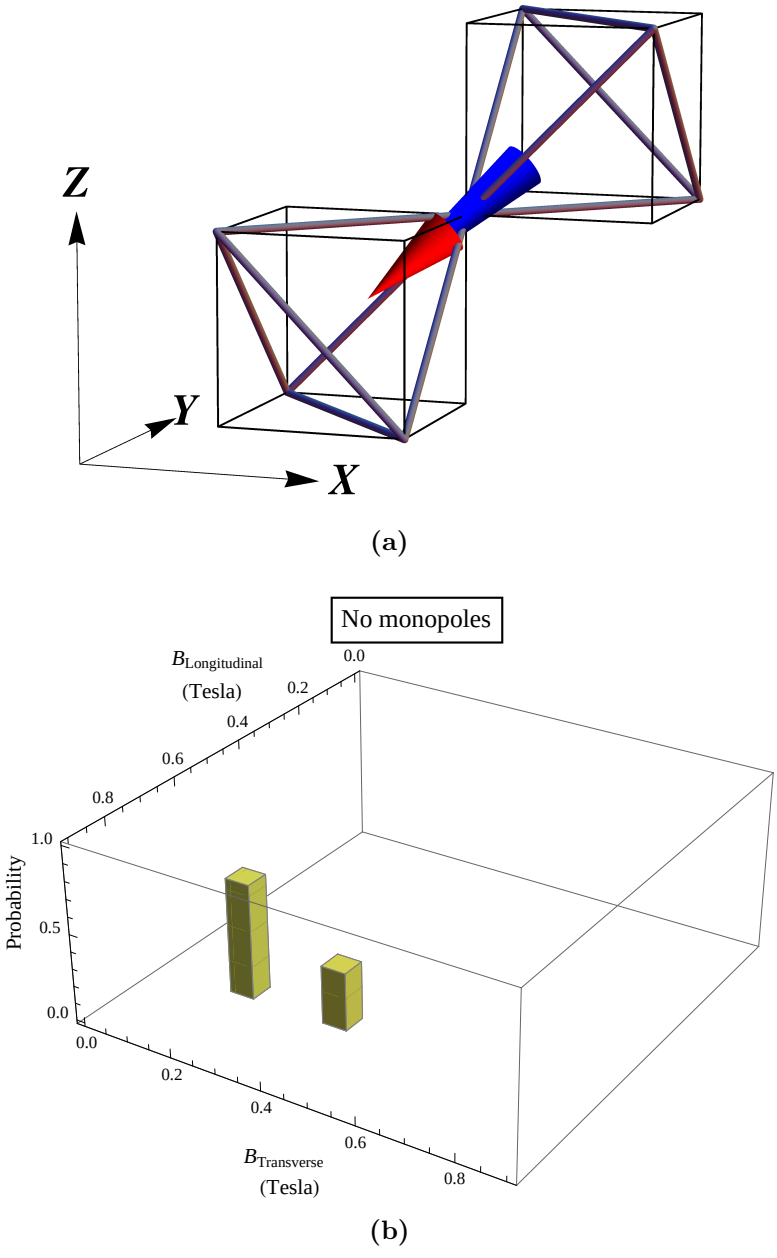

Figure 3.9: Two-tetrahedra cluster without any monopole (2in-2out in both tetrahedra). The top panel (a) reproduce the geometry of the cluster showing only the central spin that is fixed throughout the calculation (in analogy with Fig. 3.8b). The bottom panel (b) shows the histograms of the dipolar-field distributions resulting on the central site from all the possible states of the neighbouring dipoles. The resulting fields on the central RE-site now show the same strong longitudinal component along the local $\langle 111 \rangle$ direction.

cluster with all the dipoles arranged in one of the possible configurations for the degenerate ground state (2in-2out in all tetrahedron). Analogously to the two-tetrahedra case, this model has been used to calculate the dipolar fields obtained on the central site when the cluster has one monopole next to the central spin (Fig. 3.11a) and when there are no monopoles in the whole lattice (Fig. 3.13a). Furthermore the larger size of the cluster allows also the calculation of the resulting fields in the case when the monopole is moved away from the tetrahedron next to the central site but is still present in the cluster (Fig. 3.12a).

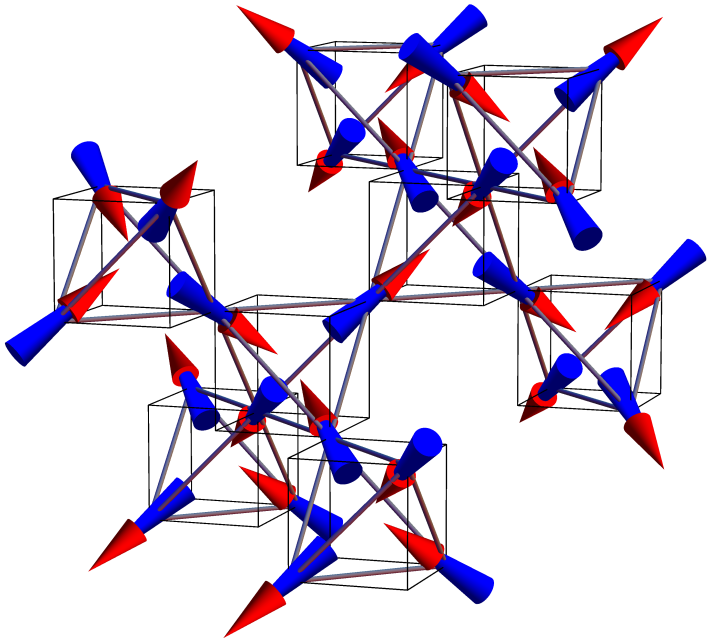

Figure 3.10: A pictorial representation of the full eight-tetrahedra cluster in one of the 6561 possible ground state configurations (2in-2out in all tetrahedra of the lattice). In the following figures (3.11-3.12) only the "skeleton" of the lattice is kept since the calculations are done for a large variety of spin states. This image has only illustrative purpose to show the geometry and complexity of an eight-tetrahedra cluster.

For this larger cluster the use of histograms is crucial to compare the different types of resulting fields. In fact the number of possible configurations compatible with a given constraint, such as a monopole in a given site, is typically of the order of a few thousands. Also for this large cluster all the configurations investigated are with the central dipole pointing downward; this is again to ensure that this is a dipole that could lead to the hopping of a North monopole by means of its upward flipping. The histograms in Fig. 3.11b, Fig. 3.12b and Fig. 3.13b provide a tool to assessthe variation of the resulting dipolar fields in the following cases respectively: when the monopole sits in the tetrahedron just below the central ion, when it is placed into a neighbouring one [11], and when it is no longer in the cluster.

[11] The case shown in Fig. 3.12a represent just one out of the possible three lower-tetrahedra not next to the central dipole.

By direct comparison with the field distributions of the two-tetrahedra case it is intriguing to realise that, although the "shapes" of the field distributions look different, the type of resulting fields shows a clear correlation between the two cluster calculations. This is evident both in the case when the monopole is next to the central dipole, (Fig. 3.8 and Fig. 3.11), and also in the case with no monopoles (Fig. 3.9 and Fig. 3.13). In the former the dipolar fields show a suppression of the longitudinal component with respect to the latter one[12]. Moreover, although the field distributions are broadened in the larger cluster, the position of the peaked values show similarities between the two clusters. This in particular is strongly evident in the cases featuring one monopole next to the central dipole, where a structure of two main peaks remains also in the larger cluster.

As already mentioned, one of the greatest benefits of considering a larger cluster is the possibility to investigate the dipolar fields resulting from the spin-configurations featuring a monopole sitting further away from the central dipole. Remarkably the corresponding dipolar field distribution in Fig. 3.12b looks more similar to the case without a monopole in Fig. 3.13b than to the case of a monopole next to the central dipole (Fig. 3.11b). Hence, although the larger cluster allows a more reliable description on the dependence between the location of the monopoles and the resulting fields on the RE-sites, it also proves that the presence of the monopole affects mainly the field at the RE-sites just next to it.

A note on Monte Carlo simulations The dominant role played by the monopole in modifying the magnetic field on a RE-site next to it, can be verified also by means of classical Monte Carlo simulations. Unpublished work, done by our collaborators C. Castelnovo and G. Sala besides Ref. [49], shows that also in a large cluster with 1024 spins the presence of a monopole characterises the field distribution on a nearby RE^{3+} ion with fields having longitudinal components peaked around zero. These results show also a good quantitative agreement with the cluster calculation presented here: there are only two neat peaks for the transverse fields found next to a monopole. These are at 0.55 Tesla and 0.03 Tesla, very similar to the values shown in the histogram in Fig. 3.11.

The localised effect of the monopole on a nearby RE-site, found in the eight-tetrahedra cluster and supported by the Monte Carlo results, justifies the reliability of the simple two-tetrahedra cluster. From the latter it was already evident the suppression of the longitudinal component as a direct consequence of the presence of a monopole. Furthermore, this seems to suggest that the transverse field spin-tunnelling can be spontaneously induced only when a monopole is sitting next to a given RE-site. This is discussed in Chapter 5 in the context of a *quantum-quench* mechanism proposed for the propagation of monopoles in spin ice materials. This model, as we shall see, is consistent not only for the typical dipolar fields on a RE-site next to a monopole, but also for the effective exchange ones which first will be derived in the next Chapter 4.

[12] This means a purely transverse field only in the case of the two-tetrahedra cluster and in some of the configurations of the eight-tetrahedra one.

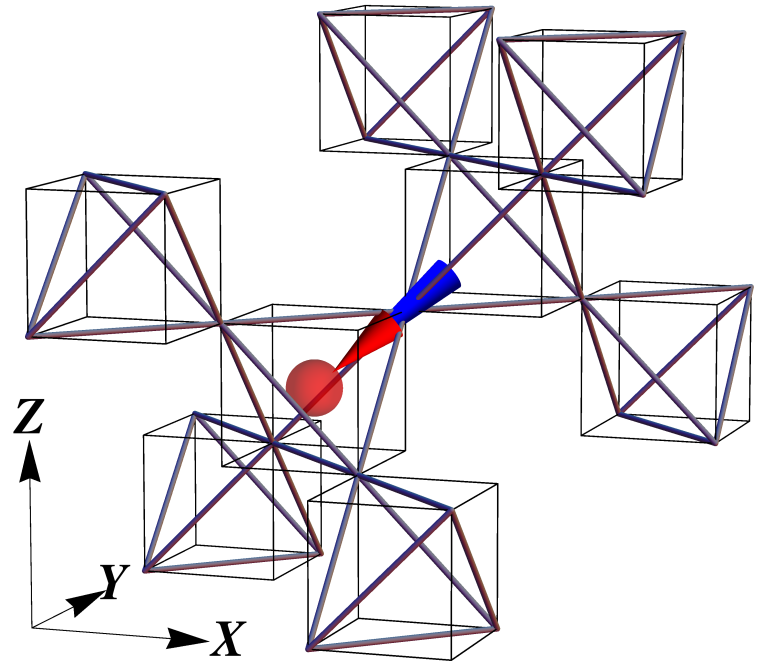

(a)

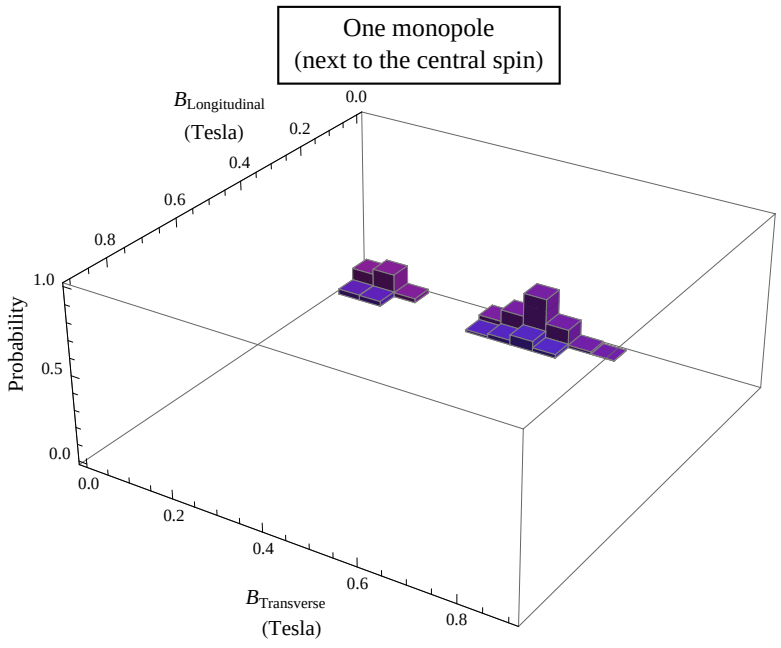

(b)

Figure 3.11: Eight-tetrahedra cluster with a North monopole in the lower tetrahedron next to the central dipole. The top panel (a) shows the geometry of the 8-tetrahedra cluster with the orientation of the central dipole and the position of the monopole fixed. The bottom panel (b) shows the histogram with the dipolar-field distributions. The spin-states corresponding to a 1-monopole next to the central ion are characterised by dipolar fields on the central ion with almost null longitudinal component along its local $\langle 111 \rangle$ direction. This result is analogous to what shown in Fig. 3.8 for the two-tetrahedra cluster; here the peaks are broadened and shifted with respect to the former case.

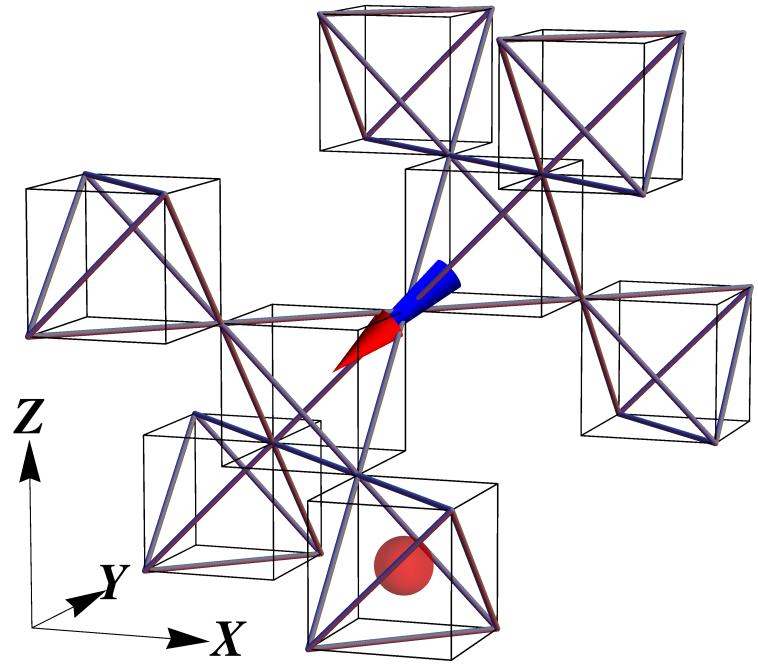

(a)

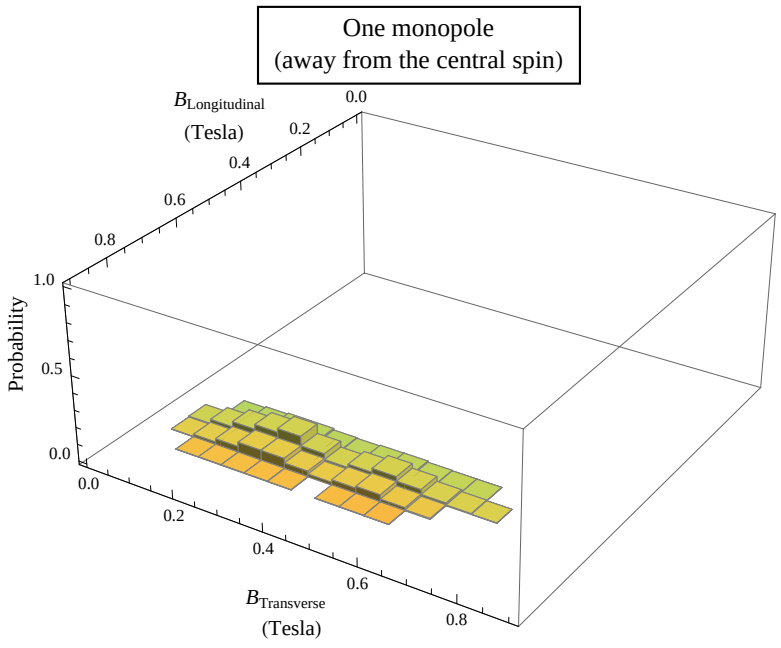

(b)

Figure 3.12: Eight-tetrahedra cluster with a North monopole in a tetrahedron further below the one in Fig. 3.11. The top panel (a) shows the geometry of the 8-tetrahedra cluster with the orientation of the central dipole and the position of the monopole fixed. The bottom panel (b) shows the histograms with the dipolar-field distributions. Here the spin-states are characterised by a broad distribution of resulting fields on the central site with strong longitudinal component along its local $\langle 111 \rangle$ direction. This is an insightful result as it shows the drastic variation in the resulting fields when the monopole hops only one site away from the tetrahedron next to the central ion (Fig. 3.11). It is also remarkable the similarity with the field histogram in Fig. 3.13b.

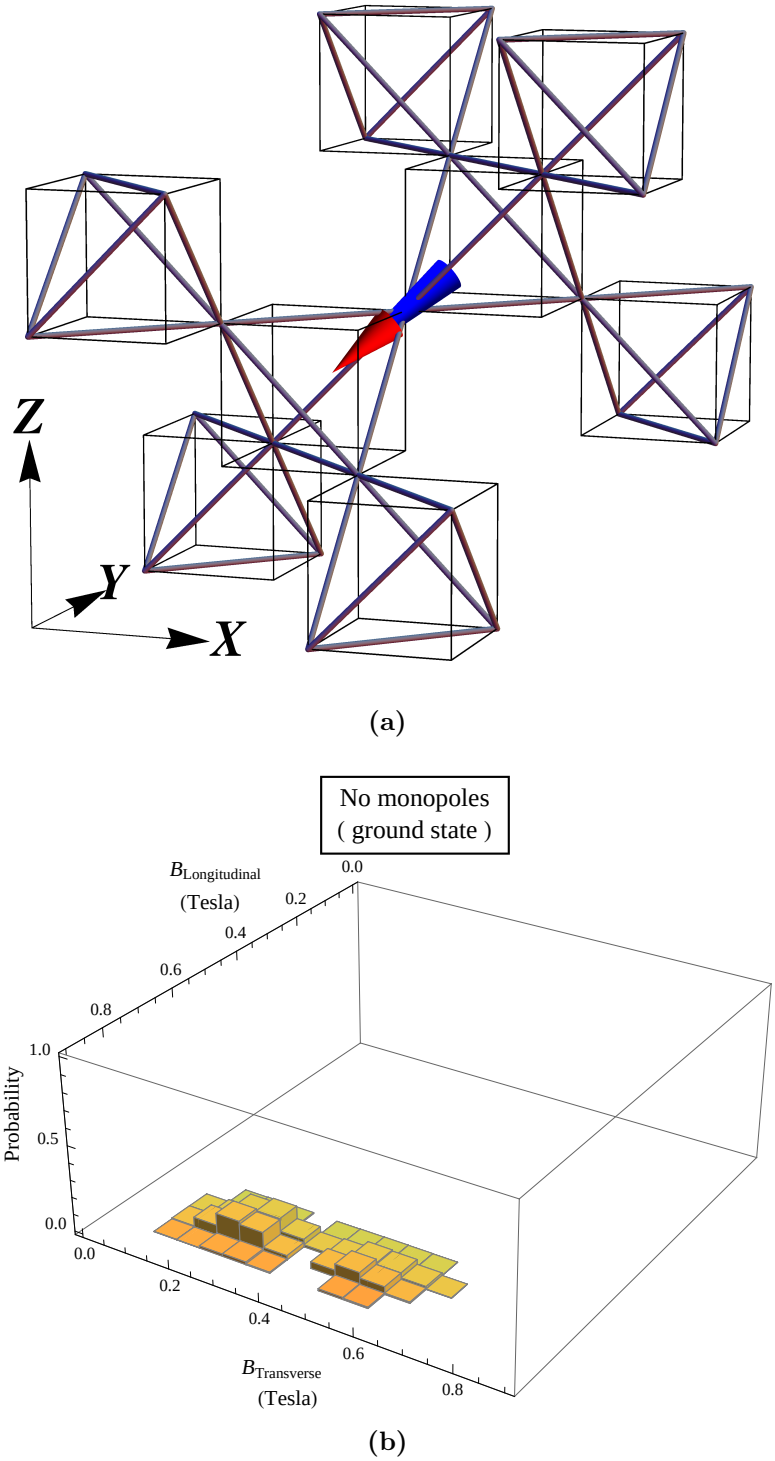

Figure 3.13: Eight-tetrahedra cluster without any monopole (ground state). The top panel (a) shows the geometry of the 8-tetrahedra cluster with only the fixed central dipole. The bottom panel (b) shows the histograms with the dipolar-field distributions. Also in this case the resulting fields on the central site have a net longitudinal component along its local ⟨111⟩ direction (slightly stronger than Fig. 3.12). This result is analogous to what shown in Fig. 3.8 for the two-tetrahedra cluster; here the peaks are broadened and shifted with respect to the former case.

"The exchange interaction is subtle and not a little mysterious, since it seems surprising that one has to go to the bother of thinking about exchange operators and identical particles when all one is dealing with is a bar magnet and a pile of iron filings. But this, as often with the subject of magnetism, is a demonstration of how quantum mechanics is at the root of many everyday phenomena. "

S. Blundell [53]

4

The effective exchange coupling

The internal magnetism of condensed matter systems is characterised by another kind of interaction whose features go beyond the intuitive representation of the classical dipolar fields: the exchange interaction. The intricate relationships between indistinguishability of particles, their spin quantum numbers and the emergence of effective magnetic fields, which can manifest at a macroscopic level, was originally investigated by Heisenberg and Dirac in the mid twenties of the last century [54]. The quantum theory of magnetism was at its early stages and the spin itself, as an intrinsic property characterising the behaviour of all fundamental particles, had just been discovered. The Pauli principle, in loose words, represents a sort of "manifesto" of this characterisation: any two identical particles with half integer spin cannot occupy the same quantum state at the same time. Focusing on electrons, as the fundamental elements whose allowed states in solid state systems are constrained under this principle, a plethora of physical mechanisms have been addressed mainly by studying their statistics or the statistics of the low energy excitations arising from their coupling with the other degrees of freedom of their environment [3, 55, 53, 56, 57, 58].

This chapter is entirely dedicated to the role of exchange interactions in the microscopic description of the spin-ice magnetic features. Primarily because in general these represent the building blocks for the current understanding of this and similar pyrochlore systems [6]; secondarily for the particular interest in investigating the influence of the exchange mechanism with respect to the quantum spin-tunnelling presented in this thesis.

It is believed that, because of the strength of the dipolar fields, the exchange ones do not play a major role in the spin-ice physics [59]; more precisely the frustrated ground state of the system is characterised by an *antiferromagnetic* exchange interaction that is overcome by the dipolar contribution, already at a nearest neighbour level [5]. Nonetheless, the effective *ferromagnetic* coupling between the neighbouring Ising spins contains a "trace" of exchange, not least in its measured strength resulting from the sum

of the dipolar and the exchange contributions [5, 12, 52]. The magnitudes of the two respective constants are of comparable orders but the directions of the resulting fields can in general be different. Studying how the resulting fields combine, beyond the level of approximation where each magnetic ion is considered as a classical dipole with local Ising anisotropy, is necessary when dynamical properties of the systems are investigated. However, since the spin-flip mechanism accounting for the propagation of the monopoles consists of quantum spin-tunnelling of one RE-ion surrounded by a multitude of others sitting in their local Ising state (see Chapter 5), a *static* approximation for the fields originating from their possible configurations is suitable as it accounts for the frozen environment surrounding the monopole.

In the following sections the mechanism of exchange is discussed from the simplest and most general cases to the more specific ones of interest for the spin ice systems. Since the mathematical framework to describe it depends on the interplay between classical and quantum mechanical features in the model considered, it is emphasised how each level of approximation accounts for a certain level of agreement with what is already known from theories and experiments.

4.1 Exchange interaction and effective spin Hamiltonian

The striking and charming feature of exchange interactions is the variety of possible phenomena arising from something as simple as the practical consequences of dealing with (quantum) objects that are not distinguishable. For example the low temperature magnetic ordering, leading to the macroscopic magnetic fields in ferromagnetic materials, is a direct consequence of the Pauli principle interaction between the electrons in solids. Typically in insulators the indistinguishability of particles with half-integer spins translates into an effective form of magnetic interactions between the ionic sites. Since these complex systems can be very diverse, offering a unique description of the way exchange mechanisms lead to effective magnetic interactions would risk losing part of the physical properties of some systems. The fundamental ingredients defining exchange, however, are the same for any kind of microscopic quantum systems. Hence, to revisit the conceptual implications under the exchange interactions, it is convenient to start by discussing the simplest case where indistinguishability leads to magnetism: the two-electron problem.

4.1.1 Origin of exchange: two-electron wave functions

This section on the emergence of exchange interaction form the two-electron model follows very closely the derivation given in sections 1.3 and 4.2 of Ref. [53].

The relationship between exchange interactions in quantum mechanics and the emergence of magnetism in "everyday life" can be illustrated, in a simplified version, by considering a two-electron system [53, 60]. The quantum state of a single electron is defined by $\psi(r)\chi_s$, the product of the spatial and spin wave functions. For a system of two electrons the correct wave function for the joint system is deduced from the *spin-statistics theorem*: the wave function of a system of identical fermions changes sign (i.e. is antisymmetric) when two particles are swapped [1]. In the following it is

[1] For a system of bosons (particles with integer spin) the wave function is symmetric when two

discussed how the spin and the spatial parts of the wave function combine in a system of two electrons; their allowed states, arising from the fermionic exchange properties, lead to the emergence of an *effective* magnetic interaction.

In quantum mechanics the interaction of any two angular momenta $\mathbf{j}_1, \mathbf{j}_2$ is described by the operator $\hat{\mathbf{j}}_1 \cdot \hat{\mathbf{j}}_2$. Hence in a two-electron system the spin-interaction part of the Hamiltonian will be proportional to

$$\hat{\mathbf{s}}_1 \cdot \hat{\mathbf{s}}_2 \tag{4.1}$$

where $\hat{\mathbf{s}}_i \equiv (\hat{s}_i^x, \hat{s}_i^y, \hat{s}_i^z)$ is the spin operator for each of the two electrons ($i = 1, 2$). From the combination of angular momenta, the spin operator $\hat{\mathbf{S}} = \hat{\mathbf{s}}_1 + \hat{\mathbf{s}}_2$ for their joint system gives

$$(\hat{\mathbf{S}})^2 = (\hat{\mathbf{s}}_1)^2 + (\hat{\mathbf{s}}_2)^2 + 2\hat{\mathbf{s}}_1 \cdot \hat{\mathbf{s}}_2 \,, \tag{4.2}$$

so that the interaction term in Eq. (4.1) can be expressed as

$$\hat{\mathbf{s}}_1 \cdot \hat{\mathbf{s}}_2 = \frac{(\hat{\mathbf{S}})^2 - \left[(\hat{\mathbf{s}}_1)^2 + (\hat{\mathbf{s}}_2)^2\right]}{2} \,. \tag{4.3}$$

The single-spin operators $(\hat{\mathbf{s}}_1)^2$ and $(\hat{\mathbf{s}}_2)^2$ both have eigenvalue $s_i(s_i + 1) = 3/4$ (since $s_1 = s_2 = 1/2$), while the joint-spin operator $(\hat{\mathbf{S}})^2$ has two possible eigenvalues (since $S = 0, 1$; from $|s_1 - s_2| \leq S \leq s_1 + s_2$). Consequently, Eq. (4.3) gives two different eigenvalues for the spin-interaction:

$$\frac{S(S+1) - \left[3/2\right]}{2} = \begin{cases} \frac{1}{4} & \text{if} \quad S = 1 \\ -\frac{3}{4} & \text{if} \quad S = 0 \,. \end{cases} \tag{4.4}$$

Table 4.1 gives the eigenstates corresponding to the singlet ($S = 0$) and the triplet ($S = 1$) eigenstates in terms of the basis [2] $|\uparrow\uparrow\rangle, |\uparrow\downarrow\rangle, |\downarrow\uparrow\rangle, |\downarrow\downarrow\rangle$, built from the single-spin states $|\uparrow\rangle, |\downarrow\rangle$. The triplet states are clearly symmetric under exchange of the two spins, while the singlet state is antisymmetric.

The overall wave functions Ψ, accounting for the physical states of the two-electron system, needs to be antisymmetric. This means that the triplet χ_T and singlet χ_S spin-states are coupled respectively to antisymmetric and symmetric spatial wave functions, so that the whole state of the system is guaranteed fermionic statistics (Ψ antisymmetric). Therefore also the global wave functions can be classified in terms of triplets and singlets

$$\begin{aligned} \Psi_T &= \frac{\chi_T}{\sqrt{2}} \Big(\psi_a(\mathbf{r}_1)\psi_b(\mathbf{r}_2) - \psi_a(\mathbf{r}_2)\psi_b(\mathbf{r}_1) \Big) \\ \Psi_S &= \frac{\chi_S}{\sqrt{2}} \Big(\psi_a(\mathbf{r}_1)\psi_b(\mathbf{r}_2) + \psi_a(\mathbf{r}_2)\psi_b(\mathbf{r}_1) \Big) \,, \end{aligned} \tag{4.5}$$

particles are swapped.

[2] In this representation the first arrow refers to the z component of the spin $\hat{\mathbf{s}}_1$ and so the second one does for $\hat{\mathbf{s}}_2$.

Eigenstate	Eigenvalue	S	m_S
$\|\uparrow\uparrow\rangle$	$1/4$	1	1
$\frac{\|\uparrow\downarrow\rangle + \|\downarrow\uparrow\rangle}{\sqrt{2}}$	$1/4$	1	0
$\|\downarrow\downarrow\rangle$	$1/4$	1	-1
$\frac{\|\uparrow\downarrow\rangle - \|\downarrow\uparrow\rangle}{\sqrt{2}}$	$-3/4$	0	0

Table 4.1: Eigenstates and eigenvalues of $\hat{\mathbf{s}}_1 \cdot \hat{\mathbf{s}}_2$ together with the corresponding quantum numbers for S and m_S.

where $\psi_\alpha(\mathbf{r}_i) = \langle \mathbf{r}_i | \psi_\alpha \rangle$ are the single-electron spatial wave functions. Their respective energies are

$$\begin{aligned} E_T &= \int \Psi_T^* \hat{H} \Psi_T \, d\mathbf{r}_1 d\mathbf{r}_2 \\ E_S &= \int \Psi_S^* \hat{H} \Psi_S \, d\mathbf{r}_1 d\mathbf{r}_2 \,, \end{aligned} \tag{4.6}$$

with the spin parts χ_T and χ_S assumed normalised.

From Eqs. (4.3-4.4) we know that the triplet and singlet eigenstates of the operator $\hat{\mathbf{s}}_1 \cdot \hat{\mathbf{s}}_2$ have eigenvalues $1/4$ and $-3/4$ respectively, hence an effective Hamiltonian parametrised as

$$\hat{H} = \frac{1}{4}(E_S + 3E_T) - (E_S - E_T)\hat{\mathbf{s}}_1 \cdot \hat{\mathbf{s}}_2 \tag{4.7}$$

ensures $\hat{H}\Psi_T = E_T\Psi_T$ and $\hat{H}\Psi_S = E_S\Psi_S$. This expression is the sum of a constant energy term and a spin-dependent term whose coefficient $J = E_S - E_T$ is obtained using Eqs. (4.5-4.6):

$$J = E_S - E_T = \int \psi_a^*(\mathbf{r}_1)\psi_b^*(\mathbf{r}_2)\, \hat{H}\, \psi_a(\mathbf{r}_2)\psi_b(\mathbf{r}_1)\, d\mathbf{r}_1 d\mathbf{r}_2 \,. \tag{4.8}$$

This expression makes explicit how the strength J of the spin-spin coupling of the two electrons in Eq. (4.7) is related to the exchange of the spatial coordinate in the single-electron wave functions $\psi_\alpha(\mathbf{r}_i)$. The spin-dependent part of the two-electron Hamiltonian can be written as

$$\hat{H}^{spin} = -J\, \hat{\mathbf{s}}_1 \cdot \hat{\mathbf{s}}_2 \tag{4.9}$$

where $J > 0$ ($J < 0$) implies $E_S > E_T$ ($E_S < E_T$) so that the system has a triplet (singlet) ground state. If J is positive the interaction is ferromagnetic, otherwise, for J negative, it is antiferromagnetic.

4.1.2 Types of exchange interaction in solids

Generalising this model from a two electron system, such as the hydrogen molecule, to a many-body magnetic system is far from trivial. In general the calculation of the exchange integral J can be complicated, and the theoretical approach to take depends on the class of materials considered [53, 54]. Later in this chapter we make use of a strong-coupling perturbation theory to account for the (super) exchange interaction in magnetic pyrochlore oxides [30]. Here we only give the Hamiltonian for the Heisenberg model

$$\hat{H}^{spin} = -\sum_{i>j} J_{i,j}\, \hat{\mathbf{S}}_i \cdot \hat{\mathbf{S}}_j \,, \tag{4.10}$$

that is the generalisation of Eq. (4.9) to the case of a magnetic lattice ($i > j$ avoids double-counting the pairwise interactions). In general the spin operator $\hat{\mathbf{S}}_i$ represents the total spin of each magnetic atom; it is obtained from the coupling [3] between orbital and spin degrees of freedom of the electrons localised on site i. Then from Eq. (4.10) the magnetic interaction across the lattice is manifestly mediated by the exchange constant $J_{i,j}$, which is often assumed to couple only nearest neighbour spins and to be constant for all pairs of spins:

$$\hat{H}^{spin} = -J \sum_{\langle i,j \rangle} \hat{\mathbf{S}}_i \cdot \hat{\mathbf{S}}_j \,. \tag{4.11}$$

The above Hamiltonian is the starting point for the theoretical study of most magnetic insulators, and accounts for the long range order measured both in ferromagnetic and antiferromagnetic systems. In most magnetic compounds the so called direct exchange is often suppressed since it is unlikely that the magnetic sites, such as a RE-site, can overlap their electron wave-functions, even if the ions are packed very closely with each other. In most cases the exchange between magnetic ions is mediated by non magnetic ones, often oxygens, arranged in between them throughout the lattice; this is called *superexchange* because it is longer-ranged than the direct one and it requires delocalisation of the electrons across the M_i-O-M_j units [4]. Delocalisation and exchange over the three sites allow states where the electrons can combine into more configurations, which are equivalent to the ground state in terms of the magnetic coupling of the whole M-O-M unit, but also unstable because of the Coulomb repulsion between electrons. The admixture of the ground state with these (virtual) states, however, plays a pivotal role in stabilising the magnetic interaction; it often implies an antiferromagnetic superexchange coupling between the magnetic ions M, since configurations of anti-aligned electron-spins tend to satisfy the Pauli principle at lower energy cost than the ferromagnetic ones. Examples of these mechanisms are shown in Fig. 4.1 where antiferromagnetic and ferromagnetic coupling are compared for a simplified M-O-M system (in the case discussed in the figure M represents a transition metal ion; Mn^{+2} in MnO for example).

[3] The coupling varies depending on the type of atoms; in general it gives a total angular momentm $\hat{\mathbf{J}}_i$. Here, as often is the case, the notation $\hat{\mathbf{S}}_i$ is preferred to avoid confusion with the exchange constant J_{ij}.

[4] M-O-M represents two magnetic ions whose (super) exchange coupling is mediated via an oxygen.

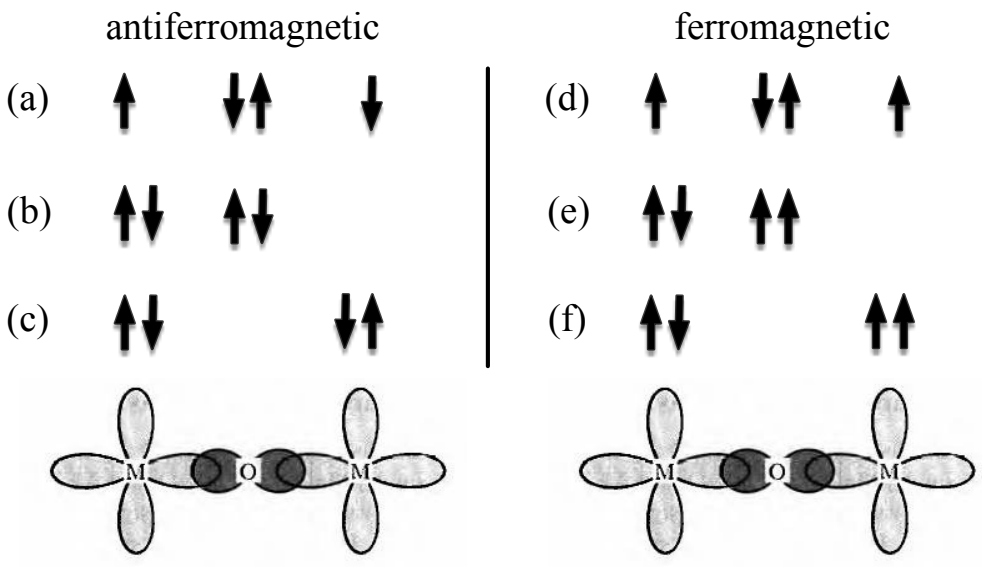

Figure 4.1: Adapted from Fig.4.3 in Ref. [53]. A simplified case of an M-O-M unit where antiferromagnetic superexchange between the M ions is compared to the ferromagnetic case. The left panel shows three possible antiferromagnetic configurations of the electrons across the three sites: (a) is the ground state which gives a net spin only on the M sites; (b) and (c) are configurations with no on-site net spin but cost Coulomb repulsion since the paired electrons are localised only on some sites. (b) and (c) are excited states favoured by the lowering of the total kinetic exchange energy. The right panel shows the ferromagnetic configurations for the same M-O-M system: (d) is the ground state with net spin on the M sites and also a net magnetisation over the whole unit; (e) and (f) are configurations with equivalent magnetisation but different net spin localisation. These configurations violate Pauli if there is only one orbital per site, as two spins cannot point in the same direction and be in the same orbital. In general the antiferromagnetic case is more common since the anti-alignment of the spins satisfies the Pauli principle straightforwardly. In this pictorial representation the exchange channels across the M-O-M are opened via hybridisation between the p orbitals of the oxygens and the d of M (a transition Metal ion).

The low temperature properties of a wide variety of magnetic materials are interpreted in terms of the exchange interactions analogous to those described by the Hamiltonian in Eq. (4.11) and shown in Fig. 4.1. In magnetic pyrochlore compounds one of the new aspects is the type of exchange Hamiltonian which needs a few "readjustments" with respect to Eq. (4.11) mainly because of two mechanisms: the particular type of geometrical constraints arising from the pyrochlore structure and the classical Ising physics emerging from the large number of unpaired electrons in Dy^{3+} and Ho^{3+} and the strong spin-orbit coupling.

4.1.3 "Classical" exchange Hamiltonians in spin ice

As mentioned in the introduction the spin ice materials show an effective ferromagnetic coupling between neighbouring RE^{3+} ions. This, however, refers to the overall interac-

tion which leads to the spin-ice frustration between the (classical) spins with local Ising anisotropy; in this case, in fact, a pictorial representation is not as immediate as the one in Fig. 4.1, for several reasons. Firstly, the shell index and the number of unpaired electrons in the RE^{3+} ions in the spin ices are higher than in the transition metal; this means a stronger spin-orbit coupling and the occurrence of Ising physics arising from the combination of Hund's rules and the symmetries of the crystalline electric fields. Secondly, a uniaxial description of the magnetic degrees of freedom is not allowed in magnetic pyrochlores because of the absence of a unique crystalline axis [61]; this implies that the magnetic-interaction Hamiltonian is often more appropriately described in terms of a local Ising axes framework like the one introduced at the beginning of this thesis.

Starting from these two arguments we deduce that a second-quantised description of the exchange in terms of many-body fermionic operators is needed to describe the role of quantum mechanical exchange in spin-tunnelling and monopole-hopping in spin ice. Before dealing with many-body operators here we summarise a first attempt to reproduce an effective magnetic field derived simply from the exchange interaction in the classical Ising Hamiltonian given in the first chapter.

Although this model is not expected to give an entirely consistent quantum-mechanical description, as it is derived from an effective classical picture, it allows a characterisation of the symmetries expected for the exchange interactions whenever a monopole is sitting in one tetrahedron of the two-tetrahedra cluster considered in the previous chapter. The main purpose is to provide a direct comparison of the effective magnetic fields due to the exchange with respect to the ones found from the dipolar interactions in Chapter 3.

We start from the classical Hamiltonian for spin ice, Eq. (1.1), truncated to the nearest-neighbour approximation:

$$H_{\rm nn} = J_{\rm eff} \sum_{\langle i,j \rangle} S_i S_j \,. \tag{4.12}$$

Here we restored the formalism that is typically used for spin ice [5, 13]: $S_i = 1, -1$ depending on whether the (classical [5]) Ising spin points inward or outward with respect to one type of tetrahedron [6]. The Hamiltonian in Eq. (4.12) is conveniently derived to work with local Ising-axes ("in-out" formalism) from Eq. (4.11), where in contrast the Ising-axis is global ("up-down" formalism), by noticing that $\hat{\boldsymbol{e}}_i \cdot \hat{\boldsymbol{e}}_j = -1/3$ with $\hat{\boldsymbol{e}}_i$ being the local unit vector, for a spin S_i, pointing towards the centre of the tetrahedron. Such notation is fully consistent with the sign convention typically ascribed to the exchange coupling constants discussed for Eq. (4.9). In fact, the ground state of this system is ferromagnetic and frustrated (2in-2out in each tetrahedron) for $J_{\rm eff} > 0$, while antiferromagnetic (4in/4out for neighbouring tetrahedra) for $J_{\rm eff} < 0$.

In spin ices the effective nearest neighbour constant is $J_{\rm eff} = J_{\rm nn} + D_{\rm nn}$, where $J_{\rm nn}$ regulates solely the Ising exchange while $D_{\rm nn}$ is the result of the n.n. truncation on the dipolar term (see Eq. (1.1)). These constants are typically expressed in Kelvin (K) in the literature [5, 13]. $D_{\rm nn} = 2.35$ K is obtained by considering the RE^{3+} ions as

[5] Here S_i are scalar variables; these are obtained by taking the spin operators $\hat{\mathbf{S}}_i/|\mathbf{S}|$ in Eq. (4.11) to the limit of an infinite (local) Ising anisotropy.

[6] There are two types of tetrahedra in the pyrochlore lattice oriented in opposite directions.

magnetic dipoles with magnitude $10\mu_B$. $J_{\rm nn} = -0.52$ K, -1.24 K for, respectively, $Ho_2Ti_2O_7$ and $Dy_2Ti_2O_7$ have been measured experimentally [5]. Hence the effective coupling in Eq. (4.12) is ferromagnetic ($J_{\rm eff} > 0$) in both HTO ($J_{\rm eff} = 1.8$ K) and DTO ($J_{\rm eff} = 1.1$ K) and accounts for the frustrated ground state which characterises spin-ice materials.

For calculating the effective-exchange fields resulting on a central RE-site of a two-tetrahedra cluster the focus is only on the antiferromagnetic coupling constant $J_{\rm nn}$. To facilitate comparisons with the results obtained from the analysis of the dipolar fields in Chapter 3, it is convenient to write the exchange Hamiltonian in the same notation used therein [7]

$$H^0_{\rm exc} = -J_{\rm nn}\, S^0_0 \sum_{j=1}^{6} S^0_j\,, \tag{4.13}$$

where now the spins S^0_i assume values ± 1 depending on $e_0 \cdot S^0_j e_j \gtrless 0$. Setting $J_{\rm nn} = J/3$ as in Ref. [5], this can be rewritten as

$$\begin{aligned} H^0_{\rm exc} &= -\frac{Jk_B}{3}\, S^0_0 \sum_{j=1}^{6} S^0_j = -Jk_B\, S^0_0\, \hat{e}_0 \cdot \sum_{j=1}^{6} S^0_j \hat{e}_j \\ &= -|\mathbf{m}| S^0_0 \hat{e}_0 \cdot \Big(\frac{Jk_B}{|\mathbf{m}|} \sum_{j=1}^{6} S^0_j \hat{e}_j\Big) = -\mathbf{m}_0 \cdot \mathbf{B}_{\rm exc}(0)\,, \end{aligned} \tag{4.14}$$

where the Boltzmann constant k_B has been introduced to ensure energies in Joules and magnetic inductions in Tesla. This gives on the central site an effective-exchange field

$$\mathbf{B}_{\rm exc}(0) = \frac{Jk_B}{|\mathbf{m}|} \sum_{j=1}^{6} S^0_j \hat{e}_j, \tag{4.15}$$

by comparison between the exchange Hamiltonian in Eq. (4.14) and a Zeeman-type interaction with the resulting field. In analogy with the dipolar fields discussed for the two-tetrahedra cluster in Eq. (3.8), it is convenient to give the exchange effective field in Eq. (4.15) as

$$\mathbf{B}_{\rm exc}(0) = J \frac{k_B}{10\mu_B} \sum_{i=1}^{3} \Big(S^0_i + S^0_{i+3}\Big)\hat{e}_i\,, \tag{4.16}$$

where the spin terms of the upper (S^0_i) and lower (S^0_{i+3}) tetrahedra are shown explicitly together with their mutual easy axis $\hat{e}_i$ (we replaced directly $|\mathbf{m}| \approx 10\mu_B$ for spin ice dipoles).

It is straightforward now to calculate the exchange contribution to the magnetic fields resulting in a site nearby a monopole. We refer to the same examples discussed in section 3.2.1 in the previous chapter, where a north monopole is sitting next to the

[7] Here the overall sign is opposite to Eq. (4.12) because $e_0 \cdot e_j = 1/3$, while the local Ising axis notation gives $\hat{\boldsymbol{e}}_i \cdot \hat{\boldsymbol{e}}_j = -1/3$. As we shall see, the local Ising axes coincide with the $\mathbf{z_i}$ axes for the local coordinate systems that will be given in Eq. (4.22).

central spin of a two-tetrahedra cluster which can undergo a flipping. Of the nine possible configurations featuring a north monopole in the lower tetrahedron, results are given given only for those represented in the left panel of Fig. 3.7, as the others can be obtained by two-fold rotations of 120 ° around the local easy axis. We find

$$\mathbf{B}_{\text{exc}}(0) = 2J\frac{k_B}{10\mu_B}\left(\hat{e}_1 - \hat{e}_3\right) \tag{4.17a}$$

$$\mathbf{B}_{\text{exc}}(0) = 2J\frac{k_B}{10\mu_B}\left(\hat{e}_2 - \hat{e}_3\right) \tag{4.17b}$$

$$\mathbf{B}_{\text{exc}}(0) = 0, \tag{4.17c}$$

for the respective configurations on the left, central and right columns of Table 3.1. Interestingly these have similarities with the ones found from the dipolar fields: the directions of the resulting fields are the same, $(-\frac{1}{\sqrt{2}}, 0, \frac{1}{\sqrt{2}})$ and $(0, -\frac{1}{\sqrt{2}}, \frac{1}{\sqrt{2}})$ respectively for the first and second case, and an identically null field in the third one. The remaining six cases for a north monopole in the lower tetrahedron are obtained by global rotations of these around the $< 111 >$ axis of the central dipole (analogously there are nine configurations for a south monopole). Hence also for the exchange all the non null-field configurations are purely transverse to the central easy axis. This means that there is no longitudinal component which would inhibit the tunnelling we found stimulated by the transverse dipolar couplings. In this case, however, the orientation of the resulting field is opposite to the corresponding dipolar cases; this happens because the resulting fields are pointing in the same direction as the dipolar ones but with strength proportional to $J < 0$ (with $J_{\text{nn}} = J/3$).

Limitations of this model for exchange. What's next? By considering this model for the exchange interactions it seems that the dipolar fields and the exchange ones tune together the resulting transverse field which induces the tunnelling of the central ion. For example if we were to consider the case of $Ho_2Ti_2O_7$ this would have any of the transverse fields with strength -0.75 T which would give a net resulting magnitude of -0.42 T once combined with the 0.33 T of the correspondent dipolar cases. Then for HTO it seems that, at least up to a nearest neighbour level, exchange changes the orientation of the overall nearest neighbour fields but it does not change their order of magnitude. The tunnelling rates from Chapter 2 then are expected to be similar to those arising from the dipolar fields analysis in Chapter 3. In the case of $Dy_2Ti_2O_7$ the higher magnitude of the exchange constant gives resulting transverse fields of strength -1.80 T, which are now even higher in magnitude than the dipolar ones (combined together they would give ≈ -1.47 T). This makes more explicit a result that was already found for HTO: the strength of the dipolar coupling constant $|D_{\text{nn}}| > |J_{\text{nn}}|$ does not imply that the dipolar fields dominate over the exchange interactions.

This result, however, is not totally surprising since this model for the exchange fields has a series of implicit approximations in it. For example the spins are still considered only as classical dipoles with Ising anisotropy. Furthermore, the directions of the resulting exchange fields are the same to the dipolar ones mainly because of the geometrical degrees of freedom which derive from the classical description of the anisotropies. The terms transverse to the local Ising axis, are not even considered as higher order

corrections. In particular for the magnetic pyrochlores, where there is not a unique crystalline axis defining the Ising anisotropy for the whole system, considering off-Ising kinds of interaction is crucial. In these systems, in fact, the superexchange between the magnetic ions is mediated via the oxygen ions sitting at the centres of the tetrahedra hosting the spins at their vertices. Hence, it is necessary to give a formulation of the exchange between the magnetic sites which takes into account the role of the oxygens in acting as a mediator of this interaction channel. The ideal framework is to consider the behaviour of the magnetic electrons of any two RE-sites which participate in the exchange mechanism and lead to an effective magnetic interaction between the RE-sites.

In the following sections we derive an effective exchange Hamiltonian for the magnetic ions the oxides $RE_2Ti_2O_7$, by means of a fourth-order strong-coupling perturbation theory adopted successfully by Onoda et al for some magnetic pyrochlores which are known for exhibiting strong quantum features [59, 30, 62]. This method derives the exchange interaction between neighbouring RE^{3+} ions using a model for virtual hopping of electrons via different quantum states. Such states are the $4f$ orbitals of the two RE ions considered, and the $2p$ orbitals of the O1 oxygen "between" them. In shorthand we refer to this 4-step virtual process as RE→O1→RE'→O1→RE, where RE and RE' are at different vertices of a tetrahedron and O1 is the oxygen ion sitting at the centre of it.

4.2 Global and local coordinate frames

To describe the hopping of electrons in different sites, it is convenient to use two *general* sets of coordinate frames: the global $\mathbf{X}, \mathbf{Y}, \mathbf{Z}$ for the O1 sites, and the local $\mathbf{x}_i, \mathbf{y}_i, \mathbf{z}_i$ for the RE-sites (as in Fig. 4.2). This distinction is necessary because of the anisotropic arrangement of the magnetic ions in this type of pyrochlore oxides. In fact, in Chapter 2 we gave a description of the quantum states $|M_J\rangle$ of a RE^{3+} ion with respect to a quantisation axis $\mathbf{z}_0$ that is parallel to the local easy axis (this was shown in Fig. 2.8 in the context of the application of a magnetic field on the $\mathbf{x_0}, \mathbf{y_0 z}_0$). Such axis together with the other system of local coordinates will be defined in section 4.2.2.

In contrast to this the oxygen ions do not exhibit magnetism since all the shells are totally filled with electrons. Hence for the O1 sites it is convenient, as reference frame, the *global* one which belongs to the space group $F_{d\bar{3}m}$ accounting for all symmetries in $RE_2Ti_2O_7$ [35].

The above considerations imply that the wave function of a given electron refers to the set of coordinates chosen for the site of the ion considered.

4.2.1 The global picture

The O1 ions, sitting in the centres of the tetrahedra of the pyrochlore lattice, belong to a diamond lattice. This is given by two fcc interpenetrating sublattices and it is convenient to group the O1 oxygens into two subclasses, depending on the fcc lattice they belong to. We call "*primary*" the O1 sites in positions

$$\mathbf{R} = n_1\mathbf{R}_1 + n_2\mathbf{R}_2 + n_3\mathbf{R}_3, \tag{4.18}$$

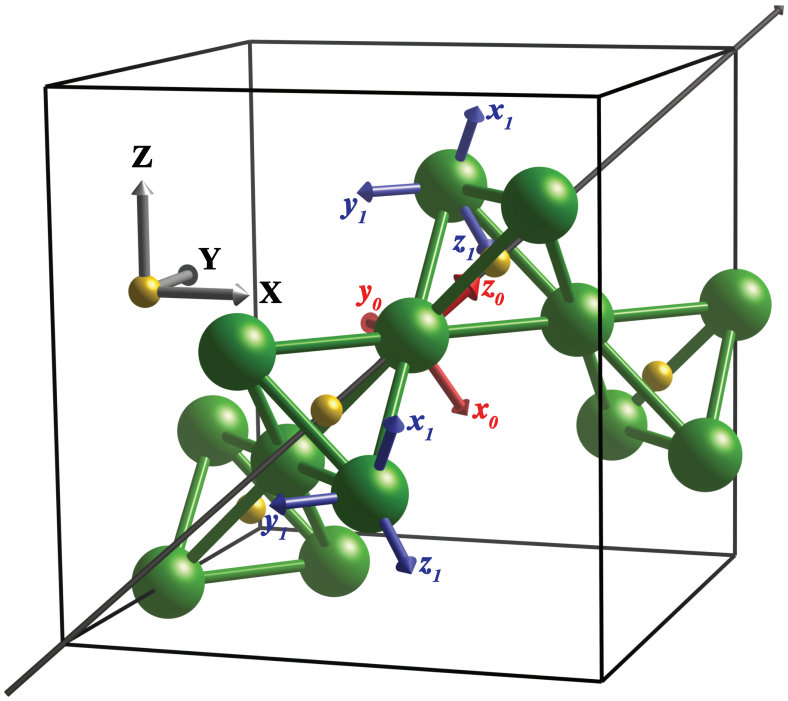

Figure 4.2: Two examples of local coordinate frames, $\mathbf{x}_0, \mathbf{y}_0, \mathbf{z}_0$ (red) and $\mathbf{x_1}, \mathbf{y_1}, \mathbf{z_1}$ (blue), for the different RE ions (green spheres), as opposed to the global coordinate frame $\mathbf{X}, \mathbf{Y}, \mathbf{Z}$ (grey). The former Cartesian coordinates are ideally suited to describe the local D_{3d} point group symmetry of the RE-ions due to the local CF environments, while the latter one is preferable for global properties, like the $F_{d\bar{3}m}$ space group symmetries, of the whole lattice. Here the global coordinate system $\mathbf{X}, \mathbf{Y}, \mathbf{Z}$ is shown on an oxygen site, since the O1 sites (yellow spheres) sitting in the centres of the RE coordination tetrahedra, mediate the exchange of electrons between the magnetic RE^{3+} ions with different local coordinates $\mathbf{x}_i, \mathbf{y}_i, \mathbf{z}_i$. The local reference coordinate system used in Chapter 2 is $\mathbf{x}_0, \mathbf{y}_0, \mathbf{z}_0$ as shown in Fig. 2.8.

with n_1, n_2, n_3 integer numbers and

$$\mathbf{R}_1 = \frac{a}{2}(0,1,1), \qquad \mathbf{R}_2 = \frac{a}{2}(1,0,1), \qquad \mathbf{R}_3 = \frac{a}{2}(1,1,0), \tag{4.19}$$

the basis for the primary fcc lattice ($a \approx 10.1$Å is the unit-cell edge in Spin Ice). The "*secondary*" O1 sites are in positions $\mathbf{R} + 2\mathbf{a}_i$, with $i = 0, 1, 2, 3$ and

$$\begin{aligned} \mathbf{a}_0 &= \frac{a}{8}(-1,-1,-1), & \mathbf{a}_1 &= \frac{a}{8}(-1,1,1), \\ \mathbf{a}_2 &= \frac{a}{8}(1,-1,1), & \mathbf{a}_3 &= \frac{a}{8}(1,1,-1). \end{aligned} \tag{4.20}$$

Note that for each primary O1 site there are 4 secondary O1 "nearest neighbours" and vice versa. On the other hand, for all the O1 sites the electronic $2p$ orbitals have local axes that are parallel to the global ones. Hence, in simple words, the quantum states

of any electron at an O1 site are given with respect to the canonical basis:

$$\mathbf{X} = (1,0,0), \qquad \mathbf{Y} = (0,1,0), \qquad \mathbf{Z} = (0,0,1), \tag{4.21}$$

where $\mathbf{Z}$ is conventionally chosen as the quantisation axis.

4.2.2 The local picture

The RE magnetic ions sit at the vertices of the corner-sharing tetrahedra: $\mathbf{r} = \mathbf{R} + \mathbf{a}_i$. These locate the midpoints between neighbouring O1 sites positioned in the centres of the tetrahedra. The local coordinate frame basis vectors at the RE-sites are

$$\mathbf{x}_0 = \frac{1}{\sqrt{6}}(1,1,-2), \qquad \mathbf{y}_0 = \frac{1}{\sqrt{2}}(-1,1,0), \qquad \mathbf{z}_0 = \frac{1}{\sqrt{3}}(1,1,1), \tag{4.22a}$$

$$\mathbf{x}_1 = \frac{1}{\sqrt{6}}(1,-1,2), \qquad \mathbf{y}_1 = -\frac{1}{\sqrt{2}}(1,1,0), \qquad \mathbf{z}_1 = \frac{1}{\sqrt{3}}(1,-1,-1), \tag{4.22b}$$

$$\mathbf{x}_2 = \frac{1}{\sqrt{6}}(-1,1,2), \qquad \mathbf{y}_2 = \frac{1}{\sqrt{2}}(1,1,0), \qquad \mathbf{z}_2 = \frac{1}{\sqrt{3}}(-1,1,-1), \tag{4.22c}$$

$$\mathbf{x}_3 = -\frac{1}{\sqrt{6}}(1,1,2), \qquad \mathbf{y}_3 = -\frac{1}{\sqrt{2}}(-1,1,0), \qquad \mathbf{z}_3 = \frac{1}{\sqrt{3}}(-1,-1,1), \tag{4.22d}$$

with $i = 0,1,2,3$, depending on the RE ion of interest. The local basis $\mathbf{x}_i, \mathbf{y}_i, \mathbf{z}_i$ corresponds to each RE-site $\mathbf{r} = \mathbf{R} + \mathbf{a}_i$. One of the reasons for the choice made in Eqs. (4.22a-4.22d) is that it satisfies the relation

$$\sum_{i=0}^{3} (\mathbf{x}_i, \mathbf{y}_i, \mathbf{z}_i) = (\mathbf{0}, \mathbf{0}, \mathbf{0})\,. \tag{4.23}$$

This ensures that all the local $\mathbf{z}_i$ directions point inward for the tetrahedron centred at the primary O1 site $\mathbf{R}$ (outward for the secondary O1 sites). Furthermore these sets of local coordinates are convenient [8] because they preserve some of the symmetries of the space group $F_{d\bar{3}m}$, for example the invariance under 180° rotations of the *whole* system about the three axes parallel to $\mathbf{X}, \mathbf{Y}, \mathbf{Z}$ and passing through the O1 sites.

4.2.3 Rotations in $\mathbb{R}^3$: the Euler angle matrix

The local coordinate frames are related to the global ones via rotations by the following paired angles:

$$\varphi_0 = \frac{\pi}{4}, \qquad \vartheta_0 = \arccos\frac{1}{\sqrt{3}}, \tag{4.24a}$$

$$\varphi_1 = 3\varphi_0, \qquad \vartheta_1 = -\pi + \vartheta_0, \tag{4.24b}$$

$$\varphi_2 = -\varphi_0, \qquad \vartheta_2 = -\pi + \vartheta_0, \tag{4.24c}$$

$$\varphi_3 = -3\varphi_0, \qquad \vartheta_3 = \vartheta_0, \tag{4.24d}$$

[8] In particular for the exchange Hamiltonian in Eq.(17) of Ref. [30].

for the RE-sites at $\mathbf{r} = \mathbf{R} + \mathbf{a}_i$, with respectively $i = 0, 1, 2, 3$.

The angles φ_i, ϑ_i are choices of the so called *Euler* angles of rotation. To understand their meaning we briefly review how rotations in $\mathbb{R}^3$ are described by means of matrices. It is known that any rotation of a vector $\mathbf{v} \in \mathbb{R}^3$ can be described as

$$\mathbf{v}' = \mathsf{R}_z(\varphi)\, \mathsf{R}_y(\vartheta)\, \mathsf{R}_z(\gamma)\, \mathbf{v}\,, \tag{4.25}$$

where $(\varphi, \vartheta, \gamma)$ is a set of *Euler* angles, and $\mathsf{R}_u(\delta)$ is the generic matrix for a rotation of angle δ around an axis u [63]. A given choice of angles $(\varphi, \vartheta, \gamma)$ and axes (x, y, z) provides a unique parametrisation of the so called Euler rotation matrix

$$\mathsf{R}(\varphi, \vartheta, \gamma) = \mathsf{R}_z(\varphi)\, \mathsf{R}_y(\vartheta)\, \mathsf{R}_z(\gamma)\,, \tag{4.26}$$

which account for the $\mathbf{v}' \to \mathbf{v}$ transformation. Although this is clearly a product of rotations only around y and z, for completeness we report here the three single-angle rotation matrices:

$$\mathsf{R}_x(\delta) = \begin{pmatrix} 1 & 0 & 0 \\ 0 & \cos\delta & -\sin\delta \\ 0 & \sin\delta & \cos\delta \end{pmatrix}, \tag{4.27a}$$

$$\mathsf{R}_y(\delta) = \begin{pmatrix} \cos\delta & 0 & \sin\delta \\ 0 & 1 & 0 \\ -\sin\delta & 0 & \cos\delta \end{pmatrix}, \tag{4.27b}$$

$$\mathsf{R}_z(\delta) = \begin{pmatrix} \cos\delta & -\sin\delta & 0 \\ \sin\delta & \cos\delta & 0 \\ 0 & 0 & 1 \end{pmatrix}. \tag{4.27c}$$

We can now give the meaning of the angles (φ_i, ϑ_i) listed in Eqs. (4.24a-4.24d) in terms of the Euler parametrisations [9] $(\varphi_i, \vartheta_i, 0)$ which account for the global $\to$ local transformations:

$$\mathbf{x}_i = \mathsf{R}(\varphi_i, \vartheta_i)\, \mathbf{X}, \tag{4.28a}$$

$$\mathbf{y}_i = \mathsf{R}(\varphi_i, \vartheta_i)\, \mathbf{Y}, \tag{4.28b}$$

$$\mathbf{z}_i = \mathsf{R}(\varphi_i, \vartheta_i)\, \mathbf{Z}, \tag{4.28c}$$

with $\mathsf{R}(\varphi_i, \vartheta_i) = \mathsf{R}_z(\varphi_i)\mathsf{R}_y(\vartheta_i)$ giving

$$\mathsf{R}(\varphi_i, \vartheta_i) = \begin{pmatrix} \cos\varphi_i \cos\vartheta_i & -\sin\varphi_i & \cos\varphi_i \sin\vartheta_i \\ \sin\varphi_i \cos\vartheta_i & \cos\varphi_i & \sin\varphi_i \sin\vartheta_i \\ -\sin\vartheta_i & 0 & \cos\vartheta_i \end{pmatrix} \equiv (\mathbf{x}_i^{\mathsf{T}}, \mathbf{y}_i^{\mathsf{T}}, \mathbf{z}_i^{\mathsf{T}}), \tag{4.29}$$

where $\mathbf{v}^{\mathsf{T}}$ represents the transpose of a vector $\mathbf{v}$. One of the properties relevant for our

[9] It is convenient to choose $\gamma_i = 0$, $\forall i = 0, 1, 2, 3$.

calculations is that the Euler rotation matrices are unitary:

$$\mathsf{R}^{-1}(\varphi,\vartheta) = \mathsf{R}^{\mathsf{T}}(\varphi,\vartheta)\,. \tag{4.30}$$

4.2.4 Rotations in the Hilbert space: the Wigner matrix

The quantum-mechanical description of a physical system requires a Hilbert space usually attached to a reference frame [63]. For example the choice of the quantisation axis **Z** for the O1 sites gives a "point of view" to depict the quantum states of the electrons occupying these sites.

When a reference frame of a quantum state $|\psi\rangle$ undergoes a rotation of angle δ around an axis u, the new state is given by

$$|\psi_u^{(\delta)}\rangle = \hat{R}_u(\delta)\,|\psi\rangle = \exp(-i\delta\hat{J}_u)\,|\psi\rangle \tag{4.31}$$

where $\hat{J}_u$ is the projection of the angular momentum operator $\hat{\mathbf{J}}$ on the rotation axis u. An arbitrary rotation in the Hilbert space, corresponding to an Euler parametrization $(\varphi,\vartheta,\gamma)$ in $\mathbb{R}^3$, is described by the rotation operator

$$\begin{aligned}\hat{R}(\varphi,\vartheta,\gamma) &= \hat{R}_z(\varphi)\hat{R}_y(\vartheta)\hat{R}_z(\gamma)\\ &= \exp(-i\varphi\hat{J}_z)\exp(-i\vartheta\hat{J}_y)\exp(-i\gamma\hat{J}_z)\,.\end{aligned} \tag{4.32}$$

with quantisation axis z. Rotations of angular momentum eigenstates are obtained by means of the so called *Wigner $\mathcal{D}$-matrix*:

$$\begin{aligned}\hat{R}(\varphi,\vartheta,\gamma)\,|j,\tilde{m}\rangle &= \sum_{m=-j}^{+j} |j,m\rangle\,\mathcal{D}^{j}_{m,\tilde{m}}(\varphi,\vartheta,\gamma)\\ &= \sum_{m=-j}^{+j} |j,m\rangle\,\langle j,m|\,\hat{R}(\varphi,\vartheta,\gamma)\,|j,\tilde{m}\rangle\ ,\end{aligned} \tag{4.33}$$

where $\{|j,m\rangle\}$ is the basis of the Hilbert space $\mathcal{E}(j)$ defined by the quantum number j of the operator $\hat{J}^2$, and $|j,\tilde{m}\rangle$ represents an eigenstate of $\hat{J}_z$ with quantum number $\tilde{m} = -j,\ldots,+j$ [63].

As already mentioned, in the case of interest to us only two Euler parameters (φ_i,ϑ_i) are needed for each global $\leftrightarrow$ local rotation. Then the Wigner matrices

$$\begin{aligned}\mathcal{R}_{m',m}(\varphi_i,\vartheta_i) &\equiv \mathcal{D}^{j}_{m',m}(\varphi_i,\vartheta_i,0)\\ &= \langle j,m'|\,\hat{R}(\varphi_i,\vartheta_i)\,|j,m\rangle\\ &= e^{-i\varphi_i m'}\,\langle j,m'|\,e^{-i\vartheta_i\hat{J}_y}\,|j,m\rangle\end{aligned} \tag{4.34}$$

correspond to the rotations $\mathsf{R}(\varphi_i,\vartheta_i)$ given in Eqs. (4.28-4.29). From now on we refer to the Wigner rotation matrix as $\mathcal{R}_{m',m}(\varphi_i,\vartheta_i)$ to use the same notation adopted by Onoda in Ref. [30]. The rotation matrices in Eq. (4.29) and Eq. (4.34) are fundamental tools to derive the hybridisation and effective-exchange Hamiltonians.

In the following section such Hamiltonians are derived by means of virtual hopping of

electrons among lattice sites with different local coordinate frames.

4.3 f-p hybridisation and second quantisation

In magnetic pyrochlore oxides there is an O1 oxygen at the centre of the tetrahedron which hosts four RE ions in its vertices [6, 30]. Because of this arrangement the $4f$ electrons of the RE ion can hop to the $2p$ levels at the O1 site. This implies that these oxygen sites allow a *super-exchange* mechanism between electrons hosted in neighbouring RE-sites. Here we derive an effective exchange Hamiltonian directly from the f-p hybridisation between the RE^{3+} and the O^{2-} ions. This expands the calculation from the two-electron case of Pr^{3+} in Ref. [30] to a more general case for RE ions with larger number of electrons in the f shell. To account for all the quantum-mechanical features, the electrons are expressed in the *second-quantised* formalism of the *many-body* theory.

4.3.1 Many-body fermionic operators

In the previous chapters we have seen how the magnetic ground-state of the Ho^{3+} ion is expressed as a linear superposition of angular momentum eigenstates $|M_J\rangle$. This type of representation is ideal for describing quantum mechanisms, such as the tunnelling of a *large* spin, where the electrons in the magnetic orbitals behave in a "cooperative" way and it is more convenient to ignore part of their "individual" properties. On the other hand the many-body formalism is a very powerful tool when dealing with microscopic mechanisms such as the exchange between single electrons in different quantum states. Hence it is necessary to introduce a few fundamental notions of many-body theory for fermions [57].

Fermions are quantum particles with a half integer spin. They are known for having a strong constraint on their physical properties: one quantum state can only be occupied by one fermion at a time (Pauli principle). In general the quantum state of n electrons can be expressed as

$$|\psi\rangle = \sum_{\mathbf{q}_1,\mathbf{q}_2\cdots\mathbf{q}_n} C_{\mathbf{q}_1,\mathbf{q}_2\cdots\mathbf{q}_n}\ \hat{a}^\dagger_{\mathbf{q}_1}\hat{a}^\dagger_{\mathbf{q}_2}\ldots\hat{a}^\dagger_{\mathbf{q}_n}\,|0\rangle \tag{4.35}$$

where $|0\rangle$ represents the vacuum state and each fermionic $\hat{a}^\dagger_{\mathbf{q}_i}$ operator creates an electron in a quantum state $\mathbf{q}_i$ (a set of quantum numbers) [10]. The coefficients $C_{\mathbf{q}_1,\mathbf{q}_2\cdots\mathbf{q}_n}$ account for the different contribution of each electronic configuration in the linear expansion. For example, since the $2p$ shell of the O^{2-} ion is totally filled, we can represent this electronic state as

$$|\Delta\rangle = \hat{p}^\dagger_{-1,-\frac{1}{2}}\hat{p}^\dagger_{-1,\frac{1}{2}}\hat{p}^\dagger_{0,-\frac{1}{2}}\hat{p}^\dagger_{0,\frac{1}{2}}\hat{p}^\dagger_{1,-\frac{1}{2}}\hat{p}^\dagger_{1,\frac{1}{2}}\,|0\rangle \tag{4.36}$$

where each $\hat{p}^\dagger_{m_l,m_s}$ represents an electron with magnetic quantum numbers m_l and m_s for the orbital and spin angular momenta respectively. In Eq. (4.36) the coefficient $C_{m_{l1},m_{s1}\ldots} = 1$ because there is only one possible configuration for a full shell.

[10] Note all fermionic operators used here are *time-independent*.

To allow a complete modelling of these quantum states it is necessary to introduce an annihilation operator $\hat{a}_{\mathbf{q}_i}$ that is defined by $\hat{a}_{\mathbf{q}_i}|0\rangle = 0$. Then the so called number operator $\hat{n}_{\mathbf{q}_i} = \hat{a}^\dagger_{\mathbf{q}_i}\hat{a}_{\mathbf{q}_i}$ accounts for the number of particles occupying a given quantum state (for a given state $\mathbf{q}_i$ only eigenvalues $n_{\mathbf{q}_i} = 0, 1$ are allowed because of the Pauli principle). A detailed discussion on the properties of the fermionic operators goes beyond the interest of this work and can be found in Ref. [57]. Here we only summarise few of their general ones and then switch to what is relevant for electrons in RE ions. The *anticommutation* relations for fermionic operators are the fundamental ingredients:

$$\begin{aligned} \{\hat{a}_{\mathbf{q}_r}, \hat{a}^\dagger_{\mathbf{q}_s}\} &= \delta_{\mathbf{q}_r,\mathbf{q}_s}\,, \\ \{\hat{a}_{\mathbf{q}_r}, \hat{a}_{\mathbf{q}_s}\} &= \{\hat{a}^\dagger_{\mathbf{q}_r}, \hat{a}^\dagger_{\mathbf{q}_s}\} = 0\,; \end{aligned} \tag{4.37}$$

the anticommutator is defined by the following relation

$$\{A, B\} \equiv AB + BA\,. \tag{4.38}$$

From the anticommutation rules in Eq. (4.37) it is straightforward to derive the following rules which account for the correct *statistics* for fermions [57]:

$$\hat{a}^2_{\mathbf{q}_r} = \hat{a}^{\dagger\,2}_{\mathbf{q}_s} = 0 \quad \Longrightarrow \quad \hat{a}^\dagger_{\mathbf{q}_s}\hat{a}^\dagger_{\mathbf{q}_s}|0\rangle = 0; \tag{4.39a}$$

$$\hat{a}_{\mathbf{q}_r}\hat{a}^\dagger_{\mathbf{q}_r} = 1 - \hat{a}^\dagger_{\mathbf{q}_r}\hat{a}_{\mathbf{q}_r} \quad \Longrightarrow \quad \begin{cases} (\hat{a}^\dagger_{\mathbf{q}_r}\hat{a}_{\mathbf{q}_r})^2 = \hat{a}^\dagger_{\mathbf{q}_r}\hat{a}_{\mathbf{q}_r}, \\ \hat{a}^\dagger_{\mathbf{q}_r}\hat{a}_{\mathbf{q}_r}(1 - \hat{a}^\dagger_{\mathbf{q}_r}\hat{a}_{\mathbf{q}_r}) = 0. \end{cases} \tag{4.39b}$$

The former prevents two particles form occupying the same state, the latter shows that the number operator $\hat{n}_{\mathbf{q}_r} = \hat{a}^\dagger_{\mathbf{q}_r}\hat{a}_{\mathbf{q}_r}$ has only the eigenvalues zero and one. Hence these two properties make explicit that from the anti-commutation relations in Eq. (4.37) the Pauli principle is satisfied. Furthermore it is straightforward to prove that the *commutator* $[\hat{n}_{\mathbf{q}_r}, \hat{n}_{\mathbf{q}_s}] = 0$, even though the individual creation and destruction operators anticommute [57].

4.3.2 Fermionic-operator representation for the magnetic quantum states of RE^{3+} ions

In analogy with the expression for a generic quantum state $|\psi\rangle$ given in Eq. (4.35), the quantum states for a RE ion are given by [11]

$$|M_J\rangle = \sum_{\mathbf{q}_1,\mathbf{q}_2\cdots\mathbf{q}_n} C^{M_J}_{\mathbf{q}_1,\mathbf{q}_2\ldots\mathbf{q}_n}\, \hat{f}^\dagger_{\mathbf{q}_1}\hat{f}^\dagger_{\mathbf{q}_2}\ldots\hat{f}^\dagger_{\mathbf{q}_n}|0\rangle\,. \tag{4.40}$$

Here $|0\rangle$ represents the vacuum state for the magnetic ion, i.e. no electrons in the $4f$ shell (empty shell). The operator $\hat{f}^\dagger_{\mathbf{q}}$ acting on the vacuum creates an f-electron in the quantum state $\mathbf{q} = m_l, m_s$. The possible values can only be $m_l = -3, -2, \ldots, 3$ for the orbital quantum number and $m_s = -1/2, 1/2$ for the spin quantum number of each electron. On the other hand, the possible states $M_J = -J, -J+1, \ldots, +J$ for the projection of the total angular momentum $M_J = \sum_n (m_l + m_s)_n$, depend in general on

[11] Note that in general permutations of fermionic operators generate different quantum states, according to the anti-commutation relations given in Eq. (4.37).

the number n of electrons (Hund's rules) populating the ground state multiplet of the RE ion. The coefficients $C^{M_J}_{\mathbf{q}_1,\mathbf{q}_2\ldots\mathbf{q}_n}$ are combinations of the Clebsh-Gordan and Wigner coefficients which regulate the compatibility between the different representation for the quantum states of the electrons (this will be discuss more in the subsection below).

A trivial example of decomposition, giving a *unique* ten-electron many-body configuration, is the polarised $|M_J = J\rangle$ state of Ho^{3+}

$$|M_J = 8\rangle = \hat{f}^\dagger_{-3,\frac{1}{2}}\hat{f}^\dagger_{-2,\frac{1}{2}}\hat{f}^\dagger_{-1,\frac{1}{2}}\hat{f}^\dagger_{0,\frac{1}{2}}\hat{f}^\dagger_{1,-\frac{1}{2}}\hat{f}^\dagger_{1,\frac{1}{2}}\hat{f}^\dagger_{2,-\frac{1}{2}}\hat{f}^\dagger_{2,\frac{1}{2}}\hat{f}^\dagger_{3,-\frac{1}{2}}\hat{f}^\dagger_{3,\frac{1}{2}}|0\rangle \ . \tag{4.41}$$

Pr^{3+} provides a counter example, where the $|M_J = J\rangle$ polarised state is given by a *mixture* of two-electrons many-body states [30]:

$$\begin{aligned}|M_J = 4\rangle = \Bigg[&\sqrt{\frac{2}{165}}\hat{f}^\dagger_{3,\frac{1}{2}}\hat{f}^\dagger_{0,\frac{1}{2}} + \frac{1}{\sqrt{165}}\hat{f}^\dagger_{2,\frac{1}{2}}\hat{f}^\dagger_{1,\frac{1}{2}} \\ &- \frac{3}{\sqrt{110}}\left(\hat{f}^\dagger_{3,\frac{1}{2}}\hat{f}^\dagger_{1,-\frac{1}{2}} + \hat{f}^\dagger_{3,-\frac{1}{2}}\hat{f}^\dagger_{1,\frac{1}{2}}\right) + \frac{3}{\sqrt{11}}\hat{f}^\dagger_{3,-\frac{1}{2}}\hat{f}^\dagger_{2,-\frac{1}{2}}\Bigg]|0\rangle \ ,\end{aligned} \tag{4.42}$$

with the $C^4_{\mathbf{q}_1,\mathbf{q}_2}$ coefficients depending on the quantum numbers $\mathbf{q}_i = m_{l_i}, m_{s_i}$ for the two electrons $i = 1, 2$ in the f-shell of the trivalent praseodymium ion.

These examples help to illustrate the results obtained when expressing the $|M_J\rangle$ states in terms of fermionic operators acting on the vacuum. The complete list of the $|M_J\rangle$ states for Pr^{3+} in terms of superposition of two-body operators is given in Appendix B of Ref. [30]. For systems with more than two electrons, this becomes extremely cumbersome and the whole list cannot fit into few pages and would have very little use for the reader (for example $|M_J = 0\rangle$ in Ho^{3+} is a superposition of more than 40 different fermionic configurations!). Part of the original work carried out in this project consisted in writing a routine capable, by means of a computer algebra, of deriving the complete list of expansions in Eq. (4.40) for Ho^{3+} and Dy^{3+} [12].

4.3.2.1 Clebsch-Gordan coefficients and Wigner-Eckart theorem: a few tips for a routine to tackle them

The many-electron $|M_J\rangle$ states, as mentioned in Chapter 1, are an ideal set of states for systems where the Russell-Saunders is a good coupling scheme for the angular momenta. Obtaining a general expression for Eq. (4.40) is practically impossible, as the way in which the electrons combine depend on the Hund's rules and so on the specific system. As a part of the work carried out during the calculations discussed in the present chapter it revealed necessary to have a method which to derive the set of states in Eq. (4.40). For these it was not derived a general analytical expression, but a routine for a computer algebra capable of calculating all the states of a given RE^{3+} ion where the angular momenta J, L, S are conserved. As the procedure is extremely cumbersome, mainly because of the coding effort to implement the commutation relations between the operators, here we mention only in general how it has been tackled.

[12] Such routine can actually be applied to a large variety of magnetic systems.

The decomposition of the total angular momentum states as

$$|J, M_J\rangle = \sum_{M_L, M_S} C^{M_J}_{M_L, M_S} \, |L, M_L; S, M_S\rangle \,, \tag{4.43a}$$

with

$$C^{M_J}_{M_L, M_S} = \langle L, M_L; S, M_S | J, M_J \rangle \tag{4.43b}$$

Clebsch-Gordan coefficients, can be found in many textbooks [43, 64, 27, 28]. Not as immediate is the derivation for the decomposition

$$|L, M_L; S, M_S\rangle = \sum_{m_l, m_s} C^{M_L, M_S}_{m_l, m_s} \, |l, m_l; s, m_s\rangle_1 \otimes \cdots \otimes |l, m_l; s, m_s\rangle_n \tag{4.44a}$$

mainly because the $C^{M_L, M_S}_{m_l, m_s}$ are not simply Clebsch-Gordan coefficients but rather products of them which derives from the multiple combination of the possible electronic states.

The evaluation of the coefficients is extremely simplified by iterations performed with a computer algebra. More specifically we implemented a method which, summarising, exploits the Wigner-Eckart theorem. Such theorem, in general, allows the calculation for the matrix elements of a rank k (spherical) tensor operator $\hat{\mathbf{T}}^k$ between any two angular momentum states as

$$\langle j, m | T^k_q | j', m' \rangle = \langle j || T^k || j' \rangle \; C^{j,m}_{j', m'; k, q}, \tag{4.45}$$

where $C^{j,m}_{j', m'; k, q} = \langle j' m'; k q | j m \rangle$ are the Clebsch-Gordan coefficients [65] and the matrix element $\langle j || T^k || j' \rangle$ is independent on m, m'. It is important to note that here $|j\rangle$ and $|j'\rangle$ are in general different total angular momenta, which is also the case for the problem of calculating $\langle l, m_l; s, m_s | L, M_L; S, M_S \rangle$ in Eq. (4.44a). Practically, the WignerEckart theorem makes the action of a spherical tensor operator of rank k on an angular momentum eigenstate equivalent to the action of "adding" a single state with angular momentum k.

This allowed us to compute the quantum states of a RE^{3+} ion starting for example by Eq. (4.41) and applying iteratively the fermionic operators to "populate" the other $|M_J\rangle$ states . The non-zero Clebsch-Gordan coefficients, and a careful implementation of the anticommutation relations in Eq. (4.39) made the rest of the game in obtaining the correct decomposition of states.

4.3.3 The f-p hybridisation Hamiltonian in the many-body formalism

In the pyrochlores $RE_2TM_2O_7$ the bond distance RE-O1 (≈ 2.2 Å) is one of the shortest known for RE oxides [6]. This gives to the RE-site a strong axial symmetry leading to the local Ising anisotropy in spin ices, e.g. the ground state crystal-field doublet of Ho^{3+} ions in $Ho_2Ti_2O_7$ discussed in Chap.2. Furthermore, although the $4f$ electrons in RE ions are known for their localisation, the vicinity between the O1 and RE ions makes their hybridisation so strong that it is necessary to consider the tunnelling of electrons (or holes) between the two different ionic sites. However, since the $2p$ orbitals of the O1

site are all occupied with electrons there is no possibility to host any further electron coming from the RE $4f$ shell. Still, because the hybridisation mixes the orbitals of the two different sites, it is necessary to introduce an *exchange* interaction between the electrons at the O1 and RE-sites (it is as if the hybridisation "opens a channel" for correlations between electrons at sites that otherwise would be isolated with each other).

The Hamiltonian for the exchange between a $4f$ electron in a RE-site and a $2p$ electron in a neighbouring O1 site is prportional to

$$\begin{aligned}\left(\hat{h}^{\tau}_{\mathbf{R}+\mathbf{a_i}}\right)^{m,\mu}_{\sigma,\eta} =& \hat{f}^{\dagger}_{\mathbf{R}+\mathbf{a_i},m,\sigma}\,(\mathcal{R}^{\dagger}_{\mathbf{R}+\mathbf{a_i}})^{m,\mu}_{\sigma,\eta}\,\hat{p}_{\mathbf{R}+(1+\tau)\mathbf{a_i},\mu,\eta} \\ &+ \hat{p}^{\dagger}_{\mathbf{R}+(1+\tau)\mathbf{a_i},\mu,\eta}\,(\mathcal{R}_{\mathbf{R}+\mathbf{a_i}})^{\mu,m}_{\eta,\sigma}\,\hat{f}_{\mathbf{R}+\mathbf{a_i},m,\sigma}\,.\end{aligned} \tag{4.46}$$

This is the building-block for the f-p hybridisation in RE oxides in terms of the many-body formalism. The first term creates an electron with $m_l = m, m_s = \sigma/2$ at the RE-site $\mathbf{r} = \mathbf{R}+\mathbf{a_i}$ and annihilates one with $m'_l = \mu, m'_s = \eta/2$ at the O1 site $\mathbf{R}+(1+\tau)\mathbf{a_i}$; the second term, hermitian conjugate (h.c.) of the former, creates an electron with $m'_l = \mu, m'_s = \eta/2$ at the O1 site $\mathbf{R}+(1+\tau)\mathbf{a_i}$ and annihilates one with $m_l = m, m_s = \sigma/2$ at the RE-site $\mathbf{r} = \mathbf{R}+\mathbf{a_i}$. The quantities $\sigma, \eta = \pm$ are introduced as shorthand notation for the two possible states of the electron spin; analogously $\tau = -1, +1$ identifies respectively the primary ($\mathbf{R}$) and secondary ($\mathbf{R}+2\mathbf{a_i}$) O1 sites [13]. Hence Eq. (4.46) gives the single-electron exchange between a RE ion and one of its two neighbouring O1 ions. The Wigner matrix elements $(\mathcal{R}_{\mathbf{R}+\mathbf{a_i}})^{\mu,m}_{\eta,\sigma} = \langle\mu,\eta|\,\hat{R}_{\mathbf{R}+\mathbf{a_i}}\,|m,\sigma\rangle$ account for the local↔global rotations between the two different onsite representations of the electronic states (as discussed in Sec.4.2). For example the matrix $(\mathcal{R}^{\dagger}_{\mathbf{R}+\mathbf{a_i}})^{m,\mu}_{\sigma,\eta}$ transforms the representation from the global frame for $\hat{p}_{\mathbf{R}+(1+\tau)\mathbf{a_i},\mu,\eta}$ to the local one for $\hat{f}^{\dagger}_{\mathbf{R}+\mathbf{a_i},m,\sigma}$.

The Hamiltonian in Eq. (4.46) is a very general f-p exchange operator. In principle can act in any superposition of states of the RE-O1 system

$$\left\{\,|\mathrm{RE}\rangle_{\mathbf{R}+\mathbf{a_i}} \otimes |\mathrm{O1}\rangle_{\mathbf{R}+(1+\tau)\mathbf{a_i}}\,\right\}, \tag{4.47}$$

as long as the choice $\tau, \mathbf{R}, \mathbf{a_i}$ for the lattice sites is consistent. More exactly the f-p exchange Hamiltonian leads to the hybridisation only of orbitals hosting the electrons in their ground state and obeying the group symmetry $F_{d\bar{3}m}$. For the oxygens, Eq. (4.36) has already shown the unique many-electron state $|\Delta\rangle$ for the ground state of the O^{2-} ion with the $2p$ shell totally filled. For RE^{3+} ions, the crystal-field ground state in general depends on the specific compound. Nonetheless this is expressed in any case as a superposition of the $|M_J\rangle$ states known in terms of the fermionic operators acting on the RE-vacuum (e.g. see Eqs. (4.40-4.42)). Hence it is straightforward to compute the action of the exchange Hamiltonian in Eq. (4.46) on the states $|M_J\rangle \otimes |\Delta\rangle$, taking

[13] This is the same notation used in Ref. [30].

into account the anti-commutation relations from Eq. (4.37) for the $\hat{f}$ and $\hat{p}$ operators

$$\{\hat{f}_{\mathbf{q}_r}, \hat{f}^\dagger_{\mathbf{q}_s}\} = \delta_{\mathbf{q}_r,\mathbf{q}_s} \qquad \{\hat{p}_{\mathbf{q}_r}, \hat{p}^\dagger_{\mathbf{q}_s}\} = \delta_{\mathbf{q}_r,\mathbf{q}_s} \tag{4.48a}$$

$$\{\hat{f}_{\mathbf{q}_r}, \hat{f}_{\mathbf{q}_s}\} = 0 \qquad \{\hat{p}_{\mathbf{q}_r}, \hat{p}_{\mathbf{q}_s}\} = 0 \tag{4.48b}$$

$$\{\hat{f}^\dagger_{\mathbf{q}_r}, \hat{f}^\dagger_{\mathbf{q}_s}\} = 0 \qquad \{\hat{p}^\dagger_{\mathbf{q}_r}, \hat{p}^\dagger_{\mathbf{q}_s}\} = 0 \tag{4.48c}$$

with particular attention to the "mixed" ones giving

$$\{\hat{f}_{\mathbf{q}_r}, \hat{p}^\dagger_{\mathbf{q}_s}\} = \{\hat{f}_{\mathbf{q}_r}, \hat{p}_{\mathbf{q}_s}\} = \{\hat{f}^\dagger_{\mathbf{q}_r}, \hat{p}^\dagger_{\mathbf{q}_s}\} = 0\,, \tag{4.49}$$

since the two operators act on different lattice sites.

In the full hybridisation Hamiltonian, made from all the possible contributions of the terms in Eq. (4.46), some of the m-μ exchange channels are suppressed; the only non-zero amplitudes $V_{m,\mu}$ are those compatible with the local symmetries [14]. The f-p electron transfer along the local z axis of the RE ion allows only $m_l = -1, 0, 1$ as values for the orbitals of the electrons [15]. These correspond to the available types of f-p bonding for the orbital hybridisation:

- $pf\pi$ bonding ($m_l = -1$) between $f_{y(5z^2-\mathcal{R}^2)}$ in RE and p_y in O1;
- $pf\sigma$ bonding ($m_l = 0$) between $f_{z(5z^2-3\mathcal{R}^2)}$ in RE and p_z in O1;
- $pf\pi$ bonding ($m_l = 1$) between $f_{x(5z^2-\mathcal{R}^2)}$ in RE and the p_x in O1;

their amplitudes $V_{m,\mu} = V_{m_l}$ are given by two Slater-Koster parameters $V_{pf\sigma} = V_0$ and $V_{pf\pi} = V_{\pm 1}$ [66, 67]. The orbitals here are all expressed with respect to the local coordinates frames given in Eqs.(4.22) for the RE ions.

Then the full RE-O1 hybridisation Hamiltonian for the whole system is obtained by summing the single-exchange Hamiltonian in Eq. (4.46) over all lattice sites and all electron quantum numbers allowed by the symmetries:

$$\hat{H}_t = \sum_{\mathbf{R}\in\text{fcc}} \sum_{\tau=\pm} \sum_{m,\mu=0,\pm1} V_m \sum_{\sigma,\eta=\pm} \left(\hat{h}^\tau_{\mathbf{R}+\mathbf{a_i}}\right)^{m,\mu}_{\sigma,\eta}\,. \tag{4.50}$$

The Hamiltonian given in Eq.(16) of Ref. [30] for the Pr^{3+}-O1 hybridisation in pyrochlore systems $Pr_2TM_2O_7$ (where TM= Zr, Sn, Hf, and Ir) is equivalent to Eq. (4.50) together with Eq. (4.46), here discussed for a more general RE^{3+}-O1 hybridisation valid for all magnetic pyrochlores $RE_2TM_2O_7$. Since in these systems each O1 sits at the centre of a tetrahedral arrangement of RE^{3+} ions, then the hybridisation of the oxygen $2p$ orbitals involves all the four magnetic ions equally and introduces correlations between their electrons. Such mechanism leads to the superexchange between neighbouring magnetic ions mediated via the intermediate O1 ions sitting nearby. In the following a derivation of the effective super-exchange Hamiltonian in the many-body formalism is presented starting from the hybridisation discussed here.

[14] $V_{m,\mu}$ is the amplitude for the hybridisation between the m orbital of the RE f shell and the μ orbital of the O1 p shell.

[15] Note this does not imply any other selection rule for terms in the same Hamiltonian; neither $m = \mu$ nor $m \neq \mu$.

4.4 From f-p hybridisation to RE-RE superexchange

In the context of exchange interactions in magnetic pyrochlore oxides, this section discusses how a theoretical model for superexchange can be derived directly from the power expansion of the f-p hybridisation between the RE and the O1 ions. In short, the effective exchange between neighbouring magnetic sites in a $RE_2TM_2O_7$ system is due to the overlap of the (O1) oxygen p-orbitals with the surrounding f-orbitals of the RE ions. The physical and mathematical approach is the same as the one discussed in section 4.1, even if, rather than using the wave functions in Eq. (4.5), the theory is developed making use of the fermionic operators in Eqs. (4.48-4.49). The second-quantised formalism is preferred, not only for being more straightforward than deriving the global wave function for a system with more than two electrons, but also for being more suitable to tackle physical mechanisms, such as exchange, where undistinguishable particles are allowed to explore complex quantum states [16].

The following subsections present a derivation of the Hamiltonian for the exchange of electrons between neighbouring RE-sites. Starting from Ref. [30], where the Hamiltonian for the effective exchange between the RE-sites of a magnetic pyrochlore is given as the result of a *strong coupling* perturbation expansion in $V_{pf\sigma}$ and $V_{pf\pi}$ (see previous section), we consider a RE-O1-RE unit complex (see pictorial representation in Fig. 4.3) to study the contribution of the possible virtual paths given by different sequences of electron-hops between an O1 oxygen and two of the RE-sites nearby (Fig. 4.5 and Fig. 4.6 show respectively the second and fourth-order processes for a RE-O1-RE unit). Only virtual paths with even powers give observable contributions; the odd ones produce new states which would correspond to rearrangements of electrons across the lattice that are not compatible with the stoichiometry of the compound.

4.4.1 Setting up the perturbation expansion

The energy scales of the perturbation expansions are parametrised in terms of four quantities characterising the virtual paths made by the electrons. These are U, the Coulomb energy for the repulsion of any two electrons on the same RE-site, Δ, the change in energy for the RE-O1-RE system if an electron is removed from the O1 site, and $V_{pf\sigma}, V_{pf\pi}$, the energy terms for the hybridisation of the orbitals.

The hybridisation between the $4f$ orbitals of a RE ion and the $2p$ orbitals of an O1 ion couples the f^n ground state with the $f^{n\pm1}$ virtual states; for the RE-site these correspond to the virtual acquisition (f^{n+1}) and ejection (f^{n-1}) of one electron (see Fig. 4.4). The local Coulomb repulsion between electrons increases with their number, hence the access to a virtual state $f^{n\pm1}$ depends on the energy cost of the local RE-O1-RE system with respect to the total (of the same unit) ground-state energy. If U is the average energy for the Coulomb interaction between any two electrons in the $4f$-shell of a fixed RE^{3+} ion, then if the shell hosts n electrons we have

$$E(n) = \frac{n(n-1)}{2}U\,. \tag{4.51}$$

[16] These can be derived from the admixtures of single-body wave functions. For example the hybridisation in Eq. (4.46) is an operator which produces hybridised quantum states when applied to the kets in Eq. (4.47) of the RE-O1 composite system.

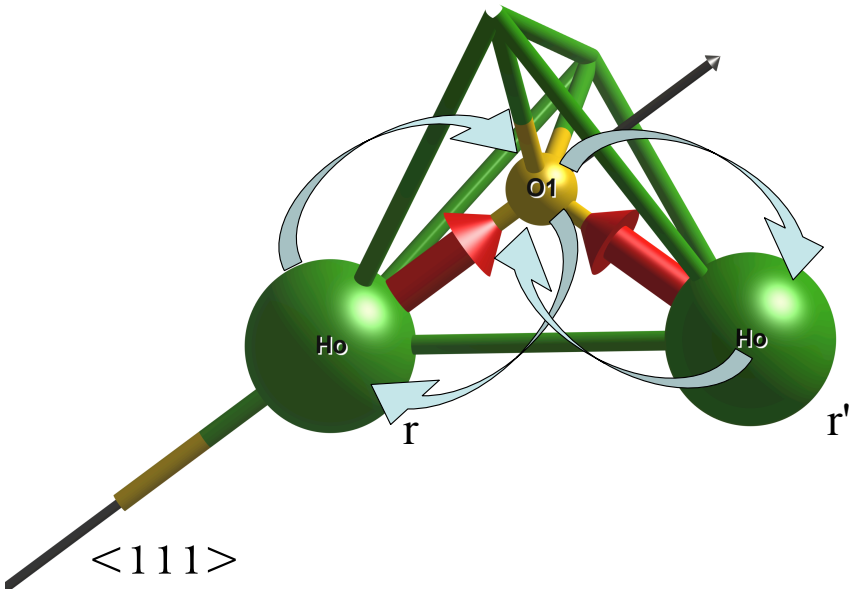

Figure 4.3: Pictorial representation of the superexchange of electrons between two neighbouring RE ions in a pyrochlore oxide. The (fully) green tubes represent the edges of the tetrahedron hosting the RE ions (green spheres); only two of them are shown sitting in r and r' coordinates, vertices of a tetrahedron of the pyrochlore lattice. The red arrows account for the orientation of the magnetic moments localised on the RE-sites (pointing inward the tetrahedron in in this case, i.e. with positive polarisation along their respective quantisation axes in Eq. (4.22)). The light-blue curly arrows mimic the four consecutive virtual hops of one electron across a RE-O1-RE unit.

This is the local Coulomb (repulsive) energy associated to a configuration of the magnetic electrons in a RE-site $\mathbf{r}$. The total energy for the ground state $\mathrm{f}_{\mathrm{r}}^{n}\mathrm{p}_{\mathrm{O1}}^{6}\mathrm{f}_{\mathrm{r}'}^{n}$ of a RE-O1-RE unit is given by

$$E(n) + 6\Delta + E'(n) = n(n-1)U + 6\Delta\,, \tag{4.52}$$

where both RE-sites, $\mathbf{r}$ and $\mathbf{r}'$, have the same number n of electrons and Δ is an estimation for the energy of the six non-magnetic electrons on the O1 site with respect to the $E(n)$ energy level of the RE. Analogously, for a virtual state the total energy is obtained by counting the number of electrons on the different sites of the RE-O1-RE system; for example $\mathrm{f}_{\mathrm{r}}^{n+1}\mathrm{p}_{\mathrm{O1}}^{5}\mathrm{f}_{\mathrm{r}'}^{n}$ is a virtual state with energy

$$E(n+1) + 5\Delta + E'(n) = n^2U + 5\Delta\,, \tag{4.53}$$

that is $\delta E = nU - \Delta$ above the ground state in Eq. (4.52). The difference in energy between a given state and the ground state gives the weight regulating the contribution of the different virtual states resulting from the perturbative power expansion.

These methods can be used to study the virtual processes of the n electrons between the RE^{3+} ions and the O1 oxygens in any $\mathrm{RE_2TM_2O_7}$ system. They also include the case of the Praseodymium zirconate and stannate in Ref. [30] where there are only $n = 2$ electrons in the 4-f shell of the Pr^{3+} ion. To make the calculation simpler it is

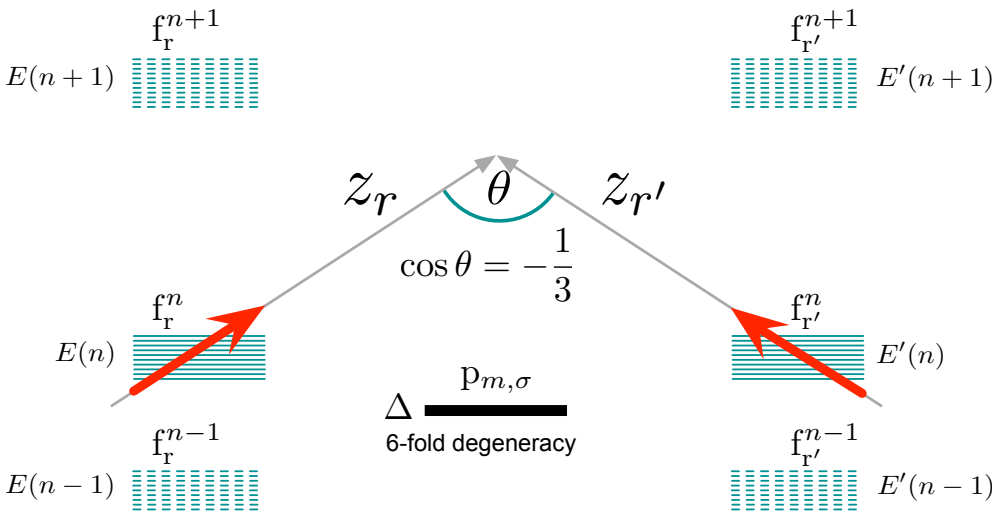

Figure 4.4: Generalisation of Fig.2 in Ref. [30] for a magnetic pyrochlore system of RE^{3+} ions with n electrons in the f shells. It represents the local energy level scheme for f and p electrons of a RE-O1-RE unit. The local quantisation axes z_r and $z_{r'}$ are shown to indicate the spins corresponding to the stable f^n electronic configurations. The green horizontal lines, behind the red arrows indicating the spins, illustrate the energy levels due to the n electrons in the RE^{3+} ions (here there are ten lines as example for the $n = 10$ electrons in the $4f$ shell of Ho^{3+}). The dotted lines above and below represent the energies of the virtual states when an electron is respectively added $(n+1)$ or removed$(n-1)$ in the RE-site.

convenient to rewrite the Hamiltonian in Eq. (4.46) as

$$\hat{h} = \hat{f}^\dagger_{m,\sigma} (\mathcal{R}^\dagger)^{m,\mu}_{\sigma,\eta} \hat{p}_{\mu,\eta} + \hat{p}^\dagger_{\mu,\eta} (\mathcal{R})^{\mu,m}_{\eta,\sigma} \hat{f}_{m,\sigma} \,, \tag{4.54}$$

where the position indices have been dropped since every RE-O1-RE unit always involves only one O1 site for each couple of n.n. RE-ions. The product of p terms

$$\hat{\tilde{h}}^{(p)} = \sum_{\substack{\mu_1,\mu_2,\ldots\mu_p=0,\pm1 \\ \eta_1,\eta_2,\ldots\eta_p=\pm}} \langle\Delta| \left(V_m \hat{h}\right)_1 \left(V_m \hat{h}\right)_2 \ldots \left(V_m \hat{h}\right)_p |\Delta\rangle \tag{4.55}$$

constitutes the main *building-block* for any order of expansion of the hybridisation Hamiltonian. In Eq. (4.55), the sum over the quantum numbers $\{\mu_i, \eta_i\}$ of the electrons in the oxygen state $|\Delta\rangle$ in Eq. (4.36) leaves only a operators acting on the RE-sites. These are made explicit only after such product is expanded in all of its terms, because the labels $\mathbf{r}$ and $\mathbf{r}'$ for the n.n. RE-sites of the same RE-O1-RE unit have to be given to the $\hat{f}$ operators only when it is time to rearrange them according to the commutation relations. The commutation relations on the lattice sites, Eqs. (4.48-4.49), imply that in general each labelling leads to a different combination of operators.

4.4.1.1 The standard procedure to derive the observables of a given order

i) Make the product of an even number of terms $V_m \hat{h}$ as in Eq. (4.55);

ii) after expanding the product, sum over the quantum numbers allowed for the electrons in the O1 orbitals (this leaves only the $\hat{f}$ operators acting on the RE-sites);
iii) label the $\hat{f}$ operators, with indices $\mathbf{r}$ and $\mathbf{r}'$, according to the virtual paths (Fig. 4.5 and Fig. 4.6 are useful respectively for the second and fourth-order powers of the expansion);
iv) assign the weight for each path according to the virtual energies spanned by the electrons;
v) rearrange the operators and remove the spurious terms (those, for example, with order lower than four in the 4-th order expansion for superexchange).

Before discussing the two different cases of the second and fourth-order terms for the $RE_2TM_2O_7$ compounds it is recommended to read first Appendix B.1; here a brief introduction of exchange and effective magnetic interaction is given in a more general context than 4.1.1. Following mainly Ref. [58], this is done using many-body fermionic operators to represent only the electrons of the magnetic sites without considering the underlying structure of the ligands of a real compounds. This kind of approach discusses and justifies the use of a strong coupling perturbation theory for the magnetic pyrochlore oxides from the more general perspective of systems with strongly correlated electrons. Being a less complex model, namely the one-band Hubbard model, where the local electrons on the non-magnetic ions are not considered, it also simplifies the understanding of the diagrams for the virtual processes, with characteristic paths and energies, considered in the following subsections 4.4.2-4.4.3. For the reader familiar with the topics discussed in Appendix B.1, the suggestion is to read directly the following two subsections after a look at Fig. B.1 which could help as a simple comparison to Fig. 4.5 and Fig. 4.6.

4.4.2 The second-order: a correction to the CF states

The second-order of perturbation in $V_{pf\sigma}, V_{pf\pi}$ produces non-vanishing effects for the RE ions. Although these are trivial and lead only to a renormalisation of the CF parameters without any explicit contribution to the effective magnetic interactions, they also represent a simpler example of the perturbative effects, compared to the exchange ones presented in the next subsection (4.4.3).

Starting form the ground state configuration $\mathrm{f}_{\mathrm{r}}^{n}\mathrm{p}_{\mathrm{O1}}^{6}\mathrm{f}_{\mathrm{r}'}^{n}$ of a RE-O1-RE unit, a double iteration of the hybridisation Hamiltonian ($p = 2$ in Eq. (4.55)) takes the system back to the same ground state only when applied both times on the same RE-site (either $\mathbf{r}$ or $\mathbf{r}'$). This is because, in contrast to the one-band Hubbard model, briefly discussed in Appendix B.1, the kinetic part of the Hamiltonian here acts on two different kinds of sub-lattice; one, magnetic, for the RE ions, the other, non-magnetic, for the O1 ions. Consequently each application of the hybridisation Hamiltonian consist in the hopping of one electron between the oxygen and only one of the RE-sites of the RE-O1-RE unit. On the other hand the kinetic term in the Hubbard Hamiltonian acts directly on two magnetic sites, so that electrons hop from one (magnetic) site to the other already at the first order; from this a second order perturbation introduces exchange interactions[58]. The first non-trivial effects from the perturbation in $V_{pf\sigma}, V_{pf\pi}$ appears at the fourth order discussed in the next subsection (4.4.3).

The diagram in Fig. 4.5 shows the total electronic state of a RE-O1-RE system evolv-

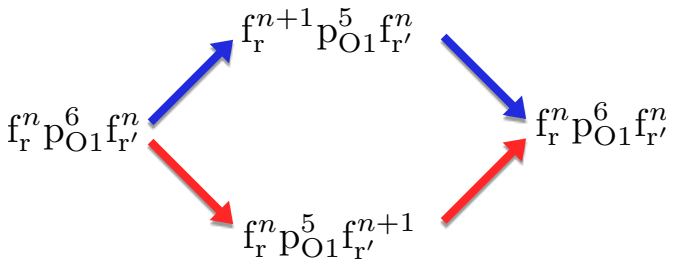

Figure 4.5: Schematic representation of the virtual electron-hops between the f-orbitals of the RE ions and the p-orbitals of the O1 ion. From left to right, the virtual processes consist in the hop of one electron from the oxygen to only one of the two RE ions of the RE-O1-RE unit; then another hop back from the same RE to the same O1. Here the blue arrows indicate the electron-hops between the RE-site $\mathbf{r}$ and O1; the red ones indicate the electron-hops between the same O1 and the other RE-site $\mathbf{r}'$. Each path, upper blue and lower red, leads to the renormalisation of the local CF parameters, for the magnetic ions in $\mathbf{r}$ and $\mathbf{r}'$ respectively .

ing under the twofold application of the hybridisation Hamiltonian. Starting from the ground state, $f_r^n p_{O1}^6 f_{r'}^n$, the system accesses only one of the two virtual states allowed, $f_r^{n+1} p_{O1}^5 f_{r'}^n$ or $f_r^n p_{O1}^5 f_{r'}^{n+1}$, and goes back to an equivalent ground state. Note that the spin-degrees of freedom are not considered in Fig. 4.5. The virtual hopping of electrons in this schematic representation does not involve any quantum number explicitly. These, however, need to be taken into account in the following analytical calculation.

The second-order building-block

According to the procedure summarised in the previous subsection, we first write down the building-block terms obtained from Eq. (4.55) for the second order of perturbation

$$\begin{aligned}\hat{\tilde{h}}^{(2)} &= \sum_{\substack{\mu_1,\mu_2=0,\pm1\\ \eta_1,\eta_2=\pm}} \langle\Delta|\left(V_m\hat{h}\right)_1\left(V_m\hat{h}\right)_2|\Delta\rangle \\ &= V_{m_1}V_{m_2}\sum_{\substack{\mu_1,\mu_2=0,\pm1\\ \eta_1,\eta_2=\pm}} \langle\Delta|\Big(\cancel{\hat{f}^\dagger_{m_1,\sigma_1}(\mathcal{R}^\dagger)^{m_1,\mu_1}_{\sigma_1,\eta_1}\hat{p}_{\mu_1,\eta_1}} + \hat{p}^\dagger_{\mu_1,\eta_1}(\mathcal{R})^{\mu_1,m_1}_{\eta_1,\sigma_1}\hat{f}_{m_1,\sigma_1}\Big) \\ &\qquad\times\Big(\hat{f}^\dagger_{m_2,\sigma_2}(\mathcal{R}^\dagger)^{m_2,\mu_2}_{\sigma_2,\eta_2}\hat{p}_{\mu_2,\eta_2} + \cancel{\hat{p}^\dagger_{\mu_2,\eta_2}(\mathcal{R})^{\mu_2,m_2}_{\eta_2,\sigma_2}\hat{f}_{m_2,\sigma_2}}\Big)|\Delta\rangle\end{aligned} \tag{4.56}$$

where the outer terms have already been cancelled because of the action of the $\hat{p}$ operators on the 2-p filled shell of the oxygen ($\langle\Delta|\hat{p}_{\mu_1,\eta_1}=0$ and $\hat{p}^\dagger_{\mu_2,\eta_2}|\Delta\rangle=0$ from Eq. (4.36)). Whence, Eq. (4.56) is simplified to

$$\hat{\tilde{h}}^{(2)} = V_{m_1}V_{m_2}\sum_{\substack{\mu_1,\mu_2=0,\pm1\\ \eta_1,\eta_2=\pm}} \langle\Delta|\Big(\hat{p}^\dagger_{\mu_1,\eta_1}(\mathcal{R})^{\mu_1,m_1}_{\eta_1,\sigma_1}\hat{f}_{m_1,\sigma_1}\times\hat{f}^\dagger_{m_2,\sigma_2}(\mathcal{R}^\dagger)^{m_2,\mu_2}_{\sigma_2,\eta_2}\hat{p}_{\mu_2,\eta_2}\Big)|\Delta\rangle \tag{4.57}$$

which, making use of the commutation relations for different lattice sites in Eq. (4.49), can be reordered as

$$\hat{\tilde{h}}^{(2)} = V_{m_1} V_{m_2} \hat{f}_{m_1,\sigma_1} \hat{f}^{\dagger}_{m_2,\sigma_2} \sum_{\substack{\mu_1,\mu_2=0,\pm1 \\ \eta_1,\eta_2=\pm}} \langle\Delta|\, \hat{p}^{\dagger}_{\mu_1,\eta_1} \hat{p}_{\mu_2,\eta_2} \,|\Delta\rangle\, (\mathcal{R}^{\dagger})^{m_2,\mu_2}_{\sigma_2,\eta_2} (\mathcal{R})^{\mu_1,m_1}_{\eta_1,\sigma_1} , \tag{4.58}$$

where the $\hat{f}$ operators do not depend on the indices of summation.

Now the $\hat{p}$ operators act directly on the oxygen state $|\Delta\rangle$ in Eq. (4.36), hence, from the equivalence

$$\begin{aligned}
&\sum_{\substack{\mu_1,\mu_2=0,\pm1 \\ \eta_1,\eta_2=\pm}} \langle\Delta|\, \hat{p}^{\dagger}_{\mu_1,\eta_1} \hat{p}_{\mu_2,\eta_2} \,|\Delta\rangle\, (\mathcal{R}^{\dagger})^{m_2,\mu_2}_{\sigma_2,\eta_2} (\mathcal{R})^{\mu_1,m_1}_{\eta_1,\sigma_1} \\
&= \sum_{\substack{\mu_1,\mu_2=0,\pm1 \\ \eta_1,\eta_2=\pm}} \langle\Delta|\, \hat{n}^{\dagger}_{\mu_1,\eta_1} \,|\Delta\rangle\, \delta_{\mu_1,\mu_2}\delta_{\eta_1,\eta_2} (\mathcal{R}^{\dagger})^{m_2,\mu_2}_{\sigma_2,\eta_2} (\mathcal{R})^{\mu_1,m_1}_{\eta_1,\sigma_1} \\
&= \sum_{\substack{\mu_1,=0,\pm1 \\ \eta_1,=\pm}} \langle\Delta|\, \hat{n}^{\dagger}_{\mu_1,\eta_1} \,|\Delta\rangle\, (\mathcal{R}^{\dagger})^{m_2,\mu_1}_{\sigma_2,\eta_1} (\mathcal{R})^{\mu_1,m_1}_{\eta_1,\sigma_1} \\
&= (\mathcal{R}^{\dagger}\mathcal{R})^{m_2,m_1}_{\sigma_2,\sigma_1} ,
\end{aligned} \tag{4.59}$$

Eq. (4.58) can be simplified to the following form:

$$\hat{\tilde{h}}^{(2)} = V_{m_1} V_{m_2}\, \hat{f}_{m_1,\sigma_1} \hat{f}^{\dagger}_{m_2,\sigma_2} (\mathcal{R}^{\dagger}\mathcal{R})^{m_2,m_1}_{\sigma_2,\sigma_1} . \tag{4.60}$$

The second-order effective Hamiltonian

Now if the two operators act on different sites, e.g. $\mathbf{r}$ and $\mathbf{r}'$, then $\hat{f}_{\mathbf{r},m_1,\sigma_1} \hat{f}^{\dagger}_{\mathbf{r}',m_2,\sigma_2} = -\hat{f}^{\dagger}_{\mathbf{r}',m_2,\sigma_2} \hat{f}_{\mathbf{r},m_1,\sigma_1}$, which means having an operator that annihilates an electron on site $\mathbf{r}$ and creates one on the other site $\mathbf{r}'$. This implies a real charge transfer which would take the RE-O1-RE unit out of its local ground state configuration. Hence this choice of site-labelling cannot be allowed to this order of perturbation; it would correspond to alternating the colours of the arrows (blue/red and red/blue) in Fig. 4.5.

In contrast, if both operators in Eq. (4.58) act only on one of the two sites the system returns to its initial ground state; this corresponds to the virtual processes shown in Fig. 4.5. The upper path, with blue arrows, corresponds to acting only on the RE-site $\mathbf{r}$ both times; the lower one, with red arrows, corresponds to acting only on $\mathbf{r}'$, the other one of the same RE-O1-RE unit. The two paths are equivalent because of the symmetries of the system (they also have the same energy above the ground state level; see Eq. (4.53)). In both cases the original ground state is recovered. Whence the effective Hamiltonian from the second order effect of the hybridisation is

$$\hat{h}^{2nd}_{eff} = \frac{2}{nU - \Delta} V_{m_1} V_{m_2} \left(1 - \hat{f}^{\dagger}_{m_2,\sigma_2} \hat{f}_{m_1,\sigma_1}\right) (\mathcal{R}^{\dagger}\mathcal{R})^{m_2,m_1}_{\sigma_2,\sigma_1} . \tag{4.61}$$

where the anti-commutation relations are now different for operators acting on the same site. This is given for a RE^{3+} ion with n electrons in the $4f$ shell; the dependence on

the RE considered is explicit in the energy weight given by the inverse of $nU - \Delta$,being the energy gap between the virtual states, Eq. (4.53), and the ground state, Eq. (4.52). The factor 2 in the numerator account for the equivalence of the two paths.

Being localised only in one of the two RE-sites of each unit at a time, the effects of the second order correspond to a renormalisation of the CF parameters obtained from the point charge model where no contribution of the ligands, i.e. hybridisation of orbitals, is estimated. The Hamiltonian in Eq. (4.61) has to be considered in one RE-site at a time, hence separately in $\mathbf{r}$ and $\mathbf{r}'$ for the same RE-O1-RE unit. In the case of study such renormalisation would be redundant since the CF parameters have been extrapolated by means of a fitting to neutron scattering (see Chap.2).

If compared to the 2nd order of perturbation in the strong-coupling limit of the one-band Hubbard model, Eq. (4.61) gives an odd result. In the latter case (briefly discussed in Appendix B.1) the second order already produces effective magnetic interactions due to exchange between the magnetic sites, while the former one only introduces local renormalisation of the single ion physics. For clarification it is useful to compare Fig. 4.5 and Fig. B.1 where it is evident that the sequence of arrows defining the two virtual paths have different colours: blue-blue (top) and red-red (bottom) for the RE pyrochlores (readjusting the CF parameters), while blue-red (top) and red-blue (bottom) for the Hubbard model (leading to exchange). The repetition of colours in the former reflects the action localised only on one of the two magnetic sites of the RE-O1-RE unit, i.e. the reason for having only a correction to the local CF parametrisation. In contrast, the latter case has blue and red arrows in each path indicating that the action of the perturbative operators is on both sites in any case. Hence to have effective exchange coupling between different RE-sites it is necessary to have a Hamiltonian which i) annihilates an electron on one magnetic site and recreates it on the other one (now there are virtually two electrons on one site and no electrons in the other, this costs an energy U to the system); ii) annihilates one of the two electrons occupying the same virtual state and recreates it on the empty site. This is the only one way to have exchange between electrons and also maintain the same ground state configuration, or equivalent, allowed by the hybridisation Hamiltonian.

In the following subsection 4.4.3, using a similar approach, it is shown [17] how the fourth order power in Eq. (4.55) opens up a wider range of virtual paths for the electron-hops. This leads to an effective magnetic interaction between the total angular momenta of two neighbouring RE ions.

4.4.3 The fourth-order: leading terms for superexchange

The fourth order in $V_{pf\sigma}, V_{pf\pi}$ is the first one giving non trivial effects for the magnetic interaction between neighbouring RE-sites of a pyrochlore oxide $RE_2TM_2O_7$. This subsection is a summary of the calculation to derive a superexchange Hamiltonian starting from the hybridisation Hamiltonian in Eqs. (4.54-4.55). Such derivation is presented explicitly for the first time in this thesis as in Ref. [30] no analytical details about this derivation are given [18]. The work of Onoda et al in Ref. [30] is focused on

[17] More details on the calculation are given in Appendix B.2.

[18] Onoda et al. give directly the Hamiltonian in Eq.(17) of Ref. [30], for the exchange of electrons between the RE-sites of a RE-O1-RE unit, as an immediate consequence of the hybridisation Hamiltonian

magnetic pyrochlores that are good candidates as *quantum* spin ices; there the quantum mechanics of the single ions physics is not strong compared to the quantum features arising from the spin-spin coupling between the RE ions. This kind of systems have magnetic ions which do not possess the Ising like anisotropy of the spin ices This is because of the coupling between the local CF environment and the small size of the dipole moment of the magnetic ions.

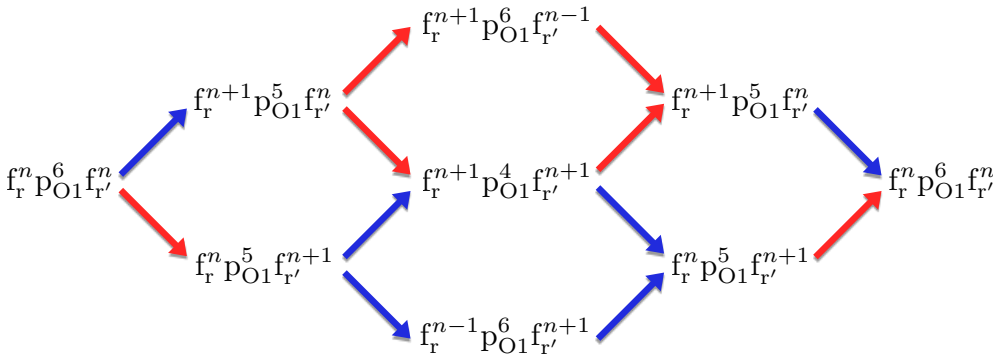

Figure 4.6: Generalisation of Fig.3(b) in Ref. [30] for a RE^{3+} ions with n electrons in the f-shell. It gives a schematic representation of the virtual paths of the electrons exchanged between two RE^{3+} ions, in $\mathbf{r}$ and $\mathbf{r'}$, via an intermediate O1 site.Each configuration $f_r p_{O1} f_{r'}$ describes the composite electron system of the three sites together: for example $f_r^n p_{O1}^6 f_{r'}^n$ is the ground-state configuration, with n electrons on each of the RE-sites and 6 on the oxygen one (this is the same configuration both at the beginning and at the end since the system has to return to its original state after exploring the intermediate virtual states). The total number of electrons is conserved, but the intermediate configurations can have different electrons on the different sites. There are 6 possible paths which are shown separately in Fig. 4.7 and Fig. 4.8. Notice that any of the paths has the same exchange mechanisms: two $r \leftrightarrow$ O1 (blue arrows) and two $r' \leftrightarrow$ O1 (red arrow).

On the other hand, since spin ices have been considered exclusively as classical systems, it is essential to understand, and ideally quantify, the quantum physics occurring at a single ion level. Once again this is extremely relevant for studying the low temperature dynamics (e.g. monopole hopping) which otherwise would be totally frozen in a purely classical system. Because of this it has been necessary to reconsider the approach proposed by Onoda in Ref. [30] for a $RE_2TM_2O_7$ system with Pr^{3+} ions (with only two electrons on the 4-f shell), and generalise it so that it could grasp the physics relevant also for "classical" systems such as $Ho_2Ti_2O_7$ and $Dy_2Ti_2O_7$. Since the mathematical procedure to derive the Hamiltonian for the effective exchange from the fourth order in $V_{pf\sigma}, V_{pf\pi}$ is rather cumbersome, most of the details are left in Appendix B.2. The following is a summary of these calculations whose main steps are described by means of the diagrams in Figs. 4.6-4.8, in analogy with the method used for the simpler second order case in subsection 4.4.2.

The diagram in Fig. 4.6 shows the total electronic configuration of a RE-O1-RE system exploring the intermediate states allowed by the fourth order virtual processes found by means of the hybridisation Hamiltonian (taking $p = 4$ in Eq. (4.55)). Analogously to the second order case, the virtual paths start with an electron hopping from the oxygen

in Eq. (4.50) (Eq.(16) in Ref. [30]) without providing any mathematical discussion about it.

ion of the ground state configuration $\mathrm{f}_{\mathrm{r}}^{n}\mathrm{p}_{\mathrm{O1}}^{6}\mathrm{f}_{\mathrm{r}'}^{n}$ to one of the two RE-sites (first arrows, blue and red, from the left in Fig. 4.6); being at the fourth order, the system can now explore more virtual states than the two allowed at the second order (Fig. 4.5). The constraint is again to recover an equivalent ground state allowed by the local Hund's rules at the end of any virtual process. In contrast to the second order case, each fourth order path has three intermediate virtual states, rather than just one, before the RE-O1-RE unit recovers the initial configuration. The possible six paths in Figs. 4.6 are shown separately in Fig. 4.7 and Fig. 4.8 to help visualising the different contribution associated to each one. To each intermediate step an energy cost is associated; this depends on the reshuffling of the $2n+6$ electrons among the three sites of the RE-O1-RE system where the virtual exchange takes place. Because of these energies, each path is characterised by a weight which depends on the energetic cost to access the three intermediate virtual states starting from the ground state. In short, the sequence of intermediate configurations for the various paths defines the energy cost of the virtual processes. The arrangement of the paths, shown separately in Fig. 4.7 and Fig. 4.8, highlights the equivalence between **(a)**, **(b)**, **(c)** and **(a′)**, **(b′)**, **(c′)** respectively. Since the distinction of the two groupings of diagrams arises from the RE-site involved in the first hop of each path (**r**, blue arrow, for the former diagrams while **r′**, red arrow, for the latter ones) the respective virtual processes must be equivalent for symmetry reasons deriving from the equivalence of the two RE-sites of the same RE-O1-RE unit[19].

The fourth-order building-block

In analogy with the procedure used for the second order case, to derive the contribution of the fourth order terms, the first step consists in expanding the product of the Hamiltonian in Eq. (4.55) for $p=4$

$$\hat{\tilde{h}}^{(4)} = \sum_{\substack{\mu_1,\mu_2,\mu_3,\mu_4=0,\pm1 \\ \eta_1,\eta_2,\eta_3,\eta_4=\pm}} \langle\Delta| \left(V_m\hat{h}\right)_1 \left(V_m\hat{h}\right)_2 \left(V_m\hat{h}\right)_3 \left(V_m\hat{h}\right)_4 |\Delta\rangle \ , \tag{4.62}$$

which, taking into account the action of the $\hat{p}$ operators on the states $|\Delta\rangle$ (see Eqs. (B.10-B.12) in Appendix B), leads to the following expression

$$\begin{aligned}\hat{\tilde{h}}^{(4)} = V_{m_1}V_{m_2}V_{m_3}V_{m_4} & \\ \times\Bigg[& \hat{f}_{m_1,\sigma_1}\hat{f}^{\dagger}_{m_2,\sigma_2}\hat{f}_{m_3,\sigma_3}\hat{f}^{\dagger}_{m_4,\sigma_4} \left(\mathcal{R}^{\dagger}\mathcal{R}\right)^{m_2,m_1}_{\sigma_2,\sigma_1}\left(\mathcal{R}^{\dagger}\mathcal{R}\right)^{m_4,m_3}_{\sigma_4,\sigma_3} \\ & + \hat{f}_{m_1,\sigma_1}\hat{f}_{m_2,\sigma_2}\hat{f}^{\dagger}_{m_3,\sigma_3}\hat{f}^{\dagger}_{m_4,\sigma_4}\Bigg(\left(\mathcal{R}^{\dagger}\mathcal{R}\right)^{m_3,m_2}_{\sigma_3,\sigma_2}\left(\mathcal{R}^{\dagger}\mathcal{R}\right)^{m_4,m_1}_{\sigma_4,\sigma_1} \\ & \qquad - \left(\mathcal{R}^{\dagger}\mathcal{R}\right)^{m_3,m_1}_{\sigma_3,\sigma_1}\left(\mathcal{R}^{\dagger}\mathcal{R}\right)^{m_4,m_2}_{\sigma_4,\sigma_2}\Bigg)\Bigg]\end{aligned} \tag{4.63}$$

where only the $\hat{f}$ operators and the rotation matrices for the angular momentum quantum numbers of the RE ions are left. At this stage the ordering of the $\hat{f}$ operators reflects the order of the product in Eq. (4.62); the operators will be rearranged af-

[19] This is shown algebraically in section B.2 of Appendix B.

terwards depending on the labelling of the position indices within a given RE-O1-RE system. The commutation relations in Eq. (4.48) will characterise the arrangement of the operators and will determine the action of the rotation matrices associated to the 4th order terms.

In the second order case it has been found that only two virtual paths are allowed by the labelling of the RE-sites of a given RE-O1-RE system (**r**-**r** and **r′**-**r′** respectively for the blue-blue and the red-red paths in Fig. 4.5). In the fourth order, six different sequences are allowed for the virtual electron-hops recovering the initial $\mathrm{f_r p_{O1} f_{r'}}$ ground state. Now the labelling will give an effective magnetic interaction between two RE-sites because each path in Fig. 4.6 corresponds to a Hamiltonian, derived from Eq. (4.63), where two $\hat{f}$ operators act on the sites **r** and two on the sites **r′** of a given RE-O1-RE unit. Before proceeding with the labelling of the operators it is convenient make the notation for the indices shorter by using **i** for the quantum numbers m_i, σ_i of an electron on the RE-site **r**. Then Eq. (4.63) can be written as

$$\begin{aligned}\hat{\tilde{h}}^{(4)} = V_1V_2V_3V_4\Big[&\hat{f}_{\mathbf{1}}\,\hat{f}^{\dagger}_{\mathbf{2}}\,\hat{f}_{\mathbf{3}}\,\hat{f}^{\dagger}_{\mathbf{4}}\,(\mathcal{R}^{\dagger}\mathcal{R})_{\mathbf{2},\mathbf{1}}\,(\mathcal{R}^{\dagger}\mathcal{R})_{\mathbf{4},\mathbf{3}}\\ &+\hat{f}_{\mathbf{1}}\,\hat{f}_{\mathbf{2}}\,\hat{f}^{\dagger}_{\mathbf{3}}\,\hat{f}^{\dagger}_{\mathbf{4}}\Big((\mathcal{R}^{\dagger}\mathcal{R})_{\mathbf{3},\mathbf{2}}\,(\mathcal{R}^{\dagger}\mathcal{R})_{\mathbf{4},\mathbf{1}}-(\mathcal{R}^{\dagger}\mathcal{R})_{\mathbf{3},\mathbf{1}}\,(\mathcal{R}^{\dagger}\mathcal{R})_{\mathbf{4},\mathbf{2}}\Big),\Big]\end{aligned} \tag{4.64}$$

where the labels for the RE-sites have not been introduced yet. Adding the labelling to distinguish the action of the f operators on the RE-sites, is necessary to determine the contribution of the different paths (see Figs. 4.7-4.8 for the diagrams decomposing the possible paths of Fig. 4.6). Now the operator $\hat{f}_{\mathbf{r},m_i,\sigma_i}$ will be represented as $\hat{f}_{\mathbf{i}}$ while $\hat{f}_{\mathbf{r'},m_i,\sigma_i}$, acting on the other site **r′** of the RE-O1-RE unit, will be $\hat{f}_{\mathbf{i'}}$.

The fourth-order effective Hamiltonian

From Eq. (4.64) it is possible to extrapolate the contribution for the virtual paths in Fig. 4.6 which are given separately in Fig. 4.7 and Fig. 4.8. Each virtual path is characterised by the labelling of the operators in the product of Eq. (4.62) [20] and by the total weight due to the energies of the intermediate states. In analogy with the 2nd order case in Eq. (4.61), these weights for the various paths are found considering the energy gap between the intermediate virtual energies (here there are more than just two)

$$\begin{aligned}n^2U+5\Delta \quad &\text{for} \quad \mathrm{f_r^{n+1}p_{O1}^5f_{r'}^n} \quad \text{and} \quad \mathrm{f_r^n p_{O1}^5 f_{r'}^{n+1}}\\ (n^2-n+1)U+6\Delta \quad &\text{for} \quad \mathrm{f_r^{n+1}p_{O1}^6f_{r'}^{n-1}} \quad \text{and} \quad \mathrm{f_r^{n-1}p_{O1}^6f_{r'}^{n+1}}\\ (n^2+n)U+4\Delta \quad &\text{for} \quad \mathrm{f_r^{n+1}p_{O1}^4f_{r'}^{n+1}}\end{aligned} \tag{4.65}$$

and the ground state energy

$$(n^2-n)U+6\Delta \quad \text{for} \quad \mathrm{f_r^n p_{O1}^6 f_{r'}^n} \tag{4.66}$$

[20] The ordering of the operators in Eq. (4.64) is kept fixed with respect to Eq. (4.62).

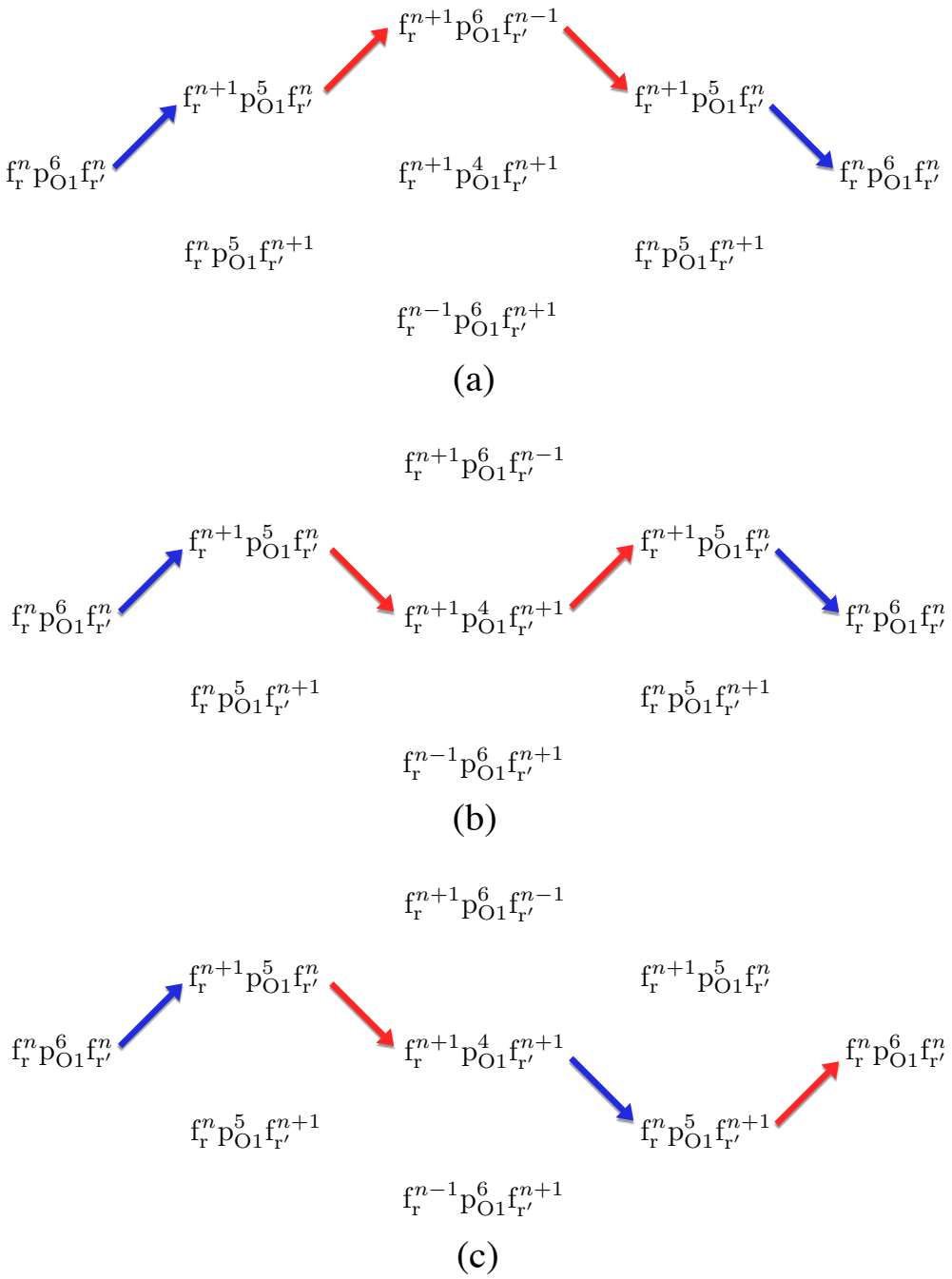

Figure 4.7: Decomposition of the virtual paths in Fig. 4.6 starting with a blue arrow (acting on the site **r**). The three diagrams help to visualise separately the different contributions to the exchange mechanism found in the fourth order of perturbation of the hybridisation Hamiltonian. The contribution of each path is also determined by the weight found from the energies associated to the hops of the electron across the virtual intermediate states between the two equivalent ground state configurations. The energies of the virtual states are estimated, as explained in subsection 4.4.1, by counting the number of electrons on each site of the RE-O1-RE unit. The weight associated to the virtual path in **(a)** is different from the two in **(b)** and **(c)** that are equivalent with each other.

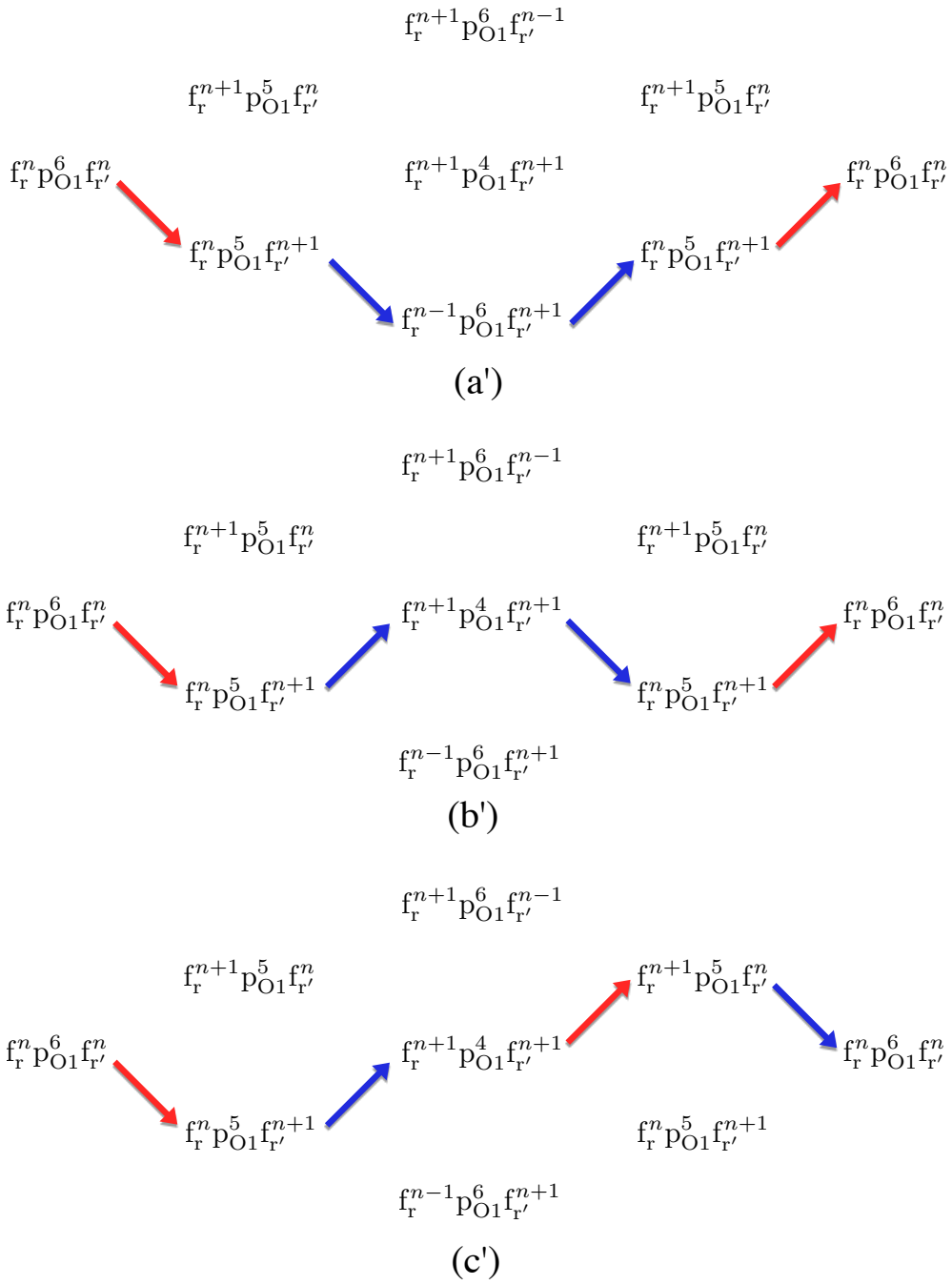

Figure 4.8: Decomposition of the virtual paths in Fig. 4.6 starting with a red arrow (acting on the site $\mathbf{r}'$). The three diagrams help to visualise separately the different contributions to the exchange mechanism left from Fig. 4.7. The weight associated to the virtual path in **(a′)** is different from the two in **(b′)** and **(c′)** that are equivalent with each other. For symmetry reason these are respectively equivalent to **(a)**, **(b)** and **(c)** in Fig. 4.7 (this is verified analytically in Appendix B.2).

of the RE-O1-RE system. From these, it is straightforward to derive the following weights characterising the six virtual paths in Fig. 4.7 and Fig. 4.8:

$$\begin{aligned} w_{\mathbf{(a)}} = w_{\mathbf{(a')}} &= \frac{1}{U(nU-\Delta)^2} \\ w_{\mathbf{(b)}} = w_{\mathbf{(b')}} &= \frac{1}{2(nU-\Delta)^3} \\ w_{\mathbf{(c)}} = w_{\mathbf{(c')}} &= \frac{1}{2(nU-\Delta)^3}\,. \end{aligned} \tag{4.67}$$

These are valid for any RE-O1-RE system whose RE^{3+} ions at the ground state have n electrons in the $4f$ shell; U is the energy cost for the Coulomb repulsion between two electrons on the same RE-site. Now it is possible to gather up the analytical results for the virtual fourth order processes allowed by Eq. (4.62).

The fourth order processes for the blue-red-blue-red paths **(a)** and **(b)** in Fig. 4.7 correspond to the following Hamiltonian

$$\begin{aligned} \hat{h}^{4th}_{\mathbf{(a)},\mathbf{(b)}} = \frac{V_1 V_{2'} V_{3'} V_4}{(nU-\Delta)^2} \Bigg[& \frac{\hat{f}_{\mathbf{1}}\,\hat{f}^{\dagger}_{\mathbf{2'}}\,\hat{f}_{\mathbf{3'}}\,\hat{f}^{\dagger}_{\mathbf{4}}}{U} \left(\mathcal{R}^{\dagger}\mathcal{R}\right)_{\mathbf{2'},\mathbf{1}} \left(\mathcal{R}^{\dagger}\mathcal{R}\right)_{\mathbf{4},\mathbf{3'}} \\ & + \frac{\hat{f}_{\mathbf{1}}\,\hat{f}_{\mathbf{2'}}\,\hat{f}^{\dagger}_{\mathbf{3'}}\,\hat{f}^{\dagger}_{\mathbf{4}}}{2(nU-\Delta)} \Big(\delta_{\mathbf{3'},\mathbf{2'}}\,\delta_{\mathbf{4},\mathbf{1}} - \left(\mathcal{R}^{\dagger}\mathcal{R}\right)_{\mathbf{3'},\mathbf{1}} \left(\mathcal{R}^{\dagger}\mathcal{R}\right)_{\mathbf{4},\mathbf{2'}} \Big) \Bigg] \end{aligned} \tag{4.68}$$

where also the dependence on the energies associated to each of the two paths has been included. Analogously, the path **(c)** in Fig. 4.7 corresponds to

$$\hat{h}^{4th}_{\mathbf{(c)}} = \frac{V_1 V_{2'} V_{3'} V_4}{(nU-\Delta)^2}\, \frac{\hat{f}_{\mathbf{1}}\,\hat{f}_{\mathbf{3'}}\,\hat{f}^{\dagger}_{\mathbf{2'}}\,\hat{f}^{\dagger}_{\mathbf{4}}}{2(nU-\Delta)} \Big(\delta_{\mathbf{2'},\mathbf{3'}}\,\delta_{\mathbf{4},\mathbf{1}} - \left(\mathcal{R}^{\dagger}\mathcal{R}\right)_{\mathbf{2'},\mathbf{1}} \left(\mathcal{R}^{\dagger}\mathcal{R}\right)_{\mathbf{4},\mathbf{3'}} \Big). \tag{4.69}$$

In these expressions it has been used the unitarity of the Rotation matrices when acting on the same lattice site, for example $\left(\mathcal{R}^{\dagger}\mathcal{R}\right)_{\mathbf{4},\mathbf{1}} = \delta_{\mathbf{4},\mathbf{1}}$ for $\mathbf{r}$ and $\left(\mathcal{R}^{\dagger}\mathcal{R}\right)_{\mathbf{3'},\mathbf{2'}} = \delta_{\mathbf{3'},\mathbf{2'}}$ for $\mathbf{r'}$. More algebraic details about the procedure to derive these Hamiltonians can be found in subsection B.2.1 of Appendix B. These terms can be grouped together with the ones for the "primed" paths in Fig. 4.8 (see subsection B.2.1.1); then, by using the commutation relations in Eq. (4.48) and keeping only the fourth order terms [21], these lead to the following Hamiltonian accounting for the exchange of electrons between two neighbouring RE-sites $\mathbf{r}$ and $\mathbf{r'}$

$$\begin{aligned} \left(\hat{h}_{\mathrm{exc}}\right)_{\mathbf{4},\mathbf{1},\mathbf{2'},\mathbf{3'}} = & -2\,\frac{V_1 V_{2'} V_{3'} V_4}{(nU-\Delta)^2}\, \hat{f}^{\dagger}_{\mathbf{4}}\,\hat{f}_{\mathbf{1}}\,\hat{f}^{\dagger}_{\mathbf{2'}}\,\hat{f}_{\mathbf{3'}} \\ & \times \left[-\frac{1}{nU-\Delta}\delta_{\mathbf{2'},\mathbf{3'}}\,\delta_{\mathbf{4},\mathbf{1}} + \left(\frac{1}{nU-\Delta}+\frac{1}{U}\right) \left(\mathcal{R}^{\dagger}\mathcal{R}\right)_{\mathbf{2'},\mathbf{1}} \left(\mathcal{R}^{\dagger}\mathcal{R}\right)_{\mathbf{4},\mathbf{3'}} \right]. \end{aligned} \tag{4.70}$$

[21] Eq. (B.33) of Appendix B summarises the lower order terms left from the commutation relations of the fourth order expansion. These contribute to the renormalisation of the CF parameters of the point charge model, together with Eq. (4.61) from the 2nd order expansion.

At this stage it is convenient to adopt the notation used in Onoda's work [30], where the relabelling

$$\begin{aligned} \mathbf{2}' &\to \mathbf{1}' \qquad \mathbf{4} \to \mathbf{1} \\ \mathbf{3}' &\to \mathbf{2}' \qquad \mathbf{1} \to \mathbf{2}\,, \end{aligned} \tag{4.71}$$

gives [22]

$$\begin{aligned} \left(\hat{h}_{\text{exc}}\right)_{\mathbf{1},\mathbf{2},\mathbf{1}',\mathbf{2}'} = -2\,\frac{V_1 V_{1'} V_2 V_{2'}}{(nU-\Delta)^2}\,\hat{f}^{\dagger}_{\mathbf{1}}\,\hat{f}_{\mathbf{2}}\,\hat{f}^{\dagger}_{\mathbf{1}'}\,\hat{f}_{\mathbf{2}'} \\ \times\left[-\frac{1}{nU-\Delta}\delta_{\mathbf{1},\mathbf{2}}\,\delta_{\mathbf{1}',\mathbf{2}'} + \left(\frac{1}{nU-\Delta}+\frac{1}{U}\right)(\mathcal{R}^{\dagger}\mathcal{R})_{\mathbf{1},\mathbf{2}'}\,(\mathcal{R}^{\dagger}\mathcal{R})_{\mathbf{1}',\mathbf{2}}\right]. \end{aligned} \tag{4.72}$$

After summing over the allowed quantum numbers and all the nearest-neighbours lattice sites this gives

$$\hat{H}_{ff} = \sum_{\mathbf{1},\mathbf{2},\mathbf{1}',\mathbf{2}'} \left(\hat{h}_{\text{exc}}\right)_{\mathbf{1},\mathbf{2},\mathbf{1}',\mathbf{2}'} \tag{4.73}$$

where the sum over the boldface integers reads

$$\sum_{\mathbf{1},\mathbf{2},\mathbf{1}',\mathbf{2}'} \equiv \sum_{\langle \mathbf{r},\mathbf{r}'\rangle}^{n.n.} \sum_{\substack{m_1,m_2,m_1',m_2'=0,\pm1 \\ \sigma_1,\sigma_2,\sigma_1',\sigma_2'=\pm}} . \tag{4.74}$$

Eq. (4.73) and Eq. (4.72) give the Hamiltonian for the effective exchange of electrons between the magnetic sites of the pyrochlore lattice of a $RE_2TM_2O_7$. Apart for the minus sign, it is equivalent to the Hamiltonian of Eq.(17) in the work of Onoda et al. in Ref. [30]. The discrepancy in the sign might be due to the "simplified" method used here to derive the fourth order expansion. Unfortunately in Ref. [30] no analytical details are given about the derivation of the effective exchange Hamiltonian hence it is not possible to conduct any direct comparison.

Here, for consistency with the literature, the Hamiltonian is given in the same notation

[22] The notation used in Ref. [30] does not reflect the initial ordering of the hybridisation operators in Eq. (4.62), it refers to the ordering of the fourth order operators in the exchange Hamiltonian in Eq. (4.72) and Eq. (4.75).

of Eq.(17) in Ref. [30]:

$$\begin{aligned}\hat{H}_{ff} = \frac{2}{(nU-\Delta)^2} \sum_{\langle \mathbf{r},\mathbf{r}'\rangle}^{n.n.} \sum_{\substack{m_1,m_2,m_1',m_2'=0,\pm1 \\ \sigma_1,\sigma_2,\sigma_1',\sigma_2'=\pm}} & V_{m_1} V_{m_1'} V_{m_2} V_{m_2'} \\ & \times \hat{f}^{\dagger}_{\mathbf{r},m_1,\sigma_1} \hat{f}_{\mathbf{r},m_2,\sigma_2} \hat{f}^{\dagger}_{\mathbf{r}',m_1',\sigma_1'} \hat{f}_{\mathbf{r}',m_2',\sigma_2'} \\ & \times \Bigg[-\frac{1}{nU-\Delta} \delta_{\substack{m_1,m_2 \\ \sigma_1,\sigma_2}} \delta_{\substack{m_1',m_2' \\ \sigma_1',\sigma_2'}} \\ & + \left(\frac{1}{nU-\Delta} + \frac{1}{U}\right) (\mathcal{R}^{\dagger}_{\mathbf{r}} \mathcal{R}_{\mathbf{r}'})_{\substack{m_1,m_2' \\ \sigma_1,\sigma_2'}} (\mathcal{R}^{\dagger}_{\mathbf{r}'} \mathcal{R}_{\mathbf{r}})_{\substack{m_1',m_2 \\ \sigma_1',\sigma_2}} \Bigg] .\end{aligned} \tag{4.75}$$

Eq. (4.75) is the most general Hamiltonian for the fourth-order superexchange of electrons in any magnetic pyrochlore $RE_2TM_2O_7$. To summarise, $\mathbf{r}$ and $\mathbf{r}'$ are the coordinates of the neighbouring RE-sites, n is the number electrons in the f-shell of the RE^{3+} ions of the system considered, and U, Δ and $V_m = V_{pf\pi}, V_{pf\sigma}$ are the energy scales regulating the virtual mechanisms of electron hopping described in Fig. 4.4 and Fig.4.6.

In the next section this Hamiltonian is given in another representation in the context of spin ice materials, to make more explicit the magnetic features implicit in it. Such representation is different from the ones proposed in Ref. [30] and constitute a completely original part of the work presented in this thesis.

4.5 Quantum exchange interaction between RE^{3+} ions in a pyrochlore lattice

The simplest case where the exchange of electrons translates into effective magnetic interaction between the sites hosting them has been shown in section 4.1.1. In particular, in Eq. (4.8), the exchange coupling constant was derived from the symmetries of the total wave functions expressed in terms of the single electron states. The present section, analogously, discusses how to obtain an effective magnetic coupling between the RE^{3+} sites of a pyrochlore lattice using the results obtained in the two previous sections in the context of f-p hybridisation and superexchange of electrons in a RE-O1-RE system.

The fully quantum-mechanical Hamiltonian in Eq. (4.75) can be converted in the Russell-Saunders coupling scheme by projecting it onto the $|M_J\rangle \otimes |M_J'\rangle$ states expressed in terms of the fermionic operators [23]. This describes completely the effective magnetic coupling between the RE^{3+} ions of any pyrochlore $RE_2TM_2O_7$ due to the virtual exchange of electrons discussed in the previous section. In this context the quantum mechanical observables are represented in terms of matrices with dimensions $(2J+1)^2 \times (2J+1)^2$, where J is the quantum number for the total angular momentum of the RE^{3+} ion.

Despite the fact that some of the magnetic pyrochlore oxides are systems with strong

[23] A general expression for the expansion of $|M_J\rangle$ in terms of the $\hat{f}^{\dagger}_{\mathbf{r},m,\sigma}$ operators is given in Eq. (4.40).

quantum fluctuations [6, 68], such quantum-mechanical description is usually simplified by a number of approximations. These, once again, originate from the (local) constraints which the crystal-field environment imposes on the magnetic degrees of freedom of the RE^{3+} ions. In fact, as most of the properties of magnetic pyrochlores are understood in terms RE-ions behaving like pseudo-spins [6], a typical choice is to project the Hamiltonian in Eq. (4.75) only onto the subspace of the ground state doublet and work with a set of operators expressed as tensor products of the Pauli matrices, i.e. of dimensions 4×4 [30, 69, 68, 70, 71].

Because of the peculiar effects that the monopoles induce on the otherwise totally frozen state of the spin ice materials, the method presented in the following section is an "educated" compromise between a quantum mechanical description and the classical Ising typically used in this system. Namely, the quantum-mechanical exchange interaction between any two RE^{3+} ions in spin ice is given by projecting only one of them onto the ground state doublet of the crystal-field and leaving the other as "fully quantum". This approximation is proposed to estimate the (quantum) effects that the exchange interactions induce on a given RE-ion in the (classical) approximation of projecting its neighbouring spins on the frozen configurations allowed by the CF ground states [24]. It serves, in general, the purpose of investigating, and eventually quantifying, the strength of the non-Ising exchange between the spin-ice magnetic dipoles, and, more specifically for this work, it manifests as crucial for the field-induced magnetodynamics presented in the last section of Chapter 2. In Chapter 5, in the context of the hopping of monopoles, the dynamical effects due to the characteristic dipolar fields near a monopole, derived in Chapter 3, are compared to the ones induced by the exchange interactions presented below.

4.5.1 Exchange interaction between a RE^{3+} ion and a spin-ice "spin"

To describe the exchange Hamiltonian for a free quantum mechanical RE^{3+} ion coupled to another one "frozen" in a given state $|\psi\rangle$ we restore the formalism of pointer operators (often called projectors). It is preferred as it allows, at least in very general terms, the description of a Hamiltonian otherwise too cumbersome.

Starting from Eq. (4.75), by means of a computer algebra we calculate the complex expansions in Eq. (4.40) for the $|M_J\rangle$ states in terms of the fermionic operators. This enables the calculation of the matrix elements $\langle\psi| \langle\widetilde{M}_J| \hat{H}_{ff} |M_J\rangle |\psi\rangle$, which allows us, in turn, to obtain the general expression for the exchange Hamiltonian of a RE^{3+} ion

[24] Note this is approximation is classical because each spin is projected in only one of the two states of the ground state doublet. This is the state pinned by the longitudinal dipolar field induced in a typical spin-ice state. This is not the case of quantum spin ices, where the RE^{3+} ions possess quantum fluctuations which mix the ground states and it is necessary to project in the whole subspace of the doublet.

coupled to another RE^{3+} frozen in a spin-ice CF ground state $|\psi\rangle$ as

$$\begin{aligned}\hat{\mathcal{H}}_{ff}(\mathbf{r},\mathbf{r}') = \mathcal{E}_{\text{exc}}\Bigg\{ &\sum_{M_J} \left(\mathcal{X}_{M_J,M_J} + \Lambda_{M_J}\right) \; |M_J\rangle\langle M_J| \\ &+ \sum_{M_J} \Big[\mathcal{X}_{M_J,M_J+1} \; |M_J\rangle\langle M_J+1| \\ &\qquad + \mathcal{X}_{M_J,M_J+2} \; |M_J\rangle\langle M_J+2| \\ &\qquad\quad + \mathcal{X}_{M_J,M_J+3} \; |M_J\rangle\langle M_J+3| + \text{h.c.}\Big]\Bigg\}.\end{aligned} \tag{4.76}$$

The coefficients for the operators are the constant

$$\mathcal{E}_{\text{exc}} = \frac{2\,V_{pf\sigma}^4}{(nU-\Delta)^2}\left(\frac{1}{nU-\Delta}+\frac{1}{U}\right) \tag{4.77}$$

and the polynomials

$$\Lambda_{M_J} = a\sum_{p=0}^{4} \mathcal{A}_{M_J}^{(p)} x^p \tag{4.78a}$$

$$\mathcal{X}_{M_J,\widetilde{M}_J}(\mathbf{r},\mathbf{r}') \;=\; \sum_{p=0}^{4} \left(\mathcal{C}_{\mathbf{r},\mathbf{r}'}\right)^{(p)}_{M_J,\widetilde{M}_J} x^p\,, \tag{4.78b}$$

$$\text{with} \qquad x = \frac{V_{pf\pi}}{V_{pf\sigma}}\,. \tag{4.78c}$$

The coefficients $\mathcal{A}_{M_J}^{(p)}$ and $\left(\mathcal{C}_{\mathbf{r},\mathbf{r}'}\right)^{(p)}_{M_J,\widetilde{M}_J}$ for a given p-th order are different. The former are only non-trivial combinations of the Clebsch-Gordan coefficients in Eq. (4.40), the latter are products of these same coefficients with complex analytical functions [25] of the angles $(\varphi_i,\vartheta_i,\varphi_{i'},\vartheta_{i'})$ in Eq. (4.24); they relate the different coordinate systems in Eq. (4.22) with each other. The only one constant which depends on the energy scales U and Δ and is not factored out of the curly brackets is the dimensionless

$$a = -\frac{U}{(n+1)U-\Delta} \tag{4.79}$$

which is found only in Eq. (4.78a), and so only on the diagonal part of $\hat{\mathcal{H}}_{ff}$ in Eq. (4.76).

The complexity of this general expression is substantially reduced by fixing the position of the two RE^{3+} sites on the pyrochlore lattice. This, in fact, implies that all the trigonometric functions for the relative angles between the two different local coordinate systems, one for the quantum RE-ion in $\mathbf{r}$, the other for the classical one frozen in $\mathbf{r}'$, simplify to a list of complex numbers. Hence, the generic interaction in Eq. (4.76) depends only, as expected, on the parameters which are functions of the energy scales

[25] These functions are very complex and cannot be reduced to a simple expression that could fit in a few pages!

in Eq. (4.75) in Eq. (4.78c). These are $\mathcal{E}_{\rm exc}$ in Eq. (4.77), a in Eq. (4.79) and $x = V_{pf\pi}/V_{pf\sigma}$. A strategy to fix their values is given in subsection 4.5.3.

4.5.2 Quantum exchange of a RE^{3+} ion in a two-tetrahedra cluster

In the context of this *quasi-quantum* approximation to describe the effective exchange fields induced on a central ion from its neighbouring (frozen) spins, it is straightforward to derive the Hamiltonian for a RE^{3+} interacting with all the six neighbouring spins around it. This is given by

$$\hat{\mathcal{H}}_{\rm exc} = \sum_{j=1}^{6} \hat{\mathcal{H}}_{ff}(\mathbf{r}_0, \mathbf{r}_j) \tag{4.80}$$

where $\mathbf{r}_0$ denotes the position of the central RE-site and $\mathbf{r}_j$ the positions of the neighbouring frozen ions around it.

In Eq. (4.80) a given configuration of the six frozen spins corresponds to a specific Hamiltonian for the central RE^{3+} ion. In this general model, where only the exchange interaction is considered, the energies and eigenstates of such matrix account for the possible magnetic states of the central ion which arise from an effective exchange-fields induced by the surrounding spins (see examples of configurations in Fig. 4.9). The general expression of the resulting Hamiltonian in Eq. (4.80) can be summarised in terms of Eq. (4.76) with different coefficients Λ_{M_J} and $\mathcal{X}_{M_J,\widetilde{M}_J}$ which depend on the arrangement of the six spins.

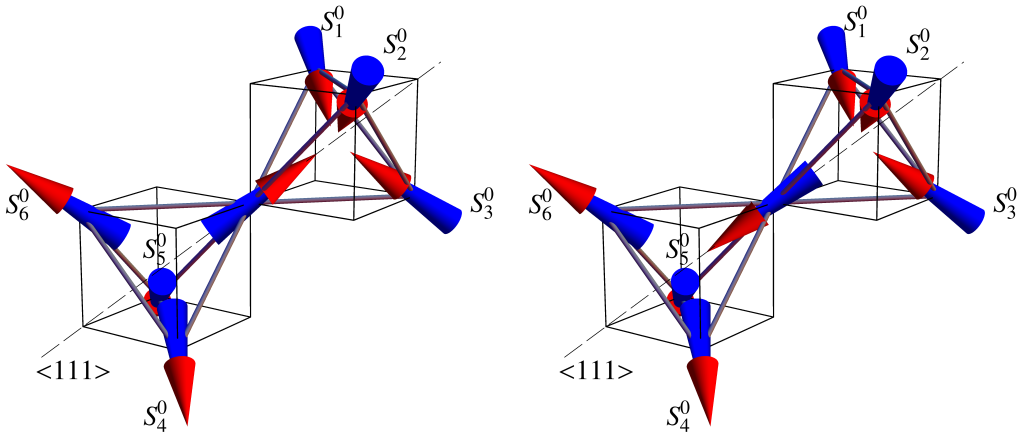

Ψ_0 Ψ_1

Figure 4.9: Antiferromagnetic coupling in a two tetrahedra cluster of the pyrochlore lattice (the dipolar interactions are neglected). The ground state is found when the spins in the tetrahedra assume the configuration *all in/all out* . This is shown in Ψ_0 (left panel) where all the spins in the lower tetrahedron point outward, while those in the upper tetrahedron point inward. This is a broken-symmetry state whose degenerate counterpart is found by inverting the direction of all spins. Ψ_1 (right panel) shows a configuration, excited with respect to Ψ_0, where only the central spin is flipped. If $J_{\rm nn}$ is the coupling constant regulating the interaction of any two spins in the cluster, then the difference in energy between Ψ_0 and Ψ_1 is given by $12J_{\rm nn}$ ($E_1 - E_0 = 6J_{\rm nn} - (-6J_{\rm nn})$).

Certain type of configurations lead to Hamiltonians which are of particular interest for the work presented in this thesis. In Chapter 3, in the context of the dipolar fields resulting on the central RE-site of a two-tetrahedra cluster, it was found that of the nine possible configurations hosting a monopole in the lower tetrahedron, six were giving a resulting fields (of the same magnitude) purely transverse to the local easy axis and three were giving an identically null field. Three archetypical cases of such were shown in Fig. 3.7. The corresponding Hamiltonians for the exchange interaction resulting on the central RE-site of these same cluster show properties which also reflect the symmetries of the different six-spin arrangements. For example, the configurations $\boldsymbol{A}$ and $\boldsymbol{B}$ in Fig. 3.7, which were giving dipolar transverse fields, lead to Hamiltonians, $\hat{\mathcal{H}}_{\text{exc}}^{(\boldsymbol{A})}$ and $\hat{\mathcal{H}}_{\text{exc}}^{(\boldsymbol{B})}$ respectively, which are both symmetric in the diagonal elements and are one the conjugate of the other. The configuration $\boldsymbol{C}$ in Fig. 3.7 with a null field, on the other hand, gives a Hamiltonian $\hat{\mathcal{H}}_{\text{exc}}^{(\boldsymbol{C})}$ for exchange with identically null off-diagonal elements and the diagonal ones identical to those of $\hat{\mathcal{H}}_{\text{exc}}^{(\boldsymbol{A})}$ and $\hat{\mathcal{H}}_{\text{exc}}^{(\boldsymbol{B})}$, i.e. also symmetric with respect to the local quantisation (easy) axis $\mathbf{z}$.

These properties are analytical and can be tested easily by fixing a coordinate system for the central ion, for example $\mathbf{x}_0, \mathbf{y}_0, \mathbf{z}_0$ from Eq. (4.22a), and, consequently, using a convenient set of $\mathbf{x}_i, \mathbf{y}_i, \mathbf{z}_i$ for the surrounding spins (for the spins $j = 1, 2, 3, 4, 5, 6$ in Fig. 4.9 the ideal choice is $\mathbf{x}_{i+3}, \mathbf{y}_{i+3}, \mathbf{z}_{i+3} = \mathbf{x}_i, \mathbf{y}_i, \mathbf{z}_i$ with $i = 1, 2, 3$ in Eq. (4.22)). The importance of the configurations $\boldsymbol{A}$, $\boldsymbol{B}$, $\boldsymbol{C}$ will be shown more explicitly in Chapter 5 in the context of the hopping of a monopole through a spin-ice cluster. At this stage it is worth anticipating that, from the properties of the Hamiltonians $\hat{\mathcal{H}}_{\text{exc}}^{(\boldsymbol{A})}, \hat{\mathcal{H}}_{\text{exc}}^{(\boldsymbol{B})}, \hat{\mathcal{H}}_{\text{exc}}^{(\boldsymbol{C})}$ discussed just above, exchange interactions promise to play a role as interesting and important as the dipolar ones. This statement derives from noticing that the statistics of configurations found in the dipolar case in Chapter 3 coincide with those found in the present one for the effective exchange.

Before implementing the exchange Hamiltonian in Eq. (4.80) in any realistic calculation it is necessary to suggest an estimation for its parameters.

4.5.3 Parametrisation for the quantum exchange of a RE^{3+} in spin-ice

To establish a choice of the parameters in Eq. (4.80) for the implementation of the exchange Hamiltonians together with the crystal-field and the dipolar one, it is convenient to consider a cluster of two tetrahedra with the spins arranged as in Ψ_0 on the lefthand side of Fig. 4.9. This configuration represents the (broken-symmetry) ground state for a system of spins with only antiferromangetic interaction. This is not a realistic configuration for the ground state of spin ice, where, in contrast, the dominant nearest neighbour ferromagnetic coupling gives a frustrated (2in-2out) degenerate ground state. Nonetheless, the character of the pure exchange coupling is notoriously antiferromagnetic with $J_{\text{nn}} = -0.52, -1.24$ Kelvin for, respectively, $Ho_2Ti_2O_7$ and $Dy_2Ti_2O_7$ [5]. In other words, the configuration Ψ_0 in Fig. 4.9 represents the ground state of a "gedanken" system with classical spins having local Ising anisotropies, like the spin-ices, but antiferromagnetic coupling between the nearest neighbours.

The classical approximation is imposed on the surrounding spins by projection on the frozen (ground) states allowed by their local crystal fields. The strategy to obtain a realistic parametrisation for the exchange Hamiltonian of a spin-ice material also needs

the auxiliary contribution of the local crystal-field Hamiltonian for the central ion. This, in turn, is the most realistic method for the parametrisation of any kind of interaction magnetic ions in solids, as the crystal-field plays typically the most important role in setting the structure of the magnetic states straight after the central ion approximation in Eq. (1.3) (the relevance of the crystal-field in spin ice has ben discussed thoroughly in Chapter 2).

Diagonalisation of the full crystal-field Hamiltonian for spin ice, for example Eq. (2.27) with the parameters in Table 2.3, together with the exchange in Eq. (4.80),

$$\hat{\mathcal{H}}_{CF} + \hat{\mathcal{H}}_{\text{exc}}, \tag{4.81}$$

gives a spectrum, for the allowed states for the RE^{3+} ion, which depends only on the parameters $\mathcal{E}_{\text{exc}}$ in Eq. (4.77), a in Eq. (4.79) and $x = V_{pf\pi}/V_{pf\sigma}$ in Eq. (4.78c). If a choice of parameters guarantees that the ground state for the central ion satisfies the antiferromagnetic alignment shown in Ψ_0 of Fig. 4.9 this is already a reasonably good set.

However, as the interest in fixing the parameters extends beyond the simple antiferromagnetic interaction, it is necessary to make an accurate choice which can be reliable also for other spin ice configurations, with particular attention to meet the needs of those featuring the presence of a monopole nearby.

According to Ref. [30], the value $x \approx -0.3$ in Eq. (4.78c) is the most appropriate one for magnetic pyrochlores. Hence the only two parameters left are $\mathcal{E}_{\text{exc}}$, which is defined positive, and a, which is negative and typically such that $-1 \leq a \leq 0$ for a system of n electrons in the f-shell.

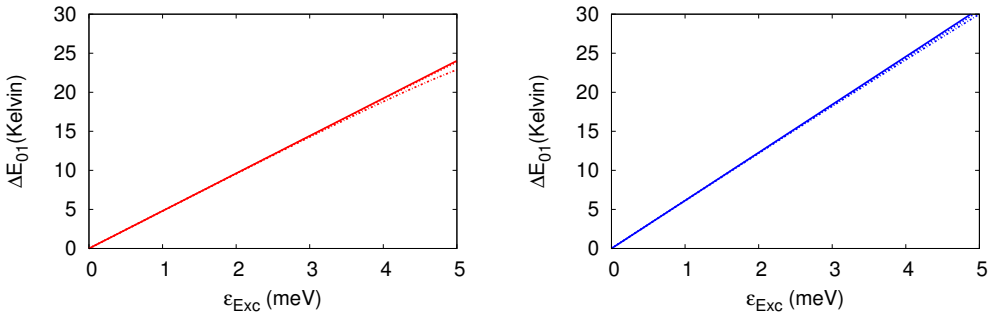

(a) HTO **(b)** DTO

Figure 4.10: Behaviour of the gap ΔE_{01} with respect to $\mathcal{E}_{\text{exc}}$ for three different curves parametric in a in both systems, HTO (left panel) and DTO (right panel). $a = 0$ is shown in a solid line, while $a = -0.5, -1$ are respectively the dotted and dotted-dashed lines. The behaviour is very similar for the three different values of a.

At this stage the good couples of parameters $\{\mathcal{E}_{\text{exc}}, a\}$ are again, primarily, those leading to the polarised ground state as in Ψ_0 of Fig. 4.9. The more a tends to zero the more stable the ground state is. Secondarily, after this has been assessed, it is convenient to see the behaviour of the first gap ΔE_{01} in the spectrum of the full Hamiltonian in Eq. (4.81) at different values of $\{\mathcal{E}_{\text{exc}}, a\}$. ΔE_{01} is the energy-gap, in the spectrum of the Hamiltonian in Eq. (4.81), between the excited configuration Ψ_1

(right panel in Fig. 4.9) where the central spin has been flipped, and the state Ψ_0 (left panel in Fig. 4.9) being the ground state favoured because of antiferromagnetic alignment with the surrounding spins.

The behaviour of ΔE_{01} vs $\mathcal{E}_{\rm exc}$ is illustrated in Fig. 4.10 for both HTO (left) and DTO (right). The three parametric curves for $a = -1, -0.5, 0$ are almost totally overlapped, showing the very weak dependence on this range of values.

Hence, for simplicity we take $a = 0$ and tune only $\mathcal{E}_{\rm exc}$ to account for the correct values of the gap. The equivalence

$$\Delta E_{01} = 12 J_{\rm nn} \tag{4.82}$$

sets the value of ΔE_{01} at which each system picks the correct $\mathcal{E}_{\rm exc}$. From the values $|J_{\rm nn}| \approx 0.52\text{K}, 1.24\text{K}$, in Ref. [5], for the nearest neighbour Ising exchange we obtain $\mathcal{E}_{\rm exc} \approx 1.4\text{meV}, 2.3\text{meV}$ respectively for HTO and DTO. These are extrapolated from the curves in Fig. 4.10 and expressed in meV in analogy with the parameters for the crystal-field in Table 2.3.

In the following Chapter the quantum-quench regulating the dynamics of a RE^{3+} ions next to a monopole is presented. This is done in the most general formalism which, as we now understand, needs to include also exchange together with dipolar interactions. The parameters used for the exchange Hamiltonian are the ones derived just above in this section.

"When correlations are robust enough, familiar classical objective reality emerges from the quantum substrate. Moreover, even a minute interaction with the environment, practically inevitable for any macroscopic object, will establish such a correlation: the environment will, in effect, measure the state of the object, and this suffices to destroy quantum coherence. The resulting decoherence plays, therefore, a vital role in facilitating the transition from quantum to classical."

W.H. Zurek [31]

5

A quantum-quench picture of monopole hopping

The present chapter has a twofold purpose in the structure of the whole thesis. Firstly, it gathers the results obtained separately in the previous chapters in a "unified theory" for spontaneous quantum-dynamics of a RE^{3+} in the presence of a monopole (section 5.1). Secondly, in a wider view concerning the propagation of a monopole through a cluster, it shows how such a model paves the way for a description of the key elements to be considered in any meaningful characterisation of the monopole dynamics (section 5.2).

The hopping of a monopole from a tetrahedron of the diamond lattice to a neighbouring one requires the flipping of the spin sitting at the vertex joining them. From the two-tetrahedra analysis conducted in Chapter 3 a statistical character in the possible fields resulting on a RE^{3+} site of a monopole has emerged: although in all cases the longitudinal component of the field is removed by the arrival of the monopole, a purely transverse field, which is necessary for quantum dynamics, has probability of 2/3 to occur. Before deducing any conclusion about the kinematic constraints which arise for the propagation of the monopoles, it is crucial to uncover the contribution of the exchange Hamiltonian derived in Chapter 4 once it is implemented in the same two-tetrahedra cluster hosting a monopole. Moreover, as the quantum-tunnelling of the RE^{3+} in Chapter 2 appeared to be dependent not only on the strength of the transverse field but also on the directions with respect to the local symmetries of the crystal-field, it is necessary to assess, primarily, the probability of tunnelling under the combined effect of exchange with dipolar fields and, secondarily, the orders of magnitude for the characteristic timescales.

To this aim, the next section focuses on a model of *quantum-quench* which we propose, in the most general formulation, as a tool to study the response of a (quantum) RE^{3+} ion under a sudden change of the local effective fields acting on it.

5.1 Quantum-quench and spontaneous magnetodynamics

The model of quantum-quench given in this section exploits the mutual interactions which nearest neighbour spins on a pyrochlore lattice induce on each other. The focus, in particular, is in investigating the magnetodynamics characterising a RE^{3+} ion in the presence of a monopole excitation nearby. The aim is to account for the spin-flip, which underlies the monopole-hopping, by means of a realistic model of spontaneous quantum-spin tunnelling.

5.1.1 A recap on the quantum dynamics of a RE^{3+} ion in spin-ice

To describe the quantum-quench mechanism we restore the formalism used in section 2.5, where the quantum dynamics of a spin-ice RE^{3+} ion were induced by means of a magnetic field transverse to the local $\langle 111 \rangle$ axis. These, from the unitary evolution in Eq. (2.38), were uniquely determined by the initial condition $|\psi(0)\rangle$ for the state of the RE^{3+} ion and the Hamiltonian $\hat{\mathcal{H}}$ accounting for its interaction with the local fields. In the simplified picture therein, the single RE^{3+} ion was studied solely in terms of the effects induced by a magnetic field $\mathbf{B}$ acting as a perturbation on the CF states, i.e. $\hat{\mathcal{H}} = \hat{\mathcal{H}}_{CF} + \hat{\mathcal{H}}_{\mathbf{B}}$ in Eq. (2.29). The interactions with the other magnetic ions in the lattice were not considered.

The time-evolution, obtained by initialising the magnetic ion in a state $|\psi(0)\rangle$ polarised along the local quantisation axis $\mathbf{z_0}$ (parallel to $\langle 111 \rangle$) and letting it evolve under a static transverse field for different magnitudes and directions on the $\mathbf{x_0}, \mathbf{y_0}$ plane in Fig. 2.8, brought to light the pivotal role of the D_{3d} crystal-field symmetry in the tunnelling mechanism of a RE^{3+} ion in spin ice. Not only does the CF spectrum characterise the timescales for the tunnelling rates $\tau \sim \hbar/\Delta E_{01}$ in Eq. (1.2) with different power laws $\Delta E_{01} \propto |\mathbf{B}|^p$ for HTO ($p = 2$) and DTO ($p = 3$), it also "monopolises" the time-dependence of the probability density $|\psi(t)|^2$. More precisely, the quantum dynamics, showed for $|\psi(0)\rangle = |-J\rangle$ in Figs. 2.12-2.14, emerged with a strong dependence on the angle of the field on the plane $\mathbf{x_0}, \mathbf{y_0}$ in Fig. 2.8; the periodicity found reflects the anti-prismatic D_{3d} symmetry of the O2 oxygens (these are stacked in triangles which lie, above and below the central ion, parallel to such transverse plane as shown in Figs. 2.3b, 2.5, 2.8).

In general, the dependence of the quantum dynamics on the angle ϕ of the transverse field manifests differently for HTO and DTO. In all cases the probability density is always distributed between the two states with opposite polarisations, i.e. the two opposite Ising configurations for the RE^{3+} ground state imposed by the CF symmetry. Within the perturbative regime $|\mathbf{B}| \leq 10\text{T}$ for the splitting in Fig. 2.9, the tunnelling mechanism can be summarised in the following behaviours:

i) a full tunnelling of the probability density always occurs for $\phi = 30\,^\circ + n\,60\,^\circ$ with n integer (this corresponds to a magnetic transverse field pointing exactly between two neighbouring O2 oxygens above and below the central RE^{3+} ion in Fig. 2.8);

ii) the tunnelling tends to be suppressed for $\phi = 0\,^\circ + n\,60\,^\circ$ with n integer (this corresponds to a magnetic transverse field pointing aligned with a RE-O2 direction in Fig. 2.8); the dependence of HTO and DTO can be very diverse depending on the strength $|\mathbf{B}|$ of the field;

iii) intermediate angles show, consistently, intermediate regimes of tunnelling.

These results called for the analysis of the effective magnetic fields resulting on a RE^{3+} ion from the configurations of the spins surrounding it. In Chapter 3 and Chapter 4, in fact, it has been shown that effective fields purely transverse to the local easy axis occur on a RE^{3+} in the presence of a monopole nearby. In the following the spin-dynamics are discussed in the quantum-quench mechanism using the initial states and the Hamiltonians from the effective fields obtained therein.

5.1.2 Setting up the Hamiltonians for the quantum-quench

In Chapter 2 the magnetic fields used in the Hamiltonian in Eq. (2.29) were tuned ad-hoc to study the interplay between the Zeeman and CF contributions. Analogously, the (polarised) initial conditions $|\psi(0)\rangle = |\pm J\rangle$ were also imposed, even if based on the educated analogy with the Ising anisotropy due to the crystal-field. The results were profoundly meaningful and already contained a complete description of the quantum dynamics of a spin-ice RE^{3+} ion induced in the occurrence of fields transverse to the local Ising axis.

The quantum-quench model goes one step beyond, using the Hamiltonian and the initial condition corresponding to the spin configurations characterising the spin-ice low temperature regimes. The only approximation consists in the "quasi-quantum" description for the interaction between the central RE^{3+} ion, treated as a quantum-mechanical object, and the surrounding ones, projected into frozen configurations of classical Ising spins.

The Hamiltonian for a RE^{3+} ion immersed in a given spin ice configuration $\mathcal{C}$ reads

$$\hat{\mathcal{H}}^{(\mathcal{C})} = \hat{\mathcal{H}}_{CF} + \hat{\mathcal{H}}^{(\mathcal{C})}_{Dip} + \hat{\mathcal{H}}^{(\mathcal{C})}_{Exc}\,, \tag{5.1}$$

in the absence of external fields applied to the material. $\hat{\mathcal{H}}_{CF}$ is conveniently tackled in terms of the Stevens' operators as in Eq. (2.27) with the CF parameters from Table 2.3b; it does not depend on the configuration of the surrounding spins. On the other hand $\hat{\mathcal{H}}^{(\mathcal{C})}_{Dip}$ and $\hat{\mathcal{H}}^{(\mathcal{C})}_{Exc}$ are totally defined from the configuration $\mathcal{C}$ of the other (frozen) spins in the lattice.

A semi-classical Zeeman interaction regulates the effect of the dipolar fields resulting on the central ion:

$$\hat{\mathcal{H}}^{(\mathcal{C})}_{Dip} = -g_J \mu_B\, \hat{\mathbf{J}} \cdot \mathbf{B}^{(\mathcal{C})}_{Dip}\,, \tag{5.2}$$

with the Bohr magneton μ_B and Landé factors $g_J = 5/4$ and $g_J = 4/3$, respectively, for Ho^{3+} and Dy^{3+}. This is uniquely determined from the dipolar field $\mathbf{B}^{(\mathcal{C})}_{Dip}$ resulting on the central RE-site $\mathbf{r_0}$, by means of Eq. (3.9), from the configuration $\mathcal{C}$ of the other classical spins (dipoles) in the pyrochlore lattice.

To account for the contribution of the exchange interaction, due only to the six nearest neighbours spins of the RE-site, we restore the quasi-quantum Hamiltonian

in Eq. (4.80),

$$\hat{\mathcal{H}}_{Exc}^{(\mathcal{C})} = \sum_{j=1}^{6} \hat{\mathcal{H}}_{ff}(\mathbf{r_0}, \mathbf{r_j}) \tag{5.3}$$

where $\mathbf{r_j}$ are the positions of the six neighbours spins around the central RE^{3+} in $\mathbf{r_0}$. This is uniquely defined by $\mathcal{C}$, the Ising configurations for the $j = 1, \ldots, 6$ spins. As a remark, this constitutes the original output of the thorough analysis done in the previous chapter where also the parameters characterising it have been fixed to allow its implementation in the quantum-quench mechanism presented below.

5.1.3 The "core" of the quantum-quench mechanism for RE^{3+} ions

The Hamiltonian $\hat{\mathcal{H}}^{(\mathcal{C})}$ in Eq. (5.1) can give different ground states for the RE^{3+} ion depending on the configuration $\mathcal{C}$ of the other spins in the lattice. Because of the strength of the crystal-field anisotropy, however, the magnetic ion will tend to *collapse* in either of the Ising states corresponding to the ground state doublet of $\hat{\mathcal{H}}_{CF}$. Which one of the two, depend on the interplay between dipolar and exchange interactions. To recover the spin-ice ground state from the collapse of the wave function of the central ion is expected to favour ferromagnetic (frustrated) alignment with the surrounding spins. As we shall see, this is the case because of the strong longitudinal component, along the local $\langle 111 \rangle$ axis, found for the dipolar fields in Chapter 3 (see for example histogram in Fig. 3.13). For a lattice-state excited above the frustrated spin-ice ground state, i.e. in the presence of the monopoles, the scenario becomes more rich, in particular for the pyrochlore sites next to a monopole where the longitudinal fields are quenched.

The focus of the quantum-quench mechanism is to study the magnetodynamics of a RE^{3+} ion in spin ice whenever a given configuration $\mathcal{C}$ for the surrounding spins undergoes a sudden change $\mathcal{C} \to \widetilde{\mathcal{C}}$. As a monopole hops by flipping adjacent spins, for example, its propagation consists in the change of one local-Ising state for each $\mathcal{C} \to \widetilde{\mathcal{C}}$ step.

Exploiting the quantum-quench mechanism for dynamics

The quantum-quench that we use to describe the quantum dynamics of a RE^{3+} ion in spin ice materials consists, in its most general formulation, in the following main steps:

i) the RE^{3+} ion sits at time $t < 0$ in the ground state $|\psi^{(\mathcal{C})}\rangle$ of $\hat{\mathcal{H}}^{(\mathcal{C})}$ for a given spin-ice state $\mathcal{C}$;

ii) the sudden change $\mathcal{C} \to \widetilde{\mathcal{C}}$ at $t = 0$ quenches the Hamiltonian to $\hat{\mathcal{H}}^{(\widetilde{\mathcal{C}})}$;

iii) the state $|\psi(t)\rangle$ of the RE^{3+} ion evolves as in Eq. (2.38)

$$|\psi(t)\rangle = e^{-i\,\hat{\mathcal{H}}t/\hbar}\,|\psi(0)\rangle\ , \tag{5.4}$$

with $|\psi(0)\rangle \equiv |\psi^{(\mathcal{C})}\rangle$ as initial condition and the Hamiltonian $\hat{\mathcal{H}} \equiv \hat{\mathcal{H}}^{(\widetilde{\mathcal{C}})}$ governing the unitary evolution;

iv) at a time $t \gtrsim \tau$, with $\tau \sim \hbar/\Delta E_{min}$ and ΔE_{min} the smallest gap of the spectrum of $\hat{\mathcal{H}}^{(\widetilde{\mathcal{C}})}$, decoherence occurs and the quantum state of the RE^{3+} collapses in a

classical state allowed by the CF symmetry (typically a local Ising state).

This sequence of time-steps is shown pictorially in Fig. 5.3 in the context of the propagation of a monopole across a pyrochlore cluster.

An ensemble of assumptions is implicit in this model of quantum-quench. Together with the "single-ion approximations" [1], now a mechanism of decoherence needs to be assumed to account for the emergence of the classical Ising state of the RE^{3+} ion which otherwise would tunnel coherently between the two CF states for an indefinite amount of time. Nonetheless, this ensemble of approximation is what actually lies, already, at the very fundamental aspects under the current "standard model" for spin-ice and its magnetic monopoles introduced in Chapter 1. These assumptions here are simply revisited, or at most "rearranged", for the description of the monopole dynamics. Not surprisingly, the latter undermine the imaginary border which, according to our "(scientific) common sense", distinguishes a classical system from a quantum one.

Furthermore, the intriguing expectation that the presence of a monopole does induce quantum dynamics of a RE^{3+} ion, according to Chapter 2, because of the characteristic effective-fields found in Chapter 3 and Chapter 4 encourages to engage with the quantum-quench model to investigate how the diverse mechanisms discussed in this thesis combine together in the picture of the monopole hopping.

5.1.4 Quantum-quench from the arrival of a monopole

To discuss the quantum-quench in the presence of a monopole we refer to Fig. 5.1 as an archetype to show the configurations of the six spins surrounding the central RE^{3+} ion before (Config. $\bar{\boldsymbol{A}}$, top panel) and after (Config. $\boldsymbol{A}$, bottom panel) the arrival of a monopole. Their role in the monopole hopping is shown more explicitly in Fig. 5.3a for the former and Fig. 5.3b for the latter. The names of the spin configurations and the labelling of the spin themselves is chosen in analogy with Fig. 3.5a.

In Chapter 3, in fact, it has been shown that Config. $\boldsymbol{A}$, in spin ice, features a north-monopole in the lower tetrahedron and induces a dipolar field on the central RE-site which is purely transverse to the local $\langle 111 \rangle$ direction. In Fig. 5.1, the bottom panel corresponds to Config. $\boldsymbol{A}$ in Fig. 3.5a and Fig. 3.7a. The only (graphical) difference is that in Fig. 5.1 the central spin is not shown; this is done to emphasise how important it is to consider also the effects of exchange interactions before determining the ground state of the central RE^{3+} ion.

Below, in section 5.1.5, according to the general procedure given in section 5.1.3, the behaviour of RE^{3+} ion in the central site of a two-tetrahedra cluster is analysed under the quantum-quench caused by the sudden change $\bar{\boldsymbol{A}} \to \boldsymbol{A}$ due to the arrival of a monopole. Before analysing the dynamics it is essential to study the two configurations, before ($t < 0$) and after ($t = 0$) the quenching occurs.

The two configurations $\bar{\boldsymbol{A}}$ and $\boldsymbol{A}$ differ only for the flip of the spin S_4^0; below they are analysed separately. The convention adopted for the directions of the spins $j = 1, \ldots, 6$ is the same used throughout Chapter 3; it considers the $\langle 111 \rangle$ axis of the central site

[1] By "single ion" approximations we mean to summarise all the hypothesis made in focusing on a given RE^{3+} ion to derive the Hamiltonian $\hat{\mathcal{H}}^{(C)}$ in Eq. (5.1). These basically cover the whole work done so far in this thesis, starting from the semi-classical CF point-charge model in Chapter 2, all the way down to the quasi-quantum effective-exchange in Chapter 4.

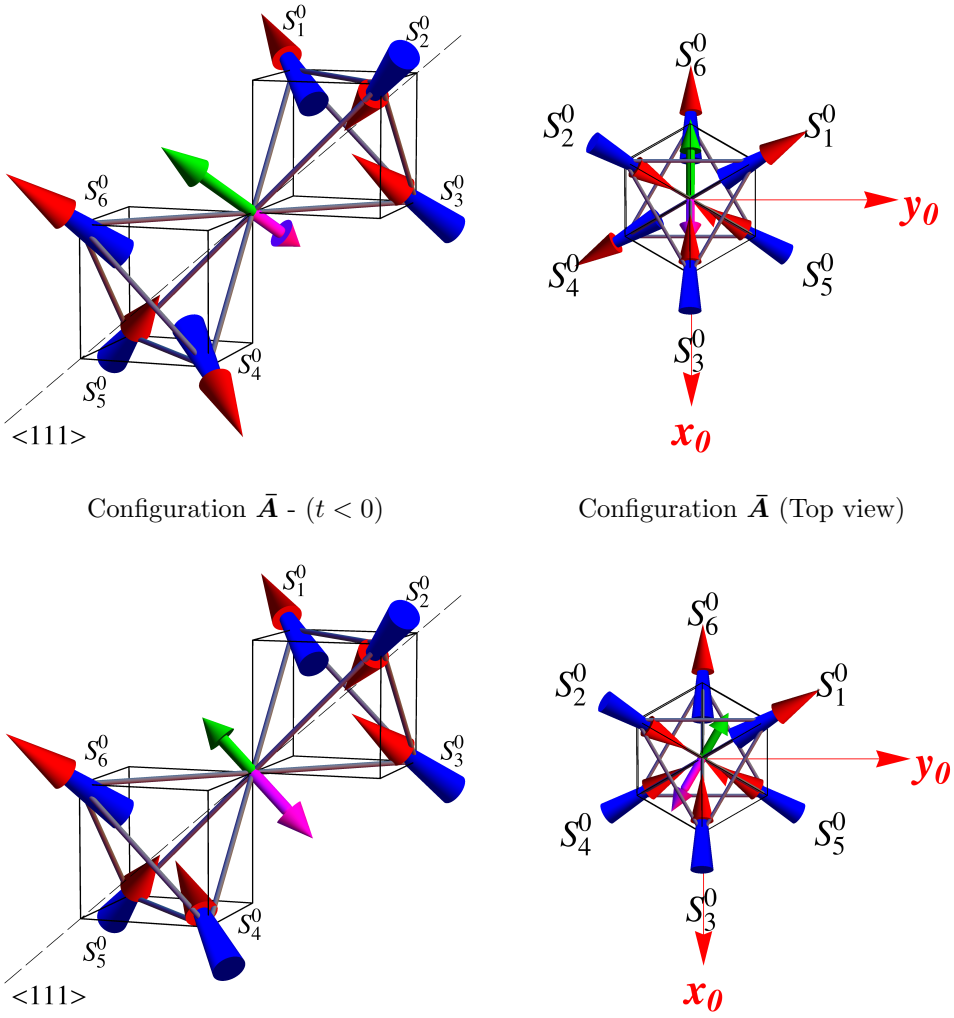

Configuration $\bar{\boldsymbol{A}}$ - $(t < 0)$ Configuration $\bar{\boldsymbol{A}}$ (Top view)

Configuration $\boldsymbol{A}$ - $(t = 0)$ Configuration $\boldsymbol{A}$ (Top view)

Figure 5.1: Example of spin-configurations, in a two-tetrahedra pyrochlore cluster, before ($\bar{\boldsymbol{A}}$, top panels) and after ($\boldsymbol{A}$, bottom panels) the arrival of a monopole. The right panels show the top views of the respective left ones. The labelling of the RE-sites is the same of Figs. 3.4-3.6. In this scheme the central spin is not shown as its ground state, in general, depends on the type of interactions with the surrounding neighbours. In both cases exchange effective-fields (magenta) are opposite to the dipolar ones (green). $\bar{\boldsymbol{A}}$ and $\boldsymbol{A}$ differ only by the flip of the spin S_4^0 by which, if the central spin points down, the monopole arrives. This is shown more explicitly in the presence of a monopole in Fig. 5.3. Fig. 5.3a corresponds to the top panel $\bar{\boldsymbol{A}}$ $(t < 0)$, while Fig. 5.3b corresponds to the bottom one $\boldsymbol{A}$ $(t = 0)$.

in Fig. 5.1 as global Ising axis of the cluster: $S_j^0 = 1$ if the spin points upward and $S_j^0 = -1$ if it points downward.

Configuration $\bar{\boldsymbol{A}}$ ($t < 0$) In the top panel the spins $S_3^0 = S_6^0 = -1$ characterise the ground state of the central ion (the contribution of the others cancels out). From this parallel alignment the ground state of the central RE^{3+} ion will be projected in one of the two CF states with opposite polarisation. If only the exchange interactions were present, the spin would collapse upward ($S_0^0 = 1$) to favour antiferromagnetic alignment with S_3^0, S_6^0. However, since in the real spin-ice ground state the dipolar (ferromagnetic) interactions overcome the exchange ones, the ground state of the full $\hat{\mathcal{H}}^{(\bar{\boldsymbol{A}})}$ in Eq. (5.1) is expected to give a central spin pointing downward.

This is confirmed in Table 5.1 where the magnetic moment $\mathbf{m} = g_J \langle \hat{\mathbf{J}} \rangle$ in units of μ_B is calculated as expectation value of the angular momentum operator $\hat{\mathbf{J}} = (\hat{J}_x, \hat{J}_y, \hat{J}_z)$ over the ground state $|\psi^{(\bar{\boldsymbol{A}})}\rangle$ of $\hat{\mathcal{H}}^{(\bar{\boldsymbol{A}})}$. $\mathbf{m}$ is conveniently expressed in spherical values $(|\mathbf{m}|, \theta, \phi)$ for the local coordinate system $\mathbf{x}_0, \mathbf{y}_0, \mathbf{z}_0$, in Eq. (4.22a), of the central RE^{3+} ion. This is the same coordinate system in Eq. (2.30) used for the quantum dynamics of a RE^{3+} ion; in Fig. 2.8 from a top view ($\mathbf{z}_0$ outward of the plane). In complete analogy with Chapter 2 the angle ϕ is on the plane $\mathbf{x_0}, \mathbf{y_0}$, transverse to the $\langle 111 \rangle$ direction in Fig. 5.1, while θ is the polar angle with respect to $\mathbf{z}_0$. The magnitudes ($|\mathbf{m}| = 9.8\mu_B$) and the polar angles ($\theta = 180\,^\circ$) found for the *purely dipolar* and *dipolar with exchange* model justify the classical approximation of magnetic dipole $|\mathbf{m}| \approx 10\mu_B$ pointing down. The angle $\theta = 0\,^\circ$ obtained in the (hypothetic) case of *pure exchange* also confirms the consistency of the model (exchange result in the opposite direction forcing the spin to point upward). In the context of the quantum-quench these will constitute the initial conditions, since Config. $\bar{\boldsymbol{A}}$ represents the state of the cluster before the arrival of the monopole. This confirms also the correct assumption of the polarised initial condition used in section 2.5.

Configuration $\boldsymbol{A}$ ($t = 0$) The bottom panel ($\boldsymbol{A}$) in Fig. 5.1 differs from the top one ($\bar{\boldsymbol{A}}$) only because of S_4^0 pointing upward: now $S_1^0 = S_4^0 = 1$. This means that the parallel alignment of S_1^0, S_4^0 cancels, for the central ion, any contribution along the $\langle 111 \rangle$ direction that was due to S_3^0, S_6^0. The longitudinal component of the interactions is quenched! Only the transverse components of the interactions due to $S_1^0, S_4^0, S_3^0, S_6^0$ are left and the resulting ground state is, in general, a superposition of the two opposite Ising configurations.

This "classical" picture for the resulting effect of the surrounding spins on the central site, is confirmed in Table 5.1. The direction of the magnetic moment resulting from the ground state $|\psi^{(\boldsymbol{A})}\rangle$ of $\hat{\mathcal{H}}^{(\boldsymbol{A})}$ is always purely transverse to the $\langle 111 \rangle$ direction ($\theta = 90\,^\circ$). The magnitude is incredibly small compared to the case $\bar{\boldsymbol{A}}$. For the case of dipolar interaction, the angle $\phi = 150\,^\circ$ shows that the ground state of the magnetic ion points perfectly aligned with the field resulting from the surrounding ions[2]. For the exchange case the magnetic moment points, again, exactly in the opposite direction of the dipolar field ($\phi = -30\,^\circ$). This last result was not necessarily expected as we couldn't make

[2] The unit vector $\{-1/\sqrt{2}, 0, 1/\sqrt{2}\}$ of the transverse field in Fig. 3.7a is expressed in Cartesian components for the $\mathbf{X}, \mathbf{Y}, \mathbf{Z}$ coordinate system. It is straightforward to show that this corresponds to $(\theta, \phi) = (90\,^\circ, 150\,^\circ)$ for $\mathbf{x}_0, \mathbf{y}_0, \mathbf{z}_0$ in Figs. 2.8 (see also top view at the bottom of Fig. 5.1).

	Config. $\bar{\boldsymbol{A}}$	Config. $\boldsymbol{A}$
Only Dipolar	$(9.80, 180, 120)$	$(0.0061, 90, 150)$
Only Exchange	$(9.80, 0.02, 0)$	$(0.0066, 90, -30)$
Dipolar + Exchange	$(9.79, 180, 88.57)$	$(0.0006, 90, -30)$

(a) HTO

	Config. $\bar{\boldsymbol{A}}$	Config. $\boldsymbol{A}$
Only Dipolar	$(9.84, 179.9, 120)$	$(0.0083, 90, 150)$
Only Exchange	$(9.84, 0.14, 0)$	$(0.0425, 90, -30)$
Dipolar + Exchange	$(9.85, 180, 22.67)$	$(0.0342, 90, -30)$

(b) DTO

Table 5.1: Values of $\mathbf{m} = g_J \langle \hat{\mathbf{J}} \rangle$ from the ground states of $\hat{\mathcal{H}}^{(\bar{\boldsymbol{A}})}$ (left) and $\hat{\mathcal{H}}^{(\boldsymbol{A})}$ (right) for the central Ho^{3+} ion in HTO at the top (a) and Dy^{3+} ion in DTO at the bottom (b). The spherical values $(|\mathbf{m}|, \theta, \phi)$ are given with respect to the local system of coordinate used for the central RE-site $\mathbf{x}_0, \mathbf{y}_0, \mathbf{z}_0$. The magnitude $|\mathbf{m}|$ is in units of μ_B; the angles are expressed in degrees. θ is the polar angle with respect to $\mathbf{z}_0$ parallel $\langle 111 \rangle$ axis in Fig. 5.1, and ϕ the azimuthal angle with respect to $\mathbf{x}_0$ in Fig. 2.8.

any straightforward prediction on the interplay between the combination of the quasi-quantum exchange and the semi-classical dipolar effect on the central RE^{3+} ion. At the same time this is not entirely new as also the "classical" exchange analysis done in section 4.1.3 was giving an effective-exchange field pointing opposite to the dipolar one. The opposite directions of the effective fields on the central site are pictorially represented in Fig. 5.1 by means of two opposite pointers of different colours (the lengths of the pointers is only to mimic the relative strengths): green for the dipolar fields, magenta for the effective-exchange ones.

The result that exchange overcomes the dipolar interaction in $\boldsymbol{A}$ is not entirely a new result; it was found already in the classical approximation in section 4.1.3. The way it happens now, nonetheless, is quite different. It is not possible to conduct an analogous comparison as the analytical form of the exchange Hamiltonian in Eq. (4.76) cannot straightforwardly be converted into a classical analogue magnetic field. From the expectation values of the ground states shown in Table 5.1 the resulting field has both for HTO and DTO a net component parallel to exchange (i.e. exchange dominates). Interestingly the values dipolar and exchange separately are of the same orders of

magnitude for HTO, while of for DTO they differ by one order of magnitude. This, according to such analysis, on the expectation values seems to justify the resulting two orders of magnitude of difference between HTO and DTO when compared to the case with both type of interactions.

A very important result of this analysis is that the direction of the ground state of the central ion in $\boldsymbol{A}$ confirms a resulting effective-field purely perpendicular and at angles $\phi = 150\,^\circ, 30\,^\circ$ for which the full tunnelling is guaranteed from the results in section 2.5. In the following section this is discussed more explicitly in the context of the quantum dynamics of the central ion in Fig. 5.1 which are induced by the quantum-quench $\bar{\boldsymbol{A}} \to \boldsymbol{A}$.

All the results found here using the configuration $\boldsymbol{A}$ in Fig. 3.7 of Chapter 3 may also be verified for the case $\boldsymbol{B}$ of the same figure. The case $\boldsymbol{C}$ therein does not play any explicit role in the quantum dynamics of a RE^{3+} ion under the two-tetrahedra analysis as it leads to null transverse fields [3]. The lower order dipolar contributions from further neighbours are likely to characterise the dynamics in this case (this might be a direction for further studies).

5.1.5 Quantum spin tunnelling of a RE^{3+} ion next to a monopole

The time-evolution for the RE^{3+} ion undergoing the quantum-quench $\bar{\boldsymbol{A}} \to \boldsymbol{A}$ in Fig. 5.1, is illustrated in the diagrams of Fig. 5.2 for HTO (left) and DTO (right). For consistency with the analysis of the previous section, the panels show the quantum dynamics of the central RE^{3+} for three different choices of n.n. coupling. From top to bottom these are: only dipolar, only exchange and dipolar together with exchange (the latter being the most realistic one for spin-ices).

The plots of the probability density confirm the occurrence of a full tunnelling for all cases, which is consistent with the effective fields found pointing at angles $(\theta, \phi) = (90\,^\circ, 30\,^\circ + n60\,^\circ)$ with n integer (see section 2.5). The curves for the average $\langle \hat{J}_z(t) \rangle$ accordingly oscillate from the initial condition to the opposite side, highlighting the full tunnelling of the probability density at $t = \tau$. For intermediate times the probability is distributed between the two far ends of the M_J axis; the distribution of the probability can be inspected from the intensity of yellow in the density plots and from the value of their average in $\langle \hat{J}_z(t) \rangle$. Since in this case the initial condition are proper of the system, i.e. $|\psi(0)\rangle = |\psi^{(\boldsymbol{A})}\rangle$, the "jitter" in $\langle \hat{J}_z(t) \rangle$ that was observed in the polarised initial conditions in section 2.5 is now suppressed (the curves are smooth without oscillations). In general a manifestation of the jitter has to be implicit in any kind of measurement, as the observable used in general would not commute with the crystal-field Hamiltonian. It is likely though that the oscillations would be absorbed in the noise signal because of their elevated frequency. A stronger manifestation of the oscillations in $\langle \hat{J}_z(t) \rangle$ is expected in analogous systems, for example $Tb_2Ti_2O_7$, where the polarisation of the ground state of the Tb^{3+} ion is less pronounced and the splitting with the first excited states of the CF leads to a stronger admixture between the quantum states.

The flipping-timescales are in general different depending on the system and on the in-

[3] The dipolar fields are identically null as shown in section 3.2.1. The effective exchange fields are null as the exchange Hamiltonian, as pointed out in section 4.5.2, has no transverse components being a purely diagonal interaction in the $|M_J\rangle$ basis.

teraction between the spins. These are listed in Table 5.2; the highest and lowest values are found for, respectively, only dipolar and only exchange in DTO. The contribution of exchange characterises strongly the output of the tunnelling rates when it is considered together with the dipolar fields. In both HTO and DTO it seems that exchange imposes a characteristic timescale of few microseconds. This shows that the analysis of the different strength in the (static) magnetic moment of ground states found in the previous section does not necessarily imply very different timescales. In fact, as it was thoroughly discussed in Chapter 2, the timescales are more directly related to the splitting ΔE_{01} due to the (effective) transverse fields between the quasi-bonding and quasi-antibonding configuration levels ($\tau \sim \hbar/\Delta E_{01}$).

	HTO	DTO
$\tau^{(Dip)}$	$6.97\,\mu$s	$19.31\,\mu$s
$\tau^{(Exc)}$	$0.13\,\mu$s	$0.25\,\mu$s
$\tau^{(Dip+Exc)}$	$1.36\,\mu$s	$0.56\,\mu$s

Table 5.2: The quantum-quench spin-tunnelling rates for HTO (left) and DTO (right). The values correspond to the time after which the probability density in Fig. 5.2 first tunnels from one polarised part of the M_J axis to the opposite one.

The values of τ found in the purely dipolar model highlight the relevance of the different power laws in ΔE_{01} in Fig. 2.9 for the magnitude $|\mathbf{B}| = 0.33$ Tesla of the dipolar field induced by the monopole. On this note it is worth opening a little digression about the realistic values of the dipolar field in the presence of a monopole. The Monte Carlo histograms obtained by C. Castelnovo and G. Sala, where a large spin-ice cluster is considered, are peaked in purely transverse fields of $|\mathbf{B}| = 0.55\,\mathrm{T}$, $0.03\,\mathrm{T}$ (these reflect a simple shift in the results of the cluster in Fig. 3.11). Unfortunately, at present, the simulations do not provide informations about the resulting directions of the dipolar field on the transverse plane, hence there the occurrence of full tunnelling is not guaranteed. Nonetheless, the timescales are expected to increase accordingly to Fig. 2.9. This would consist in a very little change for $|\mathbf{B}| = 0.55\mathrm{T}$ but, more importantly, it would imply the emergence of a new range of timescales in the order of the millisecond for $|\mathbf{B}| = 0.03\,\mathrm{T}$. Since the cluster calculations in Chapter 3 show how localised the effect of a monopole is for the fields of a RE^{3+}, here only the two-tetrahedra cluster are considered. Moreover, timescales of the order of the microseconds are less likely as quantum oscillation timescales (decoherence is expected to occur).

In the tunnelling which consider only exchange it is essential to bear in mind that the effective fields act in a direction that is opposite to the dipolar ones. This is shown

very neatly in the middle panels for the time evolution in Fig. 5.1 where the quantum mechanical tunnelling for the same system is completely reversed because of the initial condition and evolution Hamiltonian based on a system (with no dipolar interactions) which favours antiferromagnetic alignment.

This is relevant also for the case in which both interactions are considered (bottom panels in Fig. 5.1). It shows that the effect of the exchange in the whole picture is not only to induce an opposing polarisation but also to combine with the dipolar interactions in a constructive mechanism for tunnelling. The result may be of particular interest in speculating the sophisticated nature of the exchange interaction in a complex system such as spin-ice. It seems that the (antiferromagnetic) tensorial nature of the exchange interaction reveals itself as an underlying correlation of the spin-ice manifold which is suppressed in the frozen state by the longitudinal dipolar fields, but then fully restored in the presence of monopoles as they quench the longitudinal components of the dipolar fields.

The leading role of the exchange mechanism in the tunnelling of magnetic ions with large effective spin is common, for example, in molecular-magnets. In a tentative comparison between these systems it is interesting to note that molecular magnets are characterised by tunnelling rates typically of the orders of microseconds [32]. Moreover, the recent work in Ref. [34], carried out on single Ho^{3+} ions on a highly conductive substrate shows that the interplay between the symmetries of the crystal-field and an applied magnetic field holds the key in determining the decoherence timescales. Notably, the CF symmetry D_{3n} for their system has exactly the same terms in the Hamiltonian of the spin-ice RE^{3+} ions [34]. The main result they achieve is the ability to extend the timescales for decoherence well beyond the typical microseconds by tuning externally applied magnetic fields. From a speculative viewpoint, this is of interest for the tunnelling of RE^{3+} ions in spin ice where an extension of the timescales is found because of the role played by the dipolar fields. This is encouraged by the analytical perturbative approach in Appendix A, where it is shown in detail how the occurrence of the power-laws for ΔE_{01} is a unique consequence of the matrix elements of the field perturbation over the CF ground-states which reflect the symmetry of the system. The presence of exchange is expected to give non null matrix elements because of the multi-off-diagonal components which appear in Eq. (4.76). Further detailed studies need to be conducted on the role of exchange in coupling with the local symmetry of the crystal-field environment. It is important to underline that at this stage, the effect on the exchange interaction does look as a reduction in the stretching of the timescales that are found only in the presence of (classical) magnetic fields.

The results shown in this section establish the occurrence of the full-tunnelling in the quantum-quench $\bar{\boldsymbol{A}} \to \boldsymbol{A}$. Exactly analogous is the case $\bar{\boldsymbol{B}} \to \boldsymbol{B}$ ($\boldsymbol{B}$ can be visualised in Fig. 3.7). The case $\bar{\boldsymbol{C}} \to \boldsymbol{C}$ in not considered as the resulting effective fields are null, as commented closing the previous section. This can represent the ideal system to study the lower order effects due to the further dipolar interactions; in this case long timescales of the order of microseconds are expected and no suppression from exchange can be considered as this is only a nearest neighbour interactions for the RE^{3+} in spin-ice.

The implications of the quantum-quench and the statistics found for the full-tunnelling of a RE^{3+} ion in spin ice are discussed in the following section in the context of the

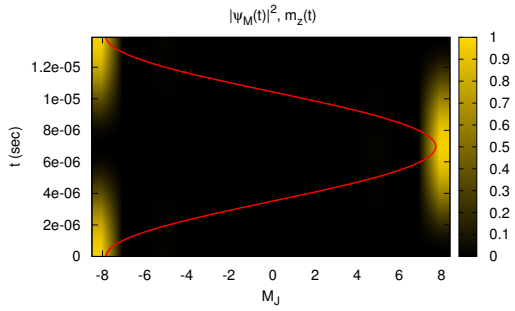

HTO - n.n. Dipolar only

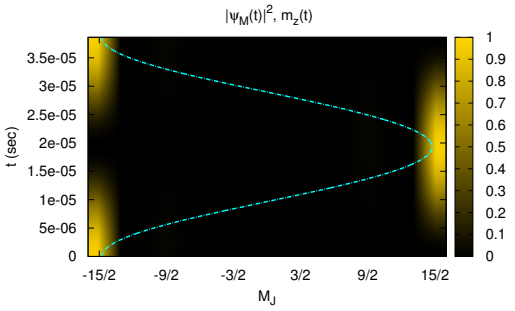

DTO - n.n. Dipolar only

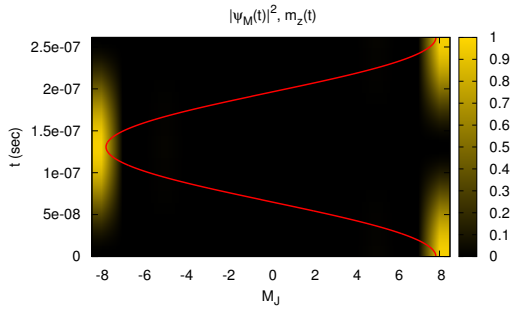

HTO - n.n. Exchange only

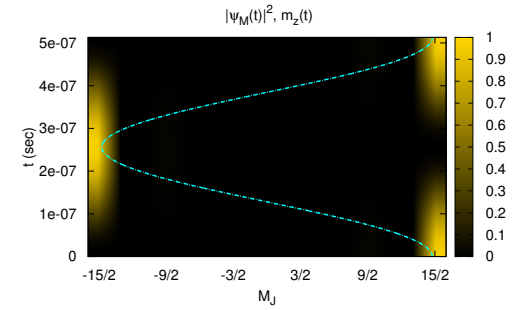

DTO - n.n. Exchange only

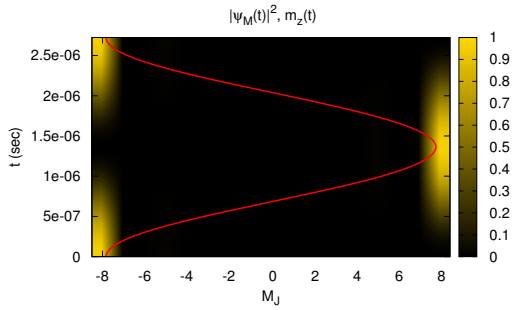

HTO - n.n. Dipolar + Exchange

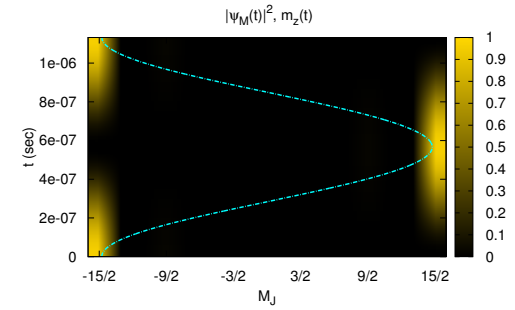

DTO - n.n. Dipolar + Exchange

Figure 5.2: Time-evolution from the quantum-quench mechanism for HTO (left) and DTO (right). In analogy with Figs. 2.12-2.14, the density plots show the probability density $|\psi(t)|^2 = |\langle M_J|\psi(t)\rangle|^2$, and, overlaid, the curves for $\langle \hat{J}_z(t)\rangle$ with $|\psi(t)\rangle$ state of the RE^{3+} ion at time t. The top, central and bottom panels represent the time-evolution for the quantum-quench of a RE^{3+} ion in the centre of a two-tetrahedra cluster with, respectively, only dipolar, only exchange and dipolar together with exchange interactions. In all cases we find full tunnelling as a consequence of the local symmetries: the effective fields due to a monopole are always at angles $\phi = 30\,^\circ + n\,60\,^\circ$ with n integer. The small oscillations in $\langle \hat{J}_z(t)\rangle$ (jitter) are suppressed as the initial conditions are now the ground-states of the Hamiltonian for the central RE^{3+} ion in a cluster with surrounding spins as shown in the top panel Fig. 5.1 (in Chapter 2 ad-hoc polarised states $|M_J\rangle = \pm|J\rangle$ were imposed). In the case with only exchange interactions (central panels) the whole process is reversed (in M_J, hence in the local $\mathbf{z_0}$) as the effective fields point exactly in opposite directions compared to the dipolar ones.

propagation of a monopole across a cluster.

5.2 Monopole hopping and the problem of decoherence

From the model of quantum-quench given in the previous section it is possible to draw an enriched picture for the propagation of a monopole.

Magnetic susceptibility experiments suggest that monopoles propagate according to Brownian motion with a temperature-independent diffusion constant [20]. In this context the athermal character of the diffusion constant is invoked as evidence of quantum tunnelling of the spin involved in the monopole hop. Beside, out of equilibrium experiments consisting of thermal quenches [22] and field quenches [23] reveal the dependence of the relaxation rates on the kinematic constraints the ice-rules on the pyrochlore lattice impose on the hopping of the monopoles. On this issue, a particular relevance is given to spin-configurations, such as the one in Fig. 3.4, which consist in non contractible monopole-antimonopole (bound) pairs. The impact of such bound pairs is detected also by other experimental means [21, 19] and so far seem to be the main mechanism for the occurrence of distinct relaxation rates typical in spin-ice materials.

The quantum-quench, exploiting the statistical two-tetrahedra analysis, allows a refinement in the possible paths which the monopole can undertake whenever it hops through a lattice of tetrahedra frozen in the 2in-2out state. Moreover, the insights from the tunnelling provide a lower bound of the decoherence timescales which need to be considered for the occurrence itself of the monopole-hopping.

5.2.1 A "quantum-quench" view on the propagation of a monopole

A pictorial representation for the motion of a monopole in spin-ice is given in Fig. 5.3. The four panels account for the different "time-lapses" describing the hopping of the monopole from the tetrahedron it occupies in Fig. 5.3a to the one where it ends up in Fig. 5.3d.

In the context of the quantum-quench model, the focus is again on a two-tetrahedra cluster whose central spin undergoes the same quench $\bar{\boldsymbol{A}} \rightarrow \boldsymbol{A}$ previously analysed. The possibility to focus on the central site of a larger cluster only in terms of the "quantum-quench two-tetrahedra view" is justified from the histograms of the dipolar fields in Figs. 3.11-3.13 which predict the sudden removal of the longitudinal dipolar field (for the central site) occurring "exactly" at the time-lapse ($t = 0$) when the monopole arrives (Fig. 5.3c).

In such a pictorial representation the hopping time-scale is considered of the order of the tunnelling-rate τ assumed to be an estimation of the decoherence timescale which transposes a tunnelling into an effective flip. In loose words, we take the simplified view that the full flip occurs around the first half period in Fig. 5.2. At present, this is a reasonable approximation as the one presented here is only an *a posteriori* analysis on the motion of a monopole in a frozen arrangement of the spins in the pyrochlore lattice. In practise it would be necessary to set a more sophisticated description of the RE^{3+} ion time-evolution to consider also the coupling with an environmental bath.

The tunnelling-rates coupled to the statistic dependence of the hopping on the spin-

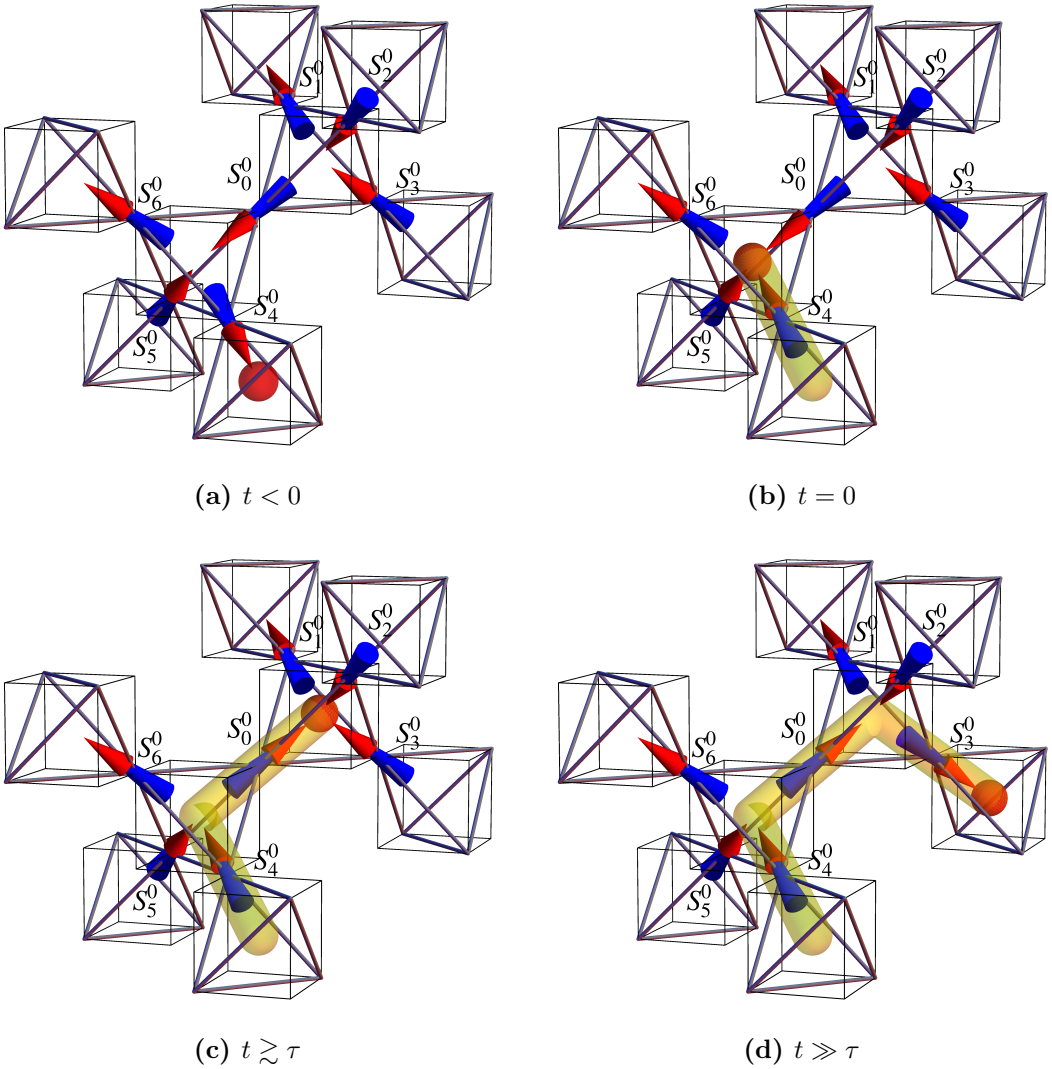

(a) $t < 0$ **(b)** $t = 0$

(c) $t \gtrsim \tau$ **(d)** $t \gg \tau$

Figure 5.3: Pictorial representation for the propagation of a monopole in spin ice. This example shows four consecutive "snapshots" (a,b,c,d) of a north-monopole hopping across the diamond lattice by means of three consecutive spin flips on adjacent pyrochlore sites. The cluster consists of eight tetrahedra, as in Figs. 3.11-3.13. Only the seven central spins are shown to emphasise the two-tetrahedra clusters in Figs. 5.1, highlighting the effects on the central site due to the configurations of the nearest neighbours. In (a), at a time $t < 0$, the monopole sits in a tetrahedron away from the central RE-site which is pinned down by a longitudinal dipolar field (Fig. 5.1a). In (b), at $t = 0$, the arrival of the monopole quenches the longitudinal field. The central ion can tunnel coherently as in Fig. 5.2 because of the purely transverse effective-fields (Fig. 5.1c). The occurrence of decoherence at $t \gtrsim \tau$ consists in the hopping of the monopole in the (c) configuration. Depending on the configuration of the nearest and next nearest neighbours spins the monopole can proceed on its propagation across the lattice (d). The yellow "tube" traces the trajectory of the monopole which leaves a chain of flipped spins behind it (often called a Dirac string).

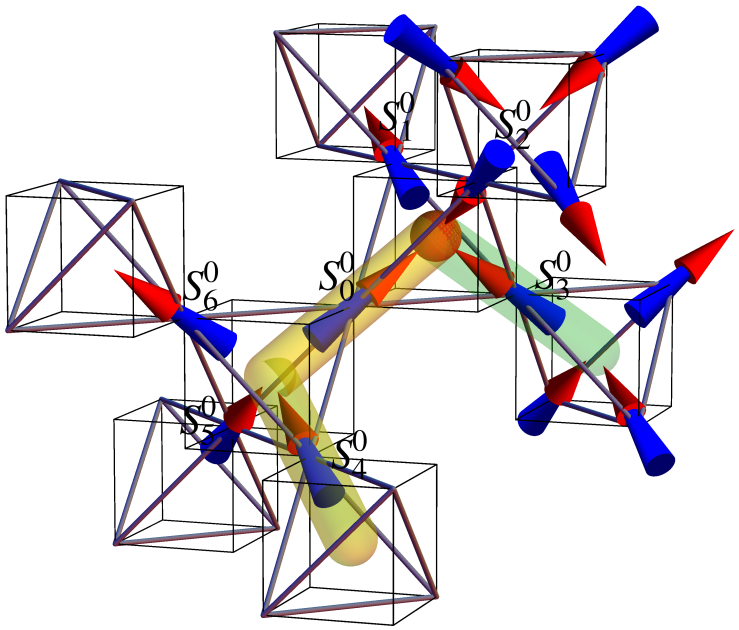

(a)

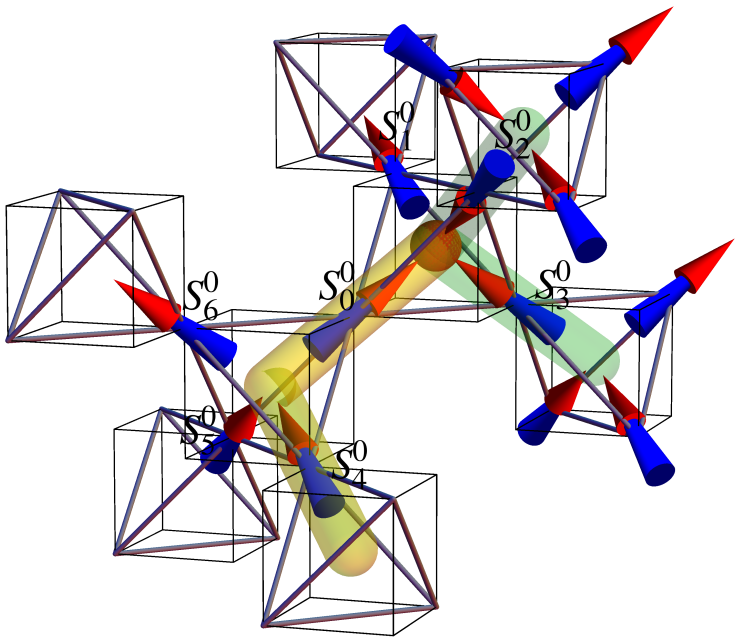

(b)

Figure 5.4: Comparison between a "1-way" and a "2-way" spin configuration for the monopole hopping; the cluster shows more in detail the spin-structure of the spins in the vicinity of the monopole in Fig. 5.3c. In both cases the monopole, from its current position shown, can either go backward (through S_0^0), or flip through S_3^0 (S_1^0 cannot flip because it would not make the monopole hop but rather produce a higher energy excitation). In the bottom panel though, going through S_2^0 is also allowed (note two green tubes departing from the monopole towards two different directions). In contrast, in the top panel the occurrence of flipping for S_2^0 is suppressed (in a n.n. analysis) as the spins surrounding it create a null on-site effective field (note S_0^0, S_1^0, S_3^0 have opposing counterparts beyond S_2^0, hence only one green-channel).

configurations offer a more "quasi-deterministic" view in the propagation of a monopole. A theoretical model for a realistic coupling of the system with the experimental probes represents the next step inx assessing the predictive power of the present theory. On this note, it is important to emphasise that the current predictions already give a good estimation of the low temperature dynamics as they are based on a hopping athermal timescale which is set as an external parameter [25, 26]. The present model, aim to be a refinement of these and promises to cover range of temperatures where the current theories collapse. There is no current use of temperature in the theory present in this thesis. However, the two different levels of description, with one eye on the local physics of the RE^{3+} ion and the other on the effective fluctuations induced by the surrounding neighbouring dipoles, are likely to be apt in differentiating the effect of the temperatures on two separate scales and, at the same time, in combining together in the unified modelling allowed by the quantum-quench.

Although the theoretical model presented in this thesis is based on an accurate description of the microscopic implications of the monopoles in a spin-ice material, its ability to make predictions is conditioned to its statistical character and cannot be considered deterministic in a rigorous sense. The present statement may seem redundant, not only because of the uncertainty which characterise the statistics of any microscopic system even more because spin-ice is intrinsically is defined by its geometrical frustration (i.e. intrinsically disordered). Nonetheless, as recent studies investigate the occurrence of a *true* spin-ice ground state [72, 73, 74], it may be tempting to think that in the quantum-quench picture of monopole motion the "history of the monopole" can be deduced uniquely by the compelling constraints induced by the ice-ruled states. As shown in Fig. 5.4 the trajectory of a monopole can be defined only once it has been traced. In this figure the time-frame of Fig. 5.3c is shown in two different possibilities: the top one, coinciding with the consequent occurrence of Fig. 5.3d, shows that the spin configurations of the further spins are such that the monopole can go only down one way; the bottom one is an instance in which the two totally equivalent (from an ice-rule perspective) neighbouring spin-configurations give two possible channels for the hopping of a monopole. In other words, this analysis shows that the statistical ratio 2/3 does not imply that the monopole will only encounter two out three (including the backward one) propagation channels in each tetrahedron, but, more in general, it describes statistically the possibility for the occurrence of the hopping.

The quantum-quench model, despite its localised approximation which neglects the contribution of the long-ranged dipolar fields, offers a neat picture accounting for a meaningful characterisation of the propagation of monopoles. More in general, thanks to its underlying (quantum) degrees of freedom, it promises also to be ideal for testing non-equilibrium dynamics where the whole system undergoes sudden quenches imposed by external probes [24].

Below is presented an estimation of the effective mass of the monopole obtained directly from the tunnelling rates in Table 5.2 to emphasise the localised character which can be defined for the monopoles thanks to a microscopic quantum decryption of the RE^{3+} ions.

Mass of a monopole

The propagation of the monopoles is subject to (asymmetrical) local constraints which inhibit the full mapping of its motion with the one of a tight binding model. Nonetheless it is intriguing to exploit the timescales derived in section 5.1.5 and see the estimation of the effective mass of the monopoles that is predicted.

This can be realised by setting

$$\mathrm{t} \sim \hbar/\tau \tag{5.5}$$

for the hopping energy term of a tight-binding monopole-model, where τ is the timescale for the hopping to occur. Using

$$E_k \sim 2\mathrm{t}\cos(ka) \approx \frac{\hbar^2 k^2}{2m^*} \tag{5.6}$$

we can extrapolate

$$m^* = \frac{\hbar^2}{2\mathrm{t}a^2} \sim \frac{\hbar\tau}{2a^2}. \tag{5.7}$$

In spin-ice a would be the distance between the centres of two adjacent tetrahedra. As the nearest neighbours for the RE^{3+} ions is $r_{nn} \approx 3.54\text{Å}$, it is reasonable, for simplicity, to approximate $a \sim 10^{-10}\,\mathrm{m}$. Analogously the timescale of the hopping is averaged as $\tau \sim 1\,\mu\mathrm{s}$, interpolating the most realistic tunnelling rates for HTO and DTO in Table 5.2, which leads to

$$m^* \sim 10^{-20}\,\mathrm{Kg}\,. \tag{5.8}$$

From this it is straightforward to obtain the monopole's de Broglie wavelength:

$$\lambda^* = \frac{h}{\sqrt{2m^* k_B T}} \sim 10^{-12}\,\mathrm{m} \quad \text{at} \quad T = 1\,\mathrm{K} \tag{5.9}$$

which is $\lambda \ll a$, meaning that the monopoles are heavily localised. This is consistent with the standard view that monopoles are classical particles, and shows that involving local quantum dynamics of the RE^{3+} does not undermine the classical view of the monopoles. The underlying quantum dynamics is in turn exploited as a mechanism from which classicality emerges from the quantum substrate. On this note, in the following section, a little digression about decoherence is presented.

5.2.2 A note on decoherence

The current view on the propagation of the monopoles, which we assess here by means of a quantum-quench, consists in the occurrence of consecutive spin flips. So far there has been no fulfilling interpretation of how this might occur.

The model presented here is the first realistic description for the occurrence of the tunnelling. However, the tunnelling per se does not lead to a full flip of the spin. The quantum mechanical time-evolution, because of its unitarity, predicts coherent

oscillations for an indefinite time. To account for the actual spin-flip in the previous section we assumed a time of decoherence coinciding with the tunnelling rate (this is defined as the amount of oscillation from one extreme of the polarisation axis to the opposite one).

In order to obtain a more realistic description of the time-evolution, it is necessary to introduce a mechanism of decoherence. There are several theories which describe quantum mechanical evolutions of systems coupled to a bath of phonons present in the substrate. However, among the others there is a line of research dedicated to the mechanism of decoherence that has been exploited in the context of quantum theory of information [**?**, 75]. Such theories promise to be relevant for spin-ice as they do not treat the environment as a simple bath which causes decoherence by destroying quantum fluctuations. In contrast, they consider the evolution of the system with the environment in a "constructive way", namely the environment is considered as an entity of selection of the preferred states which make the classical observables emerge from the quantum ones through a process of stabilisation that is called *Einselection* (Environment Induced Superselection).

Developing a theory of this kind is beyond the scope of this work. Nonetheless it is important to emphasise the crucial role that decoherence plays in stabilising the occurrence itself of a classical object such as the monopole. From the experimental signatures which show the monopoles are objects heavily localised, it is tempting to speculate whether this stabilisation is the consequence of a process of "self-selection" which the underlying degrees of freedom of the system do in establishing the monopoles as the entities responsible for the thermodynamics observed. This represents a challenge for the current understanding of spin-ice materials and promises to shed an original type of light on these systems since this kind of approach has not been adopted so far.

"There is a new world beyond Landau's theories. The new world is rich and exciting."

X.G. Wen [2]

6

Conclusions and outlook

The emergence of magnetic monopole excitations in spin-ice materials represents a peculiar instance of outgrowth of classical quasiparticles from a quantum substrate. The combined effect of the topological properties of the pyrochlore lattice and the ferromagnetic frustration between the classical magnetic dipoles [5] is, per se, the realisation of a new state of matter, i.e. the vacuum which the monopoles populate [22]. None of the chemical constituents of the compounds $Ho_2Ti_2O_7$ and $Dy_2Ti_2O_7$, however, can be considered as an individual classical entity prior to the crystallisation [7, 6], hence it is essential to bear in mind the complex structure where such an effective-vacuum is defined. In these systems, in fact, the occurrence of a classical behaviour of the magnetic RE^{3+} ions is ultimately a consequence of the strong quantum correlations between the electrons in their unfilled shells [44, 27]. The magnetic moments in classical spin-ice materials are not the result of nano-sized agglomerates as in artificial spin-ice [76, 77], but rather the individual RE^{3+} ions with well defined quantum mechanical properties [27]. Besides, the bonding distance between any RE^{3+} ion and the O^{2-} oxygen (O1) in the centre of a tetrahedron is one of the shortest measured in magnetic compounds [6] and, indeed, an antiferromagnetic component of (quantum) superexchange coupling between neighbouring RE^{3+} ions is measured in experiments [5]. These factors are only a fraction of the complex organisation defining the quantum substrate from which the classical frustration, and so the monopoles, in spin-ice materials emerge. As such, an investigation of the microscopic structure of these materials is a challenge and promises to enrich the landscape of the spin-ice physics and, more generally, of the border between classical reality and quantum-mechanical observables [31].

From an experimental point of view, beside the success of the classical spin-ice picture of frustration and monopoles [9, 15, 16, 21], different experimental techniques expect quantum mechanical interpretations to give a richer description of the characteristic slow dynamics which occur at different temperature regimes [78, 17, 21, 19] (some of these are still under debate). The occurrence of a quantum spin-tunnelling, in

particular, is highlighted by the temperature-independent dynamics observed with ac-susceptibility and muon spin rotation techniques [78, 79, 19, 20, 80], and it needs to be taken into account to assess the flipping of the spins across the high energy CF barrier separating the two Ising-like configurations. These are some of the elements suggesting that a microscopical model of the underlying magnetic interactions at a quantum mechanical level can shed light into some of the current shaded regions left from the purely classical viewpoints.

The work presented in this thesis consists in a microscopic study of the quantum mechanical properties of the magnetic RE^{3+} ions in spin-ice materials. The main trend has been a characterisation of the new classical and quantum degrees of freedom which occur in the RE^{3+} ions at the vertices of a tetrahedron hosting a monopole, with the aim of establishing a unified view for the microscopic mechanisms regulating the monopole-hopping. Following the hierarchical structure that sets the energy scales for the physics of a spin-ice material this was achieved by :

i) analysing the quantum mechanics of a single RE^{3+} ion (Chapter 2),

ii) determining the strength of the (classical) dipolar fields acting on it (Chapter 3),

iii) developing an original model for the (quantum) exchange interactions between neighbouring RE^{3+} ions (Chapter 4).

The results obtained by pursuing these three tasks led to the formulation of the model of quantum-quench given in Chapter 5 to provide a realistic description for the hopping of the monopoles.

In this thesis there is no explicit study of the coupling with experimental probes; the approach is deliberately directed on the investigation of the structural, topological and statistical properties that can be assessed simply by "looking more deeply" into the system from the original perspectives opened by the discovery of the monopoles.

The original view that we gain from these studies may be summarised in the quantum-dynamical character which emerges for the RE^{3+} ions in the presence of a monopole, in spite of what one may expect from a classical quasiparticle. The quantum-quench model in Chapter 5, which summarises most of the work in a monopole-hopping view, seems to intercept the manifestation of a monopole between the two instants defining the occurrence of a localised quantum fluctuation (RE^{3+} quantum-spin tunnelling) and vice versa defines the quantum fluctuation as the necessary means which enable the monopole to manifest an itinerant character. It is important to emphasise that the quantum mechanical effects found remain localised in the vicinity of a monopole, mainly as a consequence of the strong dipolar interactions which act as "pointer operators", in a view familiar to the quantum-information theoretical language [**?**, 81], and make any other quantum fluctuation collapse in the classical background. It is intriguing to speculate, in a Quantum-Darwinistic view [75], whether spin-ice could represent an instance where classical physics emerge as a sort of "self organisation" of the underlying quantum degrees of freedom which, in contrast, are hidden in the background environment by the standard classical view. Such degrees of freedom might be, for example, the pointer states imposed by the local symmetry of the crystal field environment. These latter arguments, however, are given here only in a speculative fashion.

On the other hand experiments can definitely test the ability of the quantum-quench

model and the other results presented in this thesis. Beyond the ones already mentioned that are directly related to the spontaneous dynamics of tunnelling [79, 82, 20], also non-equilibrium experiments [23, 24] are good candidates to establish the versatility of the these theoretical tools. Other experiments based on chemical variations in the nature of the materials, for example in the context of oxygen vacancies modifying the crystal-field structure [83], have already shown how microscopical modifications my affect the behaviour of the monopoles. Last but not least, the recent investigations about violation of the zero-entropy spin-ice ground state [72, 74] pose questions which envisage the importance of a quantum-mechanical view, as it has been already shown in other theoretical studies [73]. In this context also the analysis on the possible mutual interference of the dipolar fields implicit in Eq. (3.9) may lead to insights to the open questions.

To conclude, the key developments representing an original output of the present work are listed separately in the next page, following the same order as they appear throughout the thesis to help the reader in localising the "hot spots" across the whole manuscript.

Key original results

Chapter 2

- study of the splitting ΔE_{01} of the crystal-field (CF) ground-state doublet for a spin-ice RE^{3+} ion under a magnetic field purely transverse to the local $\langle 111 \rangle$ direction (section 2.4.1; Figs. 2.9-2.10)
- explanation of the different power laws behaviour of ΔE_{01} ($\propto |\mathbf{B}|^2$ for HTO, $\propto |\mathbf{B}|^3$ for DTO) by means of an analytical third-order degenerate perturbation theory (Appendix A; Eqs. (A.23,A.31,A.41,A.43))
- study of the quantum tunnelling of a spin-ice RE^{3+} ion with emphasis on the interplay between applied fields and the local crystal-field symmetries (section 2.5; Figs. 2.12-2.14)

Chapter 3

- method to evaluate the dipolar fields on a given RE-site in terms of pairwise equidistant spins (section 3.1; Eq. (3.9) is the generic analytical formula for a cluster of $2n + 1$ dipoles)
- discovery of the ratio 2/3 in the statistic of configurations with a monopole in a two-tetrahedra cluster which can lead to an actual spin-flip (section 3.2.1; in particular Fig. 3.7)
- quenching of the longitudinal dipolar field from the arrival of a monopole (section 3.2.2.2, in particular Figs. 3.11-3.13)

Chapter 4

- computer-algebra routine capable of evaluating the many-body exchange interactions for RE^{3+} ions in a pyrochlore Oxide (the method briefly described in section 4.3.2.1 is of general use as it calculates, for a generic magnetic ion, the exact decomposition of the angular momentum eigenstates in terms of many-body fermionic operators)
- generalisation of the superexchange Hamiltonian from Ref. [30] for any RE^{3+} ion in a magnetic pyrochlore oxide, by means of a strong-coupling fourth-order perturbation theory (section 4.4 from Eq. (4.50) to Eq. (4.75); more details in Appendinx B.2)
- original quasi-quantum (analytical) expression for the exchange interaction of a quantum RE^{3+} in a cluster of six frozen neighbouring RE^{3+} (section 4.5; Eq. (4.76))

Chapter 5

- quantum-quench model; this is useful for a general description of the response of a RE^{3+} ion under a sudden perturbation and, more specifically, for the estimation of spontaneous spin-tunnelling probability and characteristic timescales of a RE^{3+} in the presence of a monopole (section 5.1.5; Table 5.2 , Fig. 5.2)

A

Perturbation theory for a RE-ion in a D_{3d} symmetry under a magnetic transverse field

A.1 Degenerate Perturbation Theory

In this appendix we give more details about the *perturbative* results given in Sec.2.4.1, mainly in Eqs. (2.33a-2.35). In particular the focus is on the case of a perturbation applied to a system with a doubly degenerate ground state (GS), because this is what characterises both systems discussed in this thesis and most magnetic pyrochlore compounds. Before dealing with the details of such cases it is necessary to introduce perturbation theories in quantum mechanics in the most general context.

A.1.1 Preliminaries on perturbation theories for quantum systems

We start by considering a generic quantum system that can be described by the following Hamiltonian

$$\hat{H} = \hat{H}_0 + \lambda \hat{V} \tag{A.1}$$

where λV is a small perturbation with respect to H_0 (unperturbed Hamiltonian) whose Schrödinger equation

$$\hat{H}_0 \left|\psi_n^{(0)}\right\rangle = E_n^{(0)} \left|\psi_n^{(0)}\right\rangle \tag{A.2}$$

can be solved exactly ($\langle\psi_n^{(0)}\left|\psi_m^{(0)}\right\rangle = \delta_{nm}$). The perturbative parameter λ tunes the applied perturbation and allows to describe eigenstates and eigenenergies of the full Hamiltonian as power expansions (up to a certain (j) order) of the unperturbed ones. In particular λ is a real number such that $\lim_{\lambda\to 0} H = H_0$. This is the condition for *adiabatic continuity* , and it guarantees that, when we decrease the perturbation down

to zero, the eigenfunctions and eigenvalues of $\hat{H}$ match (continuously) the respective ones of $\hat{H}_0$ (for more details about perturbation theory in general see Ref. [64]).

For the systems studied in this thesis, it is relevant to consider the case where the n-th energy level is the ground state *doublet* (GS) of a quantum system solved by Eq.(A.2) (in the present work $\hat{H}_0 \equiv \hat{\mathcal{H}}_{CF}$, in Eq.(2.27) of the main text). This means that two states $|\psi_0^{(0)}\rangle, |\psi_1^{(0)}\rangle$ in Eq.(A.2) have the same energy (for example the ground state doublet $E_{GS}^{(0)}$ of the crystal-field Hamiltonian for HTO and DTO). We study how this doublet can be resolved by means of a perturbing potential $\hat{V}$ (a magnetic field in the case of interest; see Eqs. (2.34,2.31)). In loose words, here is presented *how* a perturbation splits a doublet into two different energy levels$E_\pm$. Emphasis is given to the role of the symmetries of the unperturbed Hamiltonian in characterising the order of perturbation j which actually lifts definitively the degeneracy. The main reason for emphasising this is the relevance of the perturbations in driving systems out of equilibrium, inducing dynamics which cannot be described only in terms of the exactly solved Hamiltonian $\hat{H}_0$.

The effect of the perturbation on the two levels originating from the doublet splitting is described by the following expansion in power of the perturbative parameter λ:

$$\begin{aligned} E_+ &= E_{GS}^{(0)} + \lambda E_+^{(1)} + \lambda^2 E_+^{(2)} + \lambda^3 E_+^{(3)} + \dots \\ E_- &= E_{GS}^{(0)} + \lambda E_-^{(1)} + \lambda^2 E_-^{(2)} + \lambda^3 E_-^{(3)} + \dots \end{aligned} \tag{A.3}$$

Here $E_\pm^{(j)}$ represents the j-th order energy corrections involved to approximate the *exact* energies $E_\pm$ (note the unperturbed level is doubly degenerate; i.e. the *zero*-th order term is $E_{GS}^{(0)}$ is both). This shows that although $\hat{H}_0$ has a degeneracy in $E_{GS}^{(0)}$, still this won't be the case when we consider the $\hat{H}$. More precisely this means that each energy will correspond to only one of the two states

$$\begin{aligned} |\chi_+\rangle &= |\chi_+^{(0)}\rangle + \lambda\,|\chi_+^{(1)}\rangle + \lambda^2\,|\chi_+^{(2)}\rangle + \lambda^3\,|\chi_+^{(3)}\rangle + \dots \\ |\chi_-\rangle &= |\chi_-^{(0)}\rangle + \lambda\,|\chi_-^{(1)}\rangle + \lambda^2\,|\chi_-^{(2)}\rangle + \lambda^3\,|\chi_-^{(3)}\rangle + \dots \end{aligned} \tag{A.4}$$

This is the Schrödinger equation for the exact two states $|\chi_\pm\rangle$, here expressed as a power series of λ. If we substitute Eqs. (A.3-A.4) into

$$\hat{H}\,|\chi_\pm\rangle = E_\pm\,|\chi_\pm\rangle\,, \tag{A.5}$$

and we group the terms with the same power of λ, we find the following equations for the different orders in perturbation (here we show from 0-th to 3-rd order)

$$(\hat{H}_0 - E_{GS}^{(0)})\,|\chi_\pm^{(0)}\rangle = 0, \tag{A.6}$$

$$(\hat{H}_0 - E_{GS}^{(0)})\,|\chi_\pm^{(1)}\rangle = -(\hat{V} - E_\pm^{(1)})\,|\chi_\pm^{(0)}\rangle\,, \tag{A.7}$$

$$(\hat{H}_0 - E_{GS}^{(0)})\,|\chi_\pm^{(2)}\rangle = -(\hat{V} - E_\pm^{(1)})\,|\chi_\pm^{(1)}\rangle + E_\pm^{(2)}\,|\chi_\pm^{(0)}\rangle\,, \tag{A.8}$$

$$(\hat{H}_0 - E_{GS}^{(0)})\,|\chi_\pm^{(3)}\rangle = -(\hat{V} - E_\pm^{(1)})\,|\chi_\pm^{(2)}\rangle + E_\pm^{(2)}\,|\chi_\pm^{(1)}\rangle + E_\pm^{(3)}\,|\chi_\pm^{(0)}\rangle\,. \tag{A.9}$$

The corrections $E_{\pm}^{(j)}$ and $|\chi_{\pm}^{(j)}\rangle$ can be derived from these equations by means of perturbative analytical methods. In the following the focus is on the so called Rayleigh-Schrödinger perturbation theory.

A.1.2 The Rayleigh-Schrödinger method

As already mentioned, the advantage of a perturbation theory consists mainly in expressing the eigenstates and energies of $\hat{H}$ in terms of those found for $\hat{H}_0$. Hence, according to Eq.(A.4), if we find the coefficients $c_n^{\pm}$, $d_n^{\pm}$, $e_n^{\pm}$, $f_n^{\pm}$ in the following equations [1]

$$|\chi_{\pm}^{(0)}\rangle = \sum_{r=0,1} c_r^{\pm} |\psi_r^{(0)}\rangle \,, \tag{A.10}$$

$$|\chi_{\pm}^{(1)}\rangle = \sum_{n} d_n^{\pm} |\psi_n^{(0)}\rangle \,, \tag{A.11}$$

$$|\chi_{\pm}^{(2)}\rangle = \sum_{n} e_n^{\pm} |\psi_n^{(0)}\rangle \,, \tag{A.12}$$

$$|\chi_{\pm}^{(3)}\rangle = \sum_{n} f_n^{\pm} |\psi_n^{(0)}\rangle \,, \tag{A.13}$$

then we can express the two states $|\chi_{\pm}\rangle$ in Eq.(A.5) in terms of $\{|\psi_n^{(0)}\rangle\}$, the set of eigenvectors of the unperturbed Hamiltonian, Eq.(A.2). Moreover the Rayleigh-Schrödinger method consists in multiplying the different Eqs. (A.6) by the various $\langle\psi_n^{(0)}|$ so that we can find the energy corrections as a function of these coefficients and of the matrix elements $V_{nm} = \langle\psi_n^{(0)}| \hat{V} |\psi_m^{(0)}\rangle$. Here we briefly show how to proceed with this method in order to get $E_{\pm}^{(j)}$ for $j = 1, 2, 3$.

1st order The case of the first order degenerate perturbation theory can be found in many text books on quantum mechanics. Here, following the method given in Ref. [64], only little details are given, as an introduction of the original results for higher orders presented in this thesis.

Summarising, if we multiply the first order Eq.(A.7) by $\langle\psi_0^{(0)}|$ and $\langle\psi_1^{(0)}|$, we find the following

$$\begin{aligned} c_0^{\pm} V_{00} + c_1^{\pm} V_{01} &= E_{\pm}^{(1)} c_0^{\pm} \,, \\ c_0^{\pm} V_{10} + c_1^{\pm} V_{11} &= E_{\pm}^{(1)} c_1^{\pm} \,. \end{aligned} \tag{A.14}$$

To get this result we used the linear combinations Eqs. (A.10-A.11) in Eq.(A.7).This

[1] Note that the zero-th order terms $|\chi_{\pm}^{(0)}\rangle$ are linear combination only of the lowest $|\psi_0^{(0)}\rangle, |\psi_1^{(0)}\rangle$. In fact when the perturbation is absent, there is no mixing between the vectors in the eigenspace of $E_{GS}^{(0)}$ and those from the excited levels.

system can be rewritten as a 2-dim eigenvalue problem

$$\begin{pmatrix} V_{00} & V_{01} \\ V_{10} & V_{11} \end{pmatrix} \begin{pmatrix} c_0^{\pm} \\ c_1^{\pm} \end{pmatrix} = E_{\pm}^{(1)} \begin{pmatrix} c_0^{\pm} \\ c_1^{\pm} \end{pmatrix} , \tag{A.15}$$

that gives

$$\begin{aligned} E_+^{(1)} &= \frac{1}{2}\left[V_{00} + V_{11} + \sqrt{(V_{00} - V_{11})^2 + 4|V_{01}|^2}\right] \\ E_-^{(1)} &= \frac{1}{2}\left[V_{00} + V_{11} - \sqrt{(V_{00} - V_{11})^2 + 4|V_{01}|^2}\right], \end{aligned} \tag{A.16}$$

and the corresponding coefficients

$$\begin{aligned} \frac{c_0^+}{c_1^+} &= -\frac{V_{11} - E_{GS_+}^{(1)}}{V_{01}} , \\ \frac{c_0^-}{c_1^-} &= -\frac{V_{11} - E_{GS_-}^{(1)}}{V_{01}} . \end{aligned} \tag{A.17}$$

The difference $E_+^{(1)} - E_-^{(1)} = \sqrt{(V_{00} - V_{11})^2 + 4|V_{01}|^2}$ is the first order correction for the splitting, given in Eq.(2.35). Note that if $V_{01} = 0$ and $V_{00} = V_{11}$ there is no splitting (both levels have a first order shift $E_{\pm}^{(1)} = V_{00}$) and the coefficients $c_0^{\pm}, c_1^{\pm}$ in Eq.(A.10) remain undetermined.

Analogously if we multiply the same Eq.(A.7) by $\langle\psi_k^{(0)}|$ with $k = 2, 3, ...$ we obtain

$$d_k^{\pm} = \frac{c_0^{\pm} V_{k0} + c_1^{\pm} V_{k1}}{E_{GS}^{(0)} - E_k^{(0)}}. \tag{A.18}$$

Note that this is only a part of the coefficients in Eq.(A.11), the remaining $d_0^{\pm}$ and $d_1^{\pm}$ are still undetermined.

2nd order By multiplying $\langle\psi_0^{(0)}|$ and $\langle\psi_1^{(0)}|$ by Eq.(A.8) we obtain

$$\begin{aligned} &\langle\psi_0^{(0)}| (\hat{H}_0 - E_{GS}^{(0)}) \sum_n e_n^{\pm} |\psi_n^{(0)}\rangle = \\ &\qquad - \langle\psi_0^{(0)}| (\hat{V} - E_{\pm}^{(1)}) \sum_n d_n^{\pm} |\psi_n^{(0)}\rangle + E_{\pm}^{(2)} \sum_{r=0,1} c_r^{\pm} \langle\psi_0^{(0)} |\psi_r^{(0)}\rangle , \\ &\langle\psi_1^{(0)}| (\hat{H}_0 - E_{GS}^{(0)}) \sum_n e_n^{\pm} |\psi_n^{(0)}\rangle = \\ &\qquad - \langle\psi_1^{(0)}| (\hat{V} - E_{\pm}^{(1)}) \sum_n d_n^{\pm} |\psi_n^{(0)}\rangle + E_{\pm}^{(2)} \sum_{r=0,1} c_r^{\pm} \langle\psi_1^{(0)} |\psi_r^{(0)}\rangle . \end{aligned} \tag{A.19}$$

Here, since both $\langle\psi_0^{(0)}|$ and $\langle\psi_1^{(0)}|$ give energy $E_{GS}^{(0)}$, the terms on the left vanish and, by using Eq.(A.18), we can rewrite this system as

$$\begin{aligned} c_0^{\pm} E_{\pm}^{(2)} &= d_0^{\pm}(E_{\pm}^{(1)} - V_{00}) - d_1^{\pm} V_{01} - \sum_{k>1} \frac{c_0^{\pm}|V_{0k}|^2 + c_1^{\pm} V_{0k} V_{k1}}{E_{GS}^{(0)} - E_k^{(0)}}, \\ c_1^{\pm} E_{\pm}^{(2)} &= d_1^{\pm}(E_{\pm}^{(1)} - V_{11}) - d_0^{\pm} V_{10} - \sum_{k>1} \frac{c_0^{\pm} V_{1k} V_{k0} + c_1^{\pm}|V_{1k}|^2}{E_{GS}^{(0)} - E_k^{(0)}}. \end{aligned} \tag{A.20}$$

If a splitting was found already at the first order (i.e. we know $E_{\pm}^{(1)}$ and $c_0^{\pm}, c_1^{\pm}$), this is an inhomogeneous system of 2 equations for the real variable $E_{\pm}^{(2)}$ and the complex ones $d_0^{\pm}, d_1^{\pm}$. However, this is not the case in the systems of our interest since $V_{00} = V_{11} = V_{10} = V_{01} = 0$ (see the next section), so the second order Eqs.(A.20) reduces to

$$\begin{aligned} c_0^{\pm}\, E_{\pm}^{(2)} &= c_0^{\pm} \sum_{k>1} \frac{|V_{0k}|^2}{\Delta E_k^{(0)}} + c_1^{\pm} \sum_{k>1} \frac{V_{0k} V_{k1}}{\Delta E_k^{(0)}} \\ c_1^{\pm}\, E_{\pm}^{(2)} &= c_0^{\pm} \sum_{k>1} \frac{V_{1k} V_{k0}}{\Delta E_k^{(0)}} + c_1^{\pm} \sum_{k>1} \frac{|V_{1k}|^2}{\Delta E_k^{(0)}} \end{aligned} \tag{A.21}$$

where $\Delta E_k^{(0)} = E_{GS}^{(0)} - E_k^{(0)}$. It is convenient to rewrite this system of two equations for the variables $c_0^{\pm}, c_1^{\pm}$ in terms of the 2-dim eigenvalue problem

$$\begin{pmatrix} \displaystyle\sum_{k>1} \frac{|V_{0k}|^2}{\Delta E_k^{(0)}} & \displaystyle\sum_{k>1} \frac{V_{0k} V_{k1}}{\Delta E_k^{(0)}} \\ \displaystyle\sum_{k>1} \frac{V_{1k} V_{k0}}{\Delta E_k^{(0)}} & \displaystyle\sum_{k>1} \frac{|V_{1k}|^2}{\Delta E_k^{(0)}} \end{pmatrix} \begin{pmatrix} c_0^{\pm} \\ c_1^{\pm} \end{pmatrix} = E_{\pm}^{(2)} \begin{pmatrix} c_0^{\pm} \\ c_1^{\pm} \end{pmatrix}. \tag{A.22}$$

Then, using the same algebra for Eq.(A.15), we find

$$\begin{aligned} E_{\pm}^{(2)} = \frac{1}{2} \Bigg\{ & \sum_{k>1} \frac{|V_{0k}|^2 + |V_{1k}|^2}{\Delta E_k^{(0)}} \\ & \pm \sqrt{\left(\sum_{k>1} \frac{|V_{0k}|^2 - |V_{1k}|^2}{\Delta E_k^{(0)}} \right)^2 + 4 \left| \sum_{k>1} \frac{V_{0k} V_{k1}}{\Delta E_k^{(0)}} \right|^2} \Bigg\} \end{aligned} \tag{A.23}$$

and

$$\frac{c_0^{\pm}}{c_1^{\pm}} = - \frac{\displaystyle\sum_{k>1} \frac{|V_{1k}|^2}{\Delta E_k^{(0)}} - E_{GS_{\pm}}^{(2)}}{\displaystyle\sum_{k>1} \frac{V_{0k} V_{k1}}{\Delta E_k^{(0)}}}. \tag{A.24}$$

The difference $E_+^{(2)} - E_-^{(2)}$ is the coefficient of λ^2 on the righthand side of Eq.(2.35). It is important to underline that if the matrix in Eq.(A.22) is a multiple of the identity, i.e. if

$$\sum_{k>1} \frac{V_{0k}V_{k1}}{\Delta E_k^{(0)}} = 0 \quad \text{and} \quad \sum_{k>1} \frac{|V_{0k}|^2}{\Delta E_k^{(0)}} = \sum_{k>1} \frac{|V_{1k}|^2}{\Delta E_k^{(0)}}, \tag{A.25}$$

then there is still no splitting (both levels have a second order shift $E_\pm^{(2)} = \sum_{k>1} \frac{|V_{0k}|^2}{\Delta E_k^{(0)}}$) and the coefficients $c_0^\pm, c_1^\pm$ are still undetermined (note that in this case also $d_0^\pm, d_1^\pm$ are undetermined). This last possibility is the case of DTO, in which no second order splitting is found (the degeneracy of the GS is not lifted because the doublet level shifts with field).

If we now multiply the same Eq.(A.8) by $\langle\psi_h^{(0)}|$ with $h = 2, 3, ...$ we obtain

$$e_h^\pm = \frac{d_h^\pm E_\pm^{(1)} - \sum_n d_n^\pm V_{hn}}{\Delta E_h^{(0)}}. \tag{A.26}$$

This, in the cases of our interest ($E_\pm^{(1)} = V_{ur} = 0$ with u and $r = 0, 1$), reduces to

$$e_h^\pm = -\frac{d_0^\pm V_{h0} + d_1^\pm V_{h1} + \sum_{k>1} d_k^\pm V_{hk}}{\Delta E_h^{(0)}}, \tag{A.27a}$$

$$\text{i.e.} \qquad e_h^\pm = -\frac{d_0^\pm V_{h0} + d_1^\pm V_{h1} + \sum_{k>1} \frac{c_0^\pm V_{k0} + c_1^\pm V_{k1}}{\Delta E_k^{(0)}} V_{hk}}{\Delta E_h^{(0)}}. \tag{A.27b}$$

Hence to access the coefficients by $e_h^\pm$ with $h > 1$ it is necessary to know both $c_0^\pm, c_1^\pm$ and $d_0^\pm, d_1^\pm$.

3rd order The procedure for the third order is analogous to the second order one, hence we summarise only the main steps of the calculation. Multiplying $\langle\psi_0^{(0)}|$ and $\langle\psi_1^{(0)}|$ to Eq.(A.9) gives

$$\begin{aligned} c_0^\pm E_\pm^{(3)} &= \sum_n e_n^\pm V_{0n} - e_0^\pm E_\pm^{(1)} - d_0^\pm E_\pm^{(2)}, \\ c_1^\pm E_\pm^{(3)} &= \sum_n e_n^\pm V_{1n} - e_1^\pm E_\pm^{(1)} - d_1^\pm E_\pm^{(2)}. \end{aligned} \tag{A.28}$$

that is worth rewriting as follows:

$$\begin{aligned} c_0^\pm E_\pm^{(3)} &= e_0^\pm (V_{00} - E_\pm^{(1)}) + e_1^\pm V_{01} + \sum_{h>1} e_h^\pm V_{0h} - d_0^\pm E_\pm^{(2)}, \\ c_1^\pm E_\pm^{(3)} &= e_1^\pm (V_{11} - E_\pm^{(1)}) + e_0^\pm V_{10} + \sum_{h>1} e_h^\pm V_{1h} - d_1^\pm E_\pm^{(2)}. \end{aligned} \tag{A.29}$$

Here if a splitting was found already at the first or second order (i.e. we know $E_\pm^{(1)}, E_\pm^{(2)}$ and $c_0^\pm, c_1^\pm$), this is a inhomogeneous system of 2 equations for the real variables $E_\pm^{(3)}$ and the complex ones $d_0^\pm, d_1^\pm, e_0^\pm, e_1^\pm$. However, since $E_\pm^{(1)} = V_{ur} = 0$ in all the cases $(u \wedge r = 0, 1)$ discussed here, this becomes

$$\begin{aligned} c_0^\pm E_\pm^{(3)} &= -d_0^\pm E_\pm^{(2)} + \sum_{h>1} e_h^\pm V_{0h}, \\ c_1^\pm E_\pm^{(3)} &= -d_1^\pm E_\pm^{(2)} + \sum_{h>1} e_h^\pm V_{1h}. \end{aligned} \tag{A.30}$$

and by substituting the explicit form of the coefficients $e_h^\pm$ in Eq.(A.27b)

$$\begin{aligned} c_0^\pm E_\pm^{(3)} &= -d_0^\pm E_\pm^{(2)} - \sum_{h>1} \frac{d_0^\pm V_{h0} + d_1^\pm V_{h1} + \sum_{k>1} \frac{c_0^\pm V_{k0} + c_1^\pm V_{k1}}{\Delta E_k^{(0)}} V_{hk}}{\Delta E_h^{(0)}} V_{0h}, \\ c_1^\pm E_\pm^{(3)} &= -d_1^\pm E_\pm^{(2)} - \sum_{h>1} \frac{d_0^\pm V_{h0} + d_1^\pm V_{h1} + \sum_{k>1} \frac{c_0^\pm V_{k0} + c_1^\pm V_{k1}}{\Delta E_k^{(0)}} V_{hk}}{\Delta E_h^{(0)}} V_{1h}. \end{aligned} \tag{A.31}$$

Here, depending on the results from the second order, we have to distinguish two different cases:

- If, from the splitting found at the first or second order, the coefficcients $c_0^\pm, c_1^\pm$ are resolved as in Eq.(A.24) the only variables left are $E_\pm^{(3)}$ and $d_0^\pm, d_1^\pm$. Hence, together with the normalisation condition $\sum_n |d_n^\pm|^2 = 1$ the system of equations in Eq. (A.31) is closed and can be solved analytically (this is the case of HTO, see section A.3).
- If there is no splitting up to the second order (as happens for DTO) then also the coefficients $c_0^\pm, c_1^\pm$ are unknown together with $E_\pm^{(3)}$ and $d_0^\pm, d_1^\pm$. In this case, therefore, the number of unknown variables exceeds the number of equations even if we consider the normalisation conditions. An analytical derivation of the third order terms can be pursued by considering a symmetry breaking field which would neatly resolve the states, and then study the behaviour of the quantum states at the limit going to zero. This is not discussed in the present thesis as the understanding of the cancellation of the second order contribution is already sufficient to explain the third order dependence of the energy splitting in DTO found by exact numerical diagonalisation (this is briefly discussed in section A.3).

A.2 Matrix elements of the perturbtation

In this section we show the calculation of the matrix elements $\widetilde{V}_{nm} = \langle \psi_n^{(0)} | \, \hat{\widetilde{V}} \, | \psi_m^{(0)} \rangle$. As in the main text (see Sec.2.4.1), $|\psi_m^{(0)}\rangle$ are the eigenstates of the CF Hamiltonian

representing of a RE-ion in a D_{3d} symmetry. The dimensionless operator

$$\hat{\tilde{V}} = \hat{\tilde{J}}_+ + \hat{\tilde{J}}_- \tag{A.32}$$

is the perturbation applied to these states when a magnetic field purely transverse to the local quantisation axis of the RE-ion is considered ($\hat{\tilde{J}}_\pm = e^{\mp i\phi}\hat{J}_\pm$, with $\hat{J}_\pm$ as defined in Eq. (1.5)). More explicitly the operator $\hat{\tilde{V}}$ in Eq. (A.32) relates to $\hat{V} \equiv \mathcal{E}_{\rm CF}\,\hat{\mathbf{J}}\cdot\mathbf{B}/|\mathbf{B}|$, introduced in Sec.2.4.1, simply by $\hat{\tilde{V}} = 2\hat{V}/\mathcal{E}_{\rm CF}$. This allows a more direct comparison with the energies set by the crystal-field environment. Here dimensionless operators are preferable to highlight the role played by the symmetries involved (the tilde is used also to distinguish them from the general case discussed in the previous section). The strength of the field is obviously set in a regime where it can be considered as a perturbation; the values in Tesla are those where the power-law regimes for the splitting in Fig. 2.9 is guaranteed.

Here particular attention is given to HTO because the effects of its D_{3d} symmetry somehow "contain" the correspondent case for DTO. In the following, after characterising the possible quantum states allowed by the symmetry, it is shown how their "mixing" due to the perturbation depends on the structure of the *whole* crystal-field spectrum. This mainly consists in calculating the matrix elements $\widetilde{V}_{nm}$, using an *analytical* decomposition of the crystal-field states with respect to the angular momentum eigenstates. Such decomposition is given in Table A.1 for a certain number of states, including specific cases, such as the GS doublet and the states found by applying the perturbative potential to them, and more general ones where the number of free parameters is even larger. In Table A.1 each state $|\psi\rangle$ at the top of a column of coefficients C_M is given by a superposition $|\psi\rangle = \sum_M C_M\,|M\rangle$.

The Table A.1 is useful in particular to calculate the matrix elements $\widetilde{V}_{n0}$ and $\widetilde{V}_{n1}$, of the perturbing potential $\hat{\tilde{V}}$, which couple the two ground states of the doublet between each other and to the other excited crystal-field states. The third and fourth column show respectively $\hat{\tilde{V}}\,|\psi_0^{(0}\rangle$ and $\hat{\tilde{V}}\,|\psi_1^{(0}\rangle$ where the coefficients $j_M^\pm$, which depend only on the angle ϕ of the field in Eq. (A.32) and on the quantum numbers $\{J, M\}$, summarise the effect of the the perturbing potential on the angular momentum states:

$$\begin{aligned} \hat{\tilde{V}}\,|M\rangle &= j_M^+\,|M+1\rangle + j_M^-\,|M-1\rangle \qquad \text{with} \\ j_M^\pm &= e^{\mp i\phi}\sqrt{J(J+1) - M(M\pm 1)}. \end{aligned} \tag{A.33}$$

Furthermore, from the general properties of the ladder operators, we have

$$j_{-M}^\pm = j_{M\pm 1}^\pm\,, \tag{A.34}$$

which leads to characteristic symmetries, in the $\widetilde{V}_{nm}$ elements. A part of these, namely those for the elements $\widetilde{V}_{nm}$ with $m = 0, 1$, are crucial in the study presented below.

HTO	$\|\psi_0^{(0)}\rangle$	$\|\psi_1^{(0)}\rangle$	$\hat{\tilde{V}}\|\psi_0^{(0)}\rangle$	$\hat{\tilde{V}}\|\psi_1^{(0)}\rangle$	$\|\psi_s^{(0)}\rangle$	$\|\psi_{s'}^{(0)}\rangle$	$\|\psi_D^{(0)}\rangle$	$\|\psi_{D+1}^{(0)}\rangle$
$\|8\rangle$	g_8	0	0	$-j_7^+ g_7$	0	0	d_8	d_{-8}
$\|7\rangle$	0	$-g_7$	$j_8^- g_8$	0	0	0	d_7	d_{-7}
$\|6\rangle$	0	0	$j_5^+ g_5$	$-j_7^- g_7$	s_6	s'_6	0	0
$\|5\rangle$	g_5	0	0	$j_4^+ g_4$	0	0	d_5	$-d_{-5}$
$\|4\rangle$	0	g_4	$j_5^- g_5$	0	0	0	d_4	$-d_{-4}$
$\|3\rangle$	0	0	$j_2^+ g_2$	$j_4^- g_4$	s_3	s'_3	0	0
$\|2\rangle$	g_2	0	0	$-j_1^+ g_1$	0	0	d_2	d_{-2}
$\|1\rangle$	0	$-g_1$	$j_2^- g_2$	0	0	0	d_1	d_{-1}
$\|0\rangle$	0	0	$j_{-1}^+ g_1$	$-j_1^- g_1$	s_0	0	0	0
$\|-1\rangle$	g_1	0	0	$j_{-2}^+ g_2$	0	0	d_{-1}	$-d_1$
$\|-2\rangle$	0	g_2	$j_{-1}^- g_1$	0	0	0	d_{-2}	$-d_2$
$\|-3\rangle$	0	0	$j_{-4}^+ g_4$	$j_{-2}^- g_2$	s_3	$-s'_3$	0	0
$\|-4\rangle$	g_4	0	0	$-j_{-5}^+ g_5$	0	0	d_{-4}	d_4
$\|-5\rangle$	0	$-g_5$	$j_{-4}^- g_4$	0	0	0	d_{-5}	d_5
$\|-6\rangle$	0	0	$j_{-7}^+ g_7$	$-j_{-5}^- g_5$	$-s_6$	s'_6	0	0
$\|-7\rangle$	g_7	0	0	$j_{-8}^+ g_8$	0	0	d_{-7}	$-d_7$
$\|-8\rangle$	0	g_8	$j_{-7}^- g_7$	0	0	0	d_{-8}	$-d_8$

Table A.1: This table gives, in the case of HTO, the coefficients for the decomposition of the states at the top with respect to the angular momentum eigenstates $|M\rangle$ on the far left. A generic state $|\psi\rangle$ at the top of a column of coefficients C_M is given by a superposition $|\psi\rangle = \sum_M C_M |M\rangle$. This kind of visualisation simplifies the calculation of the matrix elements $\tilde{V}_{nm} = \langle\psi_n^{(0)}| \hat{\tilde{V}} |\psi_m^{(0)}\rangle$. A trivial example is to verify $\langle\psi_1^{(0)}|\psi_0^{(0)}\rangle = 0$ by simply looking at the first two states on the left (these are the ground-state doublet in Eq. (A.35)). Reading from the left, the states shown here are: the two eigenstates for the ground state energy, the first order terms obtained by applying $\hat{\tilde{V}}$ to them; then follow the generic decompositions for, firstly $|\psi_s^{(0)}\rangle, |\psi_{s'}^{(0)}\rangle$, the two types of singlets in the CF spectrum, and secondarily $|\psi_D^{(0)}\rangle, |\psi_{D+1}^{(0)}\rangle$ the two generic states for all the doublets (note indeed that also the GS doublet is a particular case of these ones).

A.2.1 Perturbative coupling between the ground state doublet and all crystal-field states

All the CF states for HTO can be found by numerical diagonalisation of the Hamiltonian in Eq. (2.27) using the parameters in Table 2.3. The energy spectrum of $\hat{\mathcal{H}}_{CF}$ is made of 5 singlets and 6 doublets.

The ground state doublet The ground state energy is doubly degenerate for the eigenstates

$$\begin{aligned}|\psi_0^{(0)}\rangle &= 0.982\,|+8\rangle + 0.156\,|+5\rangle + 0.065\,|+2\rangle + 0.071\,|-1\rangle + 0.049\,|-4\rangle + 0.006\,|-7\rangle \\ |\psi_1^{(0)}\rangle &= 0.982\,|-8\rangle - 0.156\,|-5\rangle + 0.065\,|-2\rangle - 0.071\,|+1\rangle + 0.049\,|+4\rangle - 0.006\,|+7\rangle\end{aligned} \tag{A.35}$$

which account for the strong Ising anisotropy characterising the magnetic ions in spin-ice materials. These same states are given respectively in the first and second column (from the left) of Table A.1 where the coefficients are given in terms of algebraic parameters which highlight the similarities and symmetries between the two states. For these two states it is immediate to verify $\langle\psi_1^{(0)}|\psi_0^{(0)}\rangle = 0$ by noticing that ther is no "overlap" between their decompositions [2].

Again because of no overlap for the decompositions it is straightforward to verify $\widetilde{V}_{00} = 0$, using respectively the first and third column, and $\widetilde{V}_{00} = 0$, using the second and the fourth one. Slighlty more cumbersome is to prove that $\widetilde{V}_{10}$ and $\widetilde{V}_{01}$ are null, since apparently they have non-zero overlap. Nonetheless their scalar product is straightforward to compute using Table A.1. Here as example we show $\langle\psi_1^{(0)}|\,\hat{\widetilde{V}}\,|\psi_0^{(0)}\rangle$:

$$\widetilde{V}_{10} = g_7 g_8\left(j_{-7}^- - j_8^-\right) + g_4 g_5\left(j_{-4}^- - j_5^-\right) + g_1 g_2\left(j_{-1}^- - j_2^-\right) = 0 \tag{A.36}$$

This expression is null because all elements within the parenthesis cancel out (see property in Eq. (A.34)).

This shows that in HTO the first all the matrix elements of the first order perturbation on the ground state doublet have zero contribution. In the case of DTO an analogous and more trivial case is found: all the first orders terms cancel because there is no direct overlap between their decompositions.

The singlets Another interesting feature of the CF eigenstates for HTO is the structure of the singlets $|\psi_s^{(0)}\rangle$ *and* $|\psi_{s'}^{(0)}\rangle$. These are shown respectively in the fifth and sixth column (from the left) of Table A.1. To avoid confusion, it is important to underline that these states have different energies and non trivial relationships between the coefficients of their decompositions (in general $s_i \neq s'_j$ for all $\{i,j\}$, also for $i = j$) [3].

[2] The absence of overlap is a strong constraint on their scalar product $\langle\psi_1^{(0)}|\psi_0^{(0)}\rangle = 0$. Since it does not depend on the values of the coefficients it is a more general property for these two states, i.e. it reflects the peculiar symmetry of the crystal-field Hamiltonian.

[3] This is because they belong to two different irreducible representations, A_{1g} and A_{2g}.

Despite the majority of their elements have null coefficients in the expansion with respect to the angular momentum states, the perturbative coupling of the singlets with the ground state doublet is non vanishing in both cases. Here we show their matrix elements for the state $\psi_0^{(0)}$:

$$\begin{aligned}\langle\psi_s^{(0)}|\,\hat{\widetilde{V}}\,|\psi_0^{(0)}\rangle &= s_3\Big(g_2 j_2^+ + g_4 j_{-4}^+\Big) + s_6\Big(g_5 j_5^+ - g_7 j_{-7}^+\Big) + s_0 g_1 j_{-1}^+ \neq 0\,,\\ \langle\psi_{s'}^{(0)}|\,\hat{\widetilde{V}}\,|\psi_0^{(0)}\rangle &= s_3'\Big(g_2 j_2^+ - g_4 j_{-4}^+\Big) + s_6'\Big(g_5 j_5^+ + g_7 j_{-7}^+\Big) \neq 0\,.\end{aligned} \tag{A.37}$$

Analogously it can be proven that also $\langle\psi_S^{(0)}|\,\hat{\widetilde{V}}\,|\psi_1^{(0)}\rangle \neq 0$ for both $S = s, s'$.

The doublets To conclude the study of the matrix elements $\widetilde{V}_{n0}$ and $\widetilde{V}_{n1}$, only the coupling of the ground state doublet with the higher excited doublets is left. Each doublet is made of two state vectors $|\psi_D^{(0)}\rangle$ and $|\psi_{D+1}^{(0)}\rangle$. These have non trivial relationships between the coefficients for their angular momentum decompositions shown in the seventh and eighth column of Table A.1.

The scalar products $\langle\psi_D^{(0)}|\,\hat{\widetilde{V}}\,|\psi_0^{(m)}\rangle$ and $\langle\psi_{D+1}^{(0)}|\,\hat{\widetilde{V}}\,|\psi_0^{(m)}\rangle$ are non null for both states of the ground state doublet ($m = 0, 1$). Here only the results for $|\psi_0^{(0)}\rangle$ are shown explicitly. The non vanishing elements

$$\begin{aligned}\langle\psi_D^{(0)}|\,\hat{\widetilde{V}}\,|\psi_0^{(0)}\rangle &= j_{-7}^- g_7 d_{-8} + j_8^- g_8 d_7 + j_{-4}^- g_4 d_{-5} + j_5^- g_5 d_4 + j_{-1}^- g_1 d_{-2} + j_2^- g_1 d_1\\ \langle\psi_{D+1}^{(0)}|\,\hat{\widetilde{V}}\,|\psi_0^{(0)}\rangle &= -j_{-7}^- g_7 d_8 + j_8^- g_8 d_{-7} + j_{-4}^- g_4 d_5 + j_5^- g_5 d_{-4} - j_{-1}^- g_1 d_2 + j_2^- g_1 d_{-1}\end{aligned} \tag{A.38}$$

can be written as

$$\begin{aligned}\langle\psi_D^{(0)}|\,\hat{\widetilde{V}}\,|\psi_0^{(0)}\rangle &= \sum_{M=2,5,8} j_M^-\Big(g(M-1)d(-M) + g(M)d(M-1)\Big) \neq 0\\ \langle\psi_{D+1}^{(0)}|\,\hat{\widetilde{V}}\,|\psi_0^{(0)}\rangle &= \sum_{M=2,5,8} (-1)^M j_M^-\Big(g(M-1)d(M) - g(M)d(-M+1)\Big) \neq 0.\end{aligned} \tag{A.39}$$

thanks to the property $j_\pm(M) = j_\pm(-M \mp 1)$ in Eq. (A.34). Analogously it can be shown that also $\langle\psi_D^{(0)}|\,\hat{\widetilde{V}}\,|\psi_1^{(0)}\rangle$ and $\langle\psi_{D+1}^{(0)}|\,\hat{\widetilde{V}}\,|\psi_1^{(0)}\rangle$ are both non vanishing.

By studying their properties with respect of the conjugation of the matrix elements (mainly coming from the terms $e^{\pm i\phi}$ in$j_M^\pm$ since all CF coefficients are real) we notice the following relationships between the perturbation elements coupling the two states of the ground state doublet to the two states of the excited doublets:

$$\begin{aligned}\langle\psi_D^{(0)}|\,\hat{\widetilde{V}}\,|\psi_1^{(0)}\rangle &= \langle\psi_0^{(0)}|\,\hat{\widetilde{V}}\,|\psi_{D+1}^{(0)}\rangle\\ \langle\psi_{D+1}^{(0)}|\,\hat{\widetilde{V}}\,|\psi_1^{(0)}\rangle &= -\langle\psi_0^{(0)}|\,\hat{\widetilde{V}}\,|\psi_D^{(0)}\rangle\,.\end{aligned} \tag{A.40}$$

These relationships show a very peculiar structure in the coupling of the ground state

doublet with the excited doublets of the crystal-field spectrum. They can be found also in the case of DTO, whose spectrum consists only of doublets. The implications of the relationships for singlets, Eq. (A.37), and for the doublets, Eq. (A.40) are discussed in the following section for both HTO and DTO.

A.3 Why there is a different splitting for HTO and DTO

The spectrum of a magnetic ion often shows degenerate energy levels when subject to electrostatic fields; any degeneracy is completely removed only by applying a magnetic field. If the strength of fields is such that the magnetic one can be considered as a little perturbation, then the methods discussed in section A.1 can be used to study analytically how the removal of the degeneracy, and also the broadening of the splitting itself, depend on the different orders of the perturbative expansion.

As discussed in section 2.1 in the main text, both HTO and DTO have the magnetic ions immersed in a crystal environment characterised by very strong effective electric fields. This allows a perturbative study of the effect of the magnetic fields as long as these are within the order of 1 Tesla. The main interest is obviously in the removal of the degeneracy of the ground state doublets; here the focus has been mainly on perturbative fields which are purely transverse to the local easy axis to the magnetic ions since they induce quantum dynamics which cannot be found in classical systems. The remarkable result found in this study is that, not only neither HTO nor DTO depend linearly on the field (i.e. there is no splitting at the first order of perturbation) but they show a different power-law dependence with respect to the transverse magnetic field. This is clearly show in Fig. 2.9 where the different slopes in found in the low fields regime in the log-log dependence corresponds to a quadratic and a cubic dependence of the splitting with respect to the perturbation.

In section A.1 a degenerate perturbation theory has been used to derive the dependence of the energy levels for a generic ground state doublet on an applied perturbation. In Eq. (A.23) the dependence of the two energy levels, fading out from the degenerate one, is shown up to the third order. The splitting $\Delta E_{01} = E_1 - E_0$ is

$$\Delta E_{01} = \lambda^2 \sqrt{\left(\sum_{k>1} \frac{\left|\widetilde{V}_{0k}\right|^2 - \left|\widetilde{V}_{1k}\right|^2}{\Delta E_{0k}^{(0)}} \right)^2 + 4 \left| \sum_{k>1} \frac{\widetilde{V}_{0k}\widetilde{V}_{k1}}{\Delta E_{0k}^{(0)}} \right|^2} + \mathcal{O}\left(\lambda^3\right) . \tag{A.41}$$

This is the same as Eq. (2.35) given in the main text where, of the first order terms, the only non vanishing ones where $\widetilde{V}_{00}, \widetilde{V}_{10}, \widetilde{V}_{01}, \widetilde{V}_{11}$. Since in A.2 it was shown that these are identically null because of the symmetries characterising HTO and DTO, this justifies the absence of any linear dependence on the transverse fields for both compounds.

Hence the quadratic dependence of the splitting for HTO account completely for the slope found from the numerical simulations (see the dashed back line interpolating perfectly the red one in the low field regime in Fig. 2.9). For DTO, however, also the second order terms vanish in subtracting the two energy levels. This is due to the property shown in Eq. (A.40).

In these systems another important property for the dependence of the splitting on the field is also found for the second order terms, because of the relationships for the doublets in Eq. (A.40). The first consequence of these is that for all doublets $|V_{0D}|^2 = |V_{1D+1}|^2$ and also $|V_{1D}|^2 = |V_{0D+1}|^2$. This implies that the first term under the square root in Eq. (A.40) cancels out immediately if the spectrum is only made of doublets. Furthermore terms such as the summation for the second term (under the modulus)

$$\sum_{k>1} \frac{\widetilde{V}_{0k}\widetilde{V}_{k1}}{\Delta E_k^{(0)}}\,, \tag{A.42}$$

is such that where k runs over the doublets it vanishes

$$\sum_D \frac{\widetilde{V}_{0D}\widetilde{V}_{D1} + \widetilde{V}_{0D+1}\widetilde{V}_{D+11}}{\Delta E_D^{(0)}} = \sum_D \frac{\widetilde{V}_{0D}\widetilde{V}_{D1} - \widetilde{V}_{D1}\widetilde{V}_{0D}}{\Delta E_D^{(0)}} = 0. \tag{A.43}$$

This shows why for systems like DTO it is necessary to consider the third order terms to finally remove the degeneracy (see blue curve in Fig. 2.9). Hence we find that the difference in the power-law dependence found for the two systems is due to the type of spectrum already present at the crystal-field level. The main reason is that if the summation in Eq.(A.42) is over the whole excited spectrum (including both doublets and singlets), then this will be equal to the sum of the contributions *only* from the singlets, like Eq.(A.37), since the terms from the doublets cancel out due to the relationships in Eq.(A.40). This is the case for HTO, where in fact we find a parabolic low field dependence, while for DTO this does not happen since no singlets are present (Kramers system) and all of the contributions from doublets cancel out (parabolic dependence suppressed).

These results show a quantum mechanical perturbation of the low field physics for HTO and DTO account for a behaviour which would be otherwise missed by a classical approach. Moreover it sheds light on the actual reason behind the numerical results showing different field-dependence for the two different systems. It is important to underline that, in fact, the perturbative analysis proved not only why the quadratic dependence of the splitting versus the field vanishes in DTO, but also that this happens because both eigenstates of the ground state respond in the same identical way to the perturbation (hence their difference cancels). On the other hand the first order terms are identically null in both systems (HTO and DTO) since the only matrix elements which would survive after subtracting the two energy levels are identically zero (hence at the first order the effect of the perturbation is null on the levels themselves; the zero splitting in this case is a trivial consequence).

B

Strong-coupling perturbation theories for effective exchange interactions

This Appendix complements Chapter 4 on the exchange interactions in magnetic pyrochlore oxides. In general the reader should read this Appendix when suggested in the main text, since the sections are not directly linked with each other. Each section is written in order to be self contained and independent from the others.

In section B.1 the exchange interactions are discussed in a well established model, the one-band Hubbard model, with electrons strongly localised on their ionic sites of a solid-state lattice. It summarises the approach, presented in Ref. [58], to derive an effective spin-spin interaction by means of fermionic operators defining a Hamiltonian with only two kinds of term for the electrons: one accounting for their kinetic energy, the other for the energy associated with their interaction.

Section B.2 gives details for the strong-coupling perturbation theory to derive a superexchange interaction in magnetic pyrochlore oxides that is used in the work of Onoda et al [30]. Such derivation constitute an original contribution of this thesis since in Ref. [30] very few details are given in how to obtain it.

B.1 The superexchange from the strong coupling limit of the Hubbard model

As briefly mentioned in subsection 4.1.2 the character of the superexchange magnetism is determined by the interplay of two main effects: the orbital overlap between distinct ions and the Coulomb repulsion (Hund's rules) between electrons on the same site.

In 1934 Kramers introduced the superexchange as a process due to the admixture of the wave functions of the cations and anions constituting a unit complex (like the M-O-M unit in Fig. 4.1). By means of perturbation theory the effective exchange interaction

between the magnetic ions was derived as a result of the excited states above the ground-state energy [54]. Later, in 1959, Anderson proposed a characterisation of the energy scales for the electrons participating to the superexchange; this is given by the so called *kinetic* term for their hopping, and a Coulombic term for their mutual repulsion [84, 85]. In this context the exchange constant, for the Heisenberg model in Eq. (4.10), is given by

$$J_{i,j} = -\frac{t_{i,j}^2}{U} \tag{B.1}$$

where $t_{i,j}$ is the matrix element for the electron-hopping between the two sites i, j and U is the average Coulomb repulsion for the electrons on the same unit complex.

In Anderson's formulation of superexchange, the electron hopping is in general a *virtual* process [54]. From this theory it was understood that the overlap of orbitals and the exchange itself do not necessarily imply a *real* charge transfer between the different parts of a unit complex.

An illustrative example is discussed by E. Fradkin in Ref. [58] starting from the one band Hubbard model

$$\hat{H} = -t \sum_{\substack{\langle \mathbf{r},\mathbf{r}' \rangle \\ \sigma=\pm}} \left(\hat{a}_\sigma^\dagger(\mathbf{r}) \hat{a}_\sigma(\mathbf{r}') + h.c. \right) + U \sum_{\mathbf{r}} \hat{n}_+(\mathbf{r}) \hat{n}_-(\mathbf{r}) \,. \tag{B.2}$$

Here the fermionic operator $\hat{a}_\sigma^\dagger(\mathbf{r})$ ($\hat{a}_\sigma(\mathbf{r})$ creates (destroys) an electron with spin $\sigma/2$ on site $\mathbf{r}$; $\hat{n}_\sigma(\mathbf{r}) \equiv \hat{a}_\sigma^\dagger(\mathbf{r}) \hat{a}_\sigma(\mathbf{r})$. The algebra for these operators is defined by the anti-commutation relations in Eq. (4.37). The two terms in the Hamiltonian represent the main contributions for a strongly-correlated electron system: the kinetic term, with t tuning the hopping of electrons between neighbouring sites, and the Coulombic term, with U tuning the onsite repulsion for two electrons on the same site. In the limit $U \ll t$ the mutual interaction is small enough to consider the electrons as a weakly-coupled gas of charges[1]. The opposite limit is more relevant to the physics of spin ice materials. For $U \gg t$ the electrons are strongly localised on the ionic sites; their motion across the lattice is reduced at the minimum necessary to allow covalent bonding. In Ref. [58] these two limits are discussed in depth. Here the focus is only on the strong-coupling limit being more relevant for the perturbation theory adopted by Onoda in Ref. [30].

If the local interaction between electrons is very strong ($U \gg t$) the system finds its minimum when the electrons are sparse in the lattice, so that the onsite repulsion is minimised. The diagrams (a) and (c) in Fig. B.1 sketch two equivalent spin configurations for the half-filling case in a system with a lattice hosting only a maximum of two (antiparallel) spins per site. Such configurations are only two of the possible eigenstates $|\alpha\rangle$ of the degenerate ground state of the Hamiltonian

$$\hat{H}_1 = U \sum_{\mathbf{r}} \hat{n}_+(\mathbf{r}) \hat{n}_-(\mathbf{r}) \,. \tag{B.3}$$

The configurations in the centre (b) of Fig. B.1 represent the (intermediate) virtual states leading to the exchange in position of two spins next to each other. These are

[1] This is usually called a *Fermi liquid*.

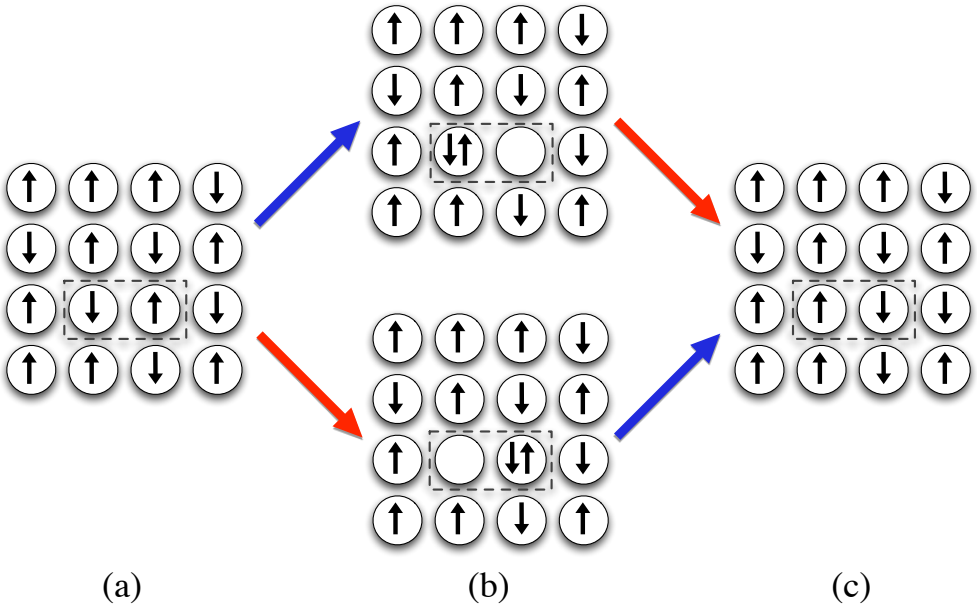

Figure B.1: Adapted from Fig.2.1 in Ref. [58]. (a) and (c) are two configurations of spins corresponding to orthogonal ground states of H_1. They differ only by exchange of two neighbouring spins (encircled by a dotted rectangle). The configurations in (b) correspond to the two virtual states intermediate between the two degenerate (a) and (c) states. The colours of the arrows refer to the action of the kinetic operator H_0 on the different sites: blue when acting on the righthand site, red for the lefthand one.

virtual because they cost an energy U above the ground-state energy which is too large for the system to be allowed as real states.

By means of Brillouin-Wigner perturbation theory [58], an effective spin-spin interaction can be derived by considering the Hamiltonian

$$\hat{H}_0 = -t \sum_{\substack{\langle \mathbf{r},\mathbf{r}' \rangle \\ \sigma=\pm}} \left(\hat{a}^\dagger_\sigma(\mathbf{r}) \hat{a}_\sigma(\mathbf{r}') + h.c. \right) \tag{B.4}$$

as very small correction to $\hat{H}_1$.

The details of the perturbation theory can be found in Ref. [58], here we give directly the spin-spin interaction obtained in the half-filling limit

$$\hat{H}'_0 = \frac{2t^2}{|U|} \sum_{\langle \mathbf{r},\mathbf{r}' \rangle} \hat{\mathbf{S}}(\mathbf{r}) \cdot \hat{\mathbf{S}}(\mathbf{r}') \ . \tag{B.5}$$

Eq. (B.5) shows that at half filling the one band Hubbard model leads to the one-half Quantum Heisenberg antiferromagnet in Eq. (4.11) with exchange coupling $J = -\frac{2t^2}{|U|}$. The factor two in the coupling constant originates from the two virtual paths leading to the exchange of the two spins. This corresponds to the two (b) virtual states in Fig. B.1 "connecting" the two configurations (a) and (c) being eigenstates of the degenerate ground state energy of $\hat{H}_1$. The blue and red arrows in Fig. B.1 distinguish the action

of the Hamiltonian on the righthand and lefthand site respectively. To have an effective exchange interaction it is necessary to act once on each of the two sites per path; other cases would take the system out of its allowed ground state configurations.

The half-filling limit of the one band Hubbard model represents an archetype for the emergence of magnetic interactions in a quantum system with strongly correlated electrons. It proves that strong localisation of electrons translates into magnetic coupling between their hosting sites. In real compounds this is due to the hybridisation between the orbitals of the different ions hosting the electrons. Although the Hubbard model does not require any detail about the underlying structure hosting the electrons, the hybridisation of the orbitals is the starting point for a more accurate approach where the magnetic interactions can manifest in more complex systems than the half filled limit of simple lattice like the one discussed here.

The magnetic pyrochlore oxides are an example of complex systems where the hybridisation between the magnetic orbitals of the RE ions and the orbitals of the O1 ions has been proposed in the form a kinetic Hamiltonian which introduces delocalisation for the electrons, which leads to the manifestation of an effective magnetic interaction. The interest in giving this short presentation is mainly to allow a comparison of the diagrams for the virtual paths of a fourth order expansion in a magnetic pyrochlore with a model, such as the one-band Hubbard model at half filling which is more commonly used in condensed matter systems.

In the following section the full derivation of an effective exchange Hamiltonian in the many-body formalism is derived from the 4th order virtual processes allowed from the hybridisation of the 4-f orbitals of the RE ions with the 2-p orbitals of the oxygen O1 ions.

B.2 Expanding the 4th order powers of the hybridisation Hamiltonian

This section provides all the analytical steps to derive the exchange Hamiltonian in Eq. (4.75) as a strong coupling perturbation expansion of Eq. (4.50) (respectively Eq.(17) and Eq.(16) in the work of Onoda et al. [30]).

As the derivation is based mainly on the term

$$\begin{aligned}\hat{h}^{\tau}_{\mathbf{i}} = \hat{f}^{\dagger}_{\mathbf{R}+\mathbf{a_i},m,\sigma}\,(\mathcal{R}^{\dagger}_{\mathbf{R}+\mathbf{a_i}})^{m,\mu}_{\sigma,\eta}\,\hat{p}_{\mathbf{R}+(1+\tau)\mathbf{a_i},\mu,\eta} \\ + \hat{p}^{\dagger}_{\mathbf{R}+(1+\tau)\mathbf{a_i},\mu,\eta}\,(\mathcal{R}_{\mathbf{R}+\mathbf{a_i}})^{\mu,m}_{\eta,\sigma}\,\hat{f}_{\mathbf{R}+\mathbf{a_i},m,\sigma}\,,\end{aligned} \tag{B.6}$$

of the hybridisation Hamiltonian in Eq. (4.50), it is convenient to rewrite such term in the more compact form

$$\hat{h}^{m,\mu}_{\sigma,\eta} = \hat{f}^{\dagger}_{m,\sigma}\,(\mathcal{R}^{\dagger})^{m,\mu}_{\sigma,\eta}\,\hat{p}_{\mu,\eta} + \hat{p}^{\dagger}_{\mu,\eta}\,(\mathcal{R})^{\mu,m}_{\eta,\sigma}\,\hat{f}_{m,\sigma}\,. \tag{B.7}$$

B.2.0.1 The 4th order building-block from the sum over the oxygen states

From Eq. (B.7) we proceed with the fourth-order expansion for one type of O1 sublattice

$$\hat{\tilde{h}}^{(4)} = \sum_{\mu_1,\mu_2,\mu_3,\mu_4=0,\pm1} \sum_{\eta_1,\eta_2,\eta_3,\eta_4=\pm} \langle\Delta| V_{m_1}\Big(\hat{h}^{m_1,\mu_1}_{\sigma_1,\eta_1}\Big) V_{m_2}\Big(\hat{h}^{m_2,\mu_2}_{\sigma_2,\eta_2}\Big) V_{m_3}\Big(\hat{h}^{m_3,\mu_3}_{\sigma_3,\eta_3}\Big) V_{m_4}\Big(\hat{h}^{m_4,\mu_4}_{\sigma_4,\eta_4}\Big) |\Delta\rangle \tag{B.8a}$$

$$= V_{m_1}V_{m_2}V_{m_3}V_{m_4} \sum_{\substack{\mu_1,\mu_2,\mu_3,\mu_4=0,\pm1\\ \eta_1,\eta_2,\eta_3,\eta_4=\pm}} \langle\Delta|\Big(\cancel{\hat{f}^\dagger_{m_1,\sigma_1}(\mathcal{R}^\dagger)^{m_1,\mu_1}_{\sigma_1,\eta_1}\hat{p}_{\mu_1,\eta_1}} + \hat{p}^\dagger_{\mu_1,\eta_1}(\mathcal{R})^{\mu_1,m_1}_{\eta_1,\sigma_1}\hat{f}_{m_1,\sigma_1}\Big) \Big(\hat{f}^\dagger_{m_2,\sigma_2}(\mathcal{R}^\dagger)^{m_2,\mu_2}_{\sigma_2,\eta_2}\hat{p}_{\mu_2,\eta_2} + \hat{p}^\dagger_{\mu_2,\eta_2}(\mathcal{R})^{\mu_2,m_2}_{\eta_2,\sigma_2}\hat{f}_{m_2,\sigma_2}\Big) \Big(\hat{f}^\dagger_{m_3,\sigma_3}(\mathcal{R}^\dagger)^{m_3,\mu_3}_{\sigma_3,\eta_3}\hat{p}_{\mu_3,\eta_3} + \hat{p}^\dagger_{\mu_3,\eta_3}(\mathcal{R})^{\mu_3,m_3}_{\eta_3,\sigma_3}\hat{f}_{m_3,\sigma_3}\Big) \Big(\hat{f}^\dagger_{m_4,\sigma_4}(\mathcal{R}^\dagger)^{m_4,\mu_4}_{\sigma_4,\eta_4}\hat{p}_{\mu_4,\eta_4} + \cancel{\hat{p}^\dagger_{\mu_4,\eta_4}(\mathcal{R})^{\mu_4,m_4}_{\eta_4,\sigma_4}\hat{f}_{m_4,\sigma_4}}\Big)|\Delta\rangle\ , \tag{B.8b}$$

where the more external terms cancel because the state $|\Delta\rangle$ is the full p-shell of the O1 oxygen. Then, the product of the terms in parenthesis leads to

$$\hat{\tilde{h}}^{(4)} = V_{m_1}V_{m_2}V_{m_3}V_{m_4} \sum_{\substack{\mu_1,\mu_2,\mu_3,\mu_4=0,\pm1\\ \eta_1,\eta_2,\eta_3,\eta_4=\pm}} \langle\Delta|\,\hat{p}^\dagger_{\mu_1,\eta_1}\hat{f}_{m_1,\sigma_1}(\mathcal{R})^{\mu_1,m_1}_{\eta_1,\sigma_1} \Big(\hat{f}^\dagger_{m_2,\sigma_2}\hat{f}_{m_3,\sigma_3}\hat{p}_{\mu_2,\eta_2}\hat{p}^\dagger_{\mu_3,\eta_3}(\mathcal{R}^\dagger)^{m_2,\mu_2}_{\sigma_2,\eta_2}(\mathcal{R})^{\mu_3,m_3}_{\eta_3,\sigma_3} + \hat{f}_{m_2,\sigma_2}\hat{f}^\dagger_{m_3,\sigma_3}\hat{p}^\dagger_{\mu_2,\eta_2}\hat{p}_{\mu_3,\eta_3}(\mathcal{R})^{\mu_2,m_2}_{\eta_2,\sigma_2}(\mathcal{R}^\dagger)^{m_3,\mu_3}_{\sigma_3,\eta_3}\Big) \hat{f}^\dagger_{m_4,\sigma_4}\hat{p}_{\mu_4,\eta_4}(\mathcal{R}^\dagger)^{m_4,\mu_4}_{\sigma_4,\eta_4}|\Delta\rangle\ , \tag{B.9a}$$

which is convenient to rewrite as

$$\begin{aligned}
\hat{\tilde{h}}^{(4)} &= V_{m_1} V_{m_2} V_{m_3} V_{m_4} \sum_{\substack{\mu_1,\mu_2,\mu_3,\mu_4=0,\pm1 \\ \eta_1,\eta_2,\eta_3,\eta_4=\pm}} \\
&\langle\Delta| \Big[\hat{f}_{m_1,\sigma_1}\, \hat{f}^\dagger_{m_2,\sigma_2}\, \hat{f}_{m_3,\sigma_3}\, \hat{f}^\dagger_{m_4,\sigma_4} \\
&\qquad \hat{p}^\dagger_{\mu_1,\eta_1}\, \hat{p}_{\mu_2,\eta_2}\, \hat{p}^\dagger_{\mu_3,\eta_3}\, \hat{p}_{\mu_4,\eta_4} \\
&\qquad\quad (\mathcal{R})^{\mu_1,m_1}_{\eta_1,\sigma_1}\, (\mathcal{R}^\dagger)^{m_2,\mu_2}_{\sigma_2,\eta_2}\, (\mathcal{R})^{\mu_3,m_3}_{\eta_3,\sigma_3}\, (\mathcal{R}^\dagger)^{m_4,\mu_4}_{\sigma_4,\eta_4} \\
&\quad + \hat{f}_{m_1,\sigma_1}\, \hat{f}_{m_2,\sigma_2}\, \hat{f}^\dagger_{m_3,\sigma_3}\, \hat{f}^\dagger_{m_4,\sigma_4} \\
&\qquad \hat{p}^\dagger_{\mu_1,\eta_1}\, \hat{p}^\dagger_{\mu_2,\eta_2}\, \hat{p}_{\mu_3,\eta_3} \hat{p}_{\mu_4,\eta_4} \\
&\qquad\quad (\mathcal{R})^{\mu_1,m_1}_{\eta_1,\sigma_1}\, (\mathcal{R})^{\mu_2,m_2}_{\eta_2,\sigma_2}\, (\mathcal{R}^\dagger)^{m_3,\mu_3}_{\sigma_3,\eta_3}\, (\mathcal{R}^\dagger)^{m_4,\mu_4}_{\sigma_4,\eta_4} \Big] |\Delta\rangle \ .
\end{aligned}$$

Here we consider the two terms separately to focus the action of the p operators on the oxygen $|\Delta\rangle$ ground state. The first term of the sum gives

$$\begin{aligned}
&\sum_{\substack{\mu_1,\mu_2,\mu_3,\mu_4=0,\pm1 \\ \eta_1,\eta_2,\eta_3,\eta_4=\pm}} \Big[\langle\Delta|\, \hat{p}^\dagger_{\mu_1,\eta_1}\, \hat{p}_{\mu_2,\eta_2}\, \hat{p}^\dagger_{\mu_3,\eta_3}\, \hat{p}_{\mu_4,\eta_4}\, |\Delta\rangle \\
&\qquad\qquad \times (\mathcal{R})^{\mu_1,m_1}_{\eta_1,\sigma_1}\, (\mathcal{R}^\dagger)^{m_2,\mu_2}_{\sigma_2,\eta_2}\, (\mathcal{R})^{\mu_3,m_3}_{\eta_3,\sigma_3}\, (\mathcal{R}^\dagger)^{m_4,\mu_4}_{\sigma_4,\eta_4} \Big] \\
&= \sum_{\substack{\mu_1,\mu_2,\mu_3,\mu_4=0,\pm1 \\ \eta_1,\eta_2,\eta_3,\eta_4=\pm}} \Big[\langle\Delta|\, \hat{n}_{\mu_1,\eta_1}\, \hat{n}_{\mu_3,\eta_3}\, |\Delta\rangle\ \delta_{\mu_1,\mu_2}\delta_{\eta_1,\eta_2}\, \delta_{\mu_3,\mu_4}\delta_{\eta_3,\eta_4} \\
&\qquad\qquad \times (\mathcal{R})^{\mu_1,m_1}_{\eta_1,\sigma_1}\, (\mathcal{R}^\dagger)^{m_2,\mu_2}_{\sigma_2,\eta_2}\, (\mathcal{R})^{\mu_3,m_3}_{\eta_3,\sigma_3}\, (\mathcal{R}^\dagger)^{m_4,\mu_4}_{\sigma_4,\eta_4} \Big] \\
&= \sum_{\substack{\mu_1,\mu_3=0,\pm1 \\ \eta_1,\eta_3=\pm}} \Big[n_{\mu_1,\eta_1}\, n_{\mu_3,\eta_3}\, (\mathcal{R}^\dagger)^{m_2,\mu_1}_{\sigma_2,\eta_1}\, (\mathcal{R})^{\mu_1,m_1}_{\eta_1,\sigma_1}\, (\mathcal{R}^\dagger)^{m_4,\mu_3}_{\sigma_4,\eta_3}\, (\mathcal{R})^{\mu_3,m_3}_{\eta_3,\sigma_3} \Big] \\
&= (\mathcal{R}^\dagger\mathcal{R})^{m_2,m_1}_{\sigma_2,\sigma_1}\, (\mathcal{R}^\dagger\mathcal{R})^{m_4,m_3}_{\sigma_4,\sigma_3}
\end{aligned} \tag{B.10}$$

This was obtained taking into account that

$$\begin{aligned}
\hat{p}^\dagger_{\mu_i,\eta_i}\, \hat{p}_{\mu_j,\eta_j}\, |\Delta\rangle &= \hat{n}_{\mu_i,\eta_i}\, \delta_{\mu_i,\mu_j}\delta_{\eta_i,\eta_j}\, |\Delta\rangle \ , \\
n_{\mu_i,\eta_i}\ |\Delta\rangle &= |\Delta\rangle \ ,
\end{aligned} \tag{B.11}$$

since $|\Delta\rangle$ has already each of the 6 p states occupied by one electron .

Similarly the second term of the sum gives

$$
\begin{aligned}
&\sum_{\substack{\mu_1,\mu_2,\mu_3,\mu_4=0,\pm1\\ \eta_1,\eta_2,\eta_3,\eta_4=\pm}} \Bigg[\langle\Delta|\hat{p}^\dagger_{\mu_1,\eta_1}\,\hat{p}^\dagger_{\mu_2,\eta_2}\,\hat{p}_{\mu_3,\eta_3}\,\hat{p}_{\mu_4,\eta_4}\,|\Delta\rangle \\
&\qquad\qquad \times (\mathcal{R}\,)_{\substack{\mu_1,m_1\\ \eta_1,\sigma_1}} (\mathcal{R}\,)_{\substack{\mu_2,m_2\\ \eta_2,\sigma_2}} (\mathcal{R}^\dagger)_{\substack{m_3,\mu_3\\ \sigma_3,\eta_3}} (\mathcal{R}^\dagger)_{\substack{m_4,\mu_4\\ \sigma_4,\eta_4}} \Bigg] \\
&= \sum_{\substack{\mu_1,\mu_2,\mu_3,\mu_4=0,\pm1\\ \eta_1,\eta_2,\eta_3,\eta_4=\pm}} \Bigg[\langle\Delta|\hat{p}^\dagger_{\mu_1,\eta_1}\left(\delta_{\mu_2,\mu_3}\delta_{\eta_2,\eta_3} - \hat{p}_{\mu_3,\eta_3}\,\hat{p}^\dagger_{\mu_2,\eta_2}\right)\hat{p}_{\mu_4,\eta_4}\,|\Delta\rangle \\
&\qquad\qquad \times (\mathcal{R}\,)_{\substack{\mu_1,m_1\\ \eta_1,\sigma_1}} (\mathcal{R}\,)_{\substack{\mu_2,m_2\\ \eta_2,\sigma_2}} (\mathcal{R}^\dagger)_{\substack{m_3,\mu_3\\ \sigma_3,\eta_3}} (\mathcal{R}^\dagger)_{\substack{m_4,\mu_4\\ \sigma_4,\eta_4}} \Bigg] \\
&= \sum_{\substack{\mu_1,\mu_2,\mu_3,\mu_4=0,\pm1\\ \eta_1,\eta_2,\eta_3,\eta_4=\pm}} \Bigg[\langle\Delta|\Big(\delta_{\mu_2,\mu_3}\delta_{\eta_2,\eta_3}\,\delta_{\mu_1,\mu_4}\delta_{\eta_1,\eta_4}\,\hat{n}_{\mu_1,\eta_1} \\
&\qquad\qquad - \delta_{\mu_1,\mu_3}\delta_{\eta_1,\eta_3}\,\delta_{\mu_2,\mu_4}\delta_{\eta_2,\eta_4}\,\hat{n}_{\mu_1,\eta_1}\,\hat{n}_{\mu_2,\eta_2}\Big)\,|\Delta\rangle \\
&\qquad\qquad \times (\mathcal{R}\,)_{\substack{\mu_1,m_1\\ \eta_1,\sigma_1}} (\mathcal{R}\,)_{\substack{\mu_2,m_2\\ \eta_2,\sigma_2}} (\mathcal{R}^\dagger)_{\substack{m_3,\mu_3\\ \sigma_3,\eta_3}} (\mathcal{R}^\dagger)_{\substack{m_4,\mu_4\\ \sigma_4,\eta_4}} \Bigg] \\
&= \sum_{\substack{\mu_1=0,\pm1\\ \eta_1=\pm}} \langle\Delta|\,\hat{n}_{\mu_1,\eta_1}\,|\Delta\rangle \times (\mathcal{R}^\dagger\mathcal{R})_{\substack{m_3,m_2\\ \sigma_3,\sigma_2}} (\mathcal{R}^\dagger)_{\substack{m_4,\mu_1\\ \sigma_4,\eta_1}} (\mathcal{R}\,)_{\substack{\mu_1,m_1\\ \eta_1,\sigma_1}} \\
&\qquad - \sum_{\substack{\mu_1,\mu_2=0,\pm1\\ \eta_1,\eta_2=\pm}} \Big(\langle\Delta|\hat{n}_{\mu_1,\eta_1}\,\hat{n}_{\mu_2,\eta_2}\,|\Delta\rangle \\
&\qquad\qquad \times (\mathcal{R}^\dagger)_{\substack{m_4,\mu_2\\ \sigma_4,\eta_2}} (\mathcal{R}\,)_{\substack{\mu_2,m_2\\ \eta_2,\sigma_2}} (\mathcal{R}^\dagger)_{\substack{m_3,\mu_1\\ \sigma_3,\eta_1}} (\mathcal{R}\,)_{\substack{\mu_1,m_1\\ \eta_1,\sigma_1}} \Big) \\
&= \quad (\mathcal{R}^\dagger\mathcal{R})_{\substack{m_3,m_2\\ \sigma_3,\sigma_2}} (\mathcal{R}^\dagger\mathcal{R})_{\substack{m_4,m_1\\ \sigma_4,\sigma_1}} - (\mathcal{R}^\dagger\mathcal{R})_{\substack{m_3,m_1\\ \sigma_3,\sigma_1}} (\mathcal{R}^\dagger\mathcal{R})_{\substack{m_4,m_2\\ \sigma_4,\sigma_2}}
\end{aligned}
\tag{B.12}
$$

Then, summarising what has been found so far, Eq. (B.8) is reduced to the general

form

$$\begin{aligned}\hat{\tilde{h}}^{(4)} &= V_{m_1}V_{m_2}V_{m_3}V_{m_4} \\ &\times\Bigg[\hat{f}_{m_1,\sigma_1}\,\hat{f}^{\dagger}_{m_2,\sigma_2}\,\hat{f}_{m_3,\sigma_3}\,\hat{f}^{\dagger}_{m_4,\sigma_4}\;(\mathcal{R}^{\dagger}\mathcal{R})^{m_2,m_1}_{\sigma_2,\sigma_1}\,(\mathcal{R}^{\dagger}\mathcal{R})^{m_4,m_3}_{\sigma_4,\sigma_3} \\ &\quad+\;\hat{f}_{m_1,\sigma_1}\,\hat{f}_{m_2,\sigma_2}\,\hat{f}^{\dagger}_{m_3,\sigma_3}\,\hat{f}^{\dagger}_{m_4,\sigma_4}\Big((\mathcal{R}^{\dagger}\mathcal{R})^{m_3,m_2}_{\sigma_3,\sigma_2}\,(\mathcal{R}^{\dagger}\mathcal{R})^{m_4,m_1}_{\sigma_4,\sigma_1} \\ &\qquad\qquad-\,(\mathcal{R}^{\dagger}\mathcal{R})^{m_3,m_1}_{\sigma_3,\sigma_1}\,(\mathcal{R}^{\dagger}\mathcal{R})^{m_4,m_2}_{\sigma_4,\sigma_2}\Big)\Bigg]\end{aligned} \tag{B.13}$$

that is the general expression of the superexchange mechanism for any of the paths shown in Fig. 4.6.

B.2.1 Gathering up the virtual paths

To compute the resulting amplitude of the superexchange it is necessary to label the operators and related indices depending on the virtual path considered. In the fourth order, six different sequences are allowed for the virtual electron-hops recovering the initial $\mathrm{f_r p_{O1} f_{r'}}$ ground state. Now the labelling will give an effective magnetic interaction between two RE-sites because each path in Fig. 4.6 corresponds to a Hamiltonian, derived from Eq. (4.63), where two $\hat{f}$ operators act on the sites $\mathbf{r}$ and two on the sites $\mathbf{r'}$ of a given RE-O1-RE unit.

Before proceeding with the labelling of the operators it is convenient to make the notation for the indices shorter by using $\mathbf{i}$ for the quantum numbers m_i, σ_i of an electron on the RE-site $\mathbf{r}$, so that Eq. (B.13) is expressed in the more compact form as

$$\begin{aligned}\hat{\tilde{h}}^{(4)} \;=\; V_1V_2V_3V_4\Bigg[&\hat{f}_{\mathbf{1}}\,\hat{f}^{\dagger}_{\mathbf{2}}\,\hat{f}_{\mathbf{3}}\,\hat{f}^{\dagger}_{\mathbf{4}}\;(\mathcal{R}^{\dagger}\mathcal{R})_{\mathbf{2},\mathbf{1}}\,(\mathcal{R}^{\dagger}\mathcal{R})_{\mathbf{4},\mathbf{3}} \\ &+\;\hat{f}_{\mathbf{1}}\,\hat{f}_{\mathbf{2}}\,\hat{f}^{\dagger}_{\mathbf{3}}\,\hat{f}^{\dagger}_{\mathbf{4}}\Big((\mathcal{R}^{\dagger}\mathcal{R})_{\mathbf{3},\mathbf{2}}\,(\mathcal{R}^{\dagger}\mathcal{R})_{\mathbf{4},\mathbf{1}}-(\mathcal{R}^{\dagger}\mathcal{R})_{\mathbf{3},\mathbf{1}}\,(\mathcal{R}^{\dagger}\mathcal{R})_{\mathbf{4},\mathbf{2}}\,.\Big)\Bigg]\end{aligned} \tag{B.14}$$

Using the diagrams in Figs. B.2-B.4 to assign the labels and the relative energy weights this will lead to the effective exchange Hamiltonian.

It is convenient to start from **(a)** and **(b)**,

$$\begin{aligned}\hat{h}^{4th}_{\mathbf{(a)},\mathbf{(b)}} = \frac{V_1V_{2'}V_{3'}V_4}{(nU-\Delta)^2}\Bigg[&\frac{\hat{f}_{\mathbf{1}}\,\hat{f}^{\dagger}_{\mathbf{2'}}\,\hat{f}_{\mathbf{3'}}\,\hat{f}^{\dagger}_{\mathbf{4}}}{U}\,(\mathcal{R}^{\dagger}\mathcal{R})_{\mathbf{2'},\mathbf{1}}\,(\mathcal{R}^{\dagger}\mathcal{R})_{\mathbf{4},\mathbf{3'}} \\ &+\frac{\hat{f}_{\mathbf{1}}\,\hat{f}_{\mathbf{2'}}\,\hat{f}^{\dagger}_{\mathbf{3'}}\,\hat{f}^{\dagger}_{\mathbf{4}}}{2(nU-\Delta)}\Big(\delta_{\mathbf{3'},\mathbf{2'}}\,\delta_{\mathbf{4},\mathbf{1}}-(\mathcal{R}^{\dagger}\mathcal{R})_{\mathbf{3'},\mathbf{1}}\,(\mathcal{R}^{\dagger}\mathcal{R})_{\mathbf{4},\mathbf{2'}}\,,\Big)\Bigg]\end{aligned} \tag{B.15}$$

respectively in the first and second term. We can rewrite the term **(b)** so that it looks more similar to **(a)** (in the rotation matrices) relabelling of the indices $\mathbf{3'} \to \mathbf{2'}, \mathbf{2'} \to \mathbf{3'}$

(only in the **(b)** term)

$$\hat{h}^{4th}_{\mathbf{(a),(b)}} = \frac{V_1 V_{2'} V_{3'} V_4}{(nU-\Delta)^2}\Bigg[\frac{\hat{f}_{\mathbf{1}}\,\hat{f}^{\dagger}_{\mathbf{2'}}\,\hat{f}_{\mathbf{3'}}\,\hat{f}^{\dagger}_{\mathbf{4}}}{U}\,(\mathcal{R}^{\dagger}\mathcal{R})_{\mathbf{2',1}}\,(\mathcal{R}^{\dagger}\mathcal{R})_{\mathbf{4,3'}} + \frac{\hat{f}_{\mathbf{1}}\,\hat{f}_{\mathbf{3'}}\,\hat{f}^{\dagger}_{\mathbf{2'}}\,\hat{f}^{\dagger}_{\mathbf{4}}}{2(nU-\Delta)}\Big(\delta_{\mathbf{2',3'}}\,\delta_{\mathbf{4,1}} - (\mathcal{R}^{\dagger}\mathcal{R})_{\mathbf{2',1}}\,(\mathcal{R}^{\dagger}\mathcal{R})_{\mathbf{4,3'}}\Big)\Bigg] \tag{B.16}$$

Then the term **(c)** is

$$\begin{aligned}\hat{h}^{4th}_{\mathbf{(c)}} &= \frac{V_1 V_{2'} V_3 V_{4'}}{(nU-\Delta)^2}\Bigg[\cancel{\frac{\hat{f}_{\mathbf{1}}\,\hat{f}^{\dagger}_{\mathbf{2'}}\,\hat{f}_{\mathbf{3}}\,\hat{f}^{\dagger}_{\mathbf{4'}}}{U}\,(\mathcal{R}^{\dagger}\mathcal{R})_{\mathbf{2',1}}\,(\mathcal{R}^{\dagger}\mathcal{R})_{\mathbf{4',3}}} \\ &\qquad + \frac{\hat{f}_{\mathbf{1}}\,\hat{f}_{\mathbf{2'}}\,\hat{f}^{\dagger}_{\mathbf{3}}\,\hat{f}^{\dagger}_{\mathbf{4'}}}{2(nU-\Delta)}\Big((\mathcal{R}^{\dagger}\mathcal{R})_{\mathbf{3,2'}}\,(\mathcal{R}^{\dagger}\mathcal{R})_{\mathbf{4',1}} - \delta_{\mathbf{3,1}}\,\delta_{\mathbf{4',2'}}\Big)\Bigg] \\ &= \frac{V_1 V_{2'} V_3 V_{4'}}{(nU-\Delta)^2}\,\frac{\hat{f}_{\mathbf{1}}\,\hat{f}_{\mathbf{2'}}\,\hat{f}^{\dagger}_{\mathbf{4'}}\,\hat{f}^{\dagger}_{\mathbf{3}}}{2(nU-\Delta)}\Big(\delta_{\mathbf{3,1}}\,\delta_{\mathbf{4',2'}} - (\mathcal{R}^{\dagger}\mathcal{R})_{\mathbf{3,2'}}\,(\mathcal{R}^{\dagger}\mathcal{R})_{\mathbf{4',1}}\Big),\end{aligned} \tag{B.17}$$

where the first term cancels because the operators $\hat{f}_{\mathbf{1}}\,\hat{f}^{\dagger}_{\mathbf{2'}}\,\hat{f}_{\mathbf{3}}\,\hat{f}^{\dagger}_{\mathbf{4'}}$ would create two electrons on $\mathbf{r'}$ and annihilate two in $\mathbf{r}$ taking the system out of the ground state configuration $\mathrm{f_r p_{O1} f_{r'}}$ of the RE-O1-RE system.

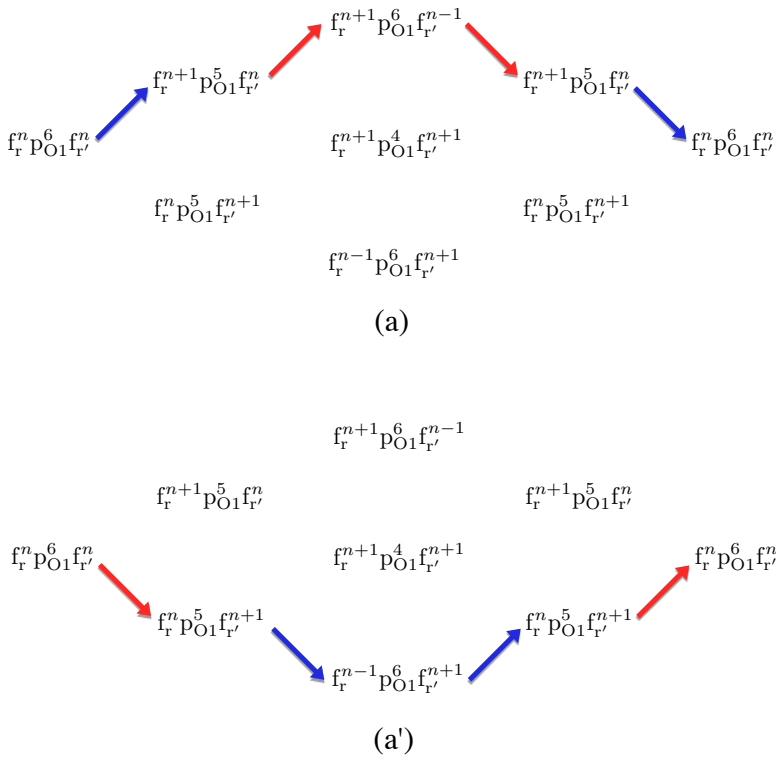

Figure B.2: The equivalent paths **(a)** and **(a′)**; see section B.2.1.1.

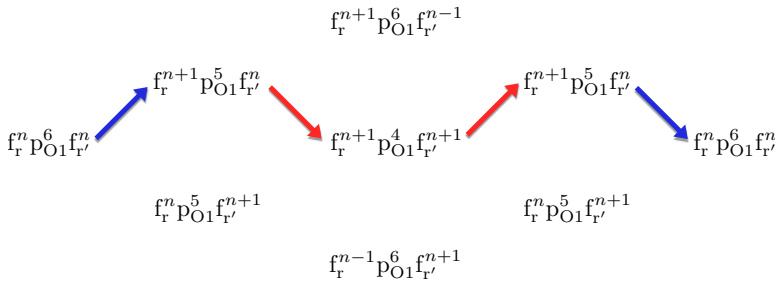

(b)

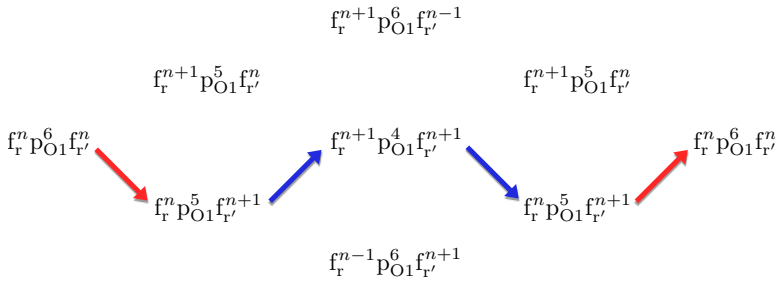

(b')

Figure B.3: The equivalent paths **(b)** and **(b′)**; see section B.2.1.1.

Relabelling the indices $\mathbf{4'} \to \mathbf{3'}, \mathbf{3} \to \mathbf{4}$ gives

$$\hat{h}^{4th}_{\mathbf{(c)}} = \frac{V_1 V_{2'} V_{3'} V_4}{(nU-\Delta)^2} \frac{\hat{f}_{\mathbf{1}}\, \hat{f}_{\mathbf{2'}}\, \hat{f}^\dagger_{\mathbf{3'}}\, \hat{f}^\dagger_{\mathbf{4}}}{2(nU-\Delta)} \left(\delta_{\mathbf{3'},\mathbf{2'}}\, \delta_{\mathbf{4},\mathbf{1}} - (\mathcal{R}^\dagger\mathcal{R})_{\mathbf{3'},\mathbf{1}}\, (\mathcal{R}^\dagger\mathcal{R})_{\mathbf{4},\mathbf{2'}} \right) \tag{B.18}$$

and $\mathbf{3'} \to \mathbf{2'}, \mathbf{2'} \to \mathbf{3'}$

$$\hat{h}^{4th}_{\mathbf{(c)}} = \frac{V_1 V_{2'} V_{3'} V_4}{(nU-\Delta)^2} \frac{\hat{f}_{\mathbf{1}}\, \hat{f}_{\mathbf{3'}}\, \hat{f}^\dagger_{\mathbf{2'}}\, \hat{f}^\dagger_{\mathbf{4}}}{2(nU-\Delta)} \left(\delta_{\mathbf{2'},\mathbf{3'}}\, \delta_{\mathbf{4},\mathbf{1}} - (\mathcal{R}^\dagger\mathcal{R})_{\mathbf{2'},\mathbf{1}}\, (\mathcal{R}^\dagger\mathcal{R})_{\mathbf{4},\mathbf{3'}} \right) \tag{B.19}$$

Now we can put **(a)**, **(b)** and **(c)** together

$$\begin{aligned} \hat{h}^{4th}_{\mathbf{(a)},\mathbf{(b)},\mathbf{(c)}} = \frac{V_1 V_{2'} V_{3'} V_4}{(nU-\Delta)^2} \Bigg[& \frac{\hat{f}_{\mathbf{1}}\, \hat{f}^\dagger_{\mathbf{2'}}\, \hat{f}_{\mathbf{3'}}\, \hat{f}^\dagger_{\mathbf{4}}}{U} (\mathcal{R}^\dagger\mathcal{R})_{\mathbf{2'},\mathbf{1}}\, (\mathcal{R}^\dagger\mathcal{R})_{\mathbf{4},\mathbf{3'}} \\ & + \frac{\hat{f}_{\mathbf{1}}\, \hat{f}_{\mathbf{3'}}\, \hat{f}^\dagger_{\mathbf{2'}}\, \hat{f}^\dagger_{\mathbf{4}}}{nU-\Delta} \left(\delta_{\mathbf{2'},\mathbf{3'}}\, \delta_{\mathbf{4},\mathbf{1}} - (\mathcal{R}^\dagger\mathcal{R})_{\mathbf{2'},\mathbf{1}}\, (\mathcal{R}^\dagger\mathcal{R})_{\mathbf{4},\mathbf{3'}} \right) \Bigg] \end{aligned} \tag{B.20}$$

B.2.1.1 The equivalence between (a′), (b′), (c′) and (a), (b), (c)

In the following the same calculations are given for the other 3 paths **(a′)**, **(b′)** and **(c′)** which we show are equivalent to **(a)**, **(b)** and **(c)** respectively.

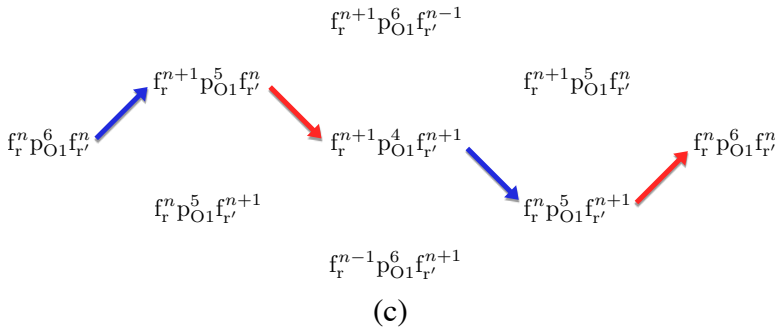

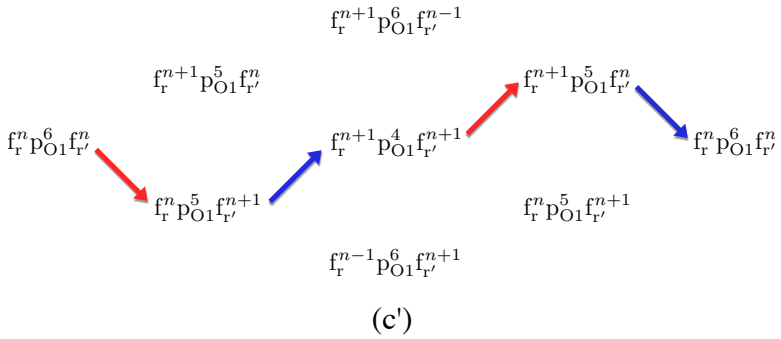

Figure B.4: Two equivalent paths **(c)** and **(c′)**; see section B.2.1.1.

Here follows **(a′)** and **(b′)**

$$\hat{h}^{4th}_{\mathbf{(a')},\mathbf{(b')}} = \frac{V_{1'}V_2V_3V_{4'}}{(nU-\Delta)^2}\left[\frac{\hat{f}_{\mathbf{1'}}\,\hat{f}^\dagger_{\mathbf{2}}\,\hat{f}_{\mathbf{3}}\,\hat{f}^\dagger_{\mathbf{4'}}}{U}\,(\mathcal{R}^\dagger\mathcal{R})_{\mathbf{2},\mathbf{1'}}\,(\mathcal{R}^\dagger\mathcal{R})_{\mathbf{4'},\mathbf{3}}\right.$$
$$\left. + \frac{\hat{f}_{\mathbf{1'}}\,\hat{f}_{\mathbf{2}}\,\hat{f}^\dagger_{\mathbf{3}}\,\hat{f}^\dagger_{\mathbf{4'}}}{2(nU-\Delta)}\left(\delta_{\mathbf{3},\mathbf{2}}\,\delta_{\mathbf{4'},\mathbf{1'}} - (\mathcal{R}^\dagger\mathcal{R})_{\mathbf{3},\mathbf{1'}}\,(\mathcal{R}^\dagger\mathcal{R})_{\mathbf{4'},\mathbf{2}}\right)\right] \tag{B.21}$$

respectively the first and second term in the sum. We can rewrite the term **(b′)** so that it looks more similar to **(a′)** (in the rotation matrices) relabelling of the indices $\mathbf{3}\to\mathbf{2},\mathbf{2}\to\mathbf{3}$ (only in the **(b′)** term)

$$\hat{h}^{4th}_{\mathbf{(a')},\mathbf{(b')}} = \frac{V_{1'}V_2V_3V_{4'}}{(nU-\Delta)^2}\left[\frac{\hat{f}_{\mathbf{1'}}\,\hat{f}^\dagger_{\mathbf{2}}\,\hat{f}_{\mathbf{3}}\,\hat{f}^\dagger_{\mathbf{4'}}}{U}\,(\mathcal{R}^\dagger\mathcal{R})_{\mathbf{2},\mathbf{1'}}\,(\mathcal{R}^\dagger\mathcal{R})_{\mathbf{4'},\mathbf{3}}\right.$$
$$\left. + \frac{\hat{f}_{\mathbf{1'}}\,\hat{f}_{\mathbf{3}}\,\hat{f}^\dagger_{\mathbf{2}}\,\hat{f}^\dagger_{\mathbf{4'}}}{2(nU-\Delta)}\left(\delta_{\mathbf{2},\mathbf{3}}\,\delta_{\mathbf{4'},\mathbf{1'}} - (\mathcal{R}^\dagger\mathcal{R})_{\mathbf{2},\mathbf{1'}}\,(\mathcal{R}^\dagger\mathcal{R})_{\mathbf{4'},\mathbf{3}}\right)\right] \tag{B.22}$$

Then the term $\mathbf{(c')}$ is

$$\begin{aligned}\hat{h}^{4th}_{\mathbf{(c')}} = \frac{V_{1'}V_2V_{3'}V_4}{(nU-\Delta)^2}\Bigg[&\cancel{\frac{\hat{f}_{\mathbf{1'}}\,\hat{f}^\dagger_{\mathbf{2}}\,\hat{f}_{\mathbf{3'}}\,\hat{f}^\dagger_{\mathbf{4}}}{U}}\,(\mathcal{R}^\dagger\mathcal{R})_{\mathbf{2},\mathbf{1'}}\,(\mathcal{R}^\dagger\mathcal{R})_{\mathbf{4},\mathbf{3'}} \\ &+\frac{\hat{f}_{\mathbf{1'}}\,\hat{f}_{\mathbf{2}}\,\hat{f}^\dagger_{\mathbf{3'}}\,\hat{f}^\dagger_{\mathbf{4}}}{2(nU-\Delta)}\Big(\,(\mathcal{R}^\dagger\mathcal{R})_{\mathbf{3'},\mathbf{2}}\,(\mathcal{R}^\dagger\mathcal{R})_{\mathbf{4},\mathbf{1'}}-\delta_{\mathbf{3'},\mathbf{1'}}\,\delta_{\mathbf{4},\mathbf{2}}\,\Big)\Bigg] \\ = \frac{V_{1'}V_2V_{3'}V_4}{(nU-\Delta)^2}\,&\frac{\hat{f}_{\mathbf{1'}}\,\hat{f}_{\mathbf{2}}\,\hat{f}^\dagger_{\mathbf{4}}\,\hat{f}^\dagger_{\mathbf{3'}}}{2(nU-\Delta)}\Big(\,\delta_{\mathbf{3'},\mathbf{1'}}\,\delta_{\mathbf{4},\mathbf{2}}\,-(\mathcal{R}^\dagger\mathcal{R})_{\mathbf{3'},\mathbf{2}}\,(\mathcal{R}^\dagger\mathcal{R})_{\mathbf{4},\mathbf{1'}}\,\Big)\end{aligned} \tag{B.23}$$

relabelling of the indices $\mathbf{3'}\to\mathbf{4'},\mathbf{4}\to\mathbf{3}$

$$\hat{h}^{4th}_{\mathbf{(c')}} = \frac{V_{1'}V_2V_{3'}V_4}{(nU-\Delta)^2}\,\frac{\hat{f}_{\mathbf{1'}}\,\hat{f}_{\mathbf{2}}\,\hat{f}^\dagger_{\mathbf{3}}\,\hat{f}^\dagger_{\mathbf{4'}}}{2(nU-\Delta)}\Big(\,\delta_{\mathbf{3},\mathbf{2}}\,\delta_{\mathbf{4'},\mathbf{1'}}\,-(\mathcal{R}^\dagger\mathcal{R})_{\mathbf{3},\mathbf{1'}}\,(\mathcal{R}^\dagger\mathcal{R})_{\mathbf{4'},\mathbf{2}}\,\Big) \tag{B.24}$$

and $\mathbf{3}\to\mathbf{2},\mathbf{2}\to\mathbf{3}$

$$\hat{h}^{4th}_{\mathbf{(c')}} = \frac{V_{1'}V_2V_{3'}V_4}{(nU-\Delta)^2}\,\frac{\hat{f}_{\mathbf{1'}}\,\hat{f}_{\mathbf{3}}\,\hat{f}^\dagger_{\mathbf{2}}\,\hat{f}^\dagger_{\mathbf{4'}}}{2(nU-\Delta)}\Big(\,\delta_{\mathbf{2},\mathbf{3}}\,\delta_{\mathbf{4'},\mathbf{1'}}\,-(\mathcal{R}^\dagger\mathcal{R})_{\mathbf{2},\mathbf{1'}}\,(\mathcal{R}^\dagger\mathcal{R})_{\mathbf{4'},\mathbf{3}}\,\Big) \tag{B.25}$$

Now we can put $\mathbf{(c')}$, $\mathbf{(b')}$ and $\mathbf{(a')}$ together (note the 2 in the denominator has been simplified because of the sum $\mathbf{(c')}+\mathbf{(b')}$)

$$\begin{aligned}\hat{h}^{4th}_{\mathbf{(a')},\mathbf{(b')},\mathbf{(c')}} = \frac{V_{1'}V_2V_3V_{4'}}{(nU-\Delta)^2}\Bigg[&\frac{\hat{f}_{\mathbf{1'}}\,\hat{f}^\dagger_{\mathbf{2}}\,\hat{f}_{\mathbf{3}}\,\hat{f}^\dagger_{\mathbf{4'}}}{U}\,(\mathcal{R}^\dagger\mathcal{R})_{\mathbf{2},\mathbf{1'}}\,(\mathcal{R}^\dagger\mathcal{R})_{\mathbf{4'},\mathbf{3}} \\ &+\frac{\hat{f}_{\mathbf{1'}}\,\hat{f}_{\mathbf{3}}\,\hat{f}^\dagger_{\mathbf{2}}\,\hat{f}^\dagger_{\mathbf{4'}}}{nU-\Delta}\Big(\,\delta_{\mathbf{2},\mathbf{3}}\,\delta_{\mathbf{4'},\mathbf{1'}}-(\mathcal{R}^\dagger\mathcal{R})_{\mathbf{2},\mathbf{1'}}\,(\mathcal{R}^\dagger\mathcal{R})_{\mathbf{4'},\mathbf{3}}\,\Big)\Bigg]\end{aligned} \tag{B.26}$$

At this stage, to compare these with the term of the "non-primed" paths, it is convenient to adopt the following relabelling

$$\begin{aligned}&\mathbf{1'}\to\mathbf{3'} \qquad \mathbf{2}\to\mathbf{4} \\ &\mathbf{4'}\to\mathbf{2'} \qquad \mathbf{3}\to\mathbf{1}\end{aligned} \tag{B.27}$$

that is

$$\begin{aligned}\hat{h}^{4th}_{\mathbf{(a')},\mathbf{(b')},\mathbf{(c')}} = \frac{V_{3'}V_4V_1V_{2'}}{(nU-\Delta)^2}\Bigg[&\frac{\hat{f}_{\mathbf{3'}}\,\hat{f}^\dagger_{\mathbf{4}}\,\hat{f}_{\mathbf{1}}\,\hat{f}^\dagger_{\mathbf{2'}}}{U}\,(\mathcal{R}^\dagger\mathcal{R})_{\mathbf{4},\mathbf{3'}}\,(\mathcal{R}^\dagger\mathcal{R})_{\mathbf{2'},\mathbf{1}} \\ &+\frac{\hat{f}_{\mathbf{3'}}\,\hat{f}_{\mathbf{1}}\,\hat{f}^\dagger_{\mathbf{4}}\,\hat{f}^\dagger_{\mathbf{2'}}}{nU-\Delta}\Big(\,\delta_{\mathbf{4},\mathbf{1}}\,\delta_{\mathbf{2'},\mathbf{3'}}-(\mathcal{R}^\dagger\mathcal{R})_{\mathbf{4},\mathbf{3'}}\,(\mathcal{R}^\dagger\mathcal{R})_{\mathbf{2'},\mathbf{1}}\,\Big)\Bigg]\end{aligned} \tag{B.28}$$

Here we recopy **(a)**, **(b)** and **(c)** for direct comparison

$$\hat{h}^{4th}_{\mathbf{(a)},\mathbf{(b)},\mathbf{(c)}} = \frac{V_1 V_{2'} V_{3'} V_4}{(nU-\Delta)^2}\Bigg[\frac{\hat{f}_{\mathbf{1}}\,\hat{f}^{\dagger}_{\mathbf{2'}}\,\hat{f}_{\mathbf{3'}}\,\hat{f}^{\dagger}_{\mathbf{4}}}{U}\,(\mathcal{R}^{\dagger}\mathcal{R})_{\mathbf{2'},\mathbf{1}}\,(\mathcal{R}^{\dagger}\mathcal{R})_{\mathbf{4},\mathbf{3'}} + \frac{\hat{f}_{\mathbf{1}}\,\hat{f}_{\mathbf{3'}}\,\hat{f}^{\dagger}_{\mathbf{2'}}\,\hat{f}^{\dagger}_{\mathbf{4}}}{nU-\Delta}\Big(\delta_{\mathbf{2'},\mathbf{3'}}\,\delta_{\mathbf{4},\mathbf{1}} - (\mathcal{R}^{\dagger}\mathcal{R})_{\mathbf{2'},\mathbf{1}}\,(\mathcal{R}^{\dagger}\mathcal{R})_{\mathbf{4},\mathbf{3'}}\,.\Big)\Bigg] \tag{B.29}$$

To look exactly the same we need to swap the rotation matrices and use double commutations for the operators which act on different sites (so that the overall sign is preserved). These are $\hat{f}_{\mathbf{3'}}\,\hat{f}^{\dagger}_{\mathbf{4}}\,\hat{f}_{\mathbf{1}}\,\hat{f}^{\dagger}_{\mathbf{2'}} = \hat{f}_{\mathbf{1}}\,\hat{f}^{\dagger}_{\mathbf{2'}}\hat{f}_{\mathbf{3'}}\,\hat{f}^{\dagger}_{\mathbf{4}}$ and $\hat{f}_{\mathbf{3'}}\,\hat{f}_{\mathbf{1}}\,\hat{f}^{\dagger}_{\mathbf{4}}\,\hat{f}^{\dagger}_{\mathbf{2'}} = \hat{f}_{\mathbf{1}}\,\hat{f}_{\mathbf{3'}}\,\hat{f}^{\dagger}_{\mathbf{2'}}\,\hat{f}^{\dagger}_{\mathbf{4}}$, so that the final result of all the paths together is basically twice the one given for a, b and c

$$\hat{h}^{4th}_{full} = 2\,\frac{V_1 V_{2'} V_{3'} V_4}{(nU-\Delta)^2}\Bigg[\frac{\hat{f}_{\mathbf{1}}\,\hat{f}^{\dagger}_{\mathbf{2'}}\,\hat{f}_{\mathbf{3'}}\,\hat{f}^{\dagger}_{\mathbf{4}}}{U}\,(\mathcal{R}^{\dagger}\mathcal{R})_{\mathbf{2'},\mathbf{1}}\,(\mathcal{R}^{\dagger}\mathcal{R})_{\mathbf{4},\mathbf{3'}} + \frac{\hat{f}_{\mathbf{1}}\,\hat{f}_{\mathbf{3'}}\,\hat{f}^{\dagger}_{\mathbf{2'}}\,\hat{f}^{\dagger}_{\mathbf{4}}}{nU-\Delta}\Big(\delta_{\mathbf{2'},\mathbf{3'}}\,\delta_{\mathbf{4},\mathbf{1}} - (\mathcal{R}^{\dagger}\mathcal{R})_{\mathbf{2'},\mathbf{1}}\,(\mathcal{R}^{\dagger}\mathcal{R})_{\mathbf{4},\mathbf{3'}}\Big)\Bigg] \tag{B.30}$$

At this stage we only need to work on the arrangement of the operators as they appear in Onoda's work [30]. Hence first we focus on the string of operators for the path **(a)**.

$$\begin{aligned}\hat{f}_{\mathbf{1}}\,\hat{f}^{\dagger}_{\mathbf{2'}}\,\hat{f}_{\mathbf{3'}}\,\hat{f}^{\dagger}_{\mathbf{4}} &= \hat{f}_{\mathbf{1}}\,\hat{f}^{\dagger}_{\mathbf{4}}\,\hat{f}^{\dagger}_{\mathbf{2'}}\,\hat{f}_{\mathbf{3'}} = (\delta_{\mathbf{1},\mathbf{4}} - \hat{f}^{\dagger}_{\mathbf{4}}\,\hat{f}_{\mathbf{1}})\hat{f}^{\dagger}_{\mathbf{2'}}\,\hat{f}_{\mathbf{3'}}\\ &= \delta_{\mathbf{1},\mathbf{4}}\,\hat{f}^{\dagger}_{\mathbf{2'}}\,\hat{f}_{\mathbf{3'}} - \hat{f}^{\dagger}_{\mathbf{4}}\,\hat{f}_{\mathbf{1}}\,\hat{f}^{\dagger}_{\mathbf{2'}}\,\hat{f}_{\mathbf{3'}}\,,\end{aligned} \tag{B.31}$$

analogously for the term representing **(b)** and **(c)**

$$\begin{aligned}\hat{f}_{\mathbf{1}}\,\hat{f}_{\mathbf{3'}}\,\hat{f}^{\dagger}_{\mathbf{2'}}\,\hat{f}^{\dagger}_{\mathbf{4}} &= \hat{f}_{\mathbf{1}}\,\hat{f}^{\dagger}_{\mathbf{4}}\,\hat{f}_{\mathbf{3'}}\,\hat{f}^{\dagger}_{\mathbf{2'}} = (\delta_{\mathbf{1},\mathbf{4}} - \hat{f}^{\dagger}_{\mathbf{4}}\,\hat{f}_{\mathbf{1}})(\delta_{\mathbf{3'},\mathbf{2'}} - \hat{f}^{\dagger}_{\mathbf{2'}}\,\hat{f}_{\mathbf{3'}})\\ &= \delta_{\mathbf{1},\mathbf{4}}\,\delta_{\mathbf{3'},\mathbf{2'}} - \delta_{\mathbf{1},\mathbf{4}}\,\hat{f}^{\dagger}_{\mathbf{2'}}\,\hat{f}_{\mathbf{3'}} - \hat{f}^{\dagger}_{\mathbf{4}}\,\hat{f}_{\mathbf{1}}\,\delta_{\mathbf{3'},\mathbf{2'}} + \hat{f}^{\dagger}_{\mathbf{4}}\,\hat{f}_{\mathbf{1}}\,\hat{f}^{\dagger}_{\mathbf{2'}}\,\hat{f}_{\mathbf{3'}}\end{aligned} \tag{B.32}$$

To be complete we group first the (*spurious*) lower order terms first

$$\hat{h}^{4th}_{spurious} = 2\,\frac{V_1 V_{2'} V_{3'} V_4}{(nU-\Delta)^2}\Bigg[\frac{\delta_{\mathbf{1},\mathbf{4}}\,\hat{f}^{\dagger}_{\mathbf{2'}}\,\hat{f}_{\mathbf{3'}}}{U}\,(\mathcal{R}^{\dagger}\mathcal{R})_{\mathbf{2'},\mathbf{1}}\,(\mathcal{R}^{\dagger}\mathcal{R})_{\mathbf{4},\mathbf{3'}} + \frac{\delta_{\mathbf{1},\mathbf{4}}\,\delta_{\mathbf{3'},\mathbf{2'}} - \delta_{\mathbf{1},\mathbf{4}}\,\hat{f}^{\dagger}_{\mathbf{2'}}\,\hat{f}_{\mathbf{3'}} - \hat{f}^{\dagger}_{\mathbf{4}}\,\hat{f}_{\mathbf{1}}\,\delta_{\mathbf{3'},\mathbf{2'}}}{nU-\Delta}\Big(\delta_{\mathbf{2'},\mathbf{3'}}\,\delta_{\mathbf{4},\mathbf{1}} - (\mathcal{R}^{\dagger}\mathcal{R})_{\mathbf{2'},\mathbf{1}}\,(\mathcal{R}^{\dagger}\mathcal{R})_{\mathbf{4},\mathbf{3'}}\Big)\Bigg] \tag{B.33}$$

and then in the following we only focus in the terms involving the effective exchange (the fourth-order ones).

Here we only replace the fourth-order terms

$$\begin{aligned}\hat{h}_{exc} = 2\,\frac{V_1V_{2'}V_{3'}V_4}{(nU-\Delta)^2}\Bigg[&\frac{-\hat{f}^\dagger_{\mathbf{4}}\,\hat{f}_{\mathbf{1}}\,\hat{f}^\dagger_{\mathbf{2'}}\,\hat{f}_{\mathbf{3'}}}{U}\,(\mathcal{R}^\dagger\mathcal{R})_{\mathbf{2',1}}\,(\mathcal{R}^\dagger\mathcal{R})_{\mathbf{4,3'}}\\&+\frac{\hat{f}^\dagger_{\mathbf{4}}\,\hat{f}_{\mathbf{1}}\,\hat{f}^\dagger_{\mathbf{2'}}\,\hat{f}_{\mathbf{3'}}}{nU-\Delta}\Big(\delta_{\mathbf{2',3'}}\,\delta_{\mathbf{4,1}}-(\mathcal{R}^\dagger\mathcal{R})_{\mathbf{2',1}}\,(\mathcal{R}^\dagger\mathcal{R})_{\mathbf{4,3'}}\Big)\Bigg]\\
=\,2\,\frac{V_1V_{2'}V_{3'}V_4}{(nU-\Delta)^2}\,\hat{f}^\dagger_{\mathbf{4}}\,\hat{f}_{\mathbf{1}}\,\hat{f}^\dagger_{\mathbf{2'}}\,\hat{f}_{\mathbf{3'}}\Bigg[&\frac{-1}{U}\,(\mathcal{R}^\dagger\mathcal{R})_{\mathbf{2',1}}\,(\mathcal{R}^\dagger\mathcal{R})_{\mathbf{4,3'}}\\&+\frac{1}{nU-\Delta}\Big(\delta_{\mathbf{2',3'}}\,\delta_{\mathbf{4,1}}-(\mathcal{R}^\dagger\mathcal{R})_{\mathbf{2',1}}\,(\mathcal{R}^\dagger\mathcal{R})_{\mathbf{4,3'}}\Big)\Bigg]\\
=\,2\,\frac{V_1V_{2'}V_{3'}V_4}{(nU-\Delta)^2}\,\hat{f}^\dagger_{\mathbf{4}}\,\hat{f}_{\mathbf{1}}\,\hat{f}^\dagger_{\mathbf{2'}}\,\hat{f}_{\mathbf{3'}}\Bigg[&\frac{1}{nU-\Delta}\delta_{\mathbf{2',3'}}\,\delta_{\mathbf{4,1}}\\&-\Big(\frac{1}{nU-\Delta}+\frac{1}{U}\Big)(\mathcal{R}^\dagger\mathcal{R})_{\mathbf{2',1}}\,(\mathcal{R}^\dagger\mathcal{R})_{\mathbf{4,3'}}\Bigg]\end{aligned}\tag{B.34}$$

which is the same as the one in Onoda's apart for an overall minus sign (this can be due to the different sign convention in switching between local to global, or more precisely in switching from antiferromagnetic to ferromagnetic Hamiltonians- to investigate). Here we rewrite it more explicitly in the same form:

$$\begin{aligned}\hat{h}^{4th}_{exc} = -2\,\frac{V_1V_{2'}V_{3'}V_4}{(nU-\Delta)^2}\,&\hat{f}^\dagger_{\mathbf{4}}\,\hat{f}_{\mathbf{1}}\,\hat{f}^\dagger_{\mathbf{2'}}\,\hat{f}_{\mathbf{3'}}\\&\times\Bigg[-\frac{1}{nU-\Delta}\delta_{\mathbf{2',3'}}\,\delta_{\mathbf{4,1}}\\&\quad+\Big(\frac{1}{nU-\Delta}+\frac{1}{U}\Big)(\mathcal{R}^\dagger\mathcal{R})_{\mathbf{2',1}}\,(\mathcal{R}^\dagger\mathcal{R})_{\mathbf{4,3'}}\Bigg]\end{aligned}\tag{B.35}$$

At this stage we can relabel the indices to use the same notation as Onoda's

$$\begin{aligned}\mathbf{2'}\to\mathbf{1'}\qquad&\mathbf{4}\to\mathbf{1}\\\mathbf{3'}\to\mathbf{2'}\qquad&\mathbf{1}\to\mathbf{2}\end{aligned}\tag{B.36}$$

that is

$$\begin{aligned}\hat{h}^{4th}_{exc} = -2\,\frac{V_1V_{1'}V_2V_{2'}}{(nU-\Delta)^2}\,&\hat{f}^\dagger_{\mathbf{1}}\,\hat{f}_{\mathbf{2}}\,\hat{f}^\dagger_{\mathbf{1'}}\,\hat{f}_{\mathbf{2'}}\\&\times\Bigg[-\frac{1}{nU-\Delta}\delta_{\mathbf{1,2}}\,\delta_{\mathbf{1',2'}}\\&\quad+\Big(\frac{1}{nU-\Delta}+\frac{1}{U}\Big)(\mathcal{R}^\dagger\mathcal{R})_{\mathbf{1,2'}}\,(\mathcal{R}^\dagger\mathcal{R})_{\mathbf{1',2}}\,.\Bigg]\end{aligned}\tag{B.37}$$

This, apart for the minus sign, for $n = 2$ electrons in the $4f$ shell, is equivalent to the main term in Eq.(17) for the case of Pr^{3+} in Onoda's work [30]. Such equivalence in shown more explicitly through Eqs. (4.71-4.75) in section 4.4.3 in the main text.

Bibliography

[1] P. W. Anderson, *Science* **177**, 393 (1972).

[2] X.-G. Wen, *Quantum Field Theory of Many-Body Systems: From the Origin of Sound to an Origin of Light and Electrons* (OUP Oxford, 2004).

[3] K. Huang, *Statistical mechanics* (Wiley, 1987).

[4] J. Vannimenus, G. Toulouse, *J Phys C* **10**, 537 (1977).

[5] S. T. Bramwell, M. J. P. Gingras, *Science* **294**, 1495 (2001).

[6] J. S. Gardner, M. J. P. Gingras, J. E. Greedan, *Reviews of Modern Physics* **82**, 53 (2010).

[7] M. A. Subramanian, A. W. Sleight, J. Karl A. Gschneidner, L. Eyring, *Chapter 107 Rare earth pyrochlores* (Elsevier, 1993), vol. Volume 16, pp. 225–248.

[8] A. P. Ramirez, A. Hayashi, R. J. Cava, R. B. Siddharthan, S. Shastry, *Nature* **399**, 333 (1999).

[9] M. J. Harris, S. T. Bramwell, D. F. McMorrow, T. Zeiske, K. W. Godfrey, *Physical Review Letters* **79**, 2554 (1997).

[10] M. Harris, *Nature* **399**, 311 (1999).

[11] M. J. Harris, S. T. Bramwell, P. C. W. Holdsworth, J. D. M. Champion, *Physical Review Letters* **81**, 4496 (1998).

[12] S. T. Bramwell, *et al.*, *Physical Review Letters* **87**, 047205 (2001).

[13] C. Castelnovo, R. Moessner, S. L. Sondhi, *Nature* **451**, 42 (2008).

[14] H. Aoki, T. Sakakibara, K. Matsuhira, Z. Hiroi, *J. Phys. Soc. Jpn* **73**, 2851 (2004).

[15] T. Fennell, *et al.*, *Science* **326**, 415 (2009).

[16] D. J. P. Morris, *et al.*, *Science* **326**, 411 (2009).

[17] S. T. Bramwell, *et al.*, *Nature* **461**, 956 (2009).

[18] S. R. Dunsiger, *et al.*, *Physical Review Letters* **107**, 207207 (2011).

[19] K. Matsuhira, *et al.*, *Journal of the Physical Society of Japan* **80**, 123711 (2011).

[20] L. Bovo, J. A. Bloxsom, D. Prabhakaran, G. Aeppli, S. T. Bramwell, *Nat Commun* **4**, 1535 (2013).

[21] S. R. Giblin, S. T. Bramwell, P. C. W. Holdsworth, D. Prabhakaran, I. Terry, *Nat Phys* **7**, 252 (2011).

[22] C. Castelnovo, R. Moessner, S. L. Sondhi, *Physical Review Letters* **104**, 107201 (2010).

[23] S. Mostame, C. Castelnovo, R. Moessner, S. L. Sondhi, *Proceedings of the National Academy of Sciences* **111**, 640 (2014).

[24] C. Paulsen, *et al.*, *Nat Phys* **10**, 135 (2014).

[25] L. D. C. Jaubert, P. C. W. Holdsworth, *Nat Phys* **5**, 258 (2009).

[26] L. D. C. Jaubert, P. C. W. Holdsworth, *Journal of Physics: Condensed Matter* **23**, 164222 (2011).

[27] J. Jensen, A. R. Mackintosh, *Rare earth magnetism: Structures and excitations* (Oxford Univ. Press, Physics Laboratory, H.C. Orsted Institute, Copenhagen University, Denmark, 1991).

[28] J. Mulak, Z. Gajek, *The Effective Crystal Field Potential* (Elsevier Science, 2000).

[29] G. Liu, B. Jacquier, *Spectroscopic Properties of Rare Earths in Optical Materials* (Springer, 2006).

[30] S. Onoda, Y. Tanaka, *Physical Review B* **83**, 094411 (2011).

[31] W. H. Zurek, *Los Alamos Science* **27**, 86 (2002).

[32] S. Bertaina, *et al.*, *Nat Nano* **2**, 39 (2007).

[33] B. Barbara, *Philosophical Transactions of the Royal Society of London A: Mathematical, Physical and Engineering Sciences* **370**, 4487 (2012).

[34] T. Miyamachi, *et al.*, *Nature* **503**, 242 (2013).

[35] T. Hahn, ed., *International Tables for Crystallography Volume A: Space-group symmetry*, vol. Volume A (Springer, 2006).

[36] M. Hutchings, F. Seitz, D. Turnbull **16**, 227 (1964).

[37] C. Görller-Walrand, K. Binnemans, *Handbook on the Physics and Chemistry of Rare Earths*, J. Karl A. Gschneidner, L. Eyring, eds. (Elsevier, North-Holland, Amsterdam, 1996), vol. 23, chap. 155, pp. 121–283.

[38] J. Sakurai, *Modern Quantum Mechanics (Revised Edition)* (Addison Wesley, 1993).

[39] H. Margeau, M. Murphy, *The Mathematics of Physics and Chemestry* (Van Nostrand, 1956).

[40] K. Takegahara, *Journal of the Physical Society of Japan* **69**, 1572 (2000).

[41] A. J. Freeman, R. E. Watson, *Physical Review* **127**, 2058 (1962).

[42] A. J. Freeman, J. P. Desclaux, *Journal of Magnetism and Magnetic Materials* **12**, 11 (1979).

[43] B. G. Wybourne, *Spectroscopic Properties of Rare Earths* (Interscience, New York, 1965).

[44] S. Hüfner, *Optical spectra of transparent rare earth compounds* (Academic Press, 1978).

[45] S. Rosenkranz, *et al.*, *Journal of Applied Physics* **87**, 5914 (2000).

[46] K. W. H. Stevens, *Proceedings of the Physical Society. Section A* **65**, 209 (1952).

[47] A. J. Kassman, *J. Chem. Phys.* **53**, 4118 (1970).

[48] B. Malkin, T. Lummen, P. van Loosdrecht, G. Dhalenne, A. Zakirov, *Journal of physics. Condensed matter: an Institute of Physics journal* **22**, 276003 (2010).

[49] G. Sala, *et al.*, *Physical Review Letters* **108**, 217203 (2012).

[50] C. Hooley, J. Quintanilla, *Physical Review Letters* **93**, 080404 (2004).

[51] J. Jackson, *Classical Electrodynamics - Third Edition* (Wiley, 1998).

[52] B. C. den Hertog, M. J. P. Gingras, *Physical Review Letters* **84**, 3430 (2000).

[53] S. Blundell, *Magnetism in Condensed Matter (Oxford Master Series in Physics)* (Oxford University Press, USA, 2001).

[54] R. White, *Quantum Theory of Magnetism: Magnetic Properties of Materials*, Springer Series in Solid-State Sciences (Springer, 2007).

[55] N. Ashcroft, D. Mermin, *Solid state physics* (Thomson Learning, Toronto, 1976).

[56] J. Annett, *Superconductivity, Superfluids and Condensates*, Oxford Master Series in Physics (OUP Oxford, 2004).

[57] A. Fetter, J. Walecka, *Quantum Theory of Many-Particle Systems* (McGraw-Hill, 1971).

[58] E. Fradkin, *Field Theories of Condensed Matter Physics* (Addison Wesley Publishing Company, 1991).

[59] S. Onoda, Y. Tanaka, *Physical Review Letters* **105**, 047201 (2010).

[60] E. Pavarini, E. Koch, U. Schollwöck, *Emergent Phenomena in Correlated Matter: Autumn School at the Forschungszentrum Jülich*, Schriften des Forschungszentrums Jülich / Reihe Modeling and Simulation: Reihe Modeling and Simulation (Forschungszentrum Jülich, Inst. for Advanced Simulation, 2013).

[61] S. T. Bramwell, M. Harris, *Journal of Physics: Condensed Matter* **10**, L215 (1998).

[62] S. Onoda, *Journal of Physics: Conference Series* **320**, 012065 (2011).

[63] M. A. Morrison, G. A. Parker, *Australian Journal of Physics* **40**, 465 (1987).

[64] B. H. Bransden, C. J. Joachain, *Quantum Mechanics, 2nd edition* (Addison-Wesley, 2000).

[65] C. Cohen-Tannoudji, . Diu, Bernard, F. Laloe, *Quantum mechanics* (Wiley New York, 1977).

[66] R. R. Sharma, *Physical Review B* **19**, 2813 (1979).

[67] J. C. Slater, G. F. Koster, *Physical Review* **94**, 1498 (1954).

[68] S. Lee, S. Onoda, L. Balents, *Physical Review B* **86**, 104412 (2012).

[69] K. A. Ross, L. Savary, B. D. Gaulin, L. Balents, *Physical Review X* **1**, 021002 (2011).

[70] J. D. Thompson, *et al.*, *Physical Review Letters* **106**, 187202 (2011).

[71] O. Benton, O. Sikora, N. Shannon, *Physical Review B* **86**, 075154 (2012).

[72] D. Pomaranski, *et al.*, *Nat Phys* **9**, 353 (2013).

[73] P. McClarty, *et al.*, *ArXiv e-prints* **1410.0451** (2014).

[74] L. Bovo, *et al.*, *Nat Commun* **5** (2014).

[75] W. H. Zurek, *Reviews of Modern Physics* **75**, 715 (2003).

[76] C. Nisoli, R. Moessner, P. Schiffer, *Reviews of Modern Physics* **85**, 1473 (2013).

[77] S. Ladak, D. E. Read, G. K. Perkins, L. F. Cohen, W. R. Branford, *Nat Phys* **6**, 359 (2010).

[78] G. Ehlers, *et al.*, *Journal of Physics: Condensed Matter* **15**, L9 (2003).

[79] G. Ehlers, *et al.*, *Journal of Physics: Condensed Matter* **16**, S635 (2004).

[80] J. Lago, S. J. Blundell, C. Baines, *Journal of Physics: Condensed Matter* **19**, 326210 (2007).

[81] L. Amico, D. Rossini, A. Hamma, V. E. Korepin, *Physical Review Letters* **108**, 240503 (2012).

[82] K. Matsuhira, Y. Hinatsu, T. Sakakibara, *Journal of Physics: Condensed Matter* **13**, L737 (2001).

[83] G. Sala, *et al.*, *Nat Mater* **13**, 488 (2014).

[84] P. W. Anderson, *Physical Review* **115**, 2 (1959).

[85] R. Luzzi, *Revista Brasileira de Física* **3** (1973).

Glossary

D_{3d} Point group symmetry (antiprismatic) of the RE^{3+} ions. 13, 76

$F_{d\bar{3}m}$ Space group symmetry of the pyrochlore lattice. 12, 76

M-O-M Metal-Oxygen-Metal unit for the ligands in a metal oxyde. 70

O1 Oxygen ion in the centre of a tetrahedron with RE^{3+} ions at the vertices. 13, 75

O2 Oxygen ions surrounding a RE^{3+} ion with antiprismatic arrangement. 13, 15, 32, 108

RE-O1-RE unit for the ligands in magnetic pyrochlore oxydes. 86, 89

Acronyms

CF crystal-field. 21, 23, 26, 38, 76, 92, 108, 115

DTO Dysprosium titanate. 13, 24, 130, 136, 140

h.c. hermitian conjugate. 84, 102

HTO Holmium titanate. 13, 24, 130, 136, 140

n.n. nearest neighbour. 3, 13, 72, 88, 115, 121

RE rare earth. 3, 6, 12, 21, 136

TM transition metal. 12